University of New Mexico
UNM Digital Repository

Fall 11-3-2016

SYNTHESIS, CHARACTERIZATION, AND APPLICATION OF MONOSIZED MESOPOROUS SILICA NANOPARTICLE-SUPPORTED LIPID BILAYERS FOR TARGETED THERAPEUTIC DELIVERY TO INDIVIDUAL CELLS

Paul Durfee
University of New Mexico

Follow this and additional works at: https://digitalrepository.unm.edu/bme_etds

Part of the Biomedical Engineering and Bioengineering Commons, Materials Science and Engineering Commons, and the Other Medicine and Health Sciences Commons

Paul Nicholas Durfee

Candidate

Chemical and Biological Engineering

Department

This dissertation is approved, and it is acceptable in quality and form for publication:

Approved by the Dissertation Committee:

C. Jeffrey Brinker, Ph.D., Chairperson

Bryce Chackerian, Ph.D.

Robert Rubin, Ph.D.

Pavan Muttil, Ph.D.

SYNTHESIS, CHARACTERIZATION, AND APPLICATION OF MONOSIZED MESOPOROUS SILICA NANOPARTICLE-SUPPORTED LIPID BILAYERS FOR TARGETED THERAPEUTIC DELIVERY TO INDIVIDUAL CELLS

by

PAUL NICHOLAS DURFEE

B.S. Biochemistry, University of New Mexico, 2004

M.S. Nanoscience and Microsystems, University of New Mexico, 2011

DISSERTATION

Submitted in Partial Fulfillment of the Requirements for the Degree of

Doctor of Philosophy Engineering

The University of New Mexico Albuquerque, New Mexico

December, 2016

DEDICATION

This dissertation is dedicated to my Family.

In particular

Nonni and Nonno Abramo,
Grandma and Grandad Durfee,

Louise and Greg,
Andrea,

Betty and Arturo,

Ana and Nichole,

Crisanto, Camillo, Ignacio, and all future Durflings that have yet to arrive on this planet,

and

Marisa, you have been my inspiration, my motivation, my partner, my support, you have sacrificed so much, and your guidance has always helped me achieve more than I ever could have imagined.

ACKNOWLEDGMENTS

Dr. Kimberly Butler and I met when she was a graduate student and I was an undergraduate student many years ago. As luck would have it, our paths crossed again when she joined the Brinker Lab. Conversations with Kim are never dull, and she has helped me so much with my research and writing. Many of the experiments described in this dissertation couldn't have been possible without Kim's help.

Finally, thank you to my family and friends for all of the support you have given me. Mom and Dad, I know raising me was difficult, but look, I earned a PhD so it was worth it, good job.

Marisa, I know this took a long time, and without your help I think I would still be waiting tables, my appreciation for you cannot be overstated, you do so much for me and our family and I am eternally grateful, best wife ever.

SYNTHESIS, CHARACTERIZATION, AND APPLICATION OF MONOSIZED MESOPOROUS SILICA NANOPARTICLE-SUPPORTED LIPID BILAYERS FOR TARGETED THERAPEUTIC DELIVERY TO INDIVIDUAL CELLS

by

Paul Nicholas Durfee

B.S. Biochemistry, University of New Mexico, 2004

M.S. Nanoscience and Microsystems, University of New Mexico, 2011

Ph.D. Engineering, University of New Mexico, 2016

ABSTRACT

Mesoporous silica nanoparticle (MSNP) supported-lipid bilayers, termed 'protocells,' represent a potentially transformative class of therapeutic and theranostic delivery vehicles. The field of targeted drug delivery poses considerable challenges that cannot be addressed with a single 'magic bullet'. Consequently, the protocell has been designed as a modular platform composed of interchangeable biocompatible components. The mesoporous silica core can have variable size and shape to direct biodistribution and controlled pore size and surface chemistry to accommodate diverse cargos. The encapsulating supported lipid bilayer can be modified with targeting and trafficking ligands as well as polyethylene glycol (PEG) to effect selective binding, endosomal escape of cargo, drug efflux prevention, and potent therapeutic delivery, while maintaining *in vivo* colloidal stability. Many nanocarrier cancer therapeutics currently under development, as well as those used in the clinical setting, rely

upon the enhanced permeability and retention (EPR) effect to passively accumulate in the tumor microenvironment and kill cancer cells. In leukemia, where leukemogenic stem cells and their progeny circulate within the peripheral blood or bone marrow, the EPR effect may not be operative. Thus, for leukemia therapeutics, it is essential to target and bind individual circulating cells. Here, we investigate protocells, an emerging class of nanocarriers, and establish the synthesis conditions and lipid bilayer composition needed to achieve highly monodisperse protocells that remain stable in complex media as assessed *in vitro* by dynamic light scattering and cryo-electron microscopy and *ex ovo* by direct imaging within a chick chorioallantoic membrane (CAM) model. We show that for vesicle fusion conditions where the lipid surface area exceeds the external surface area of the MSNP and the ionic strength exceeds 20 mM, we form monosized protocells (polydispersity index < 0.1) on MSNP cores with varying size, shape, and pore size, whose conformal zwitterionic supported lipid bilayer confers excellent stability as judged by circulation in the CAM and minimal opsonization *in vivo* in a mouse model. Having established protocell formulations that are stable colloids, we further modified them with anti-EGFR antibodies as targeting agents and re-verified their monodispersity and stability. Then using intravital imaging in the CAM we directly observed in real time the progression of selective targeting of individual leukemia cells (using the established REH leukemia cell line transduced with EGFR) and delivery of a model cargo. Overall we have established the effectiveness of the protocell platform for individual cell targeting and delivery needed for leukemia and other disseminated disease.

TABLE OF CONTENTS

LIST OF FIGURES

LIST OF TABLES

LIST OF ABBREVIATIONS

ζ: Zeta Potential

≡Si-O⁻: Deprotonated Silanol Group

≡Si-OH: Silanol Group

8-HQ: 8-hydroxyquinoline

ALL: Acute Lymphoblastic Leukemia

APTES: 3-aminopropyltriethoxysilane

Ba/F3: Murine B Precursor ALL Cell Line (EGFR negative)

Ba/F3-EGFR: Murine B Precursor ALL Cell Line Engineered for EGFR Surface Expression

BDHAC: Benzyldimethylhexadecylammonium Chloride

BET: Brunauer-Emmet-Teller

BJH: Barrett-Joyer-Halenda

BCRP: Breast Cancer Resistance Protein

CAM: Chorioallantoic Membrane

C-Dots: Cornell Dots

CMS: Colloidal Stable Mesoporous Silica Nanoparticles

Cryo-TEM: Cryogenic Transmission Electron Microscopy

CTAB: Cetyltrimethylammonium Bromide (Surfactant)

CTAC: Cetyltrimethylammonium Chloride (Surfactant)

DAPI: 4',6-Diamidino-2-Phenylindole, Dihydrochloride (Blue Nuclear Stain)

DLS: Dynamic Light Scattering

DLVO: Derjaguin-Landau-Verwey-Overbeek

DMEM: Dulbecco's Modified Eagle Medium

DMF: N,N-Dimethyl Formamide

DMPC: 1,2-dimyristoyl-sn-glycero-3-phosphocholine

DMSO: Dimethyl Sulfoxide

DOPC: 1,2-dioleoyl-sn-glycero-3-phosphocholine

DOPE: 1,2-dioleoyl-sn-glycero-3-phosphoethanolamine

DOPE-PEG₂₀₀₀: 1,2-dioleoyl-sn-glycero-3-phosphoethanolamine-N-[methoxy(polyethylene glycol)-2000] (ammonium salt)

DOPS: 1,2-dioleoyl-sn-glycero-3-phospho-L-serine

DOTAP: 1,2-dioleoyl-3-trimethylammonium-propane

DOX: Doxorubicin

DPPC: 1,2-dipalmitoyl-sn-glycero-3-phosphocholine

DPPE: 1,2-dipalmitoyl-sn-glycero-3-phosphoethanolamine

DSC: Differential Scanning Calorimetry

DSPC: 1,2-distearoyl-sn-glycero-3-phosphocholine

DSPE-PEG$_{2000}$: 1,2-distearoyl-sn-glycero-3-phosphoethanolamine-N-[methoxy(polyethylene glycol)-2000] (ammonium salt)

DSPE-PEG$_{2000}$-NH$_2$: 1,2-distearoyl-sn-glycero-3-phosphoethanolamine-N-[amino(polyethylene glycol)-2000]

DTX: Docetaxel

EA.hy926: Human Endothelial Cell Line

EDTA: Ethylenediaminetetraacetic Acid

EGFR: Epidermal Growth Factor Receptor

EISA: Evaporation Induced Self-Assembly

EPR: Enhanced Permeability and Retention

FBS: Fetal Bovine Serum

FTIR: Fourier Transform Infrared Spectroscopy

GEM: Gemcitabine

GRAS: Generally Recognized as Safe

HA: Hyaluronan

Hep3B: Human Hepatocelluar Carcinoma Cell Line

His: Histidine

hRBC: Human Red Blood Cells

K$_d$: Dissociation Constant

MCM-41: Mobil Composition of Matter No. 41

MDR: Multidrug Resistant

mMSNP: Monosized Mesoporous Silica Nanoparticle

MOLT4: Human T Cell Leukemia Cell Line (CD19 negative)

MOLT4-CD19: Human T Cell Leukemia Cell Line Engineered for CD19 Surface Expression

MRI: Magnetic Resonance Imaging

mRNA: Messenger Ribonucleic Acid

MSNP: Mesoporous Silica Nanoparticle

NALM6: Human B Cell Precursor Leukemia (CD19 positive)

NBD-Chol: 22-(N-(7-Nitrobenz-2-Oxa-1,3-Diazol-4-yl)Amino)-23,24-Bisnor-5-Cholen-3β-Ol

NIBS: Non-Invasive Backscatter Optics

PdI: Polydispersity Index

PEG: Polyethylene glycol

PEGylated: Polyethylene glycol-modified

PET: Positron Emission Tomography

POPC: 1-palmitoyl-2-oleoyl-sn-glycero-3-phosphocholine

PS: Penicillin Streptomycin

REH: Human B Cell Precursor ALL Cell Line (EGFR negative)

REH-EGFR: Human B Cell Precursor ALL Cell Line Engineered for EGFR Surface Expression

RITC: Rhodamine B Isothiocyanate

SA: Surface Area

scFv: Single Chain Variable Fragment

SD: Standard Deviation

siRNA: Small Interfering Ribonucleic Acid

shRNA: Short Hairpin Ribonucleic Acid

SLB: Supported Lipid Bilayer

SPECT: Single-Photon Emission Computed Tomography

TEA: Triethanolamine

TEOS: Tetraethyl Orthosilicate

TEM: Transmission Electron Microscopy

T_m: Transition Temperature

TPGS: D-α-tocopherol polyethylene glycol 1000 succinate

YO-PRO®-1: Green-Fluorescent Carbocyanine Nucleic Acid Stain

GOALS AND SUMMARY OF CONTRIBUTIONS

Acute lymphoblastic leukemia (ALL), is a disease characterized by malignant lymphocyte proliferation resulting in the suppression of normal hematopoiesis, and is the most common type of childhood cancer, generally occurring between the ages of 3 and 5. Treatment of pediatric leukemias have been described as one of the true success stories of modern medicine, with current treatment strategies resulting in survival rates exceeding 90 %.[1] The success of ALL treatment has come through the progressive increase in chemotherapy and the development of a risk classification scheme to identify children to more dose-intensive regimes based on calculated probability of relapse based on a specific set of identified prognostic factors including age and white blood cell counts.[2] Regardless of these advances, standard treatment methods lead to complications due to the non-specific action of chemotherapeutic agents on healthy normal cells.[3] In addition, the ~ 10 % of children that do not respond to therapy, or those who relapse, have poor prognostic outcomes despite efforts to intensify therapy including stem cell transplantation.[4-6] Next generation therapies must be developed to improve survival rates and quality of life. The pharmacological properties of traditional chemotherapeutics can be improved through targeted delivery using nanocarriers.[7-9] Passive targeting strategies, utilizing the enhanced permeability and retention (EPR) effect,[10] whereby the permeability of the tumor vasculature can direct the accumulation of nanoparticles, have overcome many of the problems associated with 'free' drugs, however they still lack cell-specific

interactions which can result in off-target effects.[11] More importantly, not all tumors exhibit an EPR effect; for example, in leukemia, leukemogenic stem cells and their progeny circulate within the peripheral blood or bone marrow, thus the EPR effect may not be operative.[12] The ability to target, bind, internalize, and delivery therapeutic cargo to individual circulating cells is critical to the future of leukemia treatment.

Early generation (i.e. polydisperse) mesoporous silica nanoparticle-supported lipid bilayers (protocells) displayed multiple promising characteristics with enhanced efficacy *in vitro* relative to liposome formulations alone, including highly specific and efficient delivery of multiple classes and combinations of cargos to several cell types.[9, 13, 14] However, the polydispersity of the first generation protocell severely limited the *in vivo* utility. Therefore, the principal goal of my graduate work was to develop, characterize, and optimize an in vivo stable nanocarrier platform capable of therapeutic delivery to individual leukemia cells with a high degree of selectivity and minimal side-effects, enabling a major step forward in leukemia treatment. To achieve this goal, I needed a platform that could simultaneously address the numerous requirements of targeted delivery, including cell specificity, nanoparticle stability, effective cargo capacity, multicomponent delivery, biocompatibility, size/shape control, prolonged circulation, and immune evasion. Although the majority of protocell studies conducted had reported *in vitro* efficacy,[13-15] more recently, reports had shown promising *in vivo* results, where passive and active targeting to solid tumors via the EPR effect had been demonstrated.[16-19] Prior to the work reported in my

dissertation, the targeting of individual cells *in vivo* or in living systems had yet to be reported, and there had been no direct observations/determinations of *in vivo* colloidal stability.

The work detailed in Chapter 1 and Chapter 6, was published as a review article, Protocells: Modular Mesoporous Silica Nanoparticle-Supported Lipid Bilayers for Drug Delivery, in the scientific journal Small. As the co-first author, I shared the majority of the literature research, writing, and revisions of this review equally with Dr. Kimberly Butler. Dr. Christophe Theron, helped research protocell targeting chemistries, and Dr. C. Jeffrey Brinker assisted in manuscript writing, review, and approval.

The work detailed in Chapters 2 – 6, was published as a research article, Mesoporous Silica Nanoparticle-Supported Lipid Bilayers (Protocells) for Active Targeting and Delivery to Individual Leukemia Cells, in the scientific journal ACS Nano. As the primary author of this article, I performed the majority of this research at the University of New Mexico. I wish to acknowledge contributions made by the following individuals. The original protocell concept was conceived of by Dr. C. Jeffrey Brinker and engineered for use in biomedical application for transfection by Dr. Juewen Liu, and further developed for targeted cargo delivery *in vitro* by Dr. Carlee Ashley.

Dr. Yu-Shen Lin designed and engineered the monosized MSNP synthesis procedures used for the core component of the monosized protocell platform and provided me with mentorship and guidance for nanoparticle

synthesis techniques. In addition, he assisted in many of the characterization techniques, the hemolysis assay, several transmission electron microscopy (TEM) images, contributed many ideas through helpful scientific discussions, and careful review and editing of the final manuscript. Dr. Darren Dunphy performed all cryogenic transmission electron microscopy (Cryo-TEM) imaging and cryo sample preparation. Ayse Muniz assisted in the *ex ovo* experiments; helping with embryo maintenance and cell/protocell injections. Dr. Kimberly Butler assisted in several of the *in vitro* and *ex ovo* experiments, provided ideas through scientific discussions, and assisted in the writing and review of this manuscript. Kevin Humphrey assisted in protocell drug loading and verified the mathematical calculations used to assess the surface area ratio of lipid to silica. Amanda Lokke helped to synthesize and provide large pore MSNPs. Dr. Jacob Agola and Dr. Stanley Chou provided helpful ideas through discussions, and provided careful review of the manuscript. Dr. I-Ming Chen provided flow cytometry support that was useful in developing the targeted nanoparticle platform, and Dr. Walker Wharton maintained and provided cells (REH, REH-EGFR, Ba/F3, Ba/F3-EGFR, MOLT4, MOLT4-CD19, and NALM6) as well as helpful ideas through scientific discussions. Dr. Jason Townson introduced the *ex ovo* chicken embryo technology to the Brinker Lab and provided microscopy and *ex ovo* embryo support for the manuscript. Dr. Cheryl Willman provided financial support and review of the manuscript. Dr. C. Jeffrey Brinker also provided financial, laboratory, and material support, mentorship, assisted in the writing, review, and approval of the manuscript. In addition, Dr. Brinker provided guidance and

overall advice on the project development and direction.

References

1. Hunger, S. P.; Lu, X.; Devidas, M.; Camitta, B. M.; Gaynon, P. S.; Winick, N. J.; Reaman, G. H.; Carroll, W. L. Improved Survival for Children and Adolescents with Acute Lymphoblastic Leukemia between 1990 and 2005: A Report from the Children's Oncology Group. *Journal of Clinical Oncology* 2012, JCO. 2011.37. 8018.

2. Smith, M.; Arthur, D.; Camitta, B.; Carroll, A. J.; Crist, W.; Gaynon, P.; Gelber, R.; Heerema, N.; Korn, E. L.; Link, M. Uniform Approach to Risk Classification and Treatment Assignment for Children with Acute Lymphoblastic Leukemia. *Journal of Clinical Oncology* 1996, 14, 18-24.

3. Oeffinger, K. C.; Hudson, M. M. Long-Term Complications Following Childhood and Adolescent Cancer: Foundations for Providing Risk-Based Health Care for Survivors. *CA: A Cancer Journal for Clinicians* 2004, 54, 208-236.

4. Einsiedel, H. G.; von Stackelberg, A.; Hartmann, R.; Fengler, R.; Schrappe, M.; Janka-Schaub, G.; Mann, G.; Hählen, K.; Göbel, U.; Klingebiel, T. Long-Term Outcome in Children with Relapsed All by Risk-Stratified Salvage Therapy: Results of Trial Acute Lymphoblastic Leukemia-Relapse Study of the Berlin-Frankfurt-Münster Group 87. *Journal of Clinical Oncology* 2005, 23, 7942-7950.

5. Rivera, G. K.; Zhou, Y.; Hancock, M. L.; Gajjar, A.; Rubnitz, J.; Ribeiro, R. C.; Sandlund, J. T.; Hudson, M.; Relling, M.; Evans, W. E. Bone Marrow Recurrence after Initial Intensive Treatment for Childhood Acute Lymphoblastic Leukemia. *Cancer* 2005, 103, 368-376.

6. Raetz, E. A.; Bhatla, T. Where Do We Stand in the Treatment of Relapsed Acute Lymphoblastic Leukemia? *ASH Education Program Book* 2012, 2012, 129-136.

7. Allen, T. M.; Cullis, P. R. Drug Delivery Systems: Entering the Mainstream. *Science* 2004, 303, 1818-1822.

8. Peer, D.; Karp, J. M.; Hong, S.; Farokhzad, O. C.; Margalit, R.; Langer, R. Nanocarriers as an Emerging Platform for Cancer Therapy. *Nat. Nanotechnol.* 2007, 2, 751-760.

9. Butler, K. S.; Durfee, P. N.; Theron, C.; Ashley, C. E.; Carnes, E. C.; Brinker, C. J. Protocells: Modular Mesoporous Silica Nanoparticle-Supported Lipid Bilayers for Drug Delivery. *Small* 2016.

10. Matsumura, Y.; Maeda, H. A New Concept for Macromolecular Therapeutics in Cancer Chemotherapy: Mechanism of Tumoritropic

Accumulation of Proteins and the Antitumor Agent Smancs. *Cancer research* 1986, 46, 6387-6392.

11. Ferrari, M. Cancer Nanotechnology: Opportunities and Challenges. *Nature Reviews Cancer* 2005, 5, 161-171.

12. Durfee, P. N.; Lin, Y.-S.; Dunphy, D. R.; Muñiz, A. J.; Butler, K. S.; Humphrey, K. R.; Lokke, A. J.; Agola, J. O.; Chou, S. S.; Chen, I. M.; Wharton, W.; Townson, J. L.; Willman, C. L.; Brinker, C. J. Mesoporous Silica Nanoparticle-Supported Lipid Bilayers (Protocells) for Active Targeting and Delivery to Individual Leukemia Cells. *ACS Nano* 2016.

13. Ashley, C. E.; Carnes, E. C.; Phillips, G. K.; Padilla, D.; Durfee, P. N.; Brown, P. A.; Hanna, T. N.; Liu, J.; Phillips, B.; Carter, M. B.; Carroll, N. J.; Jiang, X.; Dunphy, D. R.; Willman, C. L.; Petsev, D. N.; Evans, D. G.; Parikh, A. N.; Chackerian, B.; Wharton, W.; Peabody, D. S.; Brinker, C. J. The Targeted Delivery of Multicomponent Cargos to Cancer Cells by Nanoporous Particle-Supported Lipid Bilayers. *Nat. Mater.* 2011, 10, 389-397.

14. Ashley, C. E.; Carnes, E. C.; Epler, K. E.; Padilla, D. P.; Phillips, G. K.; Castillo, R. E.; Wilkinson, D. C.; Wilkinson, B. S.; Burgard, C. A.; Kalinich, R. M.; Townson, J. L.; Chackerian, B.; Willman, C. L.; Peabody, D. S.; Wharton, W.; Brinker, C. J. Delivery of Small Interfering Rna by Peptide-Targeted Mesoporous Silica Nanoparticle-Supported Lipid Bilayers. *ACS Nano* 2012, 6, 2174-2188.

15. Epler, K.; Padilla, D.; Phillips, G.; Crowder, P.; Castillo, R.; Wilkinson, D.; Wilkinson, B.; Burgard, C.; Kalinich, R.; Townson, J.; Chackerian, B.; Willman, C.; Peabody, D.; Wharton, W.; Brinker, C. J.; Ashley, C.; Carnes, E. Delivery of Ricin Toxin a-Chain by Peptide-Targeted Mesoporous Silica Nanoparticle-Supported Lipid Bilayers. *Adv. Healthcare Mater.* 2012, 1, 348-353.

16. Meng, H.; Wang, M.; Liu, H.; Liu, X.; Situ, A.; Wu, B.; Ji, Z.; Chang, C. H.; Nel, A. E. Use of a Lipid-Coated Mesoporous Silica Nanoparticle Platform for Synergistic Gemcitabine and Paclitaxel Delivery to Human Pancreatic Cancer in Mice. *ACS Nano* 2015, 9, 3540-3557.

17. Wang, D.; Huang, J.; Wang, X.; Yu, Y.; Zhang, H.; Chen, Y.; Liu, J.; Sun, Z.; Zou, H.; Sun, D.; Zhou, G.; Zhang, G.; Lu, Y.; Zhong, Y. The Eradication of Breast Cancer Cells and Stem Cells by 8-Hydroxyquinoline-Loaded Hyaluronan Modified Mesoporous Silica Nanoparticle-Supported Lipid Bilayers Containing Docetaxel. *Biomaterials* 2013, 34, 7662-7673.

18. Zhang, X.; Li, F.; Guo, S.; Chen, X.; Wang, X.; Li, J.; Gan, Y. Biofunctionalized Polymer-Lipid Supported Mesoporous Silica

Nanoparticles for Release of Chemotherapeutics in Multidrug Resistant Cancer Cells. *Biomaterials* 2014, 35, 3650-3665.

19.　Liu, X.; Situ, A.; Kang, Y.; Villabroza, K. R.; Liao, Y.; Chang, C. H.; Donahue, T.; Nel, A. E.; Meng, H. Irinotecan Delivery by Lipid-Coated Mesoporous Silica Nanoparticles Shows Improved Efficacy and Safety over Liposomes for Pancreatic Cancer. *ACS Nano* 2016, 10, 2702-2715.

CHAPTER 1

INTRODUCTION

This chapter was adapted from
Butler, K. S.*; **Durfee, P. N.***; Theron, C.; Ashley, C. E.; Carnes, E. C.; Brinker, C. J. Protocells: Modular Mesoporous Silica Nanoparticle-Supported Lipid Bilayers for Drug Delivery. Small 2016, 12, 2173−2185. (*Authors contributed equally to this work) © 2016 Wiley-VCH Verlag GmbH & Co. KGaA, Weinheim

1.1 Overview

Targeted delivery of drugs incorporated within nanoparticles can potentially ameliorate a number of problems exhibited by conventional 'free' drugs, including poor solubility, limited stability, rapid clearing, and, in particular, lack of selectivity, which results in non-specific toxicity to healthy cells and precludes dose escalations needed to combat multiple drug resistance. An ideal targeted nanoparticle drug carrier, or "nanocarrier" should have the following combined features: 1) the capacity for carrying high levels of multiple diverse molecular cargos (small molecules, drugs with varying physiochemical properties, siRNAs, peptides, imaging agents); 2) the ability to circulate in the blood *in vivo* for extended periods without elimination by the immune or excretory systems; 3) specificity for binding only to target disease cells; 4) controlled release and intracellular trafficking of the cargo; and 5) low immunogenicity and toxicity. Additionally, as the optimal biodistribution and biological interactions of the nanocarrier can vary between different diseases (and individuals), an ideal nanocarrier should also have physical and chemical properties that can be controlled and essentially tuned for the specific application. Finally, the potential to include imaging agents as well as therapeutics presents the possibility of creating theranostics, which could allow both drug delivery and the monitoring of the course of therapy to be achieved with a single nanocarrier. In the context of creating a tunable nanocarrier that can address this wide range of requirements, nanoparticle-supported lipid bilayer constructs have a distinctive combination of

features that could potentially enable their development as a 'universal' nanocarrier that is both drug and disease agnostic.

1.2 Challenges in Nanomedicine for Nanostructured Platforms

A wide variety of nanocarrier systems have been developed for the delivery of therapeutic cargo all of which have both advantages and disadvantages, which present challenges for their ultimate clinical use. Major challenges to the successful development of nanotherapeutics include: biocompatibility, ability to load and release varied therapeutic cargos, high cargo loading capacity, the ability to circulate in blood for extended periods of time, evasion of elimination by the immune or excretory systems, specific targeting of and delivery to diseased cells, and low immunogenicity. One of the most successful nanocarrier-based approaches to date is liposomal-based drug delivery, for which there are over a dozen U.S. Food and Drug Administration (FDA) approved formulations and five approved for use in cancer.[1-4] The advantages to liposomal nanocarriers are their high biocompatibility, low immunogenicity, flexible formulation, and easy and scalable synthesis.[5-7] Additionally, the specificity of liposomal formulations can be increased by addition of targeting moieties, such as antibodies, directly to the surface of the liposomes.[2, 5-9] However, it has proven difficult to identify stable lipid formulations that allow drug encapsulation but prevent leakage, making liposomes poor 'universal' nanocarriers.[10, 11] Polymeric based therapeutic nanocarriers have also been developed, and several formulations are currently undergoing clinical trials.[2] Similar to lipid formulations, many polymer based nanocarriers are

biocompatible and easy to manufacture, however they also suffer from limited stability in *in vivo* systems and dose dependent toxicity.[12, 13] In addition to the issues specific to each carrier type, both liposomes and polymer based nanoparticles share the issues of invariant size and shape, uncontrollable release profiles, and highly interdependent properties, whereby changing one property, such as loading efficiency, affects numerous other properties, such as size, charge, and stability.[5-7, 9]

Many of the challenges of nanocarrier delivery can be addressed by mesoporous silica nanoparticles (MSNP). MSNP have controllable size and shape and exhibit a high internal surface area (> 1000 m^2/g) resulting from uniform periodic arrangements of internal nanopores (ranging in diameter from 2 to > 20 nm) embedded within a silica framework.[14, 15] The major advantage of using MSNP as therapeutic nanocarriers is that their pore size and pore surface chemistries can be easily modified to accommodate a variety of cargos and that their high surface areas result in high loading capacities (*vide infra*).[15] Additionally, MSNP are biocompatible and degrade overtime with in a biological system into non-toxic silicic acid ($Si(OH)_4$) by-products.[16] However, MSNP use as a nanocarrier is limited by the rapid clearance of the particles by immune and excretory systems after injection.[16-18]

To address the limitations of liposomes, polymer conjugates, and MSNP, while taking advantage of their strengths, we developed a flexible modular nanocarrier we term a "protocell" (**Figure 1.1**).[15, 19-24] Protocells are formed by the encapsulation of MSNP cores within supported lipid bilayer (SLB)

Figure 1.1 – *Protocell Schematic*
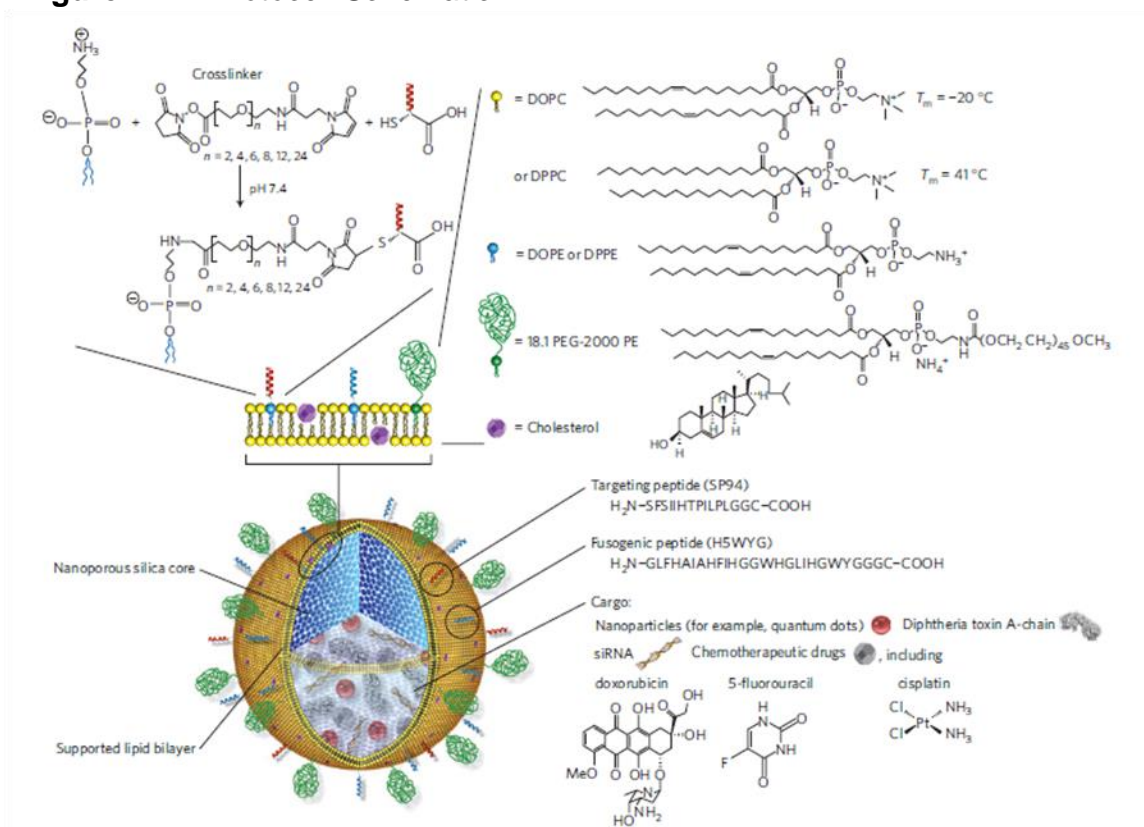
Figure 1.1 – Schematic illustration of the protocell construct. Disparate types of therapeutic and diagnostic agents, such as smaller nanoparticles, toxins, oligonucleotides and drugs, can be loaded within the mesoporous silica core. Targeting ligands, such as peptides or antibodies, and fusogenic peptides can be chemically conjugated to phosphatidylethanolamine 1,2-dioleoyl-sn-glycero-3-phosphoethanolamine (DOPE) or 1,2-dipalmitoyl-sn-glycero-3-phosphoethanolamine (DPPE), present in the limited amounts (usually 1 – 5 %) in the supported lipid bilayer (SLB), by a heterobifunctional crosslinker with a polyethylene glycol (PEG) spacer arm. The SLB can be composed of either fluid DOPC or non-fluid 1,2-dipalmitoyl-sn-glycero-3-phosphocholine (DPPC) zwitterionic phosphatidylcholine lipids along with cholesterol and can be further modified with phosphatidylethanolamine PEG-2000, or other agents, to enhance colloidal stability and decrease nonspecific interactions. Adapted and reproduced with permission.[19] © 2011, The Authors.

membranes which can then be modified by conjugation with targeting/trafficking ligands and polyethylene glycol (PEG).[18-20, 22, 25-32] They synergistically combine the advantages of liposomes (low inherent toxicity, immunogenicity, and long circulation times) with MSNPs (stability and enormous capacity for multiple cargos and disparate cargo combinations).[19, 20, 22, 24] In addition to combining the independent advantages of the MSNP and the liposome systems, the adhesion energy between the MSNP and SLB suppresses large scale membrane bilayer fluctuations responsible for liposome instability and leakage, while the SLB serves to retain soluble cargos within the MSNP. The earliest conceptual protocell was synthesized using micron-sized mesoporous silica particles.[33, 34] The first-generation nanosized protocell consisted of a hydrophilic, spherical MSNP core prepared by aerosol-assisted evaporation-induced silica-surfactant self-assembly[35] fused with either zwitterionic/cationic (1,2-dioleoyl-sn-glycero-3-phosphocholine (DOPC) / 1,2-dioleoyl-3-trimethylammonium-propane (DOTAP)) or zwitterionic/anionic (DOPC/ 1,2-dioleoyl-sn-glycero-3-phospho-L-serine (DOPS)) liposomes[24] which served to simultaneously load and seal negatively charged cargo within the MSNP and allow it to be delivered across the cell membrane. Since that time many variations of the protocell design have been reported including: lipid monolayer encapsulated hydrophobic MSNP,[18, 30] covalent attachment of lipids to enable chemically triggered release under disulfide reducing conditions,[36] polymer additives to the SLB or monolayer,[29, 30] native cell membrane encapsulated particles,[37, 38] and red blood cell mimicking lipid compositions.[39]

1.3 Modular Design and Combined Functions of Protocells

The modular design and synergistic characteristics of the protocell confer a unique combination of properties that can be further independently engineered or tuned for specific applications (**Figure 1.1**): 1) the MSNP core size can be varied from 25 nm to over 250 nm and the MSNP shape can be varied from prismatic to spherical to toroidal to rod-like;[17, 26, 35, 40-43] 2) through self-assembly, the MSNP pore diameter can be varied from 2 nm to over 20 nm,[14] and, using silane coupling chemistry, the pore surface chemistry can be varied to accommodate high concentrations of disparate cargos;[14, 44-46] 3) SLB formation, by spontaneous liposome fusion with the silica core, seals and protects sensitive cargo (**Figure 1.2A**), while SLB destabilization under acidic conditions provides for pH-triggered cargo release from the endosome;[19, 20, 22, 27-29] 4) lateral bilayer diffusivity enables recruitment of targeting ligands to cell surface receptors thereby achieving high avidity with low targeting ligand density and reducing immunogenicity and non-specific binding (**Figure 1.2B**);[19, 47] 5) the re-configurable SLB surface supports complex biomolecular interactions with the cell surface, involving, for example, targeting, immune cell evasion, and endosomal escape ligands;[18-20, 22, 27-29] 6) the silica dissolution rate and hence release of cargo can be modulated by controlling the extent of siloxane condensation during the synthesis of MSNP;[48-51] 7) both therapeutic compounds and imaging agents can be incorporated to create a theranostic nanocarrier, allowing assessment of protocell stability, biodistribution, co-localization with

Figure 1.2 – *Cryogenic TEM and Lateral Bilayer Diffusivity*
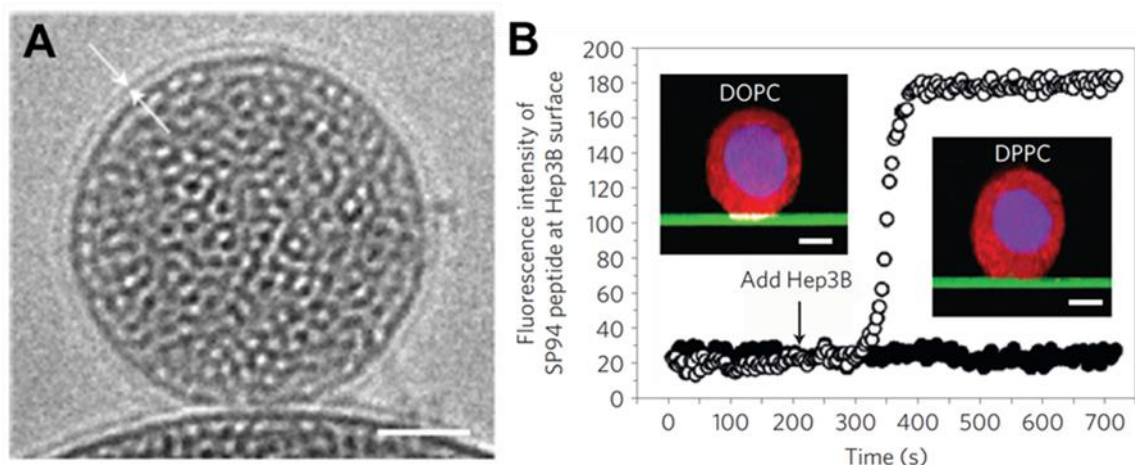
Figure 1.2 – A) Cryogenic TEM image of the protocell, the white arrows highlight the lipid bilayer on the surface of the MSNP core. Scale bar = 25 nm. B) Recruitment of Alexa Fluor 647-labelled peptide (white) to the surface of a HCC cell when peptides are displayed on a mesoporous silica thin film-supported lipid bilayer (green) composed of fluid DOPC (open circles) or solid DPPC (closed circles). Cells were labeled with CellTracker Red CMTPX (red) and Hoechst 33342 (blue). Inset scale bars = 5 µm. Adapted and reproduced with permission.[19] © 2011, The Authors.

target cells, toxicity, and efficacy at the cellular/intracellular level as well as in the whole organism.[19, 27, 28, 52, 53]

1.3.1 MSNP Core Synthesis

Mesoporous silica nanoparticles are synthesized by colloidal or aerosol-based self-assembly employing surfactants or block co-polymers as structure directing agents. Using solution based colloidal self-assembly processes derived, for example, from the original Stöber process for preparing spherical colloidal silica particles, the synthesis of micrometer- and sub micrometer-size spheres of ordered mesoporous oxide (MCM-41),[54] or a dendritic process referred to as colloidal stable mesoporous silica nanoparticles (CMS),[55] it is possible to synthesize uniformly sized populations of MSNP with spherical, prismatic, toroidal, rod-like, or hollow shapes with dimensions spanning 25 nm to over 250 nm,[26, 40-43] while in many cases maintaining low polydispersity indices (PdI) of < 0.1.[23] Using evaporation induced self-assembly (EISA),[35] it is possible to generate in a single-step spherical MSNP with a predictable power law particle size distribution spanning 25 nm to over 250 nm. The highly tunable synthesis of MSNP allows for the selection of the size, size distribution, and shape most applicable based on the proposed delivery route and target biodistribution. The MSNP pore and particle surface chemistry can be readily modified *via* reactions with silanol groups ($\equiv$Si-OH) present both within the pore interiors and on the exterior surface. Silanol groups (which are partially deprotonated to form anionic $\equiv$Si-O$^-$) are chemically accessible and can be reacted with alkoxy or chlorosilane derivatives to introduce organic functionality. Modification performed in single-

step or multi-step procedures provides an unlimited ability to 'tune' the charge, polarity, and hydrophobic/hydrophilic character of the pore and exterior particle surfaces additionally providing sites for further chemical conjugation or chelation with targeting and control ligands as well as imaging agents.

1.3.2 Cargo Content and Loading

The controlled pore size and surface chemistry allow multiple cargo types to be efficiently loaded within the MSNP, where the loading efficiency scales with the drug accessible surface area for surface chemistries with attractive drug interactions arising from electrostatic, hydrophobic, hydrogen-bonding, or other generally non-covalent forces.[15] The most common cargos are small molecule drugs like doxorubicin (DOX) that can access and interact electrostatically with the negatively charged ~ 2 nm diameter pores characteristic of MCM-41-type MSNP.[25, 27-29] Loading of hydrophilic small molecule drugs is typically done by incubating the MSNP core with the drug of interest prior to centrifugation, re-suspension in buffer and fusion of liposomes to the surface of the MSNP.[19, 27-29] To load negatively charged cargos, such as nucleic acid or proteins, the MSNP framework can be modified with aminosilanes to produce a positively charged framework.[19, 20, 22] Once the MSNP is positively charged, cargo can be loaded by incubation of the modified MSNP with the cargo of interest prior to liposome fusion. Other methods of drug loading have also been explored, including simultaneous drug loading and liposome fusion[24] as well as simultaneous SLB assembly and drug loading using a solvent exchange method.[25] To facilitate loading of larger cargo, such as plasmid DNA,[56] larger pore sizes can be

achieved with block copolymer templating agents, micro-emulsion procedures,[22] and swelling agents.[57]

The loading of hydrophobic cargo can be achieved in several ways. Using the standard protocell formulation with a SLB, the hydrophobic cargo can be loaded in the interbilayer domain of the SLB.[27] The use of the hydrophobic domain of the SLB limits the amount of hydrophobic cargo that can be loaded, but does allow for the loading of both a hydrophilic drug in the MSNP core as well as a hydrophobic drug within the same protocell.[27] Hydrophobic cargos can also be loaded from organic solvents like DMSO (or mixtures of DMSO and alcohol) followed by vacuum drying and re-suspension in buffer for liposome fusion.[58] Hydrophobic drug cargos have also been loaded in hybrid protocells composed of organosilane modified MSNP with a single lipid monolayer interacting with molecules directly on the surface of the MSNP.[18, 30, 59]

1.3.3 Liposomal Components and Protocell Assembly

The earliest protocell lipid formulations consisted zwitterionic/cationic (DOPC/DOTAP),[24, 25] zwitterionic/anionic (DOPC/DOPS),[24] or zwitterionic lipids alone (1-palmitoyl-2-oleoyl-sn-glycero-3-phosphocholine (POPC) or DOPC).[25] Since these initial formulations, the complexity of protocell lipid formulations has increased and, as depicted in **Figure 1.1**, a large variety of lipid and membrane bound components can be incorporated into the SLB. Most commonly, the major component of the SLB remains a zwitterionic lipid,[19, 20, 22, 27-29, 31, 39] although the cationic lipid, DOTAP, is still occasionally utilized.[32] In the selection of the

primary lipid component, the important design considerations are the lipid melting transition temperature, which controls the SLB fluidity/diffusivity and stability,[19] and charge, which controls non-specific interactions with cells and tissues and can affect the fusion of the SLB to the MSNP.[21, 24, 25, 60] The lipid melting transition temperature correlates with the length and degree of saturation of the alkane tails, ranging from 55°C for the saturated 18-carbon chain lipid 1,2-distearoyl-sn-glycero-3-phosphocholine (DSPC) to -17°C for the single unsaturated 18-carbon chain lipid DOPC. Higher transition temperature lipids increase stability and reduce leakage but can limit the diffusion of targeting ligands conjugated to the lipid head groups (*vide infra*) reducing multivalent interactions and binding avidity with the target cell surface.[19]

In addition to the primary lipid composition, auxiliary components can be added to control the fluidity of the SLB, increase the colloidal stability and circulation time *in vivo*, and/or add functionality to the protocell. In many formulations, cholesterol is added to control the fluidity and leakage of the SLB,[19, 20, 22, 27, 28, 39] and PEG-modified (PEGylated) lipids are commonly added to increase colloidal stability and circulation time *in vivo*.[19, 20, 22, 27, 28, 32] In addition to cholesterol and PEGylated lipids, functional lipids which provide a site for chemical conjugation are included in protocell lipid formulations to allow addition of targeting ligands.[19, 20, 22, 28, 32] The most common functional lipids utilized for addition of targeting are phosphoethanolamine lipids,[19, 20, 22, 28, 32] although other functional lipids incorporating nickel chelating agents have been demonstrated.[31] In addition to adding targeting ligands, lipids modified with polymers such as

pluronic-P123 and D-α-tocopherol polyethylene glycol 1000 succinate (TPGS) have been used to block drug resistance proteins and thereby add functionality to the lipid bilayer itself.[29, 30]

The most common method of protocell assembly is liposomal fusion, in which mixtures of lipids suspended in organic solvents are dried then hydrated in aqueous buffer, followed by extrusion through a filter to produce liposomes of the desired size. Liposomes spontaneously fuse to the surface of MSNP upon mixing due to the highly lipophilic nature of silica.[60] This phenomenon has been demonstrated using Cryo-TEM to observe the successive steps of SLB formation on a solid silica nanoparticle.[60] After fusion, excess liposomes are removed by centrifugation and the resulting protocells are resuspended.[19, 22, 28] Protocells can also be assembled by solvent exchange, wherein MSNP are dissolved in ethanolic solution followed by addition of water, which causes transfer of the lipid bilayer directly to the MSNP.[25] A third method of assembly involves adding MSNP in saline to a dried lipid film accompanied by probe sonication, wherein a SLB forms directly or through a liposomal pathway.[27] A critical consideration is the extent of drug leakage during the assembly process and the integrity of the supported lipid bilayer that can be assessed by drug leakage after assembly.[19, 27]

1.3.4 Targeting Chemistry

The multifunctionality of the protocell platform allows for the presentation of targeting agents, including peptide, molecule, and/or antibodies *via* lipid head group-modification, while maintaining biocompatibility and prolonging circulation

times by the incorporation of PEGylated and/or other modified lipids. The major concerns surrounding targeting chemistry are the choice of ligand, the chemical conjugation method, and determination of what stage in the protocell assembly process to perform the conjugation. To date, small molecule ligands such as folate and hyaluronan,[18, 28, 32, 59] and peptides[19, 20, 22] have been used for protocell targeting. Full antibodies, as well as partial antibodies, have been utilized for liposome targeting[2, 8, 61, 62] and recently have been applied to protocells as well.[63]

After selection of the targeting ligand, a conjugation strategy can then be employed to link the ligand to the protocell. Multiple conjugation strategies that covalently or non-covalently associate the targeting ligand with the functional lipid are possible and the conjugation strategy should be carefully selected to maintain functionality of the targeting ligand. The most common functional lipids utilized for addition of targeting ligands to protocells are phosphoethanolamine lipids, which are linked to the ligand utilizing covalent heterobifunctional linkers.[19, 20, 22, 28, 32] Additionally, non-covalent association of a targeting ligand with the protocell has been performed utilizing lipids with incorporated nickel chelating agents and histidine (His)-tagged targeting ligands.[31] This conjugation method is convenient because it occurs in a single-step with suitable yields, but the ligand-protocell binding interaction is weaker than other covalent strategies, risking the potential dissociation of the targeting ligand. Although only a limited number of conjugation chemistries have been utilized for targeting protocells, additional targeting strategies have been employed for liposome targeting and could be applied to protocells as well. For example, simple thiol groups can be added to

both the targeting antibodies and lipids in the liposomes, these thiol groups can be used to conjugate the targeting antibody to the liposome through disulfide bonds or maleimide crosslinking chemistry. This method has been utilized with targeting antibodies such as anti-HER2 or anti-My9, to create targeted liposomes.[64, 65] Other potential chemistries include click-chemistry[66] and avidin/biotin chemistries that have previously been employed with liposome based carriers[67, 68] and have recently been translated to protocells.[63]

Finally, the timing of lipid modification with the targeting moiety must be selected; lipids can be modified before creation of the liposome, before liposomal fusion with the MSNP, or after formation of the supported lipid bilayer. Among the earliest reported methods for the addition of targeting moieties involved modification of lipids with a folate derivative, prior to addition to the MSNP.[18, 59] This approach allows the synthesis of large quantities of targeted lipids and works well for the creation of lipid monolayer coated MSNP. However, this method is problematic for the creation of protocells as it is impossible to control the inward and outward orientation of the folate modified lipids on the liposome. To address this concern, preformed liposomes were modified prior to fusion with MSNP.[28] This method assumes the original liposome orientation to be maintained throughout MSNP fusion, which may not be the case. Most commonly, targeting moieties are conjugated to completely assembled protocells, resulting in surface-only displayed targeting ligands.[19, 22] Modification of completely assembled protocells is also amenable to non-covalent conjugation chemistries employing, for example, nickel chelating lipids that bind to His-

terminated ligands.[31] Another unique approach to targeting ligand modification involves the insertion of ligand-functionalized lipids, e.g. folate-modified lipids, after the protocell assembly.[32] Although addition of functionalized lipids after assembly is potentially simple and economical, it is difficult to predict and control the final proportion of ligand-modified lipid incorporation. Perhaps the most promising method for complete outward orientation of targeting ligand display involves a hybrid bilayer constructed by lipid monolayer deposition on an organosilane modified MSNP.[18, 59] Hybrid bilayers form *via* hydrocarbon rich tail group interaction with the hydrophobic MSNP cores, positioning targeting ligands with the correct outward orientation. This approach was demonstrated using folate-modified lipids and resulted in selective uptake *in vitro*. While many methods of protocell surface modification have been described, many other methods have yet to be reported. Thus, with the multitude of different lipid head group modifications and numerous unexplored functionalization techniques, protocell targeting remains an active area of research.

1.4 *In Vitro* Performance of Protocells

Figure 1.3 depicts the successive stages of (step 1) protocell binding, (step 2) internalization, (step 3) endosomal escape, and (step 4) nuclear targeting of desired cargo(s) by which targeted protocells selectively deliver encapsulated cargos to a cell of interest. Importantly, the fluid but stable SLB promotes lateral diffusivity and enables targeting peptides introduced at low concentrations (important for avoiding non-specific binding and immunogenicity) to be recruited to cell surface receptors (**see Figure 1.2B**), promoting high avidity

Figure 1.3 – *Protocell Internalization Schematic*
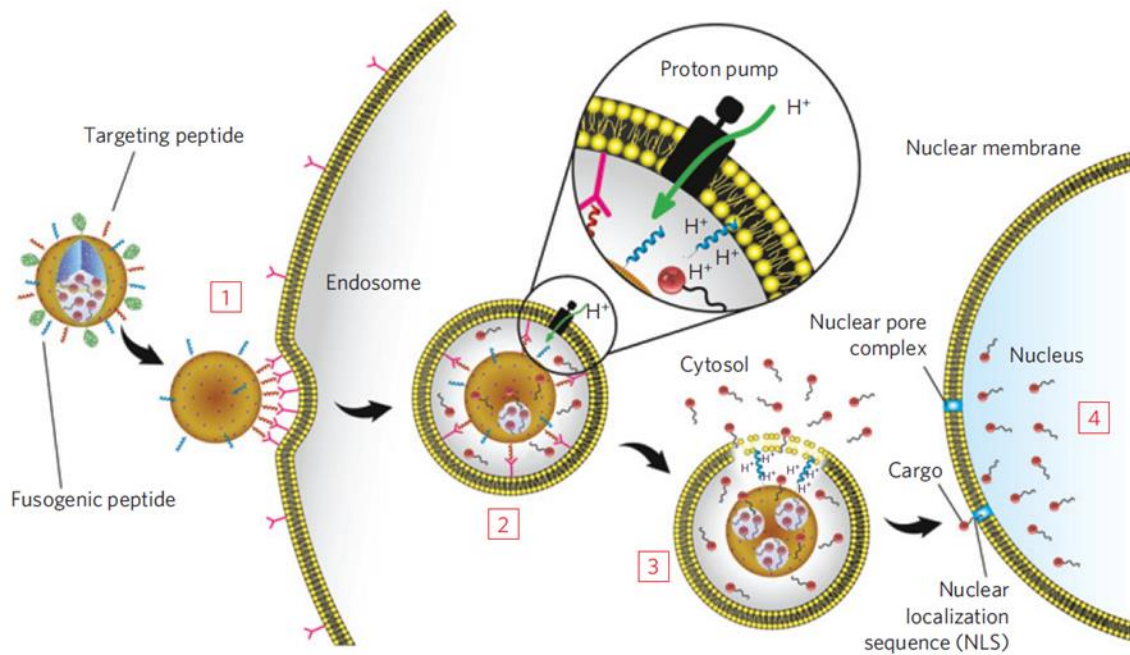
Figure 1.3 – Schematic diagram depicting the successive steps of the multivalent binding [1], internalization [2], endosomal escape [3], and delivery of cargo to the nucleus [4] of peptide targeted protocells. Adapted and reproduced with permission.[19] © 2011, The Authors.

multivalent binding and internalization by receptor mediated endocytosis (**Figure 1.3**, step 1). Dissociation constants (K_d, where K_d is inversely related to affinity) were used to quantify surface binding of SP94-targeted protocells to human hepatocellular carcinoma cell line (Hep3B), normal hepatocytes, endothelial cells, and immune cells.[19] Protocells modified with a calculated average of only six SP94 peptides per particle exhibit a 10,000-fold greater affinity for Hep3B than for normal hepatocytes, and other control cells suggesting the specificity necessary for efficacious targeted delivery *in vivo.* Furthermore, SP94-modified protocells have a 200-fold higher affinity for Hep3B than free SP94, a 1000-fold higher affinity for Hep3B than nanoparticles bearing a non-targeting control peptide, and a 10,000-fold higher affinity for Hep3B than unmodified particles.[19] The affinity of protocells is a function of both peptide density and the fluidity of the supported lipid bilayer; therefore, the K_d can be precisely controlled by changing the composition of the bilayer to include varying amounts of fluid and non-fluid lipid components (e.g. **Figure 1.1**), which is envisioned to be important for translation to *in vivo* conditions.[19] To demonstrate that binding results in internalization and cytosolic delivery (**Figure 1.3**, steps 2 and 3) of multiple cargos, **Figure 1.4** shows hyperspectral confocal images of four categories of fluorescently labelled cargo mimics delivered by a single targeted protocell. After 15 minutes (reference[19] data not shown) calcein (a drug mimic), ds-DNA (an siRNA mimic), red fluorescent protein (a toxin mimic), and quantum dots appear as punctate spots co-localized with fluorescently-labelled silica and lipid indicating incorporation into endosomes consistent with the receptor-mediated

Figure 1.4 – *Hyperspectral Confocal Imaging of Multicomponent Delivery*
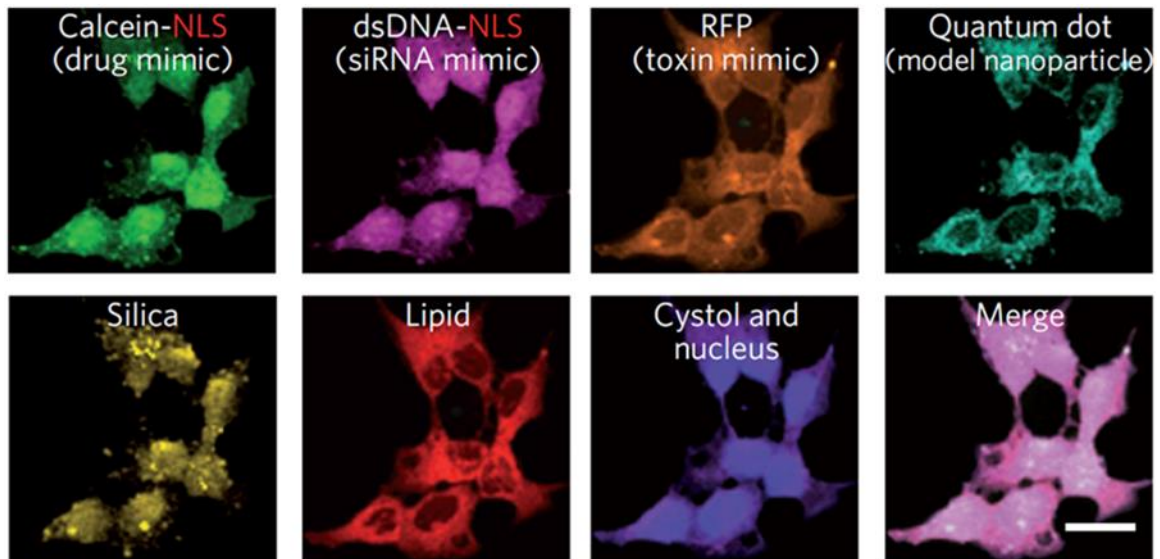
Figure 1.4 – Hyperspectral confocal imaging of targeted delivery of multicomponent cargo by protocells to Hep3B cells for 12 hours at 37 °C. Alexa Fluor 532-labeled mesoporous silica cores (yellow) were loaded with calcein, dsDNA oligonucleotide (magenta), Red Fluorescent Protein (orange), and CdSe/ZnS quantum dots (teal). Cargos were sealed in the cores by fusion of Texas Red-labeled DOPC liposomes (red). The calcein and dsDNA oligonucleotide were modified with a nuclear localization signal and show accumulation in the nucleus by 12 hours, while the RFP and the quantum dots remain in the cytosol. Scale bar = 20 μm. Adapted and reproduced with permission.[19] © 2011, The Authors.

endocytotic process depicted in **Figure 1.3** steps 1 and 2. Within 12 hours (**Figure 1.4**), calcein, ds-DNA, red fluorescent protein, and quantum dots are delivered into the cytosol, and calcein and dsDNA (both conjugated with a nuclear localization sequence) are further delivered into the nucleus (**Figure 1.3**, step 4). Delivery of the drug from the endosome into the cytosol is crucial for therapeutic efficacy and has emerged as a major problem in nanocarrier-based drug delivery. For the protocell, the natural acidification of the endosome initiates three pH-triggered events insuring endosomal escape (**Figure 1.3**, step 3). First, it reduces the SLB adhesion energy allowing leakage of cargo as confirmed *in vitro*, second, below its pKa, the endosomolytic peptide H5WYG serves as a proton sponge resulting in endosome swelling and disruption, third, for partially aminated silica cores, lowered pH increases the silica solubility, which along with diffusion controls cargo release. Thus, for protocells, delivery profiles may be tuned/optimized through variation of pore size, charge, and solubility of the silica core along with the extent of SLB modification with the endosomolytic peptide. *In vitro* delivery has also been demonstrated for other cargos including: siRNA,[22] a variety of anti-cancer drugs,[19, 25, 27-29] a photodynamic therapeutic,[59] and multiple anticancer drugs within a single protocell.[19, 27]

In addition to delivery of cargo, visualization of protocells in an *in vitro* system has been utilized to demonstrate targeting specificity and functional cellular response to drug delivery (e.g. **Figure 1.5**). Addition of targeting peptides was shown to provide specificity by demonstrating binding and internalization of protocells, shown in white in the merged images in **Figure 1.5**,

Figure 1.5 – *Confocal Microscopy Imaging of Cellular Response to Drug Delivery*
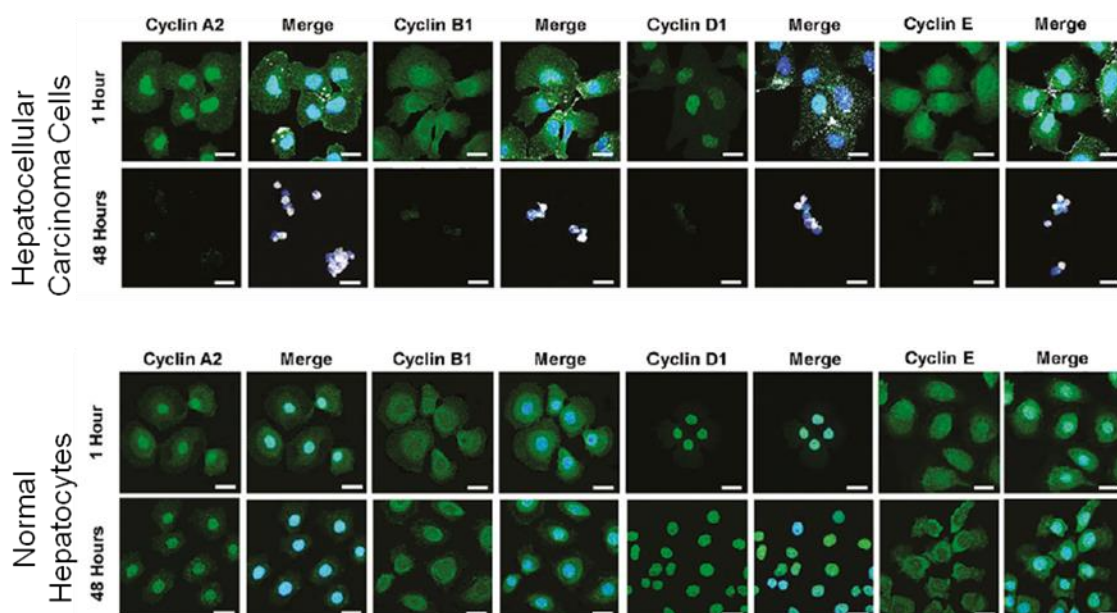
Figure 1.5 – Confocal microscopy images of Hep3B hepatocellular carcinoma cells and normal hepatocytes after exposure to an excess peptide targeted protocells loaded with an anti-cyclin siRNA cocktail for 1 hour or 48 hours at 37 °C. Cells were fixed and then imaged by confocal microscopy, protocells are shown in white, cyclins in green and nuclei in blue. Scale bar = 20 μm. Adapted and reproduced with permission.[22] © 2012, The American Chemical Society.

to HCC cells but not to normal hepatocytes.[22] These peptide targeted protocells delivered a cocktail of siRNAs to knockdown the expression of a selection of cyclin proteins. Confocal microscopy showed not only specific binding and uptake only in HCC cells but also reduction in cyclin protein expression only in the targeted cancer cells, while leaving the normal hepatocytes unaffected (**Figure 1.5**). *In vitro* imaging has been used to demonstrate specific targeting of protocells utilizing small molecule ligands, such as folic acid,[18, 32, 59] soluble protein ligands, such as epidermal growth factor,[32] polysaccharides, such as hyaluronan[28] and complex proteins, such as cell surface receptors, Ephrin-B2 and Ephrin-B3.[31]

 In vitro systems have also been used to evaluate the therapeutic efficacy of small molecule chemotherapeutic cargo delivery. Delivery of DOX or a cocktail of DOX, 5-fluorouracil, and cisplatin by peptide-targeted protocells demonstrated killing of multidrug resistant HCC cells while sparing normal hepatocytes (**Figure 1.6A**).[19] When the targeted-protocells were compared to liposomes containing the same drugs, the liposomes resulted in reduced cell killing of the HCC cells and increased toxicity to normal hepatocytes compared to targeted-protocell delivery (**Figure 1.6A**), presumably due to the leakiness of liposomal formulations.[19] The delivery of a variety of drugs by non-targeted protocells has been demonstrated *in vitro* including: colchicine,[25] gemcitabine,[27] paclitaxel,[27] docetaxel,[28] irinotecan,[29] and DOX,[30] both as single drugs[25, 28-30] and as drug cocktails.[27] *In vitro* delivery of 8-hydroxyquinoline,[28] DOX,[19] 5-fluorouracil,[19] protoporphyrin IX,[59] and cisplatin[19] by targeted protocells both

Figure 1.6 – *Evaluation of Therapeutic Efficacy*
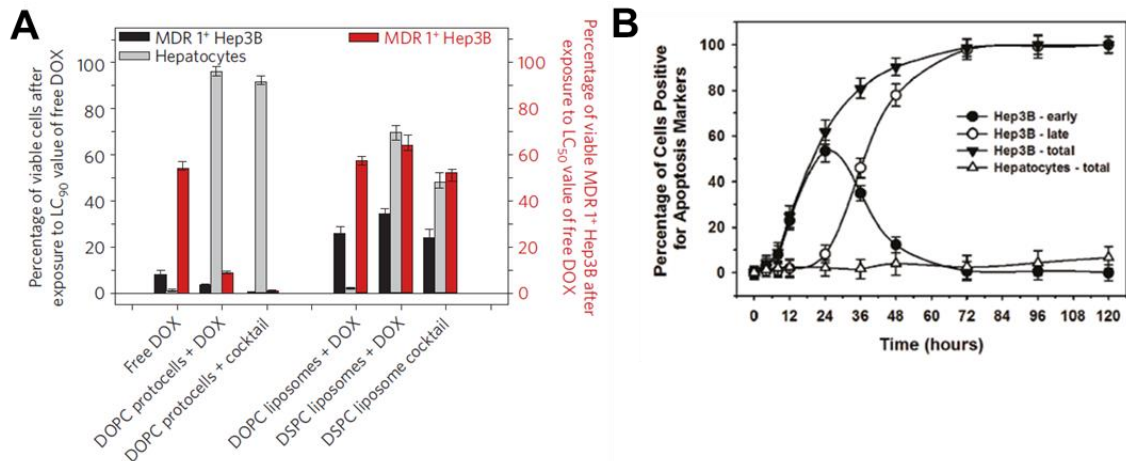
Figure 1.6 – A) Left axis (bars in grey and black): The percentage of multidrug resistant positive (MDR+) Hep3B hepatocellular carcinoma cells and normal hepatocytes that remained viable after exposure to free doxorubicin (DOX), targeted-protocell encapsulated DOX, liposomal DOX, targeted protocells containing a cocktail of chemotherapeutics or liposomes containing a cocktail of chemotherapeutics for 24 hours at 37 °C at the LC_{90} value for free DOX. Right axis (bars in red): The percentage of MDR + Hep3B cells that remain viable after exposure to free DOX, protocell encapsulated DOX, liposomal DOX, targeted protocells containing a cocktail of chemotherapeutics or liposomes containing a cocktail of chemotherapeutics for 24 hours at 37 °C at the LC_{50} value for free DOX. Adapted and reproduced with permission.[19] © 2011, The Authors. B) Induction of apoptosis by exposure to peptide targeted protocells loaded with an anti-cyclin siRNA cocktail. Cells were classified for early apoptosis (annexin V positive) or late apoptosis (annexin V and Propidium Iodide positive). Adapted and reproduced with permission.[22] © 2012, The American Chemical Society.

individually[19, 28, 59] and as cocktail[19] has also been demonstrated. In addition to the therapeutic delivery of drugs, *in vitro* efficacy and cytotoxicity of siRNA cargo has also been examined (**Figure 1.6B**).[22] Peptide targeted protocells were able to deliver a cocktail of siRNAs to reduce expression of cyclin proteins. The reduction in cyclin proteins resulted in apoptosis of HCC cells but did not cause apoptosis of the normal hepatocytes.[22] *In vitro* systems have also been used to assess the efficacy of potential therapeutic additions to the lipid bilayer such as Pluronic-123 and TPGS.[29, 30] Pluronic-123 and TPGS, when released from the lipid bilayer on the surface of the protocell, blocks drug efflux pumps present in tumor cells that result in multidrug resistance and results in increased killing of cancer cells *in vitro.*[29, 30] In addition to delivery of therapeutic cargo, *in vitro* testing has been utilized to test novel therapeutic technologies which utilize protocells such as specific cargo release by red-light photoactivation,[32] and even the expansion of protocell technology beyond cancer treatment to antiviral therapy.[31]

Finally, *in vitro* assessment provides a rapid method to evaluate the biocompatibility of various lipid compositions and protocell components prior to progressing to evaluation of toxicity, biocompatibility or therapeutic delivery in an *in vivo* system. For example, hemotoxicity testing demonstrated that a combination of phosphatidylcholine, phosphatidylserine and cholesterol, designed to mimic red blood cell membranes, was more biocompatible than phosphatidylcholine alone for the SLB formulation.[39] *In vitro* testing for biocompatibility, such as hemocompatibility, serves two major functions in the

evaluation of a nanocarrier such as the protocell. First, *in vitro* testing, including hemocompatibility, is required prior to FDA approval. Secondly, *in vitro* testing can be used to select only those formulations likely to be biocompatible for testing in *in vivo* systems.

1.5 *In Vivo* Use and Testing of Protocells

1.5.1 *In Vivo* Biocompatibility and Toxicity

A critical issue for any nanocarrier is *in vivo* toxicity and biocompatibility. Toxicity from protocells can arise from either the MSNP core or from the SLB. Although the formulations may vary and individual formulations will need to be tested for biocompatibility and toxicity, liposomes that are biocompatible and non-toxic are FDA-approved for delivery of chemotherapeutic drugs.[8] The toxicity of silicon dioxide has been studied for more than a century and amorphous silica is Generally Recognized as Safe (GRAS) by the FDA. Recently, the toxicity of silica nanoparticles has been extensively investigated, because the high surface to volume ratio of nanoparticles could lead to enhanced cellular interactions and different pathways of toxicity compared with coarse grained silica.[69] Based on the high surface to volume ratio of silica NPs, it might be anticipated that they would show higher toxicity compared with their bulk counterparts. However, the majority of evidence supports lack of toxicity and the biocompatibility of silica nanoparticles prepared by low temperature colloidal synthesis. Recently amorphous silica nanoparticle 'C-dots' (Cornell Dots) were FDA approved for diagnostic applications in a stage I human clinical trial.[70] The FDA approval for a

clinical trial of silica nanoparticles should accelerate the acceptance of amorphous, colloidally derived silica particles in medical applications.

In the case of MSNP, the intrinsic porosity of the MSNP surface reduces the extent of hydrogen bonding or electrostatic interactions with cell membranes, a potential cause of silica nanoparticle toxicity.[50] Although the porosity of MSNP should decrease their toxicity, studies of MSNP toxicity have shown variable and occasionally high toxicity. One potential reason for the variability in toxicity studies is the surfactant used to template the pores is toxic and variable amounts of this surfactant can remain within the pores of the MSNP depending on the processing.[49] However, a study which used Fourier Transform Infrared Spectroscopy (FTIR) to confirm that the template surfactant had been removed prior to toxicity testing of the MSNP found survival of all mice treated with up to 1000 mg/kg by IV injection and followed for 14 days.[48] The survival of all the animals treated with a very high dose of MSNP that did not retain surfactant shows the lack of intrinsic toxicity of the silica framework of the MSNP.

In addition to toxicity, biocompatibility must also be taken into account. In this area, the porous structure of the MSNP further enhances their biocompatibility as the high surface area and low extent of condensation of the MSNP siloxane framework promotes a high rate of dissolution into soluble silicic acid species, which are nontoxic.[49] The breakdown of the MSNP overtime into nontoxic species supports the potential of repeat and long term use of protocells to deliver drugs as the MSNP core can be cleared from the biological system overtime in a nontoxic way. Examination of animals treated with both PEG-

coated and unmodified MSNP showed excretion of the silica in both feces and urine without any signs of significant organ damage.[17] Although assessment of toxicity and biocompatibility will be important for each individual protocell formulation that is developed, biocompatibility of the individual components of the protocell should greatly reduce the potential toxicity and enhance the biocompatibility of the complete protocell. Potential toxicity is further mitigated by the high drug loading capacity of MSNP and protocells, which greatly reduces needed dosages and therefore the potential for toxicity. Finally, the ability to add cell specific targeting will further mollify potential toxicity as the protocells are directed specifically to the cells or tissues of interest and will have reduced nonspecific interactions within the body.

1.5.2 *In Vivo* Application of Protocell Technology

The most common area of research for therapeutic protocells is cancer, due to the highly toxic and non-specific nature of most cancer therapeutics. Increased specific delivery of encapsulated cancer therapeutics would address the lack of selectivity, which results in non-specific toxicity to healthy cells and prevents the dose escalation necessary to eradicate diseased cells and overcome drug resistance. The tunable nature of protocells makes them highly adaptable nanocarriers which can be easily altered to fit the needed biodistribution and drug release profile of the specific cancer. Therapeutic protocells have been used to take advantage of the EPR effect which leads to accumulation of nanosized materials in tumors. The EPR effect is due to the rapid growth of tumor vessels which are often abnormal in form and architecture.

Due to the abnormal architecture, nanosized carriers are released into the tumor tissue and trapped due to impaired lymphatic drainage often present in tumors.

Although many nanocarriers can take advantage of the EPR effect, the addition of a lipid bilayer to the surface of a drug loaded MSNP greatly increased the EPR effect compared to uncoated MSNP.[29] In addition, a comparison of uncoated MSNP to protocells both loaded with irinotecan showed a significant increase in survival and a reduction in tumor growth in mice treated with the protocells.[29] Protocells created to treat breast cancer have been further modified to address a common breast cancer resistance pathway. The tumor cells were modified to express the breast cancer resistance protein (BCRP), which confers resistance by pumping chemotherapy agents out the cells. To counteract this pump, the protocell lipid bilayer was modified with Pluronic-123, which can block the action of the BCRP. The combined delivery of Pluronic-123 with the chemotherapy agent resulted in the greatest reduction in tumor growth as well as an increase in survival.[29] The ability to both load drugs as well as modify the components in the surface of the protocell to address the BCRP demonstrates the customizability of the protocell platform. Protocell therapeutic delivery has been applied to pancreatic cancer, a notoriously difficult to treat disease, with dual drug loaded protocells.[27] Gemcitabine and paclitaxel were loaded into protocells to treat mice with both subcutaneous and orthotopic pancreatic cancer xenografts. The combined therapy protocells were more effective than single agent gemcitabine protocells or the combined free-drug treatment at tumor growth retardation in the subcutaneous tumors and in prevention of metastasis in

the orthotopic model.[27] The dual therapeutic protocells utilize the high surface area MSNP core to carry the hydrophilic drug, gemcitabine, and the hydrophobic space within the lipid bilayer to encapsulate the hydrophobic drug, paclitaxel, which can be used in low quantities in combination therapy.

In addition to studies focusing on the EPR effect, targeting moieties have been used to enhance the delivery of protocells (**Figure 1.7**). Protocells containing 8-hydroxyquinoline (8-HQ) were optimized to target breast cancer xenografts by the addition of hyaluronan to the surface.[28] Hyaluronan targets CD44, a surface marker highly expressed in breast cancer stem cells. 8-HQ alone is not toxic, but has a synergistic effect when present with a secondary chemotherapy agent and may help overcome chemoresistance. In addition to the targeted protocells loaded with 8-HQ, a non-targeted set of protocells containing docetaxel and relying on the EPR effect were also used as combination therapy. While the docetaxel loaded protocells and the targeted protocells loaded with 8-HQ had limited effect on tumor growth alone, when combined, the effect was stronger than the combined free-drugs (**Figure 1.8A**). Additionally, free- docetaxel was very toxic, resulting in significant weight loss, and this toxicity was avoided by inclusion of the drug within the protocell (**Figure 1.8B**).[28] Targeted delivery, utilizing folate, of photodynamic therapeutic protoporphyrin IX loaded protocells to mice bearing subcutaneous melanoma tumors has also been demonstrated. Delivery of the free-protoporphyrin IX alone

Figure 1.7 – *Hyaluronan Targeting Modification Schematic*

8-HQ-loaded HA-MSS   DTX-loaded MSS

Cholesterol   HA   DOPE   DOPC   18:0 PEG-2000PE
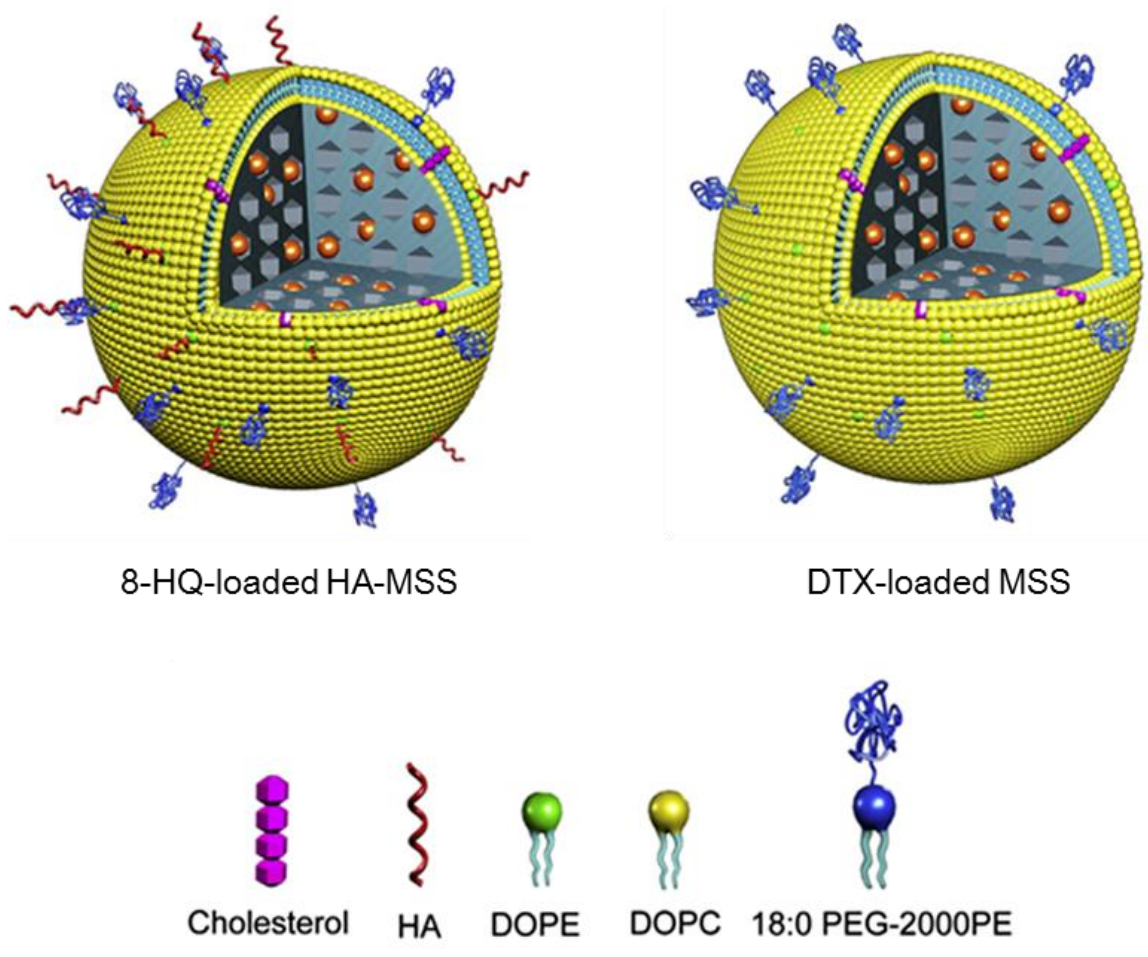
Figure 1.7 – Targeted and non-targeted protocells for treatment of breast cancer xenografts.   Schematic of protocells (MSS) both targeted with hyaluronan (HA-MSS) and loaded with 8-HQ and non-targeted protocells loaded with docetaxel (DTX). Adapted and reproduced with permission.[28] © 2013, Elsevier.

Figure 1.8 – *Anti-tumor Activity of Protocells*
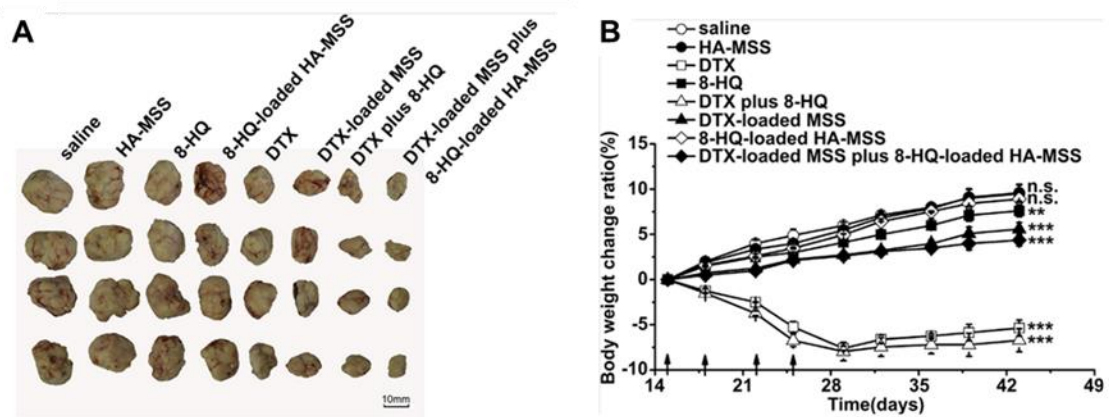
Figure 1.8 – A) Antitumor activity of free drugs in comparison to drug-loaded protocells alone or in combination with each other and free drug as shown by tumor size after 43 days. Treatments were given 4 times between day 15 and day 25. B) Assessment of toxicity by the change in body weight ratio. At day 43, the body weight change ratio was compared to saline injection by the Student's t-test. **P < 0.01, *** P < 0.001 and n.s. represents not significant (P > 0.05). Adapted and reproduced with permission.[28] © 2013, Elsevier.

or in the absence of phototherapy resulted in no response. However, delivery of the protoporphyrin in the protocell in combination with light irradiation resulted in significant reduction in tumor burden.[59]

1.6 References

1. Pérez-Herrero, E.; Fernández-Medarde, A. Advanced Targeted Therapies in Cancer: Drug Nanocarriers, the Future of Chemotherapy. *European Journal of Pharmaceutics and Biopharmaceutics* 2015, 93, 52-79.

2. Egusquiaguirre, S.; Igartua, M.; Hernández, R.; Pedraz, J. Nanoparticle Delivery Systems for Cancer Therapy: Advances in Clinical and Preclinical Research. *Clin. Transl. Oncol.* 2012, 14, 83-93.

3. Iwamoto, T. Clinical Application of Drug Delivery Systems in Cancer Chemotherapy: Review of the Efficacy and Side Effects of Approved Drugs. *Biol. Pharm. Bull.* 2013, 36, 715-718.

4. Akbarzadeh, A.; Rezaei-Sadabady, R.; Davaran, S.; Joo, S. W.; Zarghami, N.; Hanifehpour, Y.; Samiei, M.; Kouhi, M.; Nejati-Koshki, K. Liposome: Classification, Preparation, and Applications. *Nanoscale Research Letters* 2013, 8, 1-9.

5. Davis, M. E.; Chen, Z.; Shin, D. M. Nanoparticle Therapeutics: An Emerging Treatment Modality for Cancer. *Nat Rev Drug Discov* 2008, 7, 771-782.

6. Torchilin, V. P. Recent Advances with Liposomes as Pharmaceutical Carriers. *Nat. Rev. Drug Discovery* 2005, 4, 145-160.

7. Farokhzad, O. C.; Langer, R. Acs Nano. *ACS Nano* 2009, 3, 16-20.

8. Deshpande, P. P.; Biswas, S.; Torchilin, V. P. Current Trends in the Use of Liposomes for Tumor Targeting. *Nanomedicine* 2013, 8, 1509-1528.

9. Peer, D.; Karp, J. M.; Hong, S.; Farokhzad, O. C.; Margalit, R.; Langer, R. Nanocarriers as an Emerging Platform for Cancer Therapy. *Nat. Nanotechnol.* 2007, 2, 751-760.

10. Drummond, D. C.; Noble, C. O.; Guo, Z.; Hayes, M. E.; Connolly-Ingram, C.; Gabriel, B. S.; Hann, B.; Liu, B.; Park, J. W.; Hong, K.; Benz, C. C.; Marks, J. D.; Kirpotin, D. B. Development of a Highly Stable and Targetable Nanoliposomal Formulation of Topotecan. *Journal of Controlled Release* 2010, 141, 13-21.

11. Noble, C. O.; Guo, Z.; Hayes, M. E.; Marks, J. D.; Park, J. W.; Benz, C. C.; Kirpotin, D. B.; Drummond, D. C. Characterization of Highly Stable Liposomal and Immunoliposomal Formulations of Vincristine and Vinblastine. *Cancer Chemotherapy and Pharmacology* 2009, 64, 741-751.

12.   Draz, M. S.; Fang, B. A.; Zhang, P.; Hu, Z.; Gu, S.; Weng, K. C.; Gray, J. W.; Chen, F. F. Nanoparticle-Mediated Systemic Delivery of Sirna for Treatment of Cancers and Viral Infections. *Theranostics* 2014, 4, 872-892.

13.   Williford, J.-M.; Wu, J.; Ren, Y.; Archang, M. M.; Leong, K. W.; Mao, H.-Q. Recent Advances in Nanoparticle-Mediated Sirna Delivery. *Annu. Rev. Biomed. Eng.* 2014, 16, 347-370.

14.   Xiong, L.; Du, X.; Shi, B.; Bi, J.; Kleitz, F.; Qiao, S. Z. Tunable Stellate Mesoporous Silica Nanoparticles for Intracellular Drug Delivery. *Journal of Materials Chemistry B* 2015, 3, 1712-1721.

15.   Tarn, D.; Ashley, C. E.; Xue, M.; Carnes, E. C.; Zink, J. I.; Brinker, C. J. Mesoporous Silica Nanoparticle Nanocarriers: Biofunctionality and Biocompatibility. *Acc. Chem. Res.* 2013, 46, 792-801.

16.   He, Q.; Zhang, Z.; Gao, F.; Li, Y.; Shi, J. *In Vivo* Biodistribution and Urinary Excretion of Mesoporous Silica Nanoparticles: Effects of Particle Size and Pegylation. *Small* 2011, 7, 271-280.

17.   Huang, X.; Li, L.; Liu, T.; Hao, N.; Liu, H.; Chen, D.; Tang, F. The Shape Effect of Mesoporous Silica Nanoparticles on Biodistribution, Clearance, and Biocompatibility *in Vivo*. *ACS Nano* 2011, 5, 5390-5399.

18.   Wang, L.-S.; Wu, L.-C.; Lu, S.-Y.; Chang, L.-L.; Teng, I. T.; Yang, C.-M.; Ho, J.-a. A. Biofunctionalized Phospholipid-Capped Mesoporous Silica Nanoshuttles for Targeted Drug Delivery: Improved Water Suspensibility and Decreased Nonspecific Protein Binding. *ACS Nano* 2010, 4, 4371-4379.

19.   Ashley, C. E.; Carnes, E. C.; Phillips, G. K.; Padilla, D.; Durfee, P. N.; Brown, P. A.; Hanna, T. N.; Liu, J.; Phillips, B.; Carter, M. B.; Carroll, N. J.; Jiang, X.; Dunphy, D. R.; Willman, C. L.; Petsev, D. N.; Evans, D. G.; Parikh, A. N.; Chackerian, B.; Wharton, W.; Peabody, D. S.; Brinker, C. J. The Targeted Delivery of Multicomponent Cargos to Cancer Cells by Nanoporous Particle-Supported Lipid Bilayers. *Nat. Mater.* 2011, 10, 389-397.

20.   Epler, K.; Padilla, D.; Phillips, G.; Crowder, P.; Castillo, R.; Wilkinson, D.; Wilkinson, B.; Burgard, C.; Kalinich, R.; Townson, J.; Chackerian, B.; Willman, C.; Peabody, D.; Wharton, W.; Brinker, C. J.; Ashley, C.; Carnes, E. Delivery of Ricin Toxin a-Chain by Peptide-Targeted Mesoporous Silica Nanoparticle-Supported Lipid Bilayers. *Adv. Healthcare Mater.* 2012, 1, 348-353.

21.   Liu, J.; Jiang, X.; Ashley, C.; Brinker, C. J. Electrostatically Mediated Liposome Fusion and Lipid Exchange with a Nanoparticle-Supported

Bilayer for Control of Surface Charge, Drug Containment, and Delivery. *J. Am. Chem. Soc.* 2009, 131, 7567-7569.

22. Ashley, C. E.; Carnes, E. C.; Epler, K. E.; Padilla, D. P.; Phillips, G. K.; Castillo, R. E.; Wilkinson, D. C.; Wilkinson, B. S.; Burgard, C. A.; Kalinich, R. M.; Townson, J. L.; Chackerian, B.; Willman, C. L.; Peabody, D. S.; Wharton, W.; Brinker, C. J. Delivery of Small Interfering Rna by Peptide-Targeted Mesoporous Silica Nanoparticle-Supported Lipid Bilayers. *ACS Nano* 2012, 6, 2174-2188.

23. Lin, Y.-S.; Haynes, C. L. Impacts of Mesoporous Silica Nanoparticle Size, Pore Ordering, and Pore Integrity on Hemolytic Activity. *J. Am. Chem. Soc.* 2010, 132, 4834-4842.

24. Liu, J.; Stace-Naughton, A.; Jiang, X.; Brinker, C. J. Porous Nanoparticle Supported Lipid Bilayers (Protocells) as Delivery Vehicles. *J. Am. Chem. Soc.* 2009, 131, 1354-1355.

25. Cauda, V.; Engelke, H.; Sauer, A.; Arcizet, D.; Bräuchle, C.; Rädler, J.; Bein, T. Colchicine-Loaded Lipid Bilayer-Coated 50 Nm Mesoporous Nanoparticles Efficiently Induce Microtubule Depolymerization Upon Cell Uptake. *Nano Lett.* 2010, 10, 2484-2492.

26. Du, L.; Liao, S.; Khatib, H. A.; Stoddart, J. F.; Zink, J. I. Controlled-Access Hollow Mechanized Silica Nanocontainers. *Journal of the American Chemical Society* 2009, 131, 15136-15142.

27. Meng, H.; Wang, M.; Liu, H.; Liu, X.; Situ, A.; Wu, B.; Ji, Z.; Chang, C. H.; Nel, A. E. Use of a Lipid-Coated Mesoporous Silica Nanoparticle Platform for Synergistic Gemcitabine and Paclitaxel Delivery to Human Pancreatic Cancer in Mice. *ACS Nano* 2015, 9, 3540-3557.

28. Wang, D.; Huang, J.; Wang, X.; Yu, Y.; Zhang, H.; Chen, Y.; Liu, J.; Sun, Z.; Zou, H.; Sun, D.; Zhou, G.; Zhang, G.; Lu, Y.; Zhong, Y. The Eradication of Breast Cancer Cells and Stem Cells by 8-Hydroxyquinoline-Loaded Hyaluronan Modified Mesoporous Silica Nanoparticle-Supported Lipid Bilayers Containing Docetaxel. *Biomaterials* 2013, 34, 7662-7673.

29. Zhang, X.; Li, F.; Guo, S.; Chen, X.; Wang, X.; Li, J.; Gan, Y. Biofunctionalized Polymer-Lipid Supported Mesoporous Silica Nanoparticles for Release of Chemotherapeutics in Multidrug Resistant Cancer Cells. *Biomaterials* 2014, 35, 3650-3665.

30. Han, N.; Zhao, Q.; Wan, L.; Wang, Y.; Gao, Y.; Wang, P.; Wang, Z.; Zhang, J.; Jiang, T.; Wang, S. Hybrid Lipid-Capped Mesoporous Silica for Stimuli-Responsive Drug Release and Overcoming Multidrug Resistance. *ACS Appl. Mater. Interfaces* 2015, 7, 3342-3351.

31.   Porotto, M.; Yi, F.; Moscona, A.; LaVan, D. A. Synthetic Protocells Interact with Viral Nanomachinery and Inactivate Pathogenic Human Virus. *PloS one* 2011, 6, e16874.

32.   Mackowiak, S. A.; Schmidt, A.; Weiss, V.; Argyo, C.; von Schirnding, C.; Bein, T.; Bräuchle, C. Targeted Drug Delivery in Cancer Cells with Red-Light Photoactivated Mesoporous Silica Nanoparticles. *Nano Lett.* 2013, 13, 2576-2583.

33.   Buranda, T.; Huang, J.; Ramarao, G.; Ista, L. K.; Larson, R. S.; Ward, T. L.; Sklar, L. A.; Lopez, G. P. Biomimetic Molecular Assemblies on Glass and Mesoporous Silica Microbeads for Biotechnology. *Langmuir* 2003, 19, 1654-1663.

34.   Bayerl, T. M.; Bloom, M. Physical Properties of Single Phospholipid Bilayers Adsorbed to Micro Glass Beads. A New Vesicular Model System Studied by 2h-Nuclear Magnetic Resonance. *Biophys. J.* 1990, 58, 357-362.

35.   Lu, Y.; Fan, H.; Stump, A.; Ward, T. L.; Rieker, T.; Brinker, C. J. Aerosol-Assisted Self-Assembly of Mesostructured Spherical Nanoparticles. *Nature* 1999, 398, 223-226.

36.   Roggers, R. A.; Lin, V. S. Y.; Trewyn, B. G. Chemically Reducible Lipid Bilayer Coated Mesoporous Silica Nanoparticles Demonstrating Controlled Release and Hela and Normal Mouse Liver Cell Biocompatibility and Cellular Internalization. *Molecular Pharmaceutics* 2012, 9, 2770-2777.

37.   Hu, C.-M. J.; Zhang, L.; Aryal, S.; Cheung, C.; Fang, R. H.; Zhang, L. Erythrocyte Membrane-Camouflaged Polymeric Nanoparticles as a Biomimetic Delivery Platform. *Proceedings of the National Academy of Sciences* 2011, 108, 10980-10985.

38.   Hu, C.-M. J.; Fang, R. H.; Wang, K.-C.; Luk, B. T.; Thamphiwatana, S.; Dehaini, D.; Nguyen, P.; Angsantikul, P.; Wen, C. H.; Kroll, A. V.; Carpenter, C.; Ramesh, M.; Qu, V.; Patel, S. H.; Zhu, J.; Shi, W.; Hofman, F. M.; Chen, T. C.; Gao, W.; Zhang, K.; Chien, S.; Zhang, L. Nanoparticle Biointerfacing by Platelet Membrane Cloaking. *Nature* 2015, 526, 118-121.

39.   Roggers, R. A.; Joglekar, M.; Valenstein, J. S.; Trewyn, B. G. Mimicking Red Blood Cell Lipid Membrane to Enhance the Hemocompatibility of Large-Pore Mesoporous Silica. *ACS Applied Materials & Interfaces* 2014, 6, 1675-1681.

40.   Chen, Y.; Chen, H.; Zhang, S.; Chen, F.; Zhang, L.; Zhang, J.; Zhu, M.; Wu, H.; Guo, L.; Feng, J.; Shi, J. Multifunctional Mesoporous

Nanoellipsoids for Biological Bimodal Imaging and Magnetically Targeted Delivery of Anticancer Drugs. *Advanced Functional Materials* 2011, 21, 270-278.

41.   Han, L.; Zhou, Y.; He, T.; Song, G.; Wu, F.; Jiang, F.; Hu, J. One-Pot Morphology-Controlled Synthesis of Various Shaped Mesoporous Silica Nanoparticles. *Journal of Materials Science* 2013, 48, 5718-5726.

42.   Meng, H.; Yang, S.; Li, Z.; Xia, T.; Chen, J.; Ji, Z.; Zhang, H.; Wang, X.; Lin, S.; Huang, C.; Zhou, Z. H.; Zink, J. I.; Nel, A. E. Aspect Ratio Determines the Quantity of Mesoporous Silica Nanoparticle Uptake by a Small Gtpase-Dependent Macropinocytosis Mechanism. *ACS Nano* 2011, 5, 4434-4447.

43.   Trewyn, B. G.; Nieweg, J. A.; Zhao, Y.; Lin, V. S. Y. Biocompatible Mesoporous Silica Nanoparticles with Different Morphologies for Animal Cell Membrane Penetration. *Chemical Engineering Journal* 2008, 137, 23-29.

44.   Du, X.; Qiao, S. Z. Dendritic Silica Particles with Center-Radial Pore Channels: Promising Platforms for Catalysis and Biomedical Applications. *Small* 2015, 11, 392-413.

45.   Nandiyanto, A. B. D.; Kim, S.-G.; Iskandar, F.; Okuyama, K. Synthesis of Spherical Mesoporous Silica Nanoparticles with Nanometer-Size Controllable Pores and Outer Diameters. *Microporous Mesoporous Mater.* 2009, 120, 447-453.

46.   Huh, S.; Wiench, J. W.; Yoo, J.-C.; Pruski, M.; Lin, V. S. Y. Organic Functionalization and Morphology Control of Mesoporous Silicas Via a Co-Condensation Synthesis Method. *Chemistry of Materials* 2003, 15, 4247-4256.

47.   Stachowiak, J. C.; Hayden, C. C.; Sasaki, D. Y. Steric Confinement of Proteins on Lipid Membranes Can Drive Curvature and Tubulation. *Proceedings of the National Academy of Sciences* 2010, 107, 7781-7786.

48.   He, L.; Lai, H.; Chen, T. Dual-Function Nanosystem for Synergetic Cancer Chemo-/Radiotherapy through Ros-Mediated Signaling Pathways. *Biomaterials* 2015, 51, 30-42.

49.   He, Q.; Zhang, Z.; Gao, Y.; Shi, J.; Li, Y. Intracellular Localization and Cytotoxicity of Spherical Mesoporous Silica Nano- and Microparticles. *Small* 2009, 5, 2722-2729.

50.   Slowing, I. I.; Wu, C.-W.; Vivero-Escoto, J. L.; Lin, V. S. Y. Mesoporous Silica Nanoparticles for Reducing Hemolytic Activity Towards Mammalian Red Blood Cells. *Small* 2009, 5, 57-62.

51.   Brinker, C. J. a. S., G.W. *Sol-Gel Science: The Physics and Chemistry of Sol-Gel Processing*. Academic Press, Inc.: 1990.

52.   Li, C.; Yang, D.; Ma, P. a.; Chen, Y.; Wu, Y.; Hou, Z.; Dai, Y.; Zhao, J.; Sui, C.; Lin, J. Multifunctional Upconversion Mesoporous Silica Nanostructures for Dual Modal Imaging and in Vivo Drug Delivery. *Small* 2013, 9, 4150-4159.

53.   Yanes, R. E.; Tarn, D.; Hwang, A. A.; Ferris, D. P.; Sherman, S. P.; Thomas, C. R.; Lu, J.; Pyle, A. D.; Zink, J. I.; Tamanoi, F. Involvement of Lysosomal Exocytosis in the Excretion of Mesoporous Silica Nanoparticles and Enhancement of the Drug Delivery Effect by Exocytosis Inhibition. *Small* 2013, 9, 697-704.

54.   Grün, M.; Lauer, I.; Unger, K. K. The Synthesis of Micrometer- and Submicrometer-Size Spheres of Ordered Mesoporous Oxide Mcm-41. *Advanced Materials* 1997, 9, 254-257.

55.   Möller, K.; Kobler, J.; Bein, T. Colloidal Suspensions of Nanometer-Sized Mesoporous Silica. *Advanced Functional Materials* 2007, 17, 605-612.

56.   Du, X.; Shi, B.; Tang, Y.; Dai, S.; Qiao, S. Z. Label-Free Dendrimer-Like Silica Nanohybrids for Traceable and Controlled Gene Delivery. *Biomaterials* 2014, 35, 5580-5590.

57.   Shen, D.; Yang, J.; Li, X.; Zhou, L.; Zhang, R.; Li, W.; Chen, L.; Wang, R.; Zhang, F.; Zhao, D. Biphase Stratification Approach to Three-Dimensional Dendritic Biodegradable Mesoporous Silica Nanospheres. *Nano Lett.* 2014, 14, 923-932.

58.   Ferris, D. P.; Lu, J.; Gothard, C.; Yanes, R.; Thomas, C. R.; Olsen, J.-C.; Stoddart, J. F.; Tamanoi, F.; Zink, J. I. Synthesis of Biomolecule-Modified Mesoporous Silica Nanoparticles for Targeted Hydrophobic Drug Delivery to Cancer Cells. *Small* 2011, 7, 1816-1826.

59.   Teng, I. T.; Chang, Y.-J.; Wang, L.-S.; Lu, H.-Y.; Wu, L.-C.; Yang, C.-M.; Chiu, C.-C.; Yang, C.-H.; Hsu, S.-L.; Ho, J.-a. A. Phospholipid-Functionalized Mesoporous Silica Nanocarriers For selective Photodynamic Therapy of Cancer. *Biomaterials* 2013, 34, 7462-7470.

60.   Mornet, S.; Lambert, O.; Duguet, E.; Brisson, A. The Formation of Supported Lipid Bilayers on Silica Nanoparticles Revealed by Cryoelectron Microscopy. *Nano Lett.* 2005, 5, 281-285.

61.   Reynolds, J. G.; Geretti, E.; Hendriks, B. S.; Lee, H.; Leonard, S. C.; Klinz, S. G.; Noble, C. O.; Lücker, P. B.; Zandstra, P. W.; Drummond, D. C.; Olivier Jr, K. J.; Nielsen, U. B.; Niyikiza, C.; Agresta, S. V.; Wickham, T. J. Her2-Targeted Liposomal Doxorubicin Displays Enhanced Anti-

Tumorigenic Effects without Associated Cardiotoxicity. *Toxicol. Appl. Pharmacol.* 2012, 262, 1-10.

62.   Sapra, P.; Allen, T. M. Ligand-Targeted Liposomal Anticancer Drugs. *Progress in Lipid Research* 2003, 42, 439-462.

63.   Durfee, P. N.; Lin, Y.-S.; Dunphy, D. R.; Muñiz, A. J.; Butler, K. S.; Humphrey, K. R.; Lokke, A. J.; Agola, J. O.; Chou, S. S.; Chen, I. M.; Wharton, W.; Townson, J. L.; Willman, C. L.; Brinker, C. J. Mesoporous Silica Nanoparticle-Supported Lipid Bilayers (Protocells) for Active Targeting and Delivery to Individual Leukemia Cells. *ACS Nano* 2016.

64.   Sudhan Shaik, M.; Kanikkannan, N.; Singh, M. Conjugation of Anti-My9 Antibody to Stealth Monensin Liposomes and the Effect of Conjugated Liposomes on the Cytotoxicity of Immunotoxin. *Journal of Controlled Release* 2001, 76, 285-295.

65.   Park, J. W.; Hong, K.; Kirpotin, D. B.; Colbern, G.; Shalaby, R.; Baselga, J.; Shao, Y.; Nielsen, U. B.; Marks, J. D.; Moore, D.; Papahadjopoulos, D.; Benz, C. C. Anti-Her2 Immunoliposomes. *Clinical Cancer Research* 2002, 8, 1172-1181.

66.   Marqués-Gallego, P.; de Kroon, A. I. Ligation Strategies for Targeting Liposomal Nanocarriers. *BioMed research international* 2014, 2014.

67.   Torchilin, V.; Goldmacher, V.; Smirnov, V. Comparative Studies on Covalent and Noncovalent Immobilization of Protein Molecules on the Surface of Liposomes. *Biochemical and biophysical research communications* 1978, 85, 983-990.

68.   Papadia, K.; Markoutsa, E.; Antimisiaris, S. G. A Simplified Method to Attach Antibodies on Liposomes by Biotin-Streptavidin Affinity for Rapid and Economical Screening of Targeted Liposomes. *Journal of Biomedical Nanotechnology* 2014, 10, 871-876.

69.   Meng, H.; Xue, M.; Xia, T.; Ji, Z.; Tarn, D. Y.; Zink, J. I.; Nel, A. E. Use of Size and a Copolymer Design Feature to Improve the Biodistribution and the Enhanced Permeability and Retention Effect of Doxorubicin-Loaded Mesoporous Silica Nanoparticles in a Murine Xenograft Tumor Model. *ACS Nano* 2011, 5, 4131-4144.

70.   Phillips, E.; Penate-Medina, O.; Zanzonico, P. B.; Carvajal, R. D.; Mohan, P.; Ye, Y.; Humm, J.; Gönen, M.; Kalaigian, H.; Schöder, H.; Strauss, H. W.; Larson, S. M.; Wiesner, U.; Bradbury, M. S. Clinical Translation of an Ultrasmall Inorganic Optical-Pet Imaging Nanoparticle Probe. *Science Translational Medicine* 2014, 6, 260ra149.

CHAPTER 2

PROTOCELL COMPONENT SYNTHESIS AND ASSEMBLY

2.1 Overview

Given the unique challenge of nanoparticle-based delivery to leukemic cells, it is worthwhile to consider the optimal drug delivery platform. An effectively targeted nanocarrier for leukemia treatment would ideally possess the following combined characteristics: 1) uniform and controllable particle size and shape; 2) high colloidal stability under physiological and storage conditions; 3) minimal non-specific binding interactions, uptake by the MPS, or removal by excretory systems, allowing extended circulation time; 4) high specificity to diseased cells or tissues; 5) high capacity for and precise release of diverse therapeutic cargos; and 6) low cytotoxicity. Liposomes are one of the most successful classes of nanocarriers for achieving both passive and active targeted delivery, and numerous U.S. Food and Drug Administration (FDA) approved formulations exist.[1-4] Of candidate nanocarriers, liposomes exhibit many advantageous properties, including ease of synthesis, high biocompatibility, flexible formulation, targetability, and increased circulation times compared to free drugs.[5-9] However, it has proven difficult to identify stable lipid formulations that allow drug encapsulation but prevent leakage.[10, 11] Polymeric-based therapeutic nanocarriers have also been developed and several formulations are currently being tested in clinical trials.[3] Similar to liposomes, many polymer-based nanocarriers are biocompatible and easy to manufacture, however they also suffer from limited stability *in vivo* and dose dependent toxicity.[12-14] Furthermore, both liposomes and polymer-based nanoparticles suffer the issues of invariant size and shape, uncontrollable, often burst release profiles, and

highly interdependent properties, whereby changing one property, such as loading efficiency, affect numerous other properties, such as size, charge, and stability.[5, 7-9] By comparison, MSNPs have controlled size and shape, and are composed of high surface area (500 to > 1000 m^2/g) networks of uniformly sized pores whose size and surface chemistry can be varied widely to accommodate high payloads of disparate cargos.[15, 16] Furthermore, colloidal mesoporous silica is biodegradable and GRAS by the FDA.[17] The drawbacks of MSNP are that often coatings are required to contain the cargo and shield surface silanols ($\equiv$Si-OH) and deprotonated silanols ($\equiv$Si-O⁻) that are highly lipophilic and known to promote non-specific binding and mononuclear phagocytic system uptake.[18-20] In this context, MSNP-supported lipid bilayers (protocells), a rapidly emerging class of nanocarriers, have unique attributes (**Figure 2.1**). Protocells are formed by the encapsulation of the MSNP core within a SLB followed optionally by conjugation of polymers, such as PEG, and targeting and/or trafficking ligands to the surface of the SLB.[21-35] Protocells synergistically combine the advantages of liposomes, *viz.* low inherent toxicity and immunogenicity, and long circulation times, with the advantages of MSNP, *viz.* size and shape control and an enormous capacity for multiple cargos and disparate cargo combinations. Moreover, many studies have revealed that protocells and related MSNP supported bilayer nanocarriers are stable at neutral pH but exhibit pH triggered cargo release under endosomal conditions.[22-28, 33]

Figure 2.1 – *SLB Fusion and Protocell Targeting Modification Schematic*
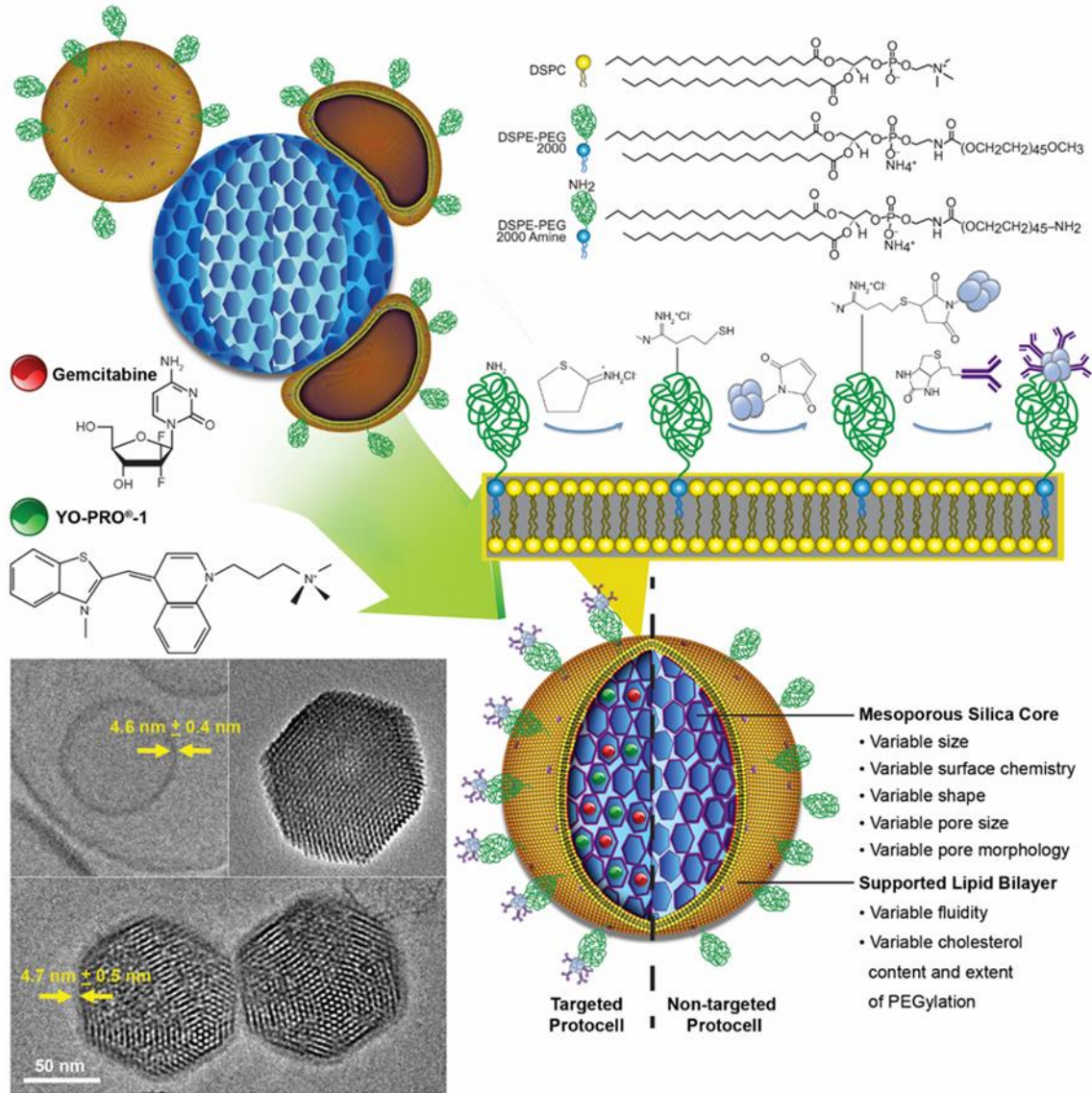
Figure 2.1 – Schematic depicting lipid vesicle fusion onto mMSNP to form mMSNP-supported lipid bilayers (protocells). Drug (gemcitabine) and/or fluorescent molecular cargo (YO-PRO®-1) loaded protocells were assembled by soaking nanoparticle cores with cargo for 24 hours in aqueous buffer followed by fusion of (DSPC:chol:DSPE-PEG$_{2000}$-NH$_2$ – 49:49:2 mol ratio (targeted formulation) or (DSPC:chol:DSPE-PEG$_{2000}$ – 54:44:2 mol ratio (non-targeted formulation) vesicles. Leukemia cell targeting was achieved by NeutrAvidin modification followed by binding to biotinylated EGFR antibodies. SLB thickness is nearly identical to that of the vesicle used for protocell synthesis as shown in Cryo-TEM images. Adapted and reproduced with permission.[36] © 2016, The American Chemical Society.

2.2 Results and Discussion

2.2.1 Synthesis Criteria for Monosized Protocells

Protocells were formed by fusion of zwitterionic lipid-based vesicles on monosized MSNP (mMSNP) cores synthesized with varying size, shape, and pore morphologies (See Materials and Methods section below for detailed synthesis procedures). Vesicle fusion on silica glass substrates to form planar supported lipid bilayers has been extensively studied using atomic force microscopy, quartz crystal microbalance, deuterium nuclear magnetic resonance, surface plasmon resonance, fluorescence microscopy and ellipsometry,[37-42] where the fusion process has been shown to involve vesicle adsorption followed (in some cases at a critical surface coverage) by vesicle rupture and desorption of excess lipid to form a bilayer separated from the glass surface by an intervening 1 to 2 nm thick water layer. Generally, the process of phospholipid vesicle fusion with smooth glass supports is governed by the same Derjaguin-Landau-Verwey-Overbeek (DLVO) forces that are responsible for colloid aggregation; hence, both vesicle-substrate and vesicle-vesicle interactions need to be considered. DLVO theory models the forces in such systems as consisting of an electrostatic interaction combining with a van der Waals attraction; as such, SLB fusion depends on pH, which controls the extent of deprotonation of surface silanol groups to form anionic $\equiv$Si-O⁻ species above pH 2, and the ionic strength and cationic component of the buffer, which dictate, respectively, the Debye length (mediating electrostatic interactions) and the cation hydration diameter.[43] Cremer and Boxer studied fusion of positively charged, neutral and negatively

charged vesicles onto glass as a function of pH (3-12) and ionic strength (0-90 mM). They found neutral and positively charged vesicles fuse under all conditions, whereas negatively charged vesicles fuse only above a critical ionic strength, which increased with pH (negative charge of silica surface). This is in keeping with expectations of DLVO theory as increasing ionic strength reduces electrostatic repulsion between vesicles and the glass surface.[43]

Although considerably fewer studies have been performed on vesicle fusion on silica nanoparticles, we anticipate that the mechanism and governing forces would be comparable but further influenced by the nanoparticle curvature. Using differential scanning calorimetry (DSC) in combination with dynamic light scattering (DLS), Savarala *et al.* studied the fusion of the zwitterionic 1,2-dimyristoyl-sn-glycero-3-phosphocholine (DMPC) vesicles on silica beads with diameters ranging from 100 to 4 – 6 nm at neutral pH and ionic strengths ranging from 0 to 0.75 mM NaCl. For a critical limiting ratio of lipid surface area to silica surface area of 1 ($SA_{lipid}:SA_{silica} = 1$), they found no (or very slow) vesicle fusion to occur in pure water and that higher ionic strengths were required to achieve fusion on successively smaller particles (100-20 nm).[44] Silica beads sized between 4 – 6 nm did not form supported lipid bilayers; rather, these beads appeared to associate with the exterior surfaces of the vesicles.[44] These results differ somewhat from flat surfaces and, in keeping with DLVO theory, suggest that, for progressively smaller particles, possible repulsive electrostatic interactions must be reduced by increasing ionic strength and/or attractive electrostatic interactions promoted by cation association with phosphocholine to

compensate for increased membrane curvature (assuming conformal SLBs). This result is consistent with a study by Garcia-Manyes *et al.* that showed the surface charge of zwitterionic DMPC liposomes at neutral pH is negative at < 100 mM NaCl solution and positive at higher ionic strength. Excess lipid *i.e.,* $SA_{lipid}:SA_{silica} > 1$ appears to promote SLB formation on silica nanoparticles.[45] Mornet *et al.* studied the fusion of 30 – 50 nm diameter negatively charged DOPC / DOPS vesicles on ~ 110 nm diameter spherical silica colloids by direct Cryo-TEM. For $SA_{lipid}:SA_{silica} = 15$ and a buffer ionic strength of 152 mM, they observed conformal ~ 5 nm thick SLBs to form by a process involving conformal vesicle adsorption followed by rupture to form SLB patches.[46] Multiple adsorption and fusion events resulted in complete SLBs that conformed to the moderate surface roughness / microporosity of the Stöber silica nanoparticle surface.[46]

Numerous researchers have studied vesicle fusion on mesoporous silica macroparticles and nanoparticles as a means to form cell-like biomimetic materials[47] and lipid bilayer encapsulated nanoparticles for drug delivery.[22-29, 33] To date, nanoparticle studies have employed primarily spherical cetyltrimethylammonium bromide (CTAB)-templated MSNP formed by aerosol-assisted EISA[22, 23, 28, 34, 35, 48] or colloidal processing and characterized by worm-like or isotropic mesopores with diameters of about 2-3 nm.[24-27, 29, 33] Direct Cryo-TEM observations of protocells have shown the bilayer thickness to range from ~ 4 – 7 nm,[25, 28, 35, 48] corresponding to that measured for solid silica nanoparticle SLBs[46] or planar SLBs.[41] SLBs span the surface mesopores and remain

conformal to the MSNP surface, as we. and others, have shown by Cryo-TEM imaging (see, for example, **Figure 2.1)**. With respect to SLB formation, surface porosity decreases the areal fraction of silica at the nanoparticle surface and, assuming spanning lipid bilayers, reduces accordingly the possible magnitude of both van der Waals and electrostatic interactions that drive vesicle fusion.

2.3 Materials and Methods

2.3.1 Materials

All chemicals and reagents were used as received. Ammonium hydroxide (NH_4OH, 28 – 30 %), 3-aminopropyltriethoxysilane (98 %, APTES), ammonium nitrate (NH_4NO_3), benzyldimethylhexadecylammonium chloride (BDHAC), n-cetyltrimethylammonium bromide (CTAB), Cetyltrimethylammonium chloride (CTAC), N,N-dimethyl formamide (DMF), rhodamine B isothiocyanate (RITC), tetraethyl orthosilicate (TEOS), cyclohexane, and triethanolamine (TEA) were purchased from Sigma-Aldrich (St. Louis, MO). Hydrochloric acid (36.5 – 38 %, HCl) was purchased from EMD Chemicals (Gibbstown, NJ). Absolute (99.5 %) and 95 % ethanol were obtained from PHARMCO-AAPER (Brookfield, CT). 1,2-dioleoyl-sn-glycero-3-phosphocholine (DOPC), 1,2-distearoyl-snglycero-3-phosphocholine (DSPC), 1,2-dioleoyl-*sn*-glycero-3-phosphoethanolamine-N-[methoxy(polyethylene glycol)-2000] (ammonium salt) (DOPE-PEG$_{2000}$), 1,2-distearoyl-sn-glycero-3-phosphoethanolamine-N-[methoxy(polyethylene glycol)-2000] (ammonium salt) (DSPE-PEG$_{2000}$), 1,2-distearoyl-*sn*-glycero-3-phosphoethanolamine-N-[amino(polyethylene glycol)-2000] (DSPE-PEG$_{2000}$-NH$_2$)

phospholipids and cholesterol (chol, ovine wool, >98 %) were purchased from Avanti Polar Lipids (Birmingham, AL). Phosphate buffered saline (PBS) was purchased from Gibco (Logan, UT).

2.3.2 Synthesis of mMSNP Composed of Hexagonally Arranged Cylindrical Pores (2.8 nm pore size), Hexagonal mMSNP

To prepare monosized dye-labeled mMSNP (~ 95 nm in diameter, ~ 130 nm in hydrodynamic size in D.I. water), 3 mg of RITC was dissolved in 2 mL of DMF followed by addition of 1.5 µL APTES.[49] The synthesis conditions of Hexagonal mMSNP is based on reported literature.[50] See **Figure 2.2** for schematic description of synthesis. The RITC-APTES solution was incubated at room temperature for at least 1 hour. Next, 290 mg of CTAB was dissolved in 150 mL of 0.51 M ammonium hydroxide solution in a 250 mL beaker, sealed with parafilm (Neenah, WI), and placed in a mineral oil bath at 50 °C. After continuously stirring for 1 hour, 3 mL of 0.88 M TEOS solution (prepared in ethanol) and 1 mL of RITC-APTES solution were combined and added immediately to the surfactant solution. After another 1 hour of continuous stirring, the particle solution was stored at 50 °C for ~ 18 hours under static conditions. Next, solution was passed through a 1.0 µm Acrodisc 25 mm syringe filter (PALL Life Sciences, Ann Arbor, MI) followed by a hydrothermal treatment at 70 °C for 24 hours. Followed procedure for CTAB removal was as described in literature.[51] Briefly, mMSNP were transferred to 75 mM ammonium nitrate solution (prepared in ethanol) then placed in an oil bath at 60 °C for 1 hour with reflux and stirring. The mMSNP were then washed in 95 % ethanol and

Figure 2.2 – *Hexagonal MSNP Synthesis Schematic*
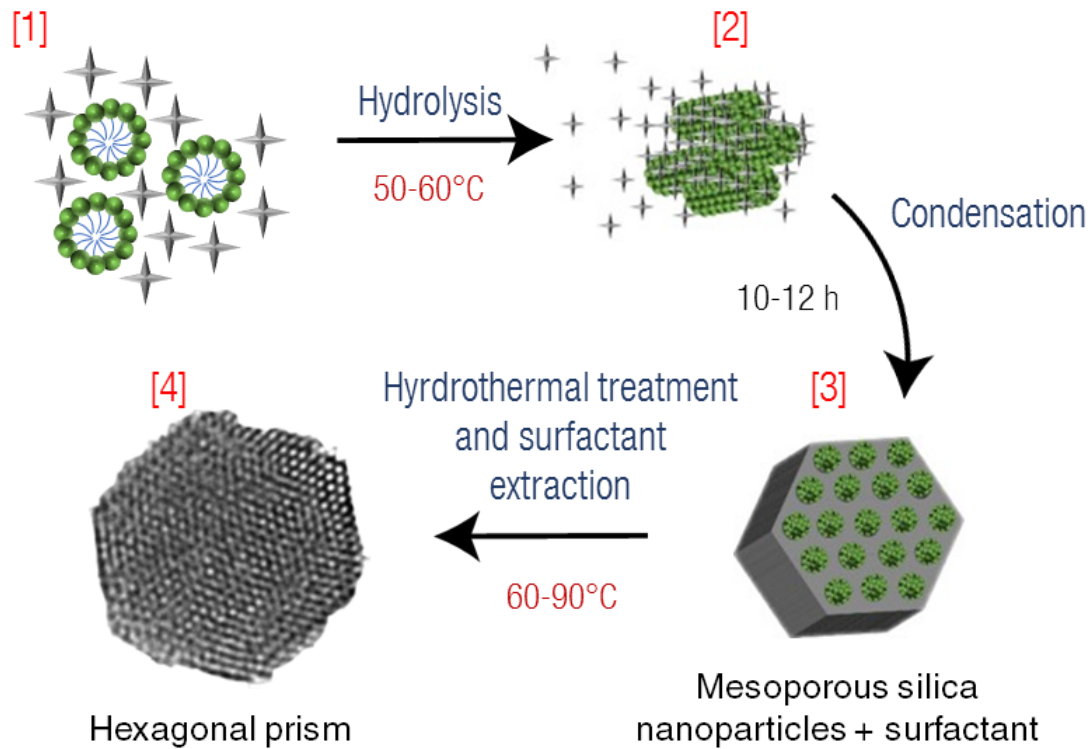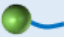
Figure 2.2 – Schematic depicting Hexagonal mMSNP synthesis process. [1] Silica precursor (TEOS) is mixed with surfactant (CTAB) under basic conditions, [2] Cooperative self-assembly of silicate micelles, [3] Silica condenses around cylindrical CTAB micelles to form mMSNP framework, and [4] Hydrothermal treatment and surfactant extraction results in mMSNP cores that can be loaded with cargo and used to support lipid bilayers.

transferred to 12 mM HCl ethanolic solution and heated at 60 °C for 2 hours with reflux and stirring. Lastly, Hexagonal mMSNP were washed in 95 % ethanol, then 99.5 % ethanol, and stored in 99.5 % ethanol.

2.3.3 Synthesis of Spherical mMSNP with Isotropic Pores (2.8 nm pore size)

To prepare monosized spherical mMSNP composed of isotropic mesopores, we used the same procedure described above for synthesis of mMSNP with hexagonally arranged pore structure. However, we substituted cationic surfactant BDHAC for CTAB as the template. The 3-dimensional isotropic pore arrangement is due to a larger micelle packing parameter of BDHAC, compared to CTAB surfactant.[52] See **Figure 2.3** for schematic description of synthesis.

2.3.4 Synthesis of Spherical mMSNP Composed of Dendritic Large Pores (5 nm, 9 nm, and 18 nm pore size)

The large pore spherical mMSNP were synthesized by a published biphase method.[53-55] Syntheses of 5 nm, 9 nm, and 18 nm pore mMSNP are based on a modified condition reported by Zhao *et al.*[55] For preparation of 5 nm dendritic pore mMSNP, 0.18 g of TEA was dissolved in 36 mL of D.I. water and 24 mL of 25 w/w % CTAC in a 100 mL round bottom flask. The surfactant solution was stirred at 150 rpm and heated at 50 °C in an oil bath. After 1 hour, 20 mL of 20 v/v % TEOS (in cyclohexane) was added to the CTAC-TEA aqueous solution. After 12 hours, the particle solution was washed with D.I. water twice by centrifugation. Further surfactant removal achieved by following the

Figure 2.3 – *Spherical Small-pore MSNP Synthesis Schematic*
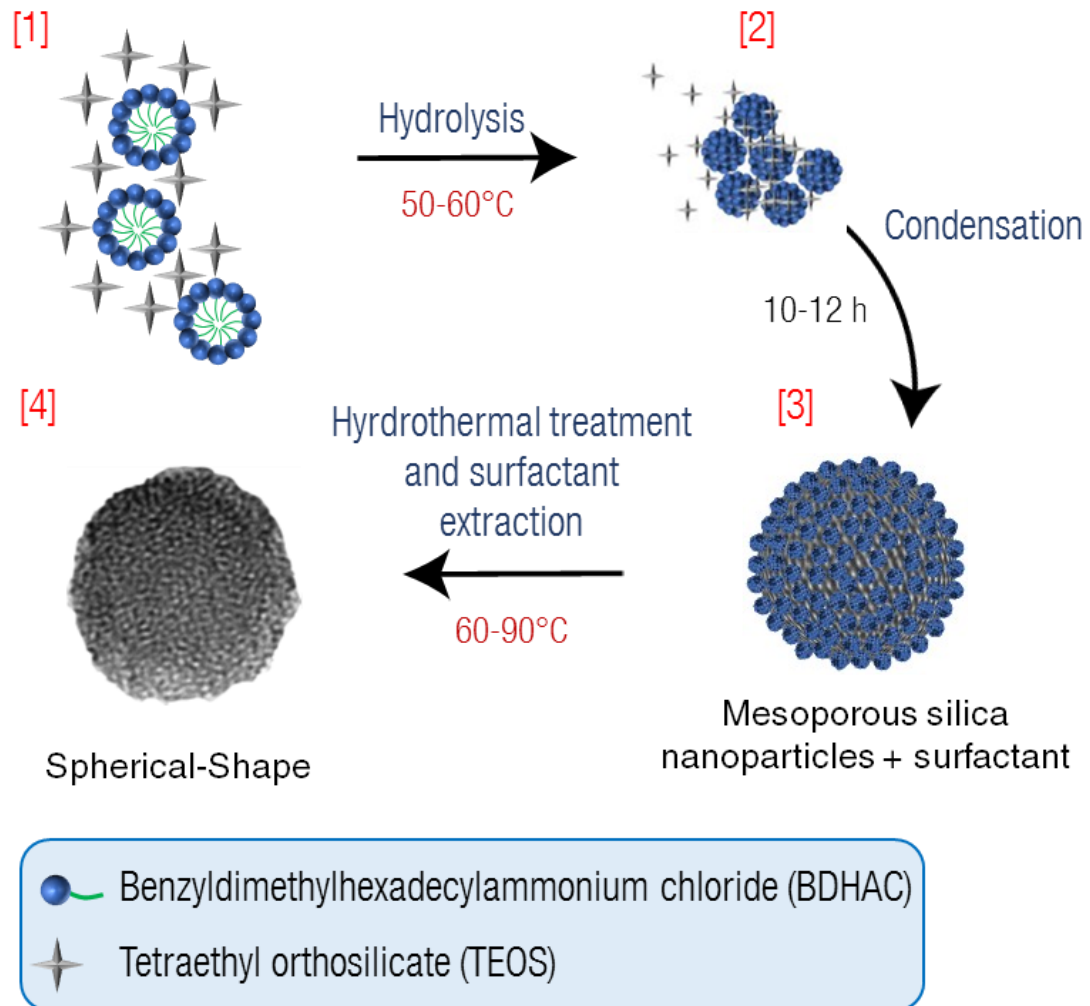
Figure 2.3 – Schematic depicting synthesis of spherical mMSNP with an anisotropic pore structure. [1] Silica precursor (TEOS) is mixed with surfactant (BDHAC) under basic conditions, [2] Cooperative self-assembly of silicate micelles, [3] Silica condenses around three-dimensional worm-like BDHAC micelles to form mMSNP framework, and [4] Hydrothermal treatment and surfactant extraction results in mMSNP cores that can be loaded with cargo and used to support lipid bilayers.

previously described conditions used in preparation of small pore mMSNP. For

synthesis of 9 nm dendritic pore mMSNP, the stirring rate and organic phase

concentration were adjusted to 300 rpm and 10 v/v % TEOS, respectively. For

synthesis of 18 nm dendritic pore mMSNP, the TEOS concentration in the

organic phase was changed to 5 v/v %. All other steps were identical. See

Figure 2.4 for schematic description of synthesis.

2.3.5 Synthesis of Rod-shaped mMSNP with Hexagonally Arranged Cylindrical Pores (2.8 nm pore size)

The shape of mMSNP can be simply tuned to rod-like morphology by

altering the CTAB concentration, stirring rate, and ammonia concentration.[56, 57]

Briefly, 0.5 g CTAB was dissolved in 150 mL of 0.22 M ammonium hydroxide

solution at 25 °C under continuous stirring (300 rpm). Next, of 1 mL TEOS was

added (drop wise) to the surfactant solution with stirring. After 1 hour, the

particle solution was aged under static conditions for 24 hours, then

subsequently transferred to a sealed container and heated to 70 °C for 24 hours.

The removal of surfactant was followed the same procedures described

previously. See **Figure 2.5** for schematic description of synthesis.

2.3.6 Liposome Preparation

Lipids and cholesterol ordered from Avanti Polar Lipids were

presolubilized in chloroform at 25 mg/mL and were stored at -20 °C. To prepare

liposomes, lipids were mixed at different mol % ratios including (54:44:2) for

Figure 2.4 – *Spherical Large-Pore MSNP Synthesis Schematic*
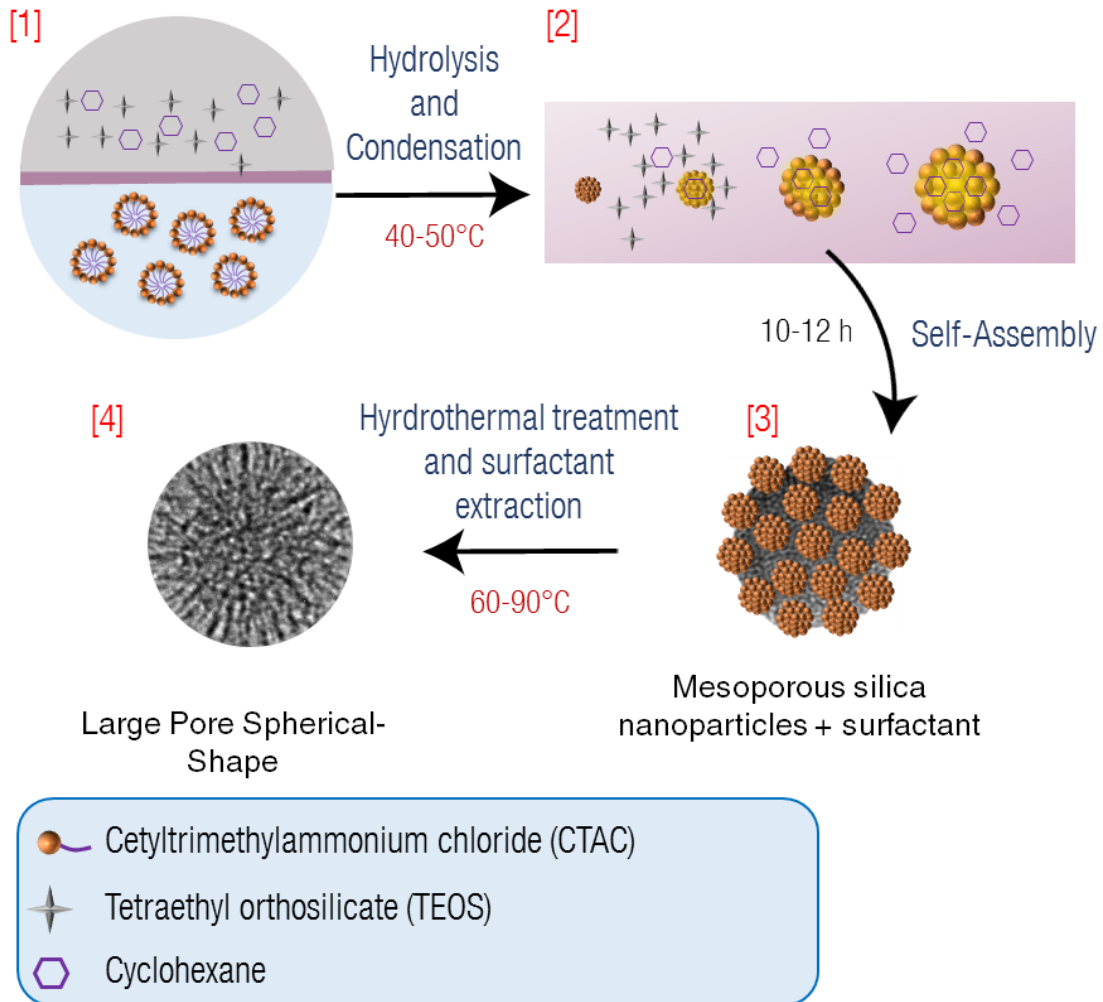
Figure 2.4 – Schematic depicting synthesis of mMSNP with larger pore structure (5, 9, and 18 nm pore diameter). [1] Silica precursor (TEOS) is mixed with cyclohexane in either 5, 10, 20 v/v % ratio (ratio influences pore size) and layered over surfactant (CTAC) dissolved in aqueous buffer, [2] Cooperative self-assembly of silicate micelles and pore swelling by cyclohexane entering the hydrophobic region of the CTAC micelles, occurring at the organic / aqueous interface, [3] Silica condenses around CTAC micelles to form mMSNP framework, and [4] Hydrothermal treatment and surfactant extraction results in large pore mMSNP cores that can be loaded with cargo and used to support lipid bilayers.

Figure 2.5 – *Rod-Shaped MSNP Synthesis Schematic*
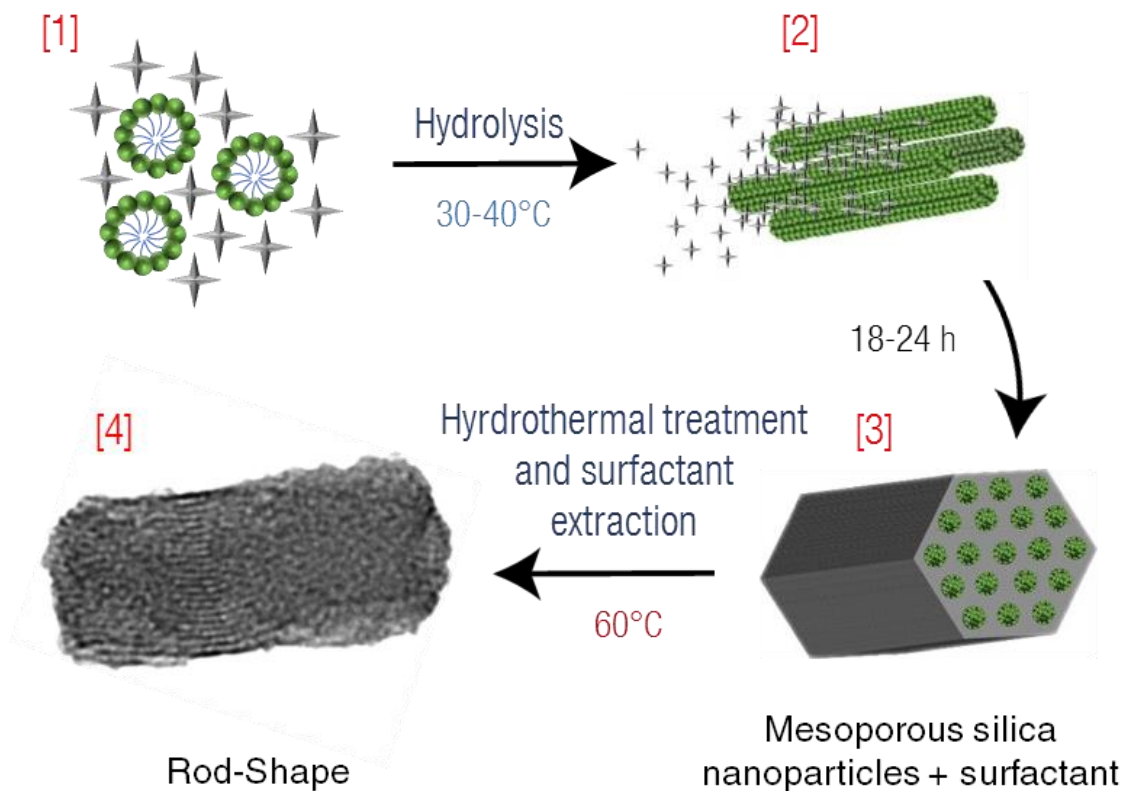
Figure 2.5 – Schematic depicting synthesis of rod-shaped mMSNP with hexagonally arranged isotropic pore structure. [1] Silica precursor (TEOS) is mixed with surfactant (CTAB) under basic conditions, [2] Cooperative self-assembly of silicate micelles, [3] Silica condenses around cylindrical CTAB micelles to form mMSNP framework, and [4] Hydrothermal treatment and surfactant extraction results in mMSNP cores that can be loaded with cargo and used to support lipid bilayers.

DOPC:chol:DOPE-PEG$_{2000}$ and DSPC:chol:DSPE-PEG$_{2000}$, and (49:49:2) for

DSPC:chol:DSPE-PEG$_{2000}$-NH$_2$ (**Table 2.1**). Lipid films were prepared by drying

lipid mixtures (in chloroform) under high vacuum to remove the organic solvent.

Then the lipid film was hydrated in 80 mM PBS and bath sonicated for 30

minutes to obtain a liposome solution. Finally, the liposome solution was further

passed through a 0.1 μm polycarbonate filter membrane (minimum 21 passes)

using a mini-extruder to produce uniform and unilamellar vesicles with

hydrodynamic diameters less than 100 nm. See **Figure 2.6** for schematic

description of liposome preparation.

2.3.7 Protocell Assembly

To form protocells, mMSNP are transferred to D.I. water at 1 mg/mL

concentration by centrifugation (15,000 x g, 10 minutes) and added to liposome

solution (2 mg/mL) in 80 mM PBS (1:1 v/v and 1:2 w/w ratios). The mixture was

bath sonicated ~ 10 s and non-fused liposomes were removed by centrifugation

(15,000 x g, 10 minutes). Pelleted protocells were redispersed in 160 mM PBS

via bath sonication, this step is repeated twice.

Table 2.1 – *Hydrodynamic Size Comparison of Liposomes*

Sample	Medium	Mol ratio (%)	Hydrodynamic Diameter (nm)	PdI
DOPC:chol:DOPE-PEG$_{2000}$	PBS	54:44:2	75.0 ± 0.9	0.139 ± 0.041
DSPC:chol:DSPE-PEG$_{2000}$	PBS	55:44:2	88.5 ± 4.2	0.142 ± 0.017
DSPC:chol:DSPE-PEG$_{2000}$-NH$_2$	PBS	49:49:2	93.5 ± 7.1	0.148 ± 0.023

Table 2.1 – Composition and representative hydrodynamic size data of liposomes used for preparation of protocells. Data represent mean ± SD, n=3. Adapted and reproduced with permission.[36] © 2016, The American Chemical Society.

Figure 2.6 – *Liposome Preparation Schematic*

DSPC:chol:DSPE-
PEG

54:44:2
(Molar Ratio %)

Dried Lipid
Film

Polydisperse
Liposomes

Monodisperse
Liposomes

Primary Components

DSPC

Cholesterol

DSPE-PEG 2000
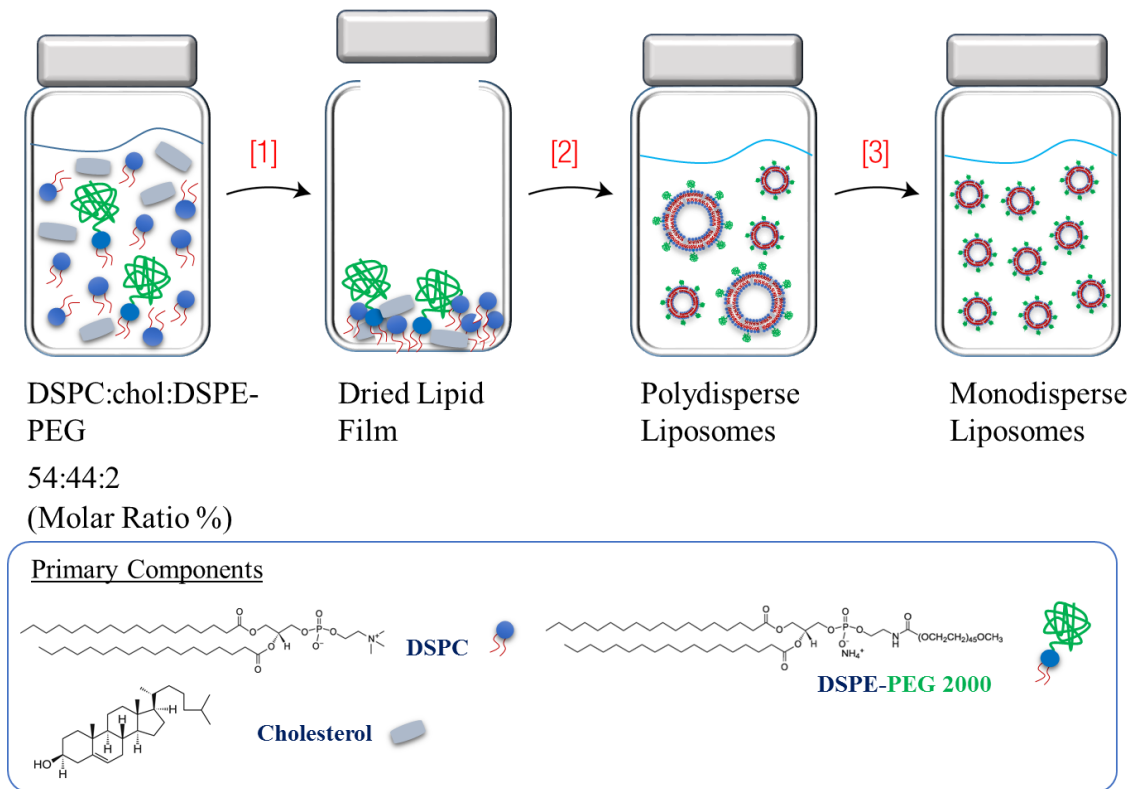
Figure 2.6 – Schematic depicting the preparation of liposomes for SLB fusion. Individual liposome components are mixed together in chloroform. [1] Solvent is evaporated under high vacuum. [2] Dried lipid films is rehydrated in aqueous buffer (PBS) then bath sonicated to produce polydisperse and multilamellar liposomes. [3] Sonicated liposomes are then extruded through a 0.1 µm polycarbonate filter membrane to produce small, uniform, unilamellar liposomes.

2.4 References

1. Allen, T. M.; Cullis, P. R. Drug Delivery Systems: Entering the Mainstream. *Science* 2004, 303, 1818-1822.

2. Iwamoto, T. Clinical Application of Drug Delivery Systems in Cancer Chemotherapy: Review of the Efficacy and Side Effects of Approved Drugs. *Biol. Pharm. Bull.* 2013, 36, 715-718.

3. Egusquiaguirre, S.; Igartua, M.; Hernández, R.; Pedraz, J. Nanoparticle Delivery Systems for Cancer Therapy: Advances in Clinical and Preclinical Research. *Clin. Transl. Oncol.* 2012, 14, 83-93.

4. Pattni, B. S.; Chupin, V. V.; Torchilin, V. P. Chem. Rev. *Chemical Reviews* 2015, 115, 10938-10966.

5. Davis, M. E.; Chen, Z.; Shin, D. M. Nanoparticle Therapeutics: An Emerging Treatment Modality for Cancer. *Nat Rev Drug Discov* 2008, 7, 771-782.

6. Deshpande, P. P.; Biswas, S.; Torchilin, V. P. Current Trends in the Use of Liposomes for Tumor Targeting. *Nanomedicine (London, U. K.)* 2013, 8, 10.2217/nnm.13.118.

7. Farokhzad, O. C.; Langer, R. Acs Nano. *ACS Nano* 2009, 3, 16-20.

8. Peer, D.; Karp, J. M.; Hong, S.; Farokhzad, O. C.; Margalit, R.; Langer, R. Nanocarriers as an Emerging Platform for Cancer Therapy. *Nat. Nanotechnol.* 2007, 2, 751-760.

9. Torchilin, V. P. Recent Advances with Liposomes as Pharmaceutical Carriers. *Nat. Rev. Drug Discovery* 2005, 4, 145-160.

10. Çağdaş, M.; Sezer, A. D.; Bucak, S. Liposomes as Potential Drug Carrier Systems for Drug Delivery. INTECH: 2014.

11. Reynolds, J. G.; Geretti, E.; Hendriks, B. S.; Lee, H.; Leonard, S. C.; Klinz, S. G.; Noble, C. O.; Lücker, P. B.; Zandstra, P. W.; Drummond, D. C.; Olivier Jr, K. J.; Nielsen, U. B.; Niyikiza, C.; Agresta, S. V.; Wickham, T. J. Her2-Targeted Liposomal Doxorubicin Displays Enhanced Anti-Tumorigenic Effects without Associated Cardiotoxicity. *Toxicol. Appl. Pharmacol.* 2012, 262, 1-10.

12. Elsabahy, M.; Wooley, K. L. Design of Polymeric Nanoparticles for Biomedical Delivery Applications. *Chem. Soc. Rev.* 2012, 41, 2545-2561.

13.	Draz, M. S.; Fang, B. A.; Zhang, P.; Hu, Z.; Gu, S.; Weng, K. C.; Gray, J. W.; Chen, F. F. Nanoparticle-Mediated Systemic Delivery of Sirna for Treatment of Cancers and Viral Infections. *Theranostics* 2014, 4, 872-892.

14.	Williford, J.-M.; Wu, J.; Ren, Y.; Archang, M. M.; Leong, K. W.; Mao, H.-Q. Recent Advances in Nanoparticle-Mediated Sirna Delivery. *Annu. Rev. Biomed. Eng.* 2014, 16, 347-370.

15.	Li, Z.; Barnes, J. C.; Bosoy, A.; Stoddart, J. F.; Zink, J. I. Mesoporous Silica Nanoparticles in Biomedical Applications. *Chem. Soc. Rev.* 2012, 41, 2590-2605.

16.	Vivero-Escoto, J. L.; Slowing, I. I.; Trewyn, B. G.; Lin, V. S. Y. Mesoporous Silica Nanoparticles for Intracellular Controlled Drug Delivery. *Small* 2010, 6, 1952-1967.

17.	Butler, K. S.; Durfee, P. N.; Theron, C.; Ashley, C. E.; Carnes, E. C.; Brinker, C. J. Protocells: Modular Mesoporous Silica Nanoparticle-Supported Lipid Bilayers for Drug Delivery. *Small* 2016.

18.	Zhang, H.; Dunphy, D. R.; Jiang, X.; Meng, H.; Sun, B.; Tarn, D.; Xue, M.; Wang, X.; Lin, S.; Ji, Z.; Li, R.; Garcia, F. L.; Yang, J.; Kirk, M. L.; Xia, T.; Zink, J. I.; Nel, A.; Brinker, C. J. Processing Pathway Dependence of Amorphous Silica Nanoparticle Toxicity: Colloidal *Vs* Pyrolytic. *J. Am. Chem. Soc.* 2012, 134, 15790-15804.

19.	Meng, H.; Yang, S.; Li, Z.; Xia, T.; Chen, J.; Ji, Z.; Zhang, H.; Wang, X.; Lin, S.; Huang, C.; Zhou, Z. H.; Zink, J. I.; Nel, A. E. Aspect Ratio Determines the Quantity of Mesoporous Silica Nanoparticle Uptake by a Small Gtpase-Dependent Macropinocytosis Mechanism. *ACS Nano* 2011, 5, 4434-4447.

20.	Brinker, C. J.; Scherer, G. W. *Sol-Gel Science: The Physics and Chemistry of Sol-Gel Processing*. Academic press: 2013.

21.	Wang, L.-S.; Wu, L.-C.; Lu, S.-Y.; Chang, L.-L.; Teng, I. T.; Yang, C.-M.; Ho, J.-a. A. Biofunctionalized Phospholipid-Capped Mesoporous Silica Nanoshuttles for Targeted Drug Delivery: Improved Water Suspensibility and Decreased Nonspecific Protein Binding. *ACS Nano* 2010, 4, 4371-4379.

22.	Ashley, C. E.; Carnes, E. C.; Epler, K. E.; Padilla, D. P.; Phillips, G. K.; Castillo, R. E.; Wilkinson, D. C.; Wilkinson, B. S.; Burgard, C. A.; Kalinich, R. M.; Townson, J. L.; Chackerian, B.; Willman, C. L.; Peabody, D. S.; Wharton, W.; Brinker, C. J. Delivery of Small Interfering Rna by Peptide-Targeted Mesoporous Silica Nanoparticle-Supported Lipid Bilayers. *ACS Nano* 2012, 6, 2174-2188.

23. Epler, K.; Padilla, D.; Phillips, G.; Crowder, P.; Castillo, R.; Wilkinson, D.; Wilkinson, B.; Burgard, C.; Kalinich, R.; Townson, J.; Chackerian, B.; Willman, C.; Peabody, D.; Wharton, W.; Brinker, C. J.; Ashley, C.; Carnes, E. Delivery of Ricin Toxin a-Chain by Peptide-Targeted Mesoporous Silica Nanoparticle-Supported Lipid Bilayers. *Adv. Healthcare Mater.* 2012, 1, 348-353.

24. Cauda, V.; Engelke, H.; Sauer, A.; Arcizet, D.; Bräuchle, C.; Rädler, J.; Bein, T. Colchicine-Loaded Lipid Bilayer-Coated 50 Nm Mesoporous Nanoparticles Efficiently Induce Microtubule Depolymerization Upon Cell Uptake. *Nano Lett.* 2010, 10, 2484-2492.

25. Meng, H.; Wang, M.; Liu, H.; Liu, X.; Situ, A.; Wu, B.; Ji, Z.; Chang, C. H.; Nel, A. E. Use of a Lipid-Coated Mesoporous Silica Nanoparticle Platform for Synergistic Gemcitabine and Paclitaxel Delivery to Human Pancreatic Cancer in Mice. *ACS Nano* 2015, 9, 3540-3557.

26. Wang, D.; Huang, J.; Wang, X.; Yu, Y.; Zhang, H.; Chen, Y.; Liu, J.; Sun, Z.; Zou, H.; Sun, D.; Zhou, G.; Zhang, G.; Lu, Y.; Zhong, Y. The Eradication of Breast Cancer Cells and Stem Cells by 8-Hydroxyquinoline-Loaded Hyaluronan Modified Mesoporous Silica Nanoparticle-Supported Lipid Bilayers Containing Docetaxel. *Biomaterials* 2013, 34, 7662-7673.

27. Zhang, X.; Li, F.; Guo, S.; Chen, X.; Wang, X.; Li, J.; Gan, Y. Biofunctionalized Polymer-Lipid Supported Mesoporous Silica Nanoparticles for Release of Chemotherapeutics in Multidrug Resistant Cancer Cells. *Biomaterials* 2014, 35, 3650-3665.

28. Ashley, C. E.; Carnes, E. C.; Phillips, G. K.; Padilla, D.; Durfee, P. N.; Brown, P. A.; Hanna, T. N.; Liu, J.; Phillips, B.; Carter, M. B.; Carroll, N. J.; Jiang, X.; Dunphy, D. R.; Willman, C. L.; Petsev, D. N.; Evans, D. G.; Parikh, A. N.; Chackerian, B.; Wharton, W.; Peabody, D. S.; Brinker, C. J. The Targeted Delivery of Multicomponent Cargos to Cancer Cells by Nanoporous Particle-Supported Lipid Bilayers. *Nat. Mater.* 2011, 10, 389-397.

29. Liu, X.; Situ, A.; Kang, Y.; Villabroza, K. R.; Liao, Y.; Chang, C. H.; Donahue, T.; Nel, A. E.; Meng, H. Irinotecan Delivery by Lipid-Coated Mesoporous Silica Nanoparticles Shows Improved Efficacy and Safety over Liposomes for Pancreatic Cancer. *ACS Nano* 2016, 10, 2702-2715.

30. Huang, W.-C.; Burnouf, P.-A.; Su, Y.-C.; Chen, B.-M.; Chuang, K.-H.; Lee, C.-W.; Wei, P.-K.; Cheng, T.-L.; Roffler, S. R. Engineering Chimeric Receptors to Investigate the Size- and Rigidity-Dependent Interaction of Pegylated Nanoparticles with Cells. *ACS Nano* 2016, 10, 648-662.

31. Mackowiak, S. A.; Schmidt, A.; Weiss, V.; Argyo, C.; von Schirnding, C.; Bein, T.; Bräuchle, C. Targeted Drug Delivery in Cancer Cells with Red-

Light Photoactivated Mesoporous Silica Nanoparticles. *Nano Lett.* 2013, 13, 2576-2583.

32. Porotto, M.; Yi, F.; Moscona, A.; LaVan, D. A. Synthetic Protocells Interact with Viral Nanomachinery and Inactivate Pathogenic Human Virus. *PloS one* 2011, 6, e16874.

33. Han, N.; Zhao, Q.; Wan, L.; Wang, Y.; Gao, Y.; Wang, P.; Wang, Z.; Zhang, J.; Jiang, T.; Wang, S. Hybrid Lipid-Capped Mesoporous Silica for Stimuli-Responsive Drug Release and Overcoming Multidrug Resistance. *ACS Appl. Mater. Interfaces* 2015, 7, 3342-3351.

34. Liu, J.; Stace-Naughton, A.; Jiang, X.; Brinker, C. J. Porous Nanoparticle Supported Lipid Bilayers (Protocells) as Delivery Vehicles. *J. Am. Chem. Soc.* 2009, 131, 1354-1355.

35. Liu, J.; Jiang, X.; Ashley, C.; Brinker, C. J. Electrostatically Mediated Liposome Fusion and Lipid Exchange with a Nanoparticle-Supported Bilayer for Control of Surface Charge, Drug Containment, and Delivery. *J. Am. Chem. Soc.* 2009, 131, 7567-7569.

36. Durfee, P. N.; Lin, Y.-S.; Dunphy, D. R.; Muñiz, A. J.; Butler, K. S.; Humphrey, K. R.; Lokke, A. J.; Agola, J. O.; Chou, S. S.; Chen, I. M.; Wharton, W.; Townson, J. L.; Willman, C. L.; Brinker, C. J. Mesoporous Silica Nanoparticle-Supported Lipid Bilayers (Protocells) for Active Targeting and Delivery to Individual Leukemia Cells. *ACS Nano* 2016.

37. Bayerl, T. M.; Bloom, M. Physical Properties of Single Phospholipid Bilayers Adsorbed to Micro Glass Beads. A New Vesicular Model System Studied by 2h-Nuclear Magnetic Resonance. *Biophys. J.* 1990, 58, 357-362.

38. Johnson, S. J.; Bayerl, T. M.; McDermott, D. C.; Adam, G. W.; Rennie, A. R.; Thomas, R. K.; Sackmann, E. Structure of an Adsorbed Dimyristoylphosphatidylcholine Bilayer Measured with Specular Reflection of Neutrons. *Biophys. J.* 1991, 59, 289-294.

39. Keller, C. A.; Glasmästar, K.; Zhdanov, V. P.; Kasemo, B. Formation of Supported Membranes from Vesicles. *Phys. Rev. Lett.* 2000, 84, 5443-5446.

40. Reviakine, I.; Brisson, A. Formation of Supported Phospholipid Bilayers from Unilamellar Vesicles Investigated by Atomic Force Microscopy. *Langmuir* 2000, 16, 1806-1815.

41. Johnson, J. M.; Ha, T.; Chu, S.; Boxer, S. G. Early Steps of Supported Bilayer Formation Probed by Single Vesicle Fluorescence Assays. *Biophys. J.* 2002, 83, 3371-3379.

42. Richter, R. P.; Brisson, A. R. Following the Formation of Supported Lipid Bilayers on Mica: A Study Combining Afm, Qcm-D, and Ellipsometry. *Biophys. J.* 2005, 88, 3422-3433.

43. Cremer, P. S.; Boxer, S. G. Formation and Spreading of Lipid Bilayers on Planar Glass Supports. *J. Phys. Chem. B* 1999, 103, 2554-2559.

44. Savarala, S.; Ahmed, S.; Ilies, M. A.; Wunder, S. L. Formation and Colloidal Stability of Dmpc Supported Lipid Bilayers on Sio2 Nanobeads. *Langmuir* 2010, 26, 12081-12088.

45. Garcia-Manyes, S.; Oncins, G.; Sanz, F. Effect of Ion-Binding and Chemical Phospholipid Structure on the Nanomechanics of Lipid Bilayers Studied by Force Spectroscopy. *Biophys. J.* 2005, 89, 1812-1826.

46. Mornet, S.; Lambert, O.; Duguet, E.; Brisson, A. The Formation of Supported Lipid Bilayers on Silica Nanoparticles Revealed by Cryoelectron Microscopy. *Nano Lett.* 2005, 5, 281-285.

47. Buranda, T.; Huang, J.; Ramarao, G.; Ista, L. K.; Larson, R. S.; Ward, T. L.; Sklar, L. A.; Lopez, G. P. Biomimetic Molecular Assemblies on Glass and Mesoporous Silica Microbeads for Biotechnology. *Langmuir* 2003, 19, 1654-1663.

48. Dengler, E. C.; Liu, J.; Kerwin, A.; Torres, S.; Olcott, C. M.; Bowman, B. N.; Armijo, L.; Gentry, K.; Wilkerson, J.; Wallace, J.; Jiang, X.; Carnes, E. C.; Brinker, C. J.; Milligan, E. D. Mesoporous Silica-Supported Lipid Bilayers (Protocells) for DNA Cargo Delivery to the Spinal Cord. *J. Controlled Release* 2013, 168, 209-224.

49. Townson, J. L.; Lin, Y.-S.; Agola, J. O.; Carnes, E. C.; Leong, H. S.; Lewis, J. D.; Haynes, C. L.; Brinker, C. J. Re-Examining the Size/Charge Paradigm: Differing *in Vivo* Characteristics of Size- and Charge-Matched Mesoporous Silica Nanoparticles. *J. Am. Chem. Soc.* 2013, 135, 16030-16033.

50. Lin, Y.-S.; Haynes, C. L. Impacts of Mesoporous Silica Nanoparticle Size, Pore Ordering, and Pore Integrity on Hemolytic Activity. *J. Am. Chem. Soc.* 2010, 132, 4834-4842.

51. Lin, Y.-S.; Abadeer, N.; Hurley, K. R.; Haynes, C. L. Ultrastable, Redispersible, Small, and Highly Organomodified Mesoporous Silica Nanotherapeutics. *J. Am. Chem. Soc.* 2011, 133, 20444-20457.

52. Chen, P.-K.; Lai, N.-C.; Ho, C.-H.; Hu, Y.-W.; Lee, J.-F.; Yang, C.-M. New Synthesis of Mcm-48 Nanospheres and Facile Replication to Mesoporous Platinum Nanospheres as Highly Active Electrocatalysts for the Oxygen Reduction Reaction. *Chem. Mater.* 2013, 25, 4269-4277.

53. Nandiyanto, A. B. D.; Kim, S.-G.; Iskandar, F.; Okuyama, K. Synthesis of Spherical Mesoporous Silica Nanoparticles with Nanometer-Size Controllable Pores and Outer Diameters. *Microporous Mesoporous Mater.* 2009, 120, 447-453.

54. Wang, J.; Sugawara-Narutaki, A.; Shimojima, A.; Okubo, T. Biphasic Synthesis of Colloidal Mesoporous Silica Nanoparticles Using Primary Amine Catalysts. *J. Colloid Interface Sci.* 2012, 385, 41-47.

55. Shen, D.; Yang, J.; Li, X.; Zhou, L.; Zhang, R.; Li, W.; Chen, L.; Wang, R.; Zhang, F.; Zhao, D. Biphase Stratification Approach to Three-Dimensional Dendritic Biodegradable Mesoporous Silica Nanospheres. *Nano Lett.* 2014, 14, 923-932.

56. Huang, X.; Li, L.; Liu, T.; Hao, N.; Liu, H.; Chen, D.; Tang, F. The Shape Effect of Mesoporous Silica Nanoparticles on Biodistribution, Clearance, and Biocompatibility *in Vivo*. *ACS Nano* 2011, 5, 5390-5399.

57. Yu, T.; Malugin, A.; Ghandehari, H. Impact of Silica Nanoparticle Design on Cellular Toxicity and Hemolytic Activity. *ACS Nano* 2011, 5, 5717-5728.

CHAPTER 3

**OPTIMIZATION AND CHARACTERIZATION OF THE PROTOCELL
PLATFORM**

3.1 Overview

The fact that the modular MSNP features of size, shape, pore size, pore volume, and pore morphology are important for their ultimate use as nanocarriers prompts us to ask how MSNP physicochemical characteristics along with processing conditions influence vesicle fusion to form MSNP-supported lipid bilayers aka 'protocells' for use as nanocarriers - where key criteria are size monodispersity, preservation of shape, and stability within physiologically relevant complex biological media. To address this question we first chose to study monosized ~ 107 nm (hydrodynamic diameter measured by DLS) single-crystal-like mMSNP composed of close-packed cylindrical pores confined within a hexagonally shaped nanoparticle that is disc-shaped in cross-section (**Figure 3.1**). This highly asymmetric mMSNP (referred to as Hexagonal mMSNP) has opposing porous surfaces adjoined by grooved silica facets, thereby providing two distinct surfaces for vesicle fusion.

3.2 Results and Discussion

3.2.1 Optimized MSNP-Supported Lipid Bilayer Fusion Conditions

To understand the roles of surface area (SA) $SA_{lipid}:SA_{silica}$ and ionic strength on vesicle fusion, we assembled protocells by mixing Hexagonal mMSNPs with ~90 nm hydrodynamic diameter liposomes (composition = DSPC, cholesterol (chol), and 1,2-distearoyl-*sn*-glycero-3-phosphoethanolamine-N-[methoxy(polyethylene glycol)-2000] (DSPE-PEG$_{2000}$) – where the molar ratio of DSPC:chol:DSPE-PEG$_{2000}$ equaled 54:44:2 – **Table 2.1**). Liposomes were

Figure 3.1 – *TEM Image of Hexagonal MSNPs Showing Asymmetry*
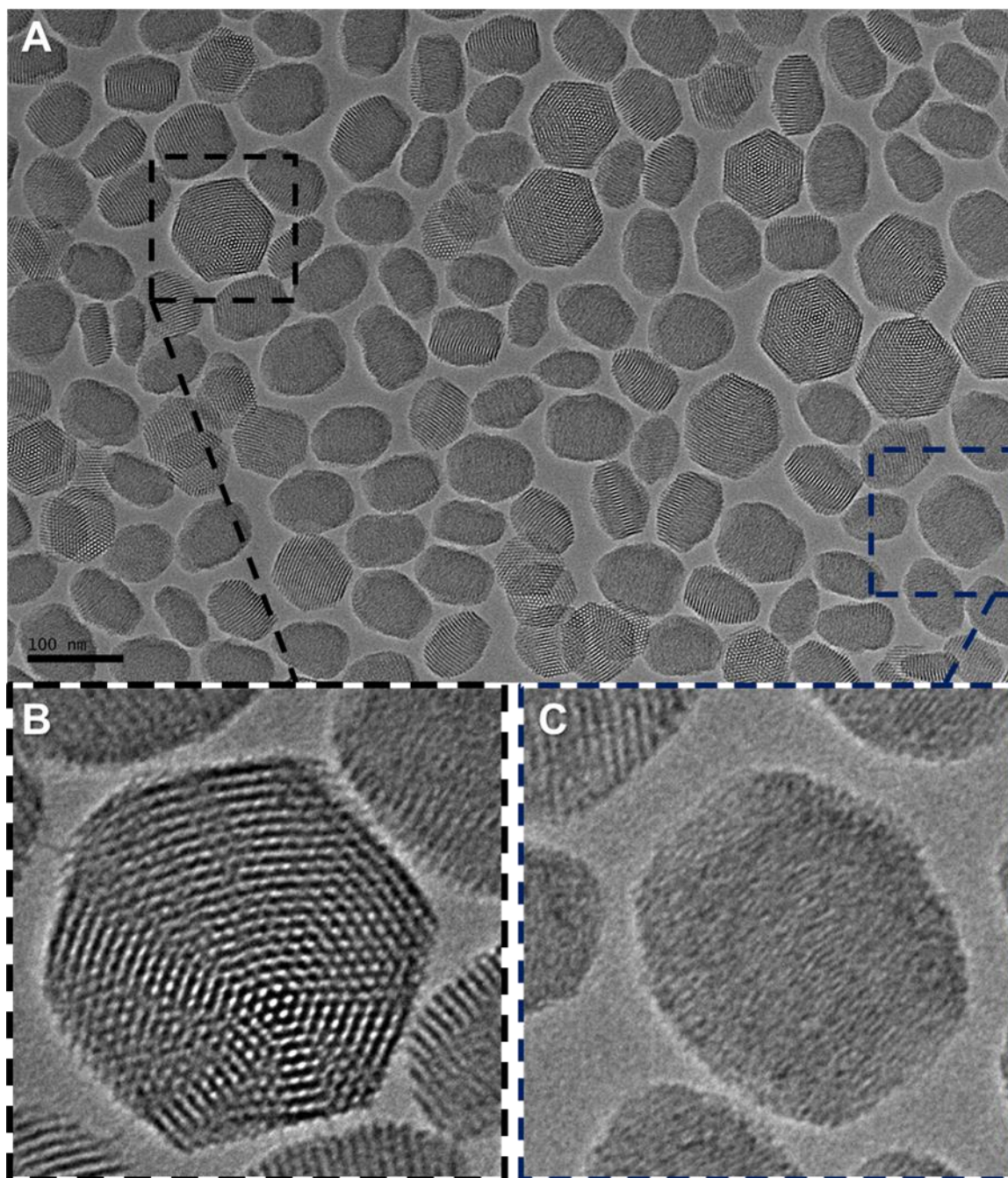
Figure 3.1 – Representative TEM image of Hexagonal mMSNPs. A) TEM image shows highly asymmetric particles with a narrow size distribution. B) Enlarged region highlights hexagonal porous silica surface. C) Enlarged region highlights grooved disc-shaped solid silica surface.

prepared by extrusion in a series of solutions consisting of 0 mM, 40 mM, 80

mM,120 mM, 160 mM, and 320 mM ionic strength phosphate buffered saline

(PBS). To complete the assembly process, the protocells were washed twice by

centrifugation and resuspended in the final buffer solution with bath sonication

and pipetting. Through variation of the lipid:silica ratio (wt:wt) and PBS

concentration, we were able to adjust the SA_{lipid}:SA_{silica} from 0 (mMSNP alone

used as a control) to 4.22:1 and the ionic strength of the fusion conditions from 0

mM (water) to 160 mM spanning physiologically relevant ranges needed for *in

vivo* applications (*vide infra*). We used a shape applicable model to calculate the

external SA_{silica} from dimensional measurements of mMSNPs obtained from TEM

images (**Table 3.1**), using the pore volume obtained from nitrogen sorption data

(**Table 3.1 and Figure 3.2**), and assuming 2.0 g/cm^3 as the silica framework

density;[1] SA_{lipid} was calculated assuming 0.59 nm^2 as the phospholipid head

group area;[2] and that cholesterol does not contribute to SA_{lipid} (**See calculation

details in Appendix A.1**). Using a Malvern Zetasizer Nano ZS, we measured

the hydrodynamic diameter, PdI, and zeta-potential (ζ) of protocells. **Figure 3.3**

plots hydrodynamic diameter and PdI as a function of SA_{lipid}:SA_{silica} and ionic

strength. Consistent with our expectations from DLVO theory, without lipid,

mMSNPs (ζ = - 28.1 mV, **Table 3.2**) aggregate with increasing ionic strength due

to the reduced Debye length and concomitant reduction in the range of

electrostatic repulsion. For samples prepared with SA_{lipid}:SA_{silica} < 1, the critical

ratio needed to exactly cover the external surface of the mMSNP with a single

phospholipid bilayer, we observed severe aggregation that increases with ionic

Sample	Hydrodynamic Core Diameter (nm)	Hydrodynamic Protocell Diameter (nm)	TEM Average dimensions (nm)	Surface area (m²/g)	Pore Volume (cm3/g)	Estimated number of mMSNPs/ 100mg	SA_{mMSNPs} /100 mg	Liposomes SA_{inner}	$SA_{liposomes}$ to SA_{mMSNPs} (2:1 mass ratio)
Hexagonal mMSNP (2.8 nm)	106.90 ± 0.54	137.30 ± 0.30	a = 44.80 ± 3.68 h = 50.68 ± 9.18	933	0.83	4.99E+14	1.20E+19	2.54E+19	2.11
Spherical mMSNP (2.8 nm)	116.07 ± 2.35	141.30 ± 0.75	d = 85.76 ± 17.92	837	0.91	3.84E+14	9.25E+18	2.54E+19	2.75
Spherical mMSNP (5 nm)	118.33 ± 0.76	145.50 ± 0.62	d = 99.32 ± 5.28	672	0.86	2.69E+14	8.35E+18	2.54E+19	3.04
Spherical mMSNP (8 nm)	139.23 ± 1.15	184.70 ± 1.06	d = 81.74 ± 4.17	741	1.1	5.62E+14	1.18E+19	2.54E+19	2.15
Spherical mMSNP (18 nm)	123.00 ± 0.30	396.90 ± 13.00	d = 97.77 ± 4.41	794	2.2	5.58E+14	1.68E+19	2.54E+19	1.51
Rod-like mMSNP (2.8 nm)	142.93 ± 1.53	172.67 ± 1.72	l = 176.68 ± 29.45 w = 81.97 ± 9.63	983	0.87	1.42E+14	8.08E+18	2.54E+19	3.14
Spherical EISA MSNP (2.8 nm)	700.00 ± 24.68	715.20 ± 49.79	-	935*	0.48*	-	-	-	-

Table 3.1 – *MSNP Shape, Shape, Size, Surface Area, and Pore Morphology Analyses*
Average hydrodynamic size comparison of mMSNPs of various size, shape, and pore morphology before and after SLB fusion, data accompanies images in Figure 3.5, data represents mean ± SD, n = 3. Average mMSNP dimensions from TEM images of mMSNPs, data represent mean ± SD, n = 50. Surface area and pore volume measurements calculated from Nitrogen sorption data, * data from the literature.[3] Estimated numbers calculated from equations described later in **Appendix A.1** and image analysis in **Appendix B.1**. Adapted and reproduced with permission.[4] © 2016, The American Chemical Society.

Figure 3.2 – *Adsorption-desorption Isotherms*
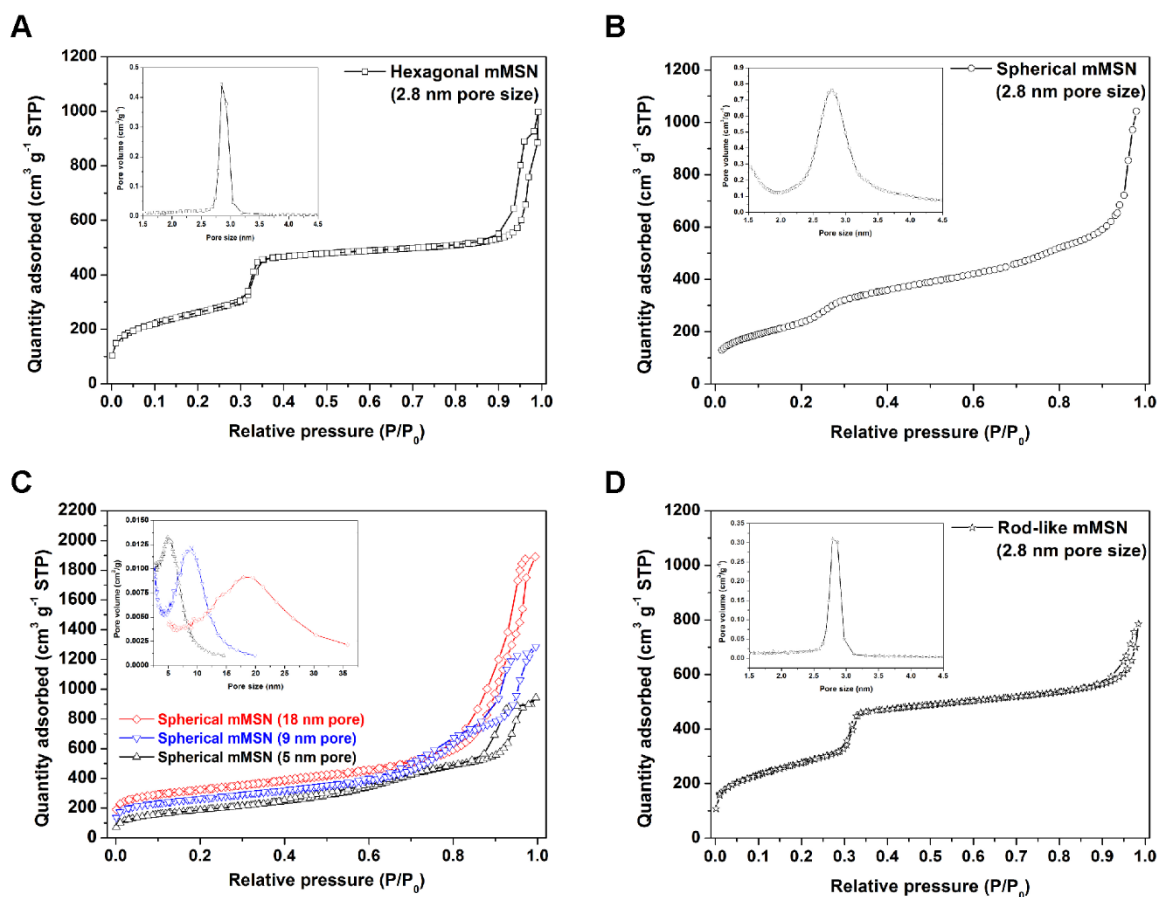
Figure 3.2 – N_2 adsorption-desorption isotherms and pore size distribution (inset) of A) Hexagonal mMSNPs with 2.8 nm pores, B) Spherical mMSNPs with 2.8 nm pores, C) Spherical mMSNPs with 5, 9, or 18 nm pores, and D) Rod-like mMSNPs with 2.8 nm pores. Adapted and reproduced with permission.[4] © 2016, The American Chemical Society. More detailed description of calculations in **Appendix A.2**.

Figure 3.3 – *Optimization of Surface Area Ratio and Ionic Strength in Protocell Assembly*
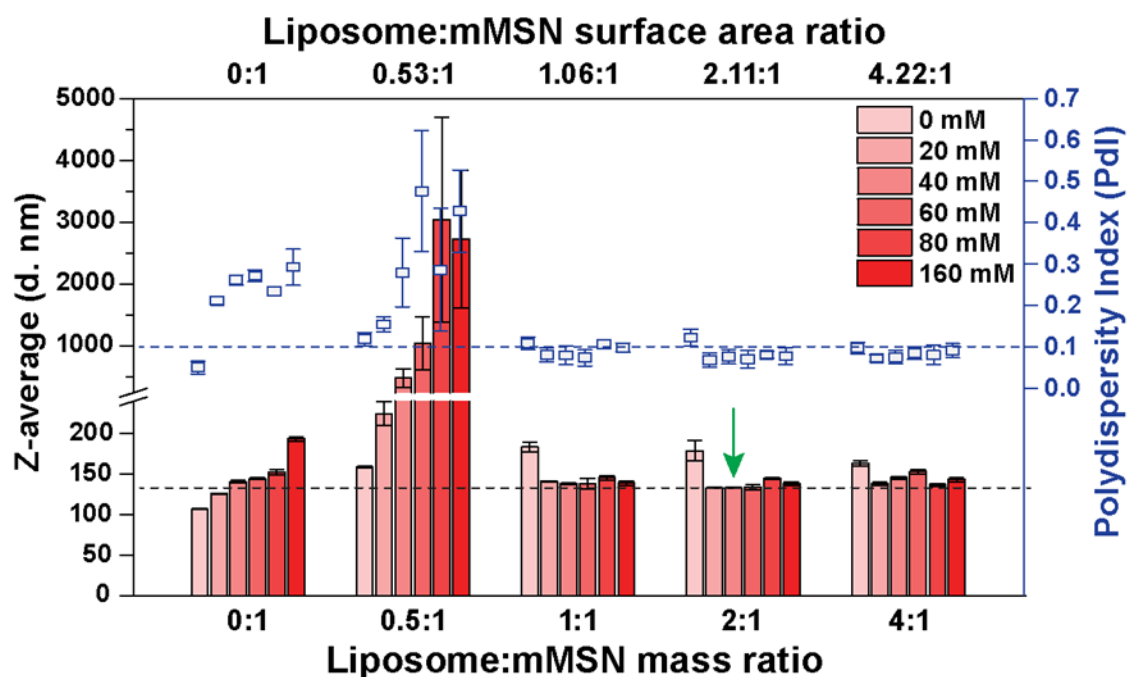
Figure 3.3 – Comparison of Hexagonal protocells prepared in differing ionic strength conditions using different liposome to mMSNP mass ratios (w:w) – bottom scale, and respective calculated inner liposome to outer mMSNP surface area ratios – top scale. Hydrodynamic size (Left axis) corresponds to bar graph with black dashed line indicating optimal protocell size range. Polydispersity index (Right axis) corresponds to box plots with blue dashed line indicating threshold for monodispersity, values below the dashed line are considered monodisperse (PdI < 0.1). Green arrow identifies the optimal ionic strength and liposome:mMSNP ratio fusion conditions used for subsequent experiments. Adapted and reproduced with permission.[4] © 2016, The American Chemical Society. Surface area calculations described in detail in **Appendix A.1**.

Table 3.2 – *Hydrodynamic Size and Zeta Potential of Protocell Components*

Sample	Medium	Hydrodynamic Diameter (nm)	PdI	Zeta potential (mV)
mMSNP	H_2O	106.90 ± 0.54	0.50 ± 0.015	-41.0 ± 0.9
mMSNP	PBS	193.4 ± 2.83	0.292 ± 0.044	-28.1 ± 1.5
DSPC:chol:DSPE-PEG$_{2000}$ Liposomes	PBS	92.54 ± 0.26	0.112 ± 0.006	-2.9 ± 0.8
Protocell	PBS	137.30 ± 0.30	0.085 ± 0.013	-3.3 ± 0.9

Table 3.2 – Hydrodynamic size characteristics and zeta potential measurements of modular protocell components. Liposome formulation DSPC:chol:DSPE-PEG$_{2000}$ (mol % 54:44:2). Data represent mean ± SD, n = 3. Adapted and reproduced with permission.[4] © 2016, The American Chemical Society.

strength indicative of aggregation of exposed silica surfaces accompanied by liposome adsorption and possible bridging. For samples prepared with $SA_{lipid}:SA_{silica} > 1$, we observed much more uniformly sized particles (PdI < 0.1) with hydrodynamic diameters *ca* 30 nm larger than the parent mMSNP and zeta-potentials in the range (ζ = - 3.3 mV, **Table 3.2**) consistent with the formation of a PEGylated zwitterionic SLB that shields the mMSNP charge and provides a repulsive hydration barrier that stabilizes the protocells within biologically relevant media (*vide infra*). The exception are samples prepared in pure water (ionic strength = 0 mM) where for all $SA_{lipid}:SA_{silica}$ we observed diameters 50 to 60 nm greater than the parent mMSNP along with a trend of increasing PdI (**Table 3.3**). Samples prepared in pure water have a zeta potential comparable to the parent mMSNP (ζ = - 41.0 mV) and aggregate when transferred to 160 mM PBS (ζ = - 28.1 mV). These ionic strength effects indicate fusion to be inhibited in pure water and are consistent with those obtained by Savarala *et al*. for fusion of single component 1,2-dipalmitoyl-sn-glycero-3-phosphocholine (DPPC) zwitterionic vesicles on solid 100 nm silica beads at $SA_{lipid}:SA_{silica}$ = 1, where ionic strengths ≥ 0.05 mM NaCl were needed for fusion as assessed by DSC.[5] Direct Cryo-TEM observation of Hexagonal mMSNPs fused with DSPC-based liposomes at $SA_{lipid}:SA_{silica}$ = 2.11:1 and ionic strength 40 mM show a conformal SLB with thickness 4.7 ± 0.5 nm (**Figure 2.1 and Figure 3.4**) observed both on the porous and grooved surfaces (**Figure 3.1**). We note the increased diameter of ~ 10 nm determined by TEM is inconsistent with the ~ 25 nm increase measured by DLS. Such discrepancies are often reported in the literature.[6, 7]

Liposome to mMSNP Fusion Conditions (w:w)	PBS Ionic Strength (mM)	Protocell Hydrodynamic size and PdI	Protocell Hydrodynamic size after transfer to 160 mM PBS and PdI	Size Increase
	0	185.37 ± 3.18 nm / 0.120 ± 0.032	659.63 ± 12.12 nm / 0.204 ± 0.035	256%
	20	130.17 ± 1.44 nm / 0.056 ± 0.018	134.97 ± 1.5 nm / 0.073 ± 0.037	4%
4:1 ratio	40	133.90 ± 1.05 nm / 0.069 ± 0.013	137.77 ± 0.81 nm / 0.089 ± 0.015	3%
	60	144.83 ± 0.25 nm / 0.106 ± 0.009	148.57 ± 0.46 nm / 0.113 ± 0.019	3%
	80	137.30 ± 1.11 nm / 0.091 ± 0.019	139.87 ± 0.81 nm / 0.074 ± 0.027	2%
	0	188.27 ± 1.91 nm / 0.120 ± 0.019	3096.33 ± 935.90 nm / 0.645 ± 0.252	1545%
	20	131.97 ± 0.72 nm / 0.067 ± 0.013	137.43 ± 1.12 nm / 0.087 ± 0.011	4%
2:1 ratio	40	132.20 ± 1.45 nm / 0.079 ± 0.022	137.30 ± 0.30 nm / 0.085 ± 0.013	4%
	60	135.17 ± 1.19 nm / 0.102 ± 0.017	137.00 ± 0.20 nm / 0.095 ± 0.030	1%
	80	140.20 ± 0.78 nm / 0.102 ± 0.018	146.33 ± 0.60 nm / 0.122 ± 0.003	4%
	0	188.07 ± 1.95 nm / 0.134 ± 0.016	5583.67 ± 290.10 nm / 0.685 ± 0.075	2868%
	20	146.40 ± 1.76 nm / 0.105 ± 0.013	151.53 ± 0.49 nm / 0.120 ± 0.024	4%
1:1 ratio	40	133.93 ± 1.29 nm / 0.110 ± 0.018	141.73 ± 0.74 nm / 0.122 ± 0.013	6%
	60	135.57 ± 0.55 nm / 0.097 ± 0.009	141.60 ± 0.52 nm / 0.128 ± 0.010	4%

Table 3.3 – *Size Change of Protocells Assembled Under Differing Ionic Strength Conditions*

Table 3.3 – Analysis of hydrodynamic size and PdI change in protocells prepared under differing PBS ionic strength conditions and transferred to physiological ionic strength (160 mM) PBS. The size change of protocells prepared in the absence of salt suggests that protocells do not form in pure water, since the size increase is clearly larger than all protocells prepared in increasing ionic strength conditions. Data represent mean ± SD, n = 3. Adapted and reproduced with permission.4 © 2016. The American Chemical Society.

Figure 3.4 – *Average Bilayer Thickness Measured by TEM*
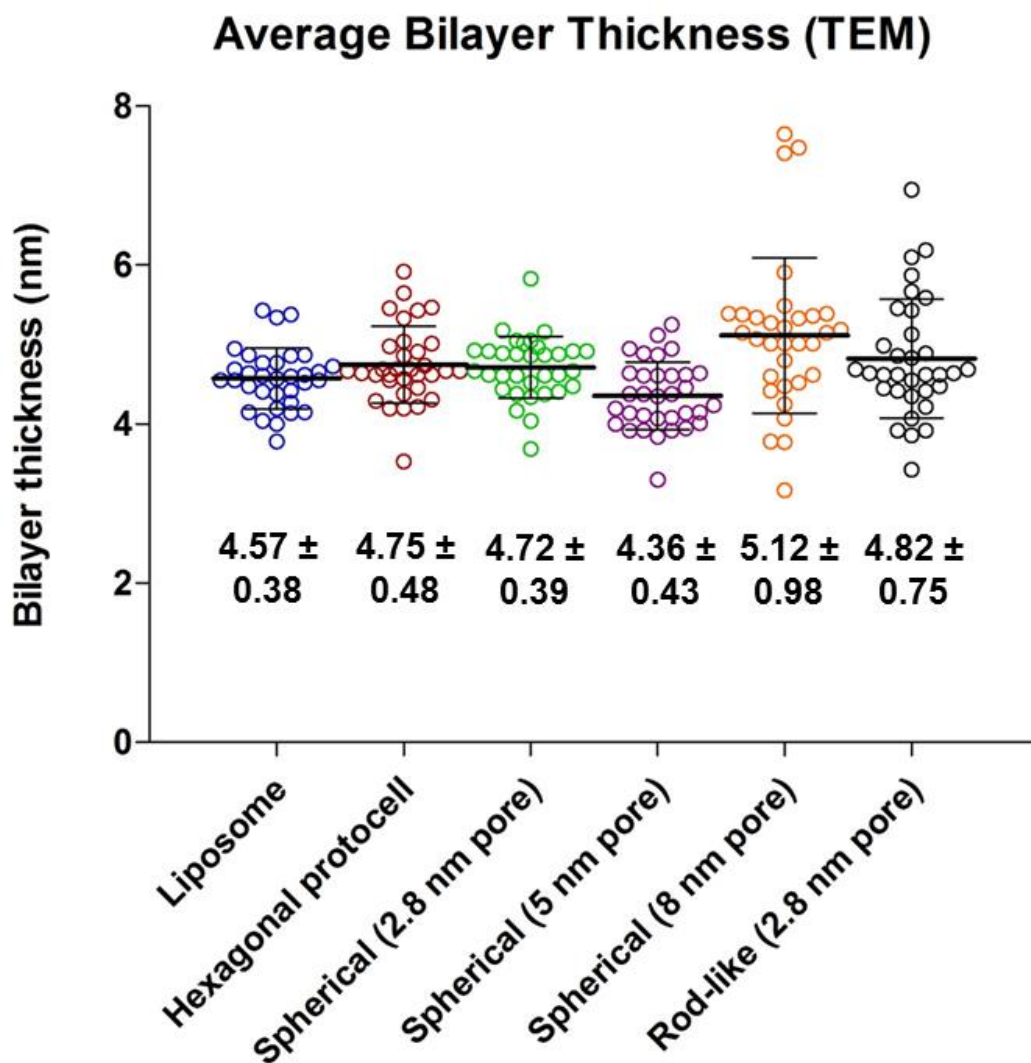
Figure 3.4 – Average lipid bilayer thickness measured from TEM images. Data represent mean ± SD, n = 33. Adapted and reproduced with permission.[4] © 2016, The American Chemical Society. See **Appendix B.2** for addition information on thickness measurements.

Considering that the SA_{lipid} of a 90 nm liposome is less than that of a Hexagonal mMSNP, multiple liposome fusion events are required to create a complete SLB (**Figure 2.1**). In time-dependent Cryo-TEM, Mornet *et al.* showed liposome fusion on 100 nm colloidal silica nanoparticles to occur by a 'two-step' process involving adsorption followed by deformation and rupture.[8] Although we did not conduct a time- dependent Cryo-TEM study, we did observe similarly evidence of deformed vesicles that conform to the mMSNPs, which likely subsequently rupture to form SLBs in a similar 'two-step' process. We should note that, although it has been suggested that SLB formation on spherical, isotropic MSNPs *via* probe sonication of dried lipid films in saline solution may proceed through a pathway other than vesicle fusion, implementing the identical probe sonication technique[7, 9] for Hexagonal mMSNPs results in protocells indistinguishable (*i.e.*, nearly identical hydrodynamic diameter and PdI) from those formed by fusion with DSPC-based liposomes at $SA_{lipid}:SA_{silica}$ = 4.22:1 and ionic strength 40 mM (**Table 3.4**). Finally, to help avoid any accompanying aggregation from occurring at the ionic strengths needed for vesicle fusion (and ultimately for *ex ovo* and *in vivo* applications, *vide infra*), we propose that conditions of excess of lipid and a low but sufficient ionic strength serve to increase the relative rate of vesicle fusion with respect to aggregation thus allowing the formation of monosized protocells with a low PdI (**Figure 3.3**).

Our results on vesicle fusion on Hexagonal mMSNP established a wide processing window in which to synthesize rather monosized protocells. As noted above, a $SA_{lipid}:SA_{silica}$ ≈ 2:1 and ionic strength 40 mM appeared to represent an

Table 3.4 – *Comparison of Assembly Conditions*

Liposome to mMSNP Fusion Conditions (w:w)	PBS Ionic Strength (mM)	Assembly conditions	Protocell Hydrodynamic size	Protocell PdI
		Liposomes bath sonicated, extruded, and mixed with mMSNPs	145.70 ± 0.92 nm	0.062 ± 0.014
4:1 ratio	40	Lipid films dried in round bottom flask, mMSNPs added to lipid film, and probe sonicated*	144.40 ± 1.39 nm	0.131 ± 0.006

Table 3.4 – Comparison of protocells assembled using the methods described in our paper and those assembled using probe sonication conditions described in the literature.[7, 9] Both methods produced protocells of similar size and monodispersity profile. Data represent mean ± SD, n = 3. Adapted and reproduced with permission.[4] © 2016, The American Chemical Society.

optimal fusion condition resulting in the smallest combination of hydrodynamic diameter and PdI (**highlighted by a green arrow in Figure 3.3**). To test how this condition depended on bilayer fluidity or charge, we prepared vesicles containing unsaturated or saturated phosphatidylcholine (*e.g.,* DOPC or DSPC) or the cationic lipid DOTAP based on liposomal formulations reported in the literature (**Table 3.5**). We found, in general, that these conditions resulted in monosized protocells for zwitterionic lipid based formulations, whereas DOTAP resulted in aggregate formation. To further understand the influence of MSNP physicochemical properties on protocell formation, we tested the optimized fusion conditions on a 'library' of MSNPs with differing shapes (*i.e.*, spherical or rod-like), particle size distributions (mMSNP or EISA MSNP), pore diameters (2.8 to 18 nm), and pore morphologies (aligned cylindrical, isotropic worm-like, and dendritic).[13-20] (See **Figure 3.5** and **Table 3.1** for a summary of the mMSNP and EISA MSNP physicochemical properties). As observed by direct Cryo-TEM observation, ~ 4 to 5 nm thick conformal SLBs formed on all of the tested particles (**Figures 3.5A-L and Figure 3.4**), and DLS showed a consistent increase in diameter of ~ 25 to 40 nm (**Figure 3.5M**). By visual examination, we observed a well-suspended and transparent dispersion of protocells in PBS contrasted with bare mMSNPs that settle under normal gravity (**Figure 3.6**). The exception was for spherical mMSNPs prepared with dendritic pore diameters of ~ 18 nm. In this case we observed, by Cryo-TEM, vesicle adsorption and deformation on the mMSNP surface but little evidence of complete SLB fusion (**Figure 3.7**). We propose that for this highly porous particle the magnitude of

Table 3.5 – *Size Comparison of Protocells Using Different SLB Formulations*

Liposome Formulation	Component mol ratio (%)	Liposome Diameter and (PdI)	mMSNP Diameter and (PdI)	Protocell Diameter and (PdI)	Fraction Size Increase	Comments
DOPC/Cholesterol	53/47	100.6 ± 2.1 nm (0.228 ± 0.007)		176.4 ± 2.8 nm (0.038 ± 0.013)	0.345	Monodisperse protocell, lacks components necessary for cell targeting
DMPC/Cholesterol	57/43	70.9 ± 0.7 nm (0.149 ± 0.006)	131.2 ± 0.7 nm (0.049 ± 0.013)	133.5 ± 2.5 nm (0.069 ± 0.012)	0.017	Monodisperse protocell, lacks components necessary for cell targeting, protocell size appears to increase with increasing acyl-chain length
DPPC/Cholesterol	55/45	79.9 ± 0.4 nm (0.166 ± 0.006)		155.1 ± 2.6 nm (0.091 ± 0.027)	0.182	
DSPC/Cholesterol	53/47	82.1 ± 0.6 nm (0.183 ± 0.007)		159.7 ± 3.4 nm (0.078 ± 0.007)	0.217	
DOTAP[10]	100	38.3 ± 0.8 nm (0.246 ± 0.017)		2925 ± 671 nm (0.363 ± 0.014)	23.7	Polydisperse protocell, large size increase, cationic SLB is cytotoxic and will increase non-specific cell interactions
DOTAP/Cholesterol[10]	56/44	60.6 ± 0.5 nm (0.203 ± 0.008)	118.2 ± 0.6 nm (0.074 ± 0.017)	3753 ± 696 nm (0.270 ± 0.243)	37.8	
DOPC/Cholesterol/DOPE/DSPE-PEG2000[3,11]	47/48/4/1	90.4 ± 0.6 nm (0.239 ± 0.012)		158.4 ± 0.8 nm (0.110 ± 0.031)	0.340	Monodisperse protocell, PEGylated component can be modified for targeting, good candidate for leukemia targeted protocell
DPPC/Cholesterol/DPPE/DSPE-PEG2000[3,11]	49/46/4/1	74.5 ± 0.9 nm (0.138 ± 0.005)		149.0 ± 0.2 nm (0.107 ± 0.013)	0.261	
DPPC/Cholesterol/DSPE-PEG 2000[7]	77.5/20/2.5	59.3 ± 1.0 nm (0.204 ± 0.002)	115.0 ± 2.3 nm (0.096 ± 0.008)	134.6 ± 0.9 nm (0.038 ± 0.013)	0.170	
DOPC[12]	100	99.5 ± 0.7 nm (0.109 ± 0.013)		197.9 ± 1.8 nm (0.082 ± 0.005)	0.558	Monodisperse protocell, size increases with SLB is larger than PEGylated formulations, lacks components necessary for cell targeting
POPC[12]	100	83.6 ± 0.5 nm (0.150 ± 0.007)	127.0 ± 1.6 nm (0.050 ± 0.016)	224.3 ± 0.8 nm (0.123 ± 0.030)	0.766	
DOPC/DOTAP[12]	47/53	46.6 ± 0.2 nm (0.257 ± 0.008)		224.6 ± 1.2 nm (0.237 ± 0.016)	0.769	Polydisperse protocell, large size increase, cationic SLB is cytotoxic and will increase non-specific cell interactions

Table 3.5 – Hydrodynamic size measurement and polydispersity index values of liposomes, Hexagonal mMSNPs, and assembled protocells using techniques described in my dissertation paper with different liposome formulations described in the literature.[3, 7, 10-12] Data represent mean ± SD, n = 3. Adapted and reproduced with permission.[4] © 2016, The American Chemical Society.

Figure 3.5 – *TEM and Cryo-TEM of MSNPs and Protocells of Varying Shape*
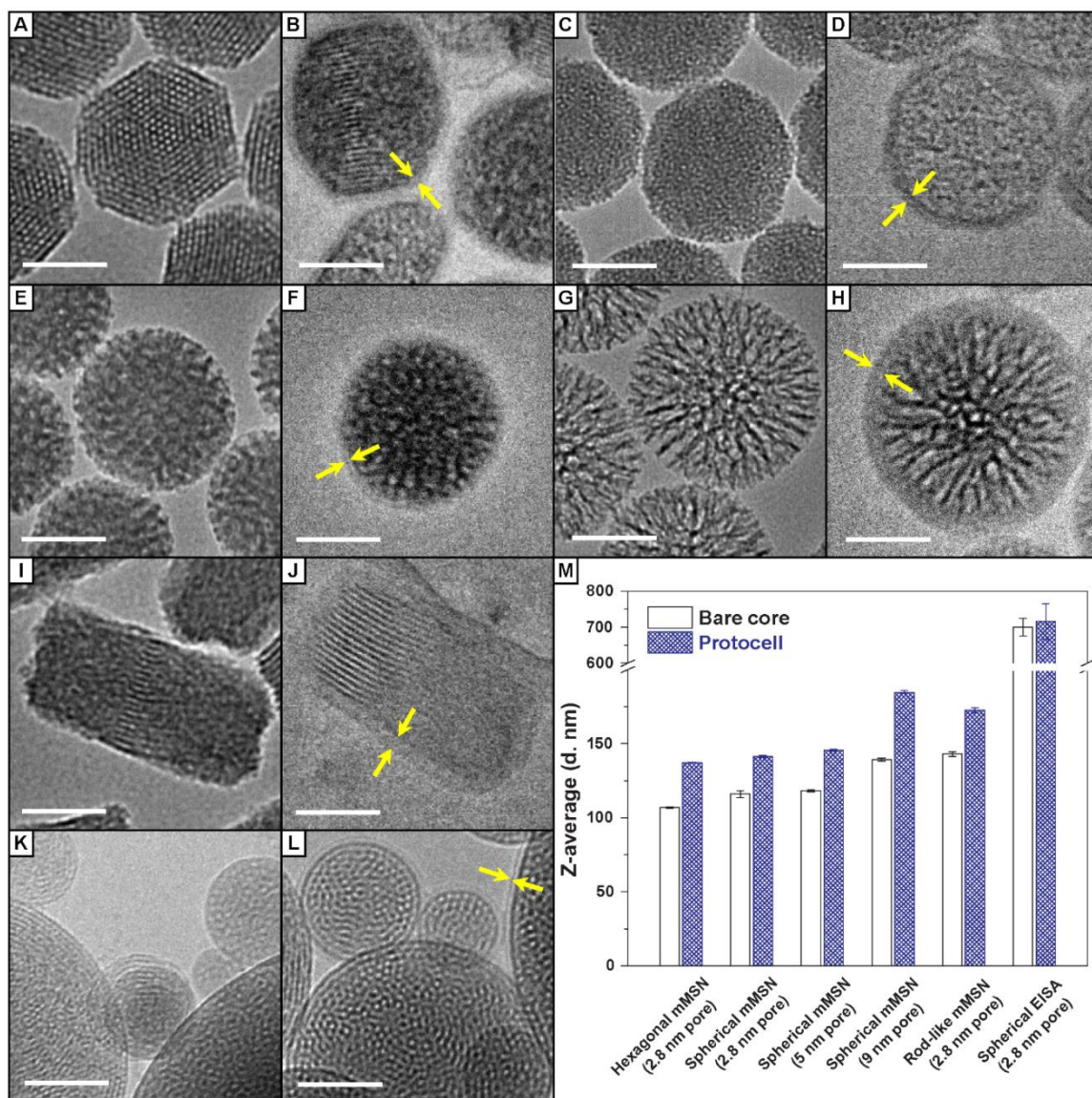
Figure 3.5 – Representative TEM and Cryo-TEM images of MSNPs and corresponding protocells of various shape and pore morphology including A) and B) Hexagonal mMSNPs and protocells, C) and D) Spherical 2.8 nm pore mMSNPs and protocells, E) and F) Spherical 5 nm pore mMSNPs and protocells, G) and H) Spherical 8 nm pore mMSNPs and protocells, I) and J) Rod-like 2.8 nm pore mMSNPs and protocells, K) and L) Aerosol assisted EISA MSNPs and protocells. Yellow arrows highlight the SLB (~ 4.6 nm) in the Cryo-TEM images. M) Hydrodynamic size analysis by DLS shows an increase in nanoparticle diameter following SLB fusion. DLS data represent mean ± SD, n = 3. Scale bars = 50 nm. L) Cryo-TEM images of EISA protocells were carried out at Baylor College of Medicine (Houston, TX) by C. Jia-Yin Fu, H. Khant and W. Chiu. Adapted and reproduced with permission.[4] © 2016, The American Chemical Society.

Figure 3.6 – *Visual Evidence of Protocell Stability in PBS*
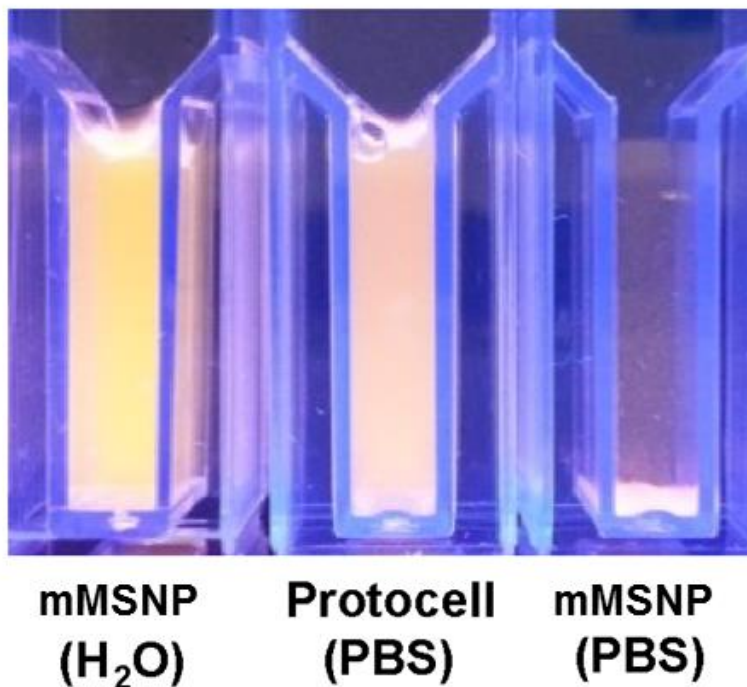
Figure 3.6 – Fluorescent mMSNPs and protocells in cuvettes illustrate the colloidal stability of mMSNPs in H_2O and aggregation driven settling of mMSNPs in 160 mM PBS, protocells remain suspended in 160 mM PBS. Adapted and reproduced with permission.[4] © 2016, The American Chemical Society.

Figure 3.7 – *Cryo-TEM of 18 nm MSNPs and Liposomes*
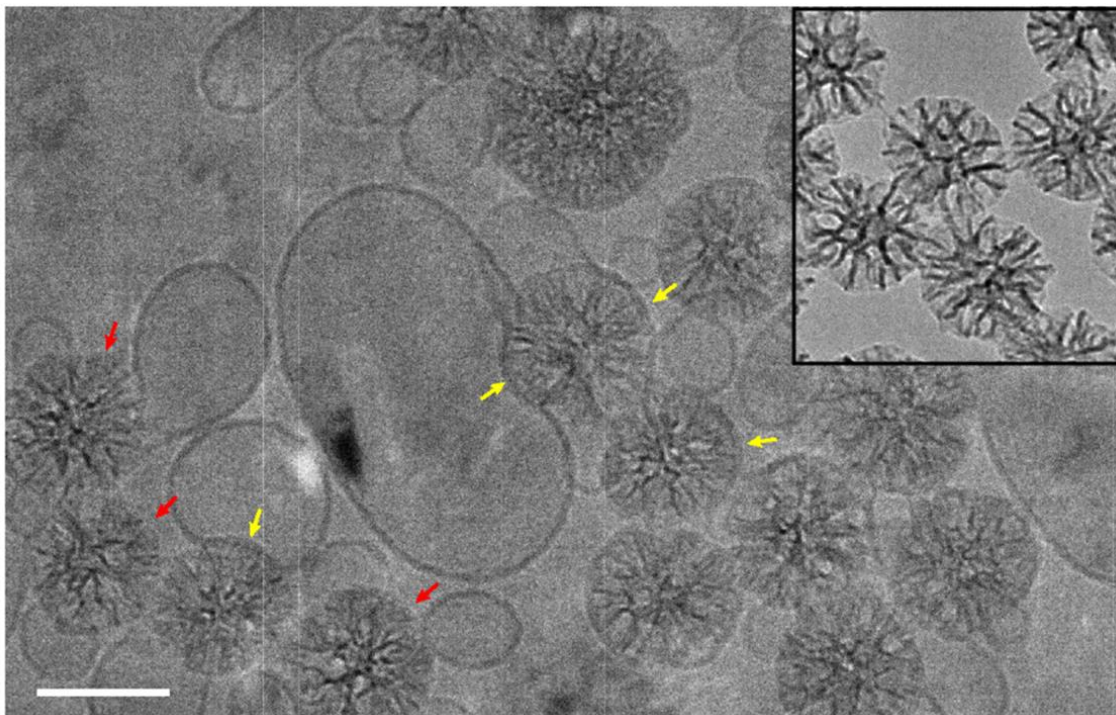
Figure 3.7 – Cryo-TEM image of 18 nm pore structured mMSNPs mixed with liposomes under optimized fusion conditions as established in **Figure 3.3** showing large lipid-associated aggregates. (Inset): conventional TEM of 18 nm pore structured mMSNPs. Yellow arrows highlight regions of liposome to silica interactions, red arrows highlight exposed silica surfaces. Scale bar = 100 nm. Corresponding hydrodynamic size measurements: mMSNPs with 18 nm pore diameter, Z-average diameter = 123.0 ± 0.3 nm (Avg PdI = 0.056 ± 0.018); lipid associated aggregates Z-average diameter = 396.9 ± 13.0 nm (Avg PdI = 0.139 ± 0.043). DLS data represent mean ± SD, n = 3. Adapted and reproduced with permission.[4] © 2016, The American Chemical Society.

possible van der Waals and electrostatic interactions (that all scale nominally with surface silica concentration) is insufficient to cause rupture/fusion to form a SLB. Moreover, the topography of the silica surface is influential in the spreading process of the SLB, where 10 – 30 nm deep scratches were found to arrest spreading of egg phosphatidylcholine bilayers on borosilicate glass due to unfavorable bending interactions needed to maintain conformity.[21, 22] It is likely that for mMSNPs there is a critical pore size above which the highly contoured regions of the pore arrest spreading and fusion. This pore size should be sensitive to the SLB composition, which dictates the bending modulus. Using unsaturated lipids and, potentially, decreasing the cholesterol content might be expected to make the membrane more flexible and promote SLB formation on mMSNPs with larger pore size,[23, 24] however, at the cholesterol concentration (44 %) used in our experiments, it is unlikely that the transition temperature (T_m) of the phosphatidylcholine SLB component is a major factor in size stability.[25] It is also conceivable that fusion might be promoted by doping the buffer with divalent ions like Ca^{2+} or Mg^{2+} that, through several possible electrostatically mediated pathways, are known to promote vesicle fusion on glass.[26, 27] Finally adsorption of drugs within the pores would in essence increase the solid fraction of the surface and potentially promote attractive DLVO interactions and vesicle fusion.

3.2.2 Factors Influencing Colloidal Stability of Monosized Protocells for Use *In Vivo*

Having established a generalized process by which to reliably form monosized protocells *in vitro*, we next studied how the physicochemical

properties of the SLB influence colloidal stability in complex biological media. As noted above, *in vivo* colloidal stability is crucial to the realization of both passive and active targeting as any process that non-selectively removes nanoparticles from circulation reduces concomitantly the number of particles that could accumulate in the tumor microenvironment due to the EPR effect or those that are available to selectively bind to target cells or tissues. Despite its importance, few papers unambiguously establish the stability of nanocarriers, which may in part explain inconsistent and unreproducible results in the literature, which are now generally recognized.[28-30] Problematic is that *in vivo* colloidal stability is difficult to predict from *in vitro* measurements. For example, we recently showed cationic MSNPs with identical size, shape, and surface charge (and therefore indistinguishable according to National Cancer Institute – Nanotechnology Characterization Laboratory standards)[28] to have completely different circulation and non-specific binding behaviors as elucidated by direct observation *ex ovo* in a chicken embryo chorioallantoic membrane (CAM) model[31] and SPECT imaging in a rat model (Adolphi *et.al.* private communication). Here, we evaluated colloidal stability by determination of hydrodynamic size and polydispersity index in complex biological media and by direct observation in the CAM model.

First, we examined how the encapsulating SLB and its fluidity affected long-term stability compared to the bare mMSNP surface. We prepared liposomes with zwitterionic lipids using either unsaturated DOPC or saturated DSPC as the major liposome component. Our comparison between DOPC and DSPC is ideal because these lipids possess nearly identical molar mass, have

the same acyl tail length, and yet exhibit T_m (-20 °C and 55 °C respectively) below and above the storage and physiological temperatures (22 °C and 37 °C, respectively). Additionally, the *cis*-configuration double bonds present in the DOPC acyl chains (absent in DSPC) are highly susceptible to oxidation, which can lead to structural instability.[32] We prepared unsaturated DOPC-based (composition = DOPC, chol, and 1,2-dioleoyl-*sn*-glycero-3-phosphoethanolamine-N-[methoxy(polyethylene glycol)-2000] (DOPE-PEG$_{2000}$) – DOPC:chol:DOPE-PEG$_{2000}$ mol ratio of 54:44:2) and saturated DSPC-based (composition = DSPC:chol:DSPE-PEG$_{2000}$ mol ratio of 54:44:2) vesicles by extrusion as previously described. Liposome compositions and hydrodynamic diameters are summarized in **Table 2.1**, where all possessed a hydrodynamic diameter < 100 nm and low PdI value < 0.2. Liposome to mMSNP fusion was achieved in 40 mM PBS as described earlier; then protocells were finally redispersed in 160 mM PBS. The formation of a complete SLB surrounding the MSNP cores was verified by combined techniques: DLS measurements showed the hydrodynamic diameter to increase uniformly by ~ 30 nm compared to mMSNPs, while maintaining a low PdI (< 0.1) (**Tables 3.1 and 3.2**). Zeta-potential measurements indicated the Hexagonal mMSNP protocells to have a zeta potential (- 3.3 mV) similar to the corresponding zwitterionic liposomes (- 2.9 mV) and much lower than the mMSNP (- 28.1 mV) (**Table 3.1**). Direct observation by Cryo-TEM (**Figure 3.5B**) showed the presence of a uniform conformal SLB surrounding the mMSNP cores.

Figure 3.8A shows changes in hydrodynamic size of protocells for 72 hours at 37 °C compared to bare mMSNP controls (see **Table 3.6** for corresponding PdI). Whereas the hydrodynamic size of bare mMSNPs increases within minutes of transfer to PBS at room temperature, and more rapidly at 37 °C, both DOPC-based and DSPC-based protocells maintain uniform size for 24 hours. Our results suggest that the colloidal stability of the protocells is primarily due to the zwitterionic SLB component rather than the PEG component, as the trends observed for DOPC and DSPC-based protocells prepared with and without PEG are nearly identical (**Figure 3.8A**). The stabilizing effect of the zwitterionic SLB can be attributed to several factors. Zwitterionic coatings are shown to increase nanoparticle stability in high salt concentration solutions due to hydration repulsion which also minimizes non-specific protein adsorption in serum containing solutions.[33-36] In addition, the presence of both positively and negatively charged functional groups on nanoparticle surfaces has been shown to increase solubility in water over a wide pH range, limit non-specific interactions with cultured cells, and display a non-toxic profile upon interaction with cells, based on cell viability assessment.[37] That the protocells are encapsulated completely within a zwitterionic SLB is evidenced by the hydrodynamic size / PdI change of bare mMSNPs, increasing from 106.9 nm / 0.050 to 193.4 nm / 0.292 in PBS after centrifugation (**Table 3.2**) along with their rapidly settling in PBS solution (**Figure 3.6**); incomplete SLB coverage would similarly result in the formation of irreversible aggregates *via* electrostatic destabilization and van der Waals forces, *vide supra*.

Figure 3.8 – *Comparison of SLB Formulation on Protocell Size Stability*
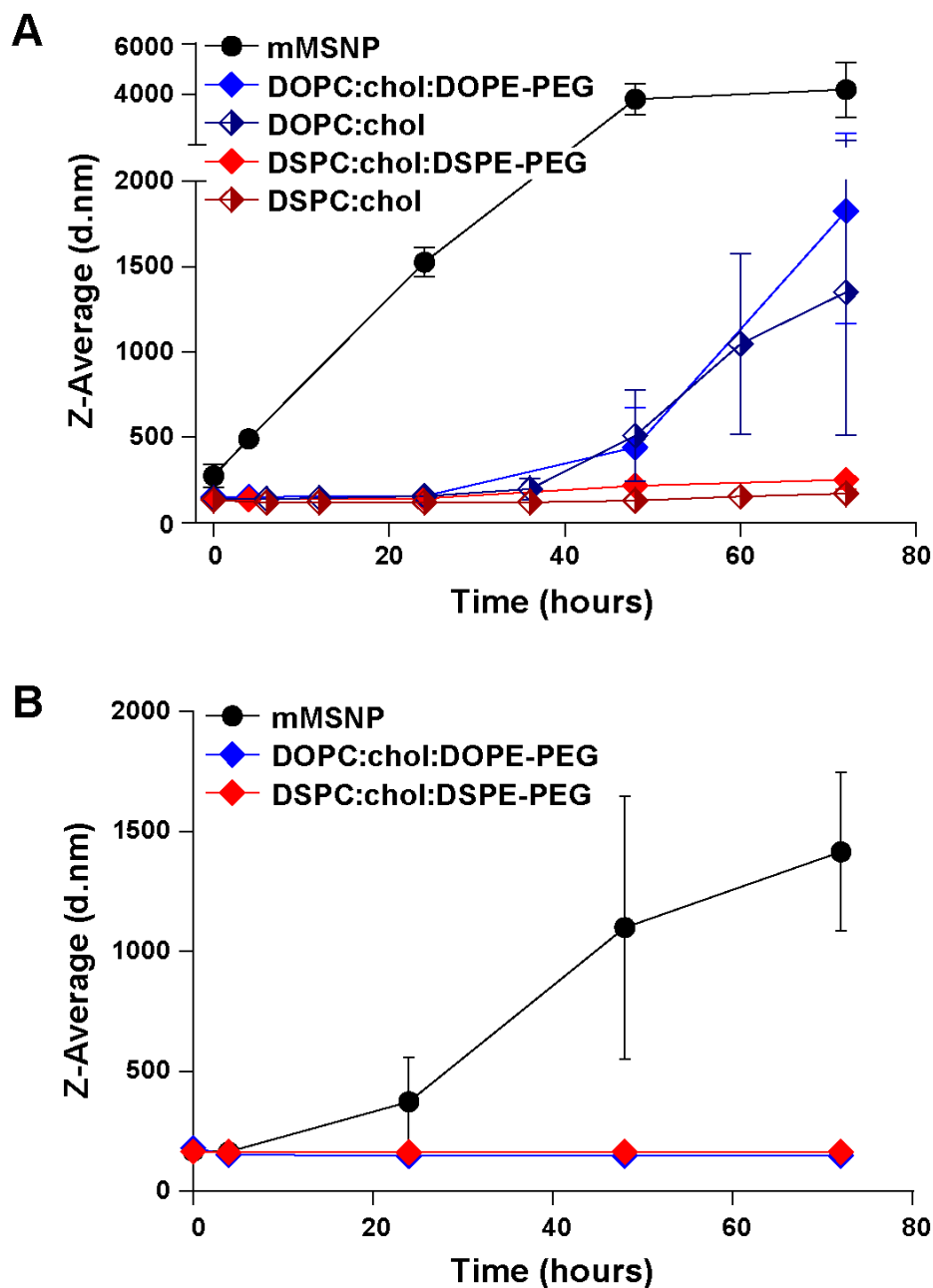
Figure 3.8 – A) Hydrodynamic size of protocells prepared with differing SLB formulations *versus* incubation time at 37 °C in 160 mM PBS. Trend in size change appears dependent on the extent of saturation of the lipid component of the SLB rather than PEGylation. B) Hydrodynamic size of PEGylated protocells prepared with differing SLB formulations *versus* incubation time at 37 °C in DMEM + 10 % FBS. All data represent mean ± SD, n = 3. Adapted and reproduced with permission.[4] © 2016, The American Chemical Society.

Sample	Media	0 h	4 h	24 h	48 h	72 h
Hexagonal mMSNP	PBS	0.242 ± 0.105	0.484 ± 0.029	0.585 ± 0.122	0.904 ± 0.191	0.902 ± 0.162
DOPC:chol Protocell	PBS	0.065 ± 0.007	0.103 ± 0.021	0.167 ± 0.024	0.669 ± 0.280	0.615 ± 0.403
DOPC:chol:DOPE-PEG$_{2000}$ Protocell	PBS	0.086 ± 0.021	0.098 ± 0.016	0.126 ± 0.021	0.466 ± 0.270	0.781 ± 0.345
DSPC:chol Protocell	PBS	0.062 ± 0.020	0.079 ± 0.016	0.078 ± 0.019	0.081 ± 0.016	0.198 ± 0.030
DSPC:chol:DSPE-PEG$_{2000}$ Protocell	PBS	0.102 ± 0.013	0.091 ± 0.015	0.108 ± 0.016	0.227 ± 0.029	0.213 ± 0.059
Hexagonal mMSNP	DMEM+10% FBS	0.137 ± 0.018	0.147 ± 0.014	0.413 ± 0.319	0.707 ± 0.162	0.642 ± 0.160
DOPC:chol:DOPE-PEG$_{2000}$ Protocell	DMEM+10% FBS	0.136 ± 0.013	0.186 ± 0.014	0.156 ± 0.020	0.154 ± 0.021	0.169 ± 0.012
DSPC:chol:DSPE-PEG$_{2000}$ Protocell	DMEM+10% FBS	0.177 ± 0.031	0.164 ± 0.034	0.163 ± 0.049	0.177 ± 0.035	0.178 ± 0.052

Table 3.6 – *MSNP and Protocell PdI Measurements*

Table 3.6 – Analysis of PdI of Hexagonal mMSNPs and protocells after incubation for 72 hours at 37°C in either PBS or DMEM + 10 % FBS. Data corresponds to size data reported in Figures 3.7A and 3.7B. Data represent mean $\pm$ SD, n = 3. Adapted and reproduced with permission.[4] © 2016, The American Chemical Society.

Concerning the influence of lipid bilayer composition on long-term stability, we find that, although both DOPC-based and DSPC-based protocells are stable for 24 hours, the size of both PEGylated and non-PEGylated DOPC-based protocells increases progressively from 24 to 72 hours in PBS. In comparison, DSPC-based protocells remain stable for > 72 hours at 37 °C in PBS (**Figure 3.8A**) and for over 6 months at room temperature (**Table 3.7**). To assess the possible role of lipid oxidation as being the cause of the instability of DOPC-based protocells, we prepared protocells in de-oxygenated PBS and determined their hydrodynamic size during storage for 7 days at 37 °C. Interestingly, we find DOPC-based protocells to remain stable in an oxygen reduced buffer, whereas they aggregate in standard PBS. In comparison, the presence or absence of oxygen made no difference in DSPC-based protocell size stability (**Figure 3.9**). This result indicates that the double bonds present in the acyl chains of unsaturated lipids are susceptible to oxidation and that lipid oxidation plays a significant role in the long-term stability of the corresponding protocells, where lipid oxidation presumably compromises the SLB leading to aggregation. Storage of protocells prepared with unsaturated lipids in de-oxygenated solvents should significantly increase 'shelf-life' needed for practical clinical translation.

Although, we have noted that colloidal stability of the protocells is primarily due to the zwitterionic SLB component, modification of nanocarriers with hydrophilic polymers have been widely shown to prolong *in vivo* circulation times, reduce protein adsorption, and reduce phagocytosis by immune cells.[38] Therefore, we used only PEGylated protocells to examine the influence of T_m in a

Sample	Medium	Original Hydrodynamic Diameter (nm)	Original PdI	Hydrodynamic Diameter (nm), 6 months, 25°C	PdI, 6 months, 25°C
Hexagonal mMSNP	H_2O	135.0 ± 1.7	0.096 ± 0.019	1275.0 ± 245.7	0.266 ± 0.061
DSPC:chol:DSPE -PEG$_{2000}$ Protocell	PBS	152.0 ± 4.7	0.089 ± 0.012	146.1 ± 1.3	0.064 ± 0.020

Table 3.7 – *Long-term Hydrodynamic Size Analysis*

Table 3.7 – Hydrodynamic size characteristics of Hexagonal mMSNP and protocells after 6-month storage under static conditions at 25 °C. SLB formulation DSPC:chol:DSPE-PEG2000 (mol % 54:44;2). Data represent mean ± SD, n = 3. Adapted and reproduced with permission.[4] © 2016, The American Chemical Society.

Figure 3.9 – *Protocell Stability Assessment under Deoxygenated Conditions*
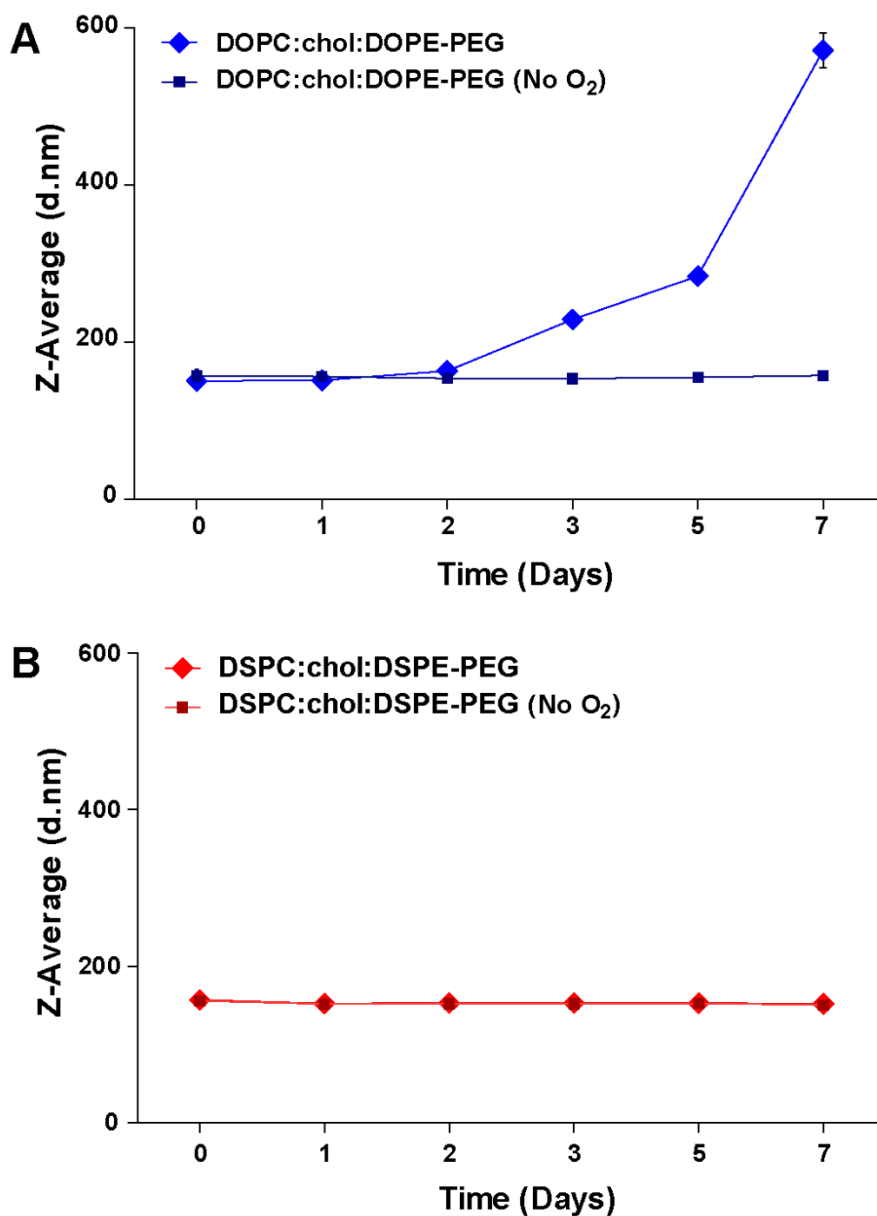
Figure 3.9 – Hydrodynamic size of A) DOPC-based protocells or B) DSPC-based protocells stored in either 160 mM standard PBS or deoxygenated PBS at 37°C for 7 days. The presence of oxygen in solution appears to cause a size increase likely due to the oxidation of the double bonds present in the acyl chains of DOPC. Neither the presence nor absence of oxygen appears to influence the size of DSPC-based protocells, as they do not contain any double bonds in the acyl chains. Data represent mean ± SD, n = 3. Adapted and reproduced with permission.[4] © 2016, The American Chemical Society.

more complex medium. We prepared protocells in PBS and then transferred them to a cell culture medium containing fetal bovine serum. Similar to the previous experiment, DSPC-based protocells maintain size stability for > 72 hours at 37 °C (**Figure 3.7A**), indicating minimal protein binding and destabilization of the SLB. Interestingly, we observe the identical size stability for DOPC-based protocells in complete media, suggesting that protein adsorption stabilizes the DOPC-based SLB and/or provides a steric barrier toward fusion and aggregation despite there being no measureable increase in hydrodynamic diameter.

Overall, we find that the zwitterionic SLB confers excellent colloidal stability to the protocell in physiologically relevant media. Both unsaturated and saturated SLBs prepared with and without PEG have greatly enhanced stability compared to the parent mMSNP. Nevertheless, the measured long-term stability of DSPC-based monosized protocells, compatibility with the majority of mMSNP cores tested, and potential to incorporate functional modifications to PEGylated lipids, in particular amine terminated 1,2-distearoyl-*sn*-glycero-3-phosphoethanolamine-N-[amino(polyethylene glycol)-2000] (DSPE-PEG$_{2000}$-NH$_2$) which can be chemically modified with a functional component, prompted us to choose the DSPC-PEG-based protocell formulation for further *in vitro, ex ovo,* and *in vivo* studies.

3.2.3 Biocompatibility and Protocell Size Stability *Ex Ovo* and *In Vivo*

Previous studies have shown mesoporous silica to be a biocompatible material; however, the interpretation of the overall biocompatibility of MSNP-based nanocarriers is complex due to several factors including methods of synthesis, physicochemical properties, size distribution, and surface modifications.[39] Therefore, to assess the influence of the SLB on biocompatibility and to determine the uniformity of the SLB coating, we incubated mMSNPs and protocells with human red blood cells (hRBCs). We observed that the hemolytic activity and potential toxicity of bare mMSNPs can be completely abolished with a SLB (**Figure 3.10**). This result supports evidence of a complete (defect-free) lipid bilayer coating that screens silanols ($\equiv$Si-OH) and anionic deprotonated silanols ($\equiv$Si-O$^-$) implicated in hemolysis[40] and, thereby, provides enhanced biocompatibility of the protocells *vis-à-vis* mMSNPs.

Earlier we established that monosized protocells maintain long-term colloidal stability in PBS and complete cell culture media; however, we sought a more rigorous test for our platform under more dynamic conditions. Protein corona formation onto nanoparticle surfaces has been shown to occur immediately upon exposure to a live animal system.[41] Thus, we examined protocell size stability after intravenous injection and circulation because, to the best of our knowledge, no current reports have examined nanoparticle stability post-injection. Fluorescent nanoparticle labeling provided useful qualitative analysis of stability within the CAM vasculature, which led us to seek quantitative measures of protocell size after separation from blood samples extracted post-

Figure 3.10 – *Hemolysis Assay*
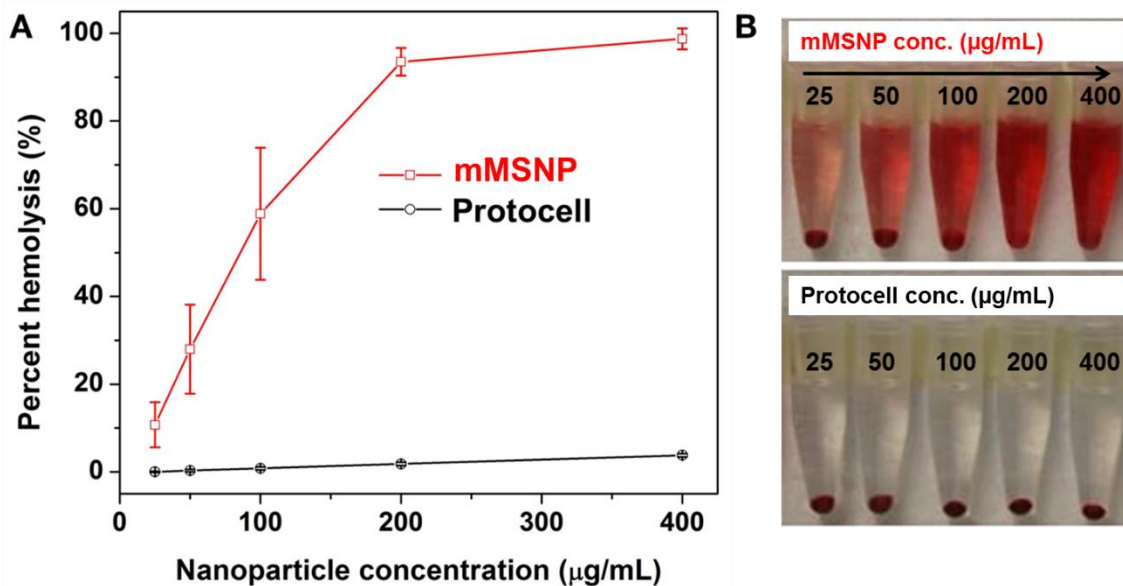
Figure 3.10 – A) Percentage of lysed human red blood cells (hRBCs) after exposure to 25, 50, 100, 200, and 400 µg/mL of mMSNPs and protocells for 2 hours at 37 °C. Data represent mean ± SD, n = 3. B) Digital photographs of hRBCs after 2 hours incubation with (top) mMSNPs or (bottom) protocells at different particle concentrations (25 to 400 µg/mL). Presence of red hemoglobin in supernatant indicates membrane damaged hRBCs. Adapted and reproduced with permission.[4] © 2016, The American Chemical Society.

injection from both CAM and *in vivo* mouse models. We detected fluorescent protocells in whole blood samples extracted from the CAM (**Figure 3.11A**); we then separated protocells from whole blood by centrifugation and the measured hydrodynamic size. Remarkably, the average protocell size is nearly identical pre- and post-injection (**Figure 3.11B**). In addition, we examined protocell size after circulation for multiple time points and found only a modest, time-dependent, average hydrodynamic diameter increase of 9 % at 30 minutes and increasing to 23 % at 240 minutes (**Figure 3.12**). We further validated *in vivo* stability characteristics by intravenous tail vein injection of protocells into a BALB/c mouse. After 10 minutes of protocell circulation, we extracted blood from the mouse, imaged fluorescent protocells in whole blood (**Figure 3.11C**), separated protocells using centrifugation, and found protocells maintain size stability in a mouse model (**Figure 3.11D**). Thus, we demonstrated qualitative and quantitative confirmation of both *ex ovo* and *in vivo* protocell stability in unique and separate model systems. While these data indicate that the protocell platform possesses a distinctive ability to circulate and avoid aggregation in a complex living system for a short period of time, we acknowledge the need for a more comprehensive analysis of protocell circulation and biodistribution in relevant *in vivo* animal models of disease in order to provide a more complete pre-clinical understanding of *in vivo* protocell performance.

Figure 3.11 – *Protocell Size Stability Post-Circulation*
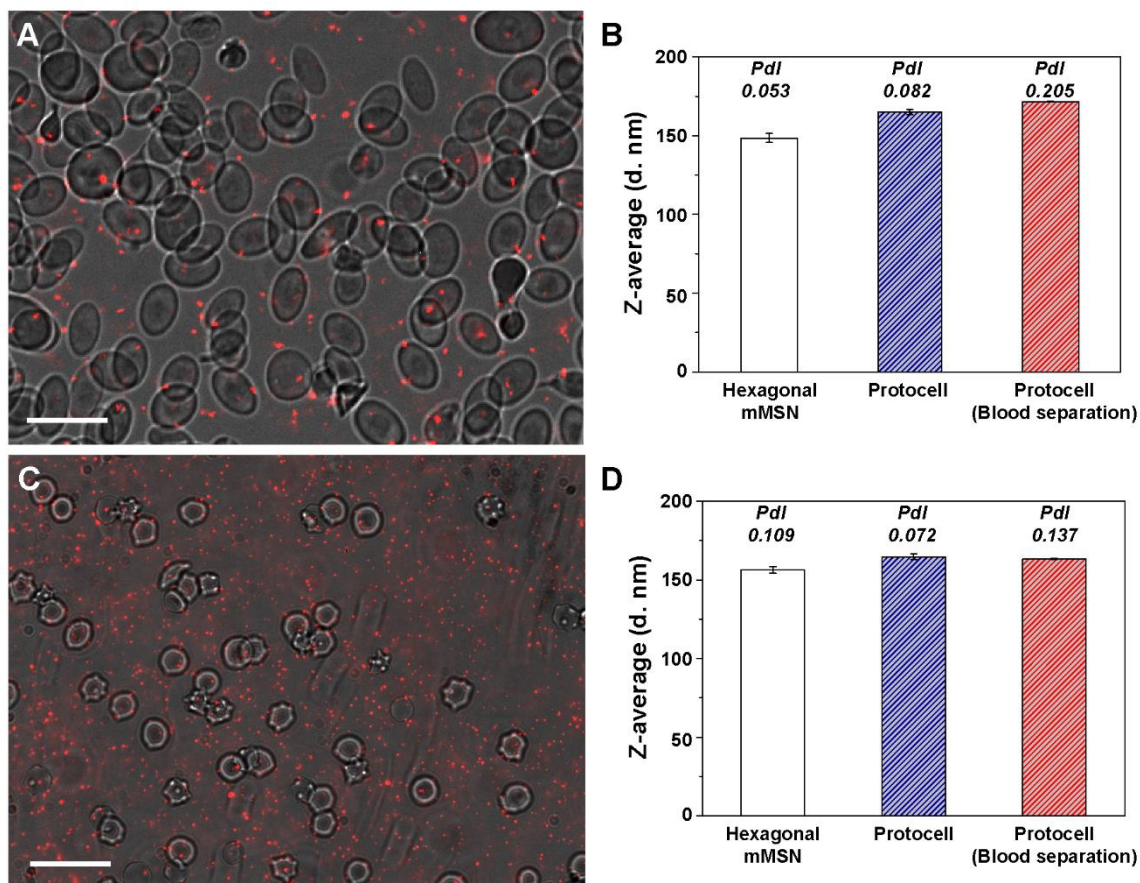
Figure 3.11 – A) Red fluorescent protocells extracted from CAM 10 minutes post-injection and imaged on glass slide with Zeiss AxioExaminer upright microscope. We observed protocells in motion moving in and out of frame in a Brownian pattern with no apparent direct association with red blood cells. B) Hydrodynamic size and PdI of core Hexagonal mMSNPs, protocells, and protocells separated from CAM blood. C) Fluorescent protocells injected and pulled from Balb/c mouse 10 minutes post-injection. D) Hydrodynamic size and PdI of core Hexagonal mMSNPs, protocells, and protocells separated from mouse blood. Injected protocells were separated from blood by variable speed centrifugation. Microscopy image scale bars = 20 μm and DLS data represent mean ± SD, n = 3. Data provides evidence of size stability A) and B) *ex ovo* and C) and D) *in vivo* as assessed by minimal change in hydrodynamic size and PdI values. Adapted and reproduced with permission.[4] © 2016, The American Chemical Society.

Figure 3.12 – *Protocell Size Stability After Separation from CAM Blood*

Protocell size (nm) after separation from CAM blood by centrifugation
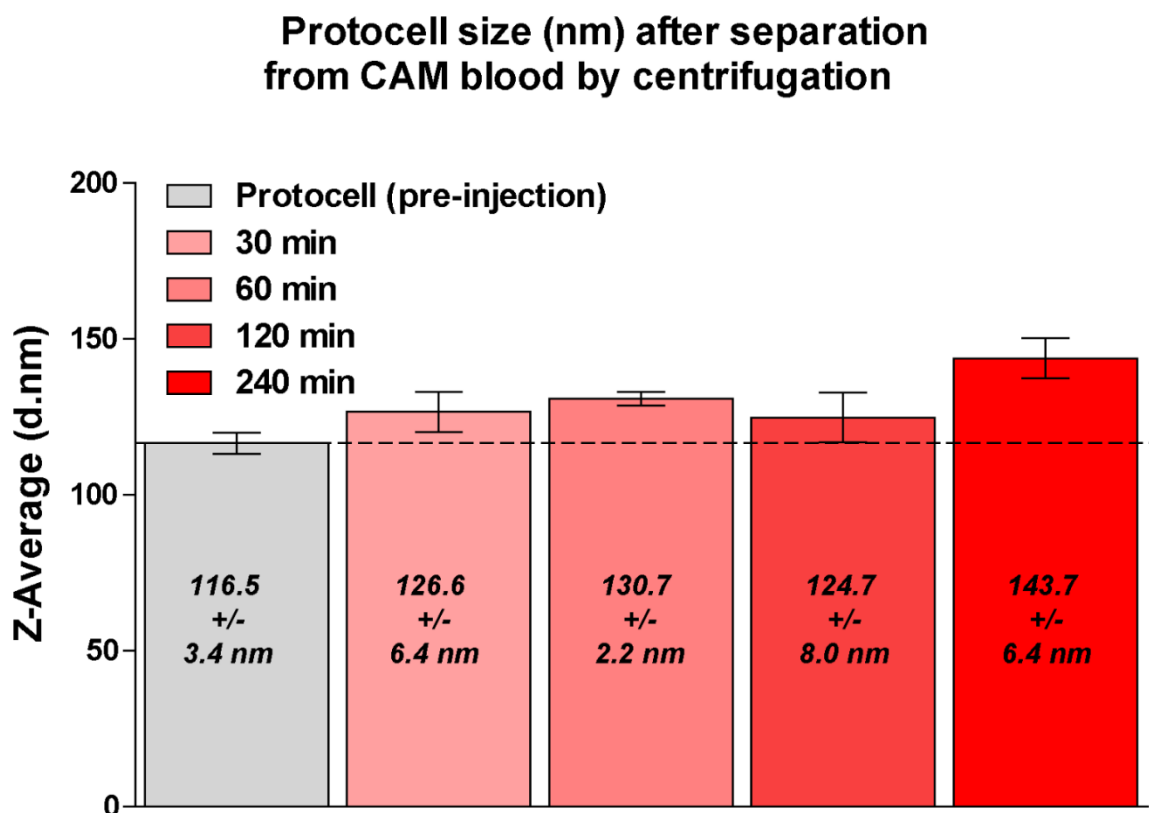
Figure 3.12 – Hydrodynamic size comparison of pre-injected protocells and protocells separated from CAM blood at different time points. Data provides evidence of size stability *ex ovo* as assessed by modest change in hydrodynamic size over multiple times up to 240 minutes in circulation. Data represent mean ± SD, n = 3. Adapted and reproduced with permission.[4] © 2016, The American Chemical Society.

3.3 Materials and Methods

3.3.1 Protocell Biocompatibility Assessment

Whole human blood was acquired from healthy donors with informed consent and stabilized in K$_2$EDTA tubes (BD Biosciences). Human RBCs were purified following reported procedure,[42] then incubated with either bare mMSNPs or protocells (25, 50, 100, 200, and 400 µg/mL) at 37 °C. After 3 hours of exposure, samples were centrifuged at 300 x g for 3 minutes, then 100 µL of supernatant from each sample was transferred to a 96-well plate. Hemoglobin absorbance was measured using a BioTek microplate reader (Winooski, VT) at 541 nm. The percent hemolysis of each sample was quantified using a reported equation (Detailed equation in **Appendix A.3**).[42]

3.3.2 Cell-Nanoparticle Interactions in *Ex Ovo* Avian Embryos

Ex ovo avian embryos were handled according to published methods,[43] with all experiments conducted following an institutional approval protocol (11-100652-T-HSC). This method included incubation of fertilized eggs (purchased from East Mountain Hatchery-Edgewood, NM) in a GQF 1500 Digital Professional egg incubator (Savannah, GA) for 3 to 4 days. Following initial *in ovo* incubation, embryos were removed from shells by cracking into 100 mL polystyrene weigh boats (VWR, Radnor, PA). *Ex ovo* embryos were then covered and incubated (~ 39 °C) with constant humidity (~ 70 %). For nanoparticle injections, ~ 50 µg (at 1 mg/mL) of bare mMSNPs or protocells in PBS were injected into secondary or tertiary veins of the CAM *via* pulled glass

capillary needles. CAM vasculature and fluorescent protocells were imaged using a customized avian embryo chamber (humidified) and a Zeiss AxioExaminer upright microscope modified with a heated stage. High speed videos were acquired on the same microscope using a Hamamatsu Orca Flash 4.0 camera.

3.3.3 Post-Circulation Size and Stability Analyses

All animal care and experimental protocols were in accordance with the National Institutes of Health and University of New Mexico School of Medicine guidelines. Ten- to twelve-week-old female BALB/c mice (Charles River Laboratories, Wilmington, MA) were administered dose of fluorescent protocells (10 mg/mL) in 150 µL PBS *via* tail vein injection. After 10 minutes of circulation, mice were euthanized and blood was drawn by cardiac puncture. Whole blood was stabilized in K_2EDTA microtainers (BD Biosciences) prior to analysis. *Ex ovo* avian embryos were administered dose of fluorescent protocells (1 mg/mL) in 50 µL PBS *via* secondary or tertiary veins of the CAM. After 10 minutes of circulation, blood was drawn *via* pulled glass capillary needles and analyzed immediately. Whole blood cells and protocell fluorescence in both mouse and avian samples were imaged on a glass slide with Zeiss AxioExaminer fixed stage microscope (Gottingen, Germany). To separate protocells from whole blood, samples were centrifuged at low speed to remove blood cells, supernatant fraction was transferred to a fresh tube then centrifuged at 15,000 x g for 10 minutes. The pellets were washed (15,000 x g for 10 minutes) twice in PBS, then protocell size was analyzed on Malvern Zetasizer Nano-ZS equipment.

3.3.4 Nanoparticle Imaging and Characterization Analyses

TEM images were acquired on a JEOL 2010 (Tokyo, Japan) equipped with a Gatan Orius digital camera system (Warrendale, PA) under a 200 kV voltage. The Cryo-TEM samples were prepared using an FEI Vitrobot Mark IV (Eindhoven, Netherlands) on Quantifoil® R1.2/1.3 holey carbon grids (sample volume of 4 µL, a blot force of 1, and blot and drain times of 4 and 0.5 seconds, respectively). Imaging was taken with a JEOL 2010 TEM at 200 kV using a Gatan model 626 cryo stage. Nitrogen adsorption-desorption isotherms of mMSNPs were obtained from on a Micromeritics ASAP 2020 (Norcross, GA) at 77 K. Samples were degassed at 120 $^{\circ}$C for 12 hours before measurements. The surface area and pore size was calculated following the Brunauer-Emmet-Teller (BET) equation in the range of P/P_o from 0.05 to 0.1 and standard Barrett-Joyer-Halenda (BJH) method. Hydrodynamic size and zeta potential data were acquired on a Malvern Zetasizer Nano-ZS equipped with a He-Ne laser (633 nm) and Non-Invasive Backscatter optics (NIBS). All samples for DLS measurements were suspended in various media (D.I. water, PBS, and DMEM+10 % FBS) at 1 mg/mL. Measurements were acquired at 25 $^{\circ}$C or 37 $^{\circ}$C. DLS measurements for each sample were obtained in triplicate. The Z-average diameter was used for all reported hydrodynamic size measurements. The zeta potential of each sample was measured in D.I. water or 1xPBS using monomodal analysis. All reported values correspond to the average of at least three independent samples. The fluorescence images were captured with a Zeiss AxioExaminer fixed stage microscope (Gottingen, Germany).

3.4 References

1. Brinker, C. J.; Scherer, G. W. *Sol-Gel Science: The Physics and Chemistry of Sol-Gel Processing*. Academic press: 2013.

2. Marsh, D. *Handbook of Lipid Bilayers*. CRC Press: 2013.

3. Ashley, C. E.; Carnes, E. C.; Phillips, G. K.; Padilla, D.; Durfee, P. N.; Brown, P. A.; Hanna, T. N.; Liu, J.; Phillips, B.; Carter, M. B.; Carroll, N. J.; Jiang, X.; Dunphy, D. R.; Willman, C. L.; Petsev, D. N.; Evans, D. G.; Parikh, A. N.; Chackerian, B.; Wharton, W.; Peabody, D. S.; Brinker, C. J. The Targeted Delivery of Multicomponent Cargos to Cancer Cells by Nanoporous Particle-Supported Lipid Bilayers. *Nat. Mater.* 2011, 10, 389-397.

4. Durfee, P. N.; Lin, Y.-S.; Dunphy, D. R.; Muñiz, A. J.; Butler, K. S.; Humphrey, K. R.; Lokke, A. J.; Agola, J. O.; Chou, S. S.; Chen, I. M.; Wharton, W.; Townson, J. L.; Willman, C. L.; Brinker, C. J. Mesoporous Silica Nanoparticle-Supported Lipid Bilayers (Protocells) for Active Targeting and Delivery to Individual Leukemia Cells. *ACS Nano* 2016.

5. Savarala, S.; Ahmed, S.; Ilies, M. A.; Wunder, S. L. Formation and Colloidal Stability of Dmpc Supported Lipid Bilayers on Sio2 Nanobeads. *Langmuir* 2010, 26, 12081-12088.

6. Lin, Y.-S.; Abadeer, N.; Hurley, K. R.; Haynes, C. L. Ultrastable, Redispersible, Small, and Highly Organomodified Mesoporous Silica Nanotherapeutics. *J. Am. Chem. Soc.* 2011, 133, 20444-20457.

7. Meng, H.; Wang, M.; Liu, H.; Liu, X.; Situ, A.; Wu, B.; Ji, Z.; Chang, C. H.; Nel, A. E. Use of a Lipid-Coated Mesoporous Silica Nanoparticle Platform for Synergistic Gemcitabine and Paclitaxel Delivery to Human Pancreatic Cancer in Mice. *ACS Nano* 2015, 9, 3540-3557.

8. Mornet, S.; Lambert, O.; Duguet, E.; Brisson, A. The Formation of Supported Lipid Bilayers on Silica Nanoparticles Revealed by Cryoelectron Microscopy. *Nano Lett.* 2005, 5, 281-285.

9. Liu, X.; Situ, A.; Kang, Y.; Villabroza, K. R.; Liao, Y.; Chang, C. H.; Donahue, T.; Nel, A. E.; Meng, H. Irinotecan Delivery by Lipid-Coated Mesoporous Silica Nanoparticles Shows Improved Efficacy and Safety over Liposomes for Pancreatic Cancer. *ACS Nano* 2016, 10, 2702-2715.

10. Liu, J.; Stace-Naughton, A.; Jiang, X.; Brinker, C. J. Porous Nanoparticle Supported Lipid Bilayers (Protocells) as Delivery Vehicles. *J. Am. Chem. Soc.* 2009, 131, 1354-1355.

11. Wang, D.; Huang, J.; Wang, X.; Yu, Y.; Zhang, H.; Chen, Y.; Liu, J.; Sun, Z.; Zou, H.; Sun, D.; Zhou, G.; Zhang, G.; Lu, Y.; Zhong, Y. The Eradication of Breast Cancer Cells and Stem Cells by 8-Hydroxyquinoline-Loaded Hyaluronan Modified Mesoporous Silica Nanoparticle-Supported Lipid Bilayers Containing Docetaxel. *Biomaterials* 2013, 34, 7662-7673.

12. Cauda, V.; Engelke, H.; Sauer, A.; Arcizet, D.; Bräuchle, C.; Rädler, J.; Bein, T. Colchicine-Loaded Lipid Bilayer-Coated 50 Nm Mesoporous Nanoparticles Efficiently Induce Microtubule Depolymerization Upon Cell Uptake. *Nano Lett.* 2010, 10, 2484-2492.

13. Lin, Y.-S.; Tsai, C.-P.; Huang, H.-Y.; Kuo, C.-T.; Hung, Y.; Huang, D.-M.; Chen, Y.-C.; Mou, C.-Y. Well-Ordered Mesoporous Silica Nanoparticles as Cell Markers. *Chem. Mater.* 2005, 17, 4570-4573.

14. Lin, Y.-S.; Haynes, C. L. Impacts of Mesoporous Silica Nanoparticle Size, Pore Ordering, and Pore Integrity on Hemolytic Activity. *J. Am. Chem. Soc.* 2010, 132, 4834-4842.

15. Chen, P.-K.; Lai, N.-C.; Ho, C.-H.; Hu, Y.-W.; Lee, J.-F.; Yang, C.-M. New Synthesis of Mcm-48 Nanospheres and Facile Replication to Mesoporous Platinum Nanospheres as Highly Active Electrocatalysts for the Oxygen Reduction Reaction. *Chem. Mater.* 2013, 25, 4269-4277.

16. Nandiyanto, A. B. D.; Kim, S.-G.; Iskandar, F.; Okuyama, K. Synthesis of Spherical Mesoporous Silica Nanoparticles with Nanometer-Size Controllable Pores and Outer Diameters. *Microporous Mesoporous Mater.* 2009, 120, 447-453.

17. Wang, J.; Sugawara-Narutaki, A.; Shimojima, A.; Okubo, T. Biphasic Synthesis of Colloidal Mesoporous Silica Nanoparticles Using Primary Amine Catalysts. *J. Colloid Interface Sci.* 2012, 385, 41-47.

18. Shen, D.; Yang, J.; Li, X.; Zhou, L.; Zhang, R.; Li, W.; Chen, L.; Wang, R.; Zhang, F.; Zhao, D. Biphase Stratification Approach to Three-Dimensional Dendritic Biodegradable Mesoporous Silica Nanospheres. *Nano Lett.* 2014, 14, 923-932.

19. Huang, X.; Li, L.; Liu, T.; Hao, N.; Liu, H.; Chen, D.; Tang, F. The Shape Effect of Mesoporous Silica Nanoparticles on Biodistribution, Clearance, and Biocompatibility *in Vivo*. *ACS Nano* 2011, 5, 5390-5399.

20. Yu, T.; Malugin, A.; Ghandehari, H. Impact of Silica Nanoparticle Design on Cellular Toxicity and Hemolytic Activity. *ACS Nano* 2011, 5, 5717-5728.

21. Sackmann, E. Membrane Bending Energy Concept of Vesicle- and Cell-Shapes and Shape-Transitions. *FEBS Lett.* 1994, 346, 3-16.

22.   Cremer, P. S.; Boxer, S. G. Formation and Spreading of Lipid Bilayers on Planar Glass Supports. *J. Phys. Chem. B* 1999, 103, 2554-2559.

23.   Henriksen, J.; Rowat, A. C.; Brief, E.; Hsueh, Y. W.; Thewalt, J. L.; Zuckermann, M. J.; Ipsen, J. H. Universal Behavior of Membranes with Sterols. *Biophysical Journal* 2006, 90, 1639-1649.

24.   Sackmann, E. Physical Basis of Self-Organization and Function of Membranes: Physics of Vesicles. *Handbook of Biological Physics* 1995, 1, 213-304.

25.   Yeagle, P. L. *The Structure of Biological Membranes*. CRC press: 2004.

26.   Nollert, P.; Kiefer, H.; Jähnig, F. Lipid Vesicle Adsorption *Versus* Formation of Planar Bilayers on Solid Surfaces. *Biophys. J.* 1995, 69, 1447.

27.   Seantier, B.; Kasemo, B. Influence of Mono- and Divalent Ions on the Formation of Supported Phospholipid Bilayers *Via* Vesicle Adsorption. *Langmuir* 2009, 25, 5767-5772.

28.   Crist, R. M.; Grossman, J. H.; Patri, A. K.; Stern, S. T.; Dobrovolskaia, M. A.; Adiseshaiah, P. P.; Clogston, J. D.; McNeil, S. E. Common Pitfalls in Nanotechnology: Lessons Learned from Nci's Nanotechnology Characterization Laboratory. *Integr. Biol.* 2013, 5, 66-73.

29.   Lin, Y.-S.; Hurley, K. R.; Haynes, C. L. Critical Considerations in the Biomedical Use of Mesoporous Silica Nanoparticles. *J. Phys. Chem. Lett.* 2012, 3, 364-374.

30.   Zarschler, K.; Prapainop, K.; Mahon, E.; Rocks, L.; Bramini, M.; Kelly, P. M.; Stephan, H.; Dawson, K. A. Diagnostic Nanoparticle Targeting of He Egf-Receptor in Complex Biological Conditions Using Single-Domain Antibodies. *Nanoscale* 2014, 6, 6046-6056.

31.   Townson, J. L.; Lin, Y.-S.; Agola, J. O.; Carnes, E. C.; Leong, H. S.; Lewis, J. D.; Haynes, C. L.; Brinker, C. J. Re-Examining the Size/Charge Paradigm: Differing *in Vivo* Characteristics of Size- and Charge-Matched Mesoporous Silica Nanoparticles. *J. Am. Chem. Soc.* 2013, 135, 16030-16033.

32.   Lis, M.; Wizert, A.; Przybylo, M.; Langner, M.; Swiatek, J.; Jungwirth, P.; Cwiklik, L. The Effect of Lipid Oxidation on the Water Permeability of Phospholipids Bilayers. *Physical Chemistry Chemical Physics* 2011, 13, 17555-17563.

33.   Estephan, Z. G.; Jaber, J. A.; Schlenoff, J. B. Zwitterion-Stabilized Silica Nanoparticles: Toward Nonstick Nano. *Langmuir* 2010, 26, 16884-16889.

34.   Zhu, Y.; Sundaram, H. S.; Liu, S.; Zhang, L.; Xu, X.; Yu, Q.; Xu, J.; Jiang, S. A Robust Graft-to Strategy to Form Multifunctional and Stealth Zwitterionic Polymer-Coated Mesoporous Silica Nanoparticles. *Biomacromolecules* 2014, 15, 1845-1851.

35.   Soo Choi, H.; Liu, W.; Misra, P.; Tanaka, E.; Zimmer, J. P.; Itty Ipe, B.; Bawendi, M. G.; Frangioni, J. V. Renal Clearance of Quantum Dots. *Nat. Biotechnol.* 2007, 25, 1165-1170.

36.   Nag, O.; Awasthi, V. Surface Engineering of Liposomes for Stealth Behavior. *Pharmaceutics* 2013, 5, 542.

37.   Breus, V. V.; Heyes, C. D.; Tron, K.; Nienhaus, G. U. Zwitterionic Biocompatible Quantum Dots for Wide Ph Stability and Weak Nonspecific Binding to Cells. *ACS Nano* 2009, 3, 2573-2580.

38.   Ferrari, M. Nanogeometry: Beyond Drug Delivery. *Nat. Nanotechnol.* 2008, 3, 131-132.

39.   Asefa, T.; Tao, Z. Biocompatibility of Mesoporous Silica Nanoparticles. *Chem. Res. Toxicol.* 2012, 25, 2265-2284.

40.   Zhang, H.; Dunphy, D. R.; Jiang, X.; Meng, H.; Sun, B.; Tarn, D.; Xue, M.; Wang, X.; Lin, S.; Ji, Z.; Li, R.; Garcia, F. L.; Yang, J.; Kirk, M. L.; Xia, T.; Zink, J. I.; Nel, A.; Brinker, C. J. Processing Pathway Dependence of Amorphous Silica Nanoparticle Toxicity: Colloidal *Vs* Pyrolytic. *J. Am. Chem. Soc.* 2012, 134, 15790-15804.

41.   Lynch, I.; Dawson, K. A. Protein-Nanoparticle Interactions. *Nano Today* 2008, 3, 40-47.

42.   Liao, K.-H.; Lin, Y.-S.; Macosko, C. W.; Haynes, C. L. Cytotoxicity of Graphene Oxide and Graphene in Human Erythrocytes and Skin Fibroblasts. *ACS Appl. Mater. Interfaces* 2011, 3, 2607-2615.

43.   Leong, H. S.; Steinmetz, N. F.; Ablack, A.; Destito, G.; Zijlstra, A.; Stuhlmann, H.; Manchester, M.; Lewis, J. D. Intravital Imaging of Embryonic and Tumor Neovasculature Using Viral Nanoparticles. *Nat. Protoc.* 2010, 5, 1406-1417.

CHAPTER 4

INFLUENCE OF PARTICLE SIZE DISPERSITY ON PROTOCELL CHARACTERISTICS

4.1 Overview

For the development of therapeutic nanocarriers specifically targeted to leukemia cells, prolonged circulation times are needed to enhance the probability of delivery to distributed cells within the blood, marrow, and other tissue spaces, and, it is reported that particle size is an important determinant in delivery to tissue sites characteristic of this disseminated disease.[1] Therefore, it is of interest to understand the effect of protocell size dispersity on *in vivo* performance. Potentially, a broad particle size distribution could effect or direct broad dissemination of protocells to differing body tissues in addition to the peripheral vasculature and other tissues (liver, spleen, bone marrow) which may harbor leukemic cells, or, protected tissues which serve as sanctuaries for leukemic cells (testes, brain) and are frequent sites of recurrent or relapsed disease following systemic chemotherapy treatment. However, it is presently unclear as to how particle size polydispersity influences particle entrapment, non-specific binding, and circulation time.

4.2 Results and Discussion

4.2.1 Influence of Protocell Size Dispersity on *In Vitro* and *Ex Ovo* Performance

In order to assess the dependence of polydispersity on non-specific binding and circulation, we compared monosized protocells with protocells assembled from MSNP cores prepared by aerosol assisted EISA as previously reported.[2] EISA cores are characterized by spherical MSNPs with a power law

particle size distribution ranging from ~ 20 to ~ 800 nm (see TEM images in

Figures 3.5K, 3.5L, and 4.1) that results from the aerosol droplet size

distribution of the aerosol generator. EISA MSNPs have a pore diameter of ~ 2.5

nm and a zeta-potential of approximately - 31 mV,[4] comparable to those of

Hexagonal mMSNPs, so the comparison of their behaviors depends principally

on polydispersity (See **Table 3.1** for other physicochemical parameters of the

EISA MSNP and protocells). Hexagonal and EISA protocells were prepared by

fusion of vesicles with composition, DSPC:chol:DSPE-PEG$_{2000}$ mol ratio of

54:44:2 according to methods described previously. The hydrodynamic diameter

and PdI of EISA protocells were ~ 715 nm and 0.434 compared to ~ 137 nm and

0.085 for hexagonal protocells (**Figure 3.5M and Table 3.1**).

To investigate the role of polydispersity on *in vitro* MSNP and protocell

non-specific binding interactions, we incubated human endothelial cells

(EA.hy926) with either fluorescently labelled EISA or mMSNP cores and their

corresponding protocells (20 µg/mL) for 4 hours with complete medium under

normal cell culturing conditions. Flow cytometry analysis showed both EISA and

mMSNP particles to have significant levels of non-specific binding to EA.hy926

cells (**Figure 4.2**) whereas for EISA MSNP the extended breadth of the FL2-H

intensity curve reflected the size, and therefore, fluorescence intensity

distribution of individual MSNPs. Correspondingly, the fluorescence intensity

binding curve for mMSNPs was rather monodisperse. For both EISA and

mMSNP derived protocells, we observe a 20-fold decrease in non-specific

binding relative to the parent core particle (**Figure 4.2, see also fluorescence**

Figure 4.1 – *Comparison Between EISA and mMSNPs*
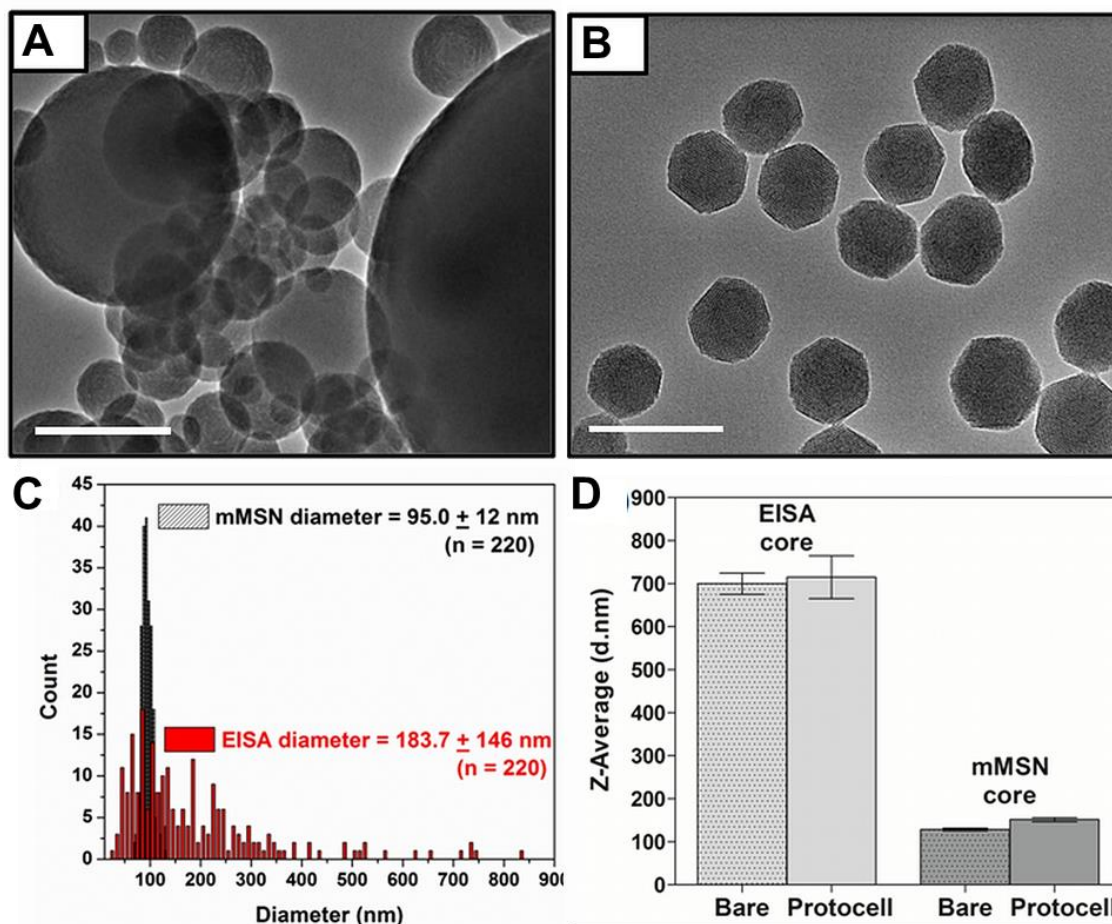
Figure 4.1 – A) Conventional TEM image of MSNPs prepared from EISA synthesis route. B) Conventional TEM image of Hexagonal mMSNPs prepared from colloidal solution-based synthesis route. Scale bars = 200 nm. C) Histogram of particle size distributions of EISA and Hexagonal mMSNP cores measured from TEM images. Data represent mean ± SD, n = 220. D) Hydrodynamic size measurement comparison of EISA and Hexagonal mMSNP cores and protocells. Data represent mean ± SD, n = 3. Adapted and reproduced with permission.[3] © 2016, The American Chemical Society.

Figure 4.2 – *Flow Cytometry Comparison of Non-Specific Binding*
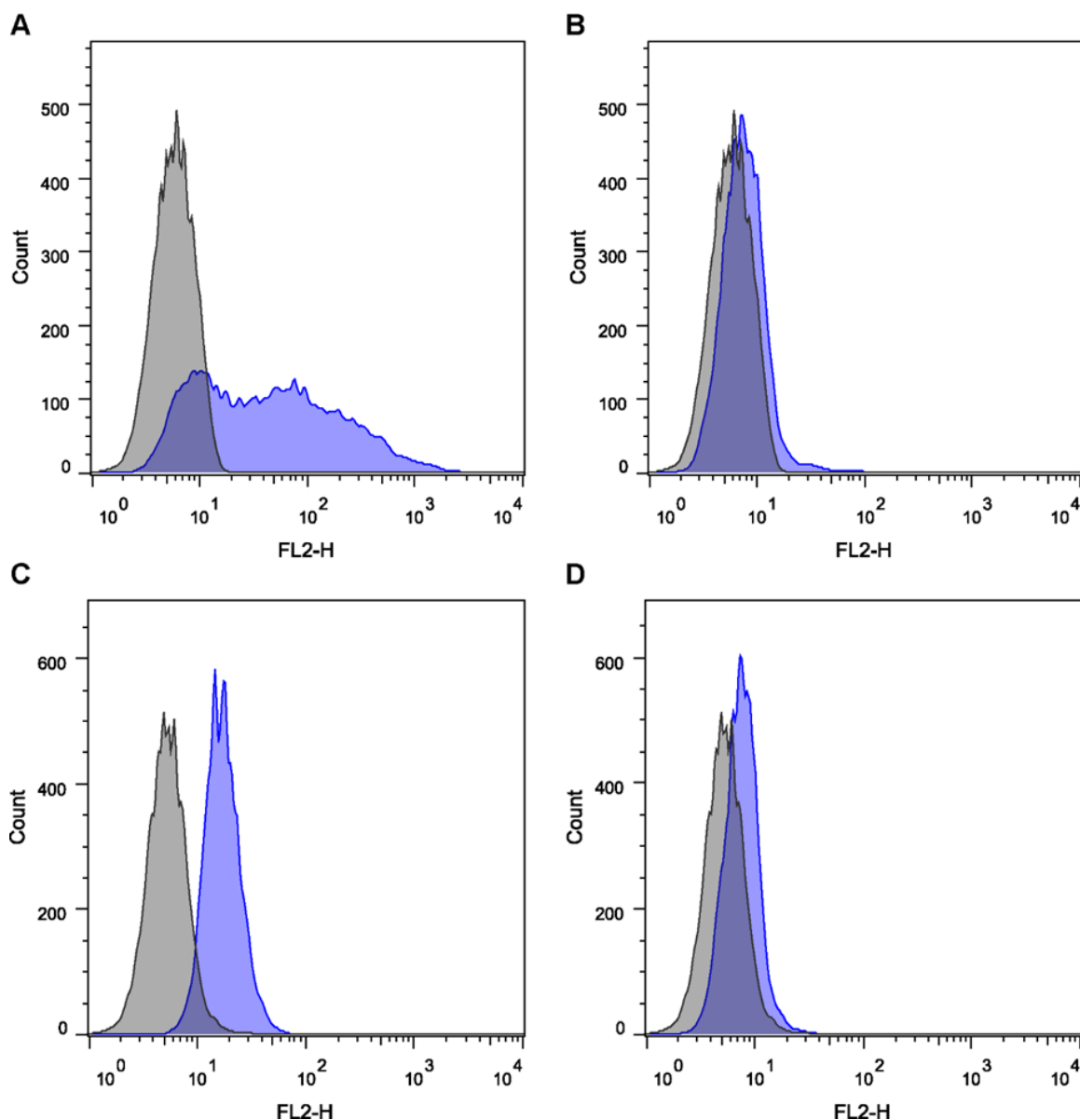
Figure 4.2 – Flow cytometry measurements of EA.hy926 endothelial cells after incubation with 20 µg/mL of A) EISA MSNP, B) EISA protocell, C) Hexagonal mMSNP, and D) monosized protocells for 4 hours. Percent population shift due to particle fluorescence (grey = control, no particle exposure, blue outline = mMSNPs or protocells). Adapted and reproduced with permission.[3] © 2016, The American Chemical Society.

microscopy images in Figure 4.3). This indicates that the conformal and complete SLB serves to effectively shield lipophilic surface silanol groups ($\equiv$Si-OH) and anionic deprotonated silanols ($\equiv$Si-O$^-$) present on the bare MSNP and known to promote internalization *via* macropinocytosis and other non-specific endocytotic pathways.[5] Our findings underscore the importance of the SLB in helping to prevent non-specific cell binding events, and support previous reports demonstrating minimal nonspecific cell binding affinity of polydisperse EISA protocells *in vitro*.[6, 7]

However, as previously noted, *in vitro* studies of nanoparticle behavior may be poor indicators of *in vivo* outcomes as they lack the complexities of *in vivo* conditions which present major obstacles to nanoparticle stability and target cell binding.[8] These obstacles include flow dynamics within the diverging and converging vasculature, opsonization by plasma proteins, uptake by the mononuclear phagocyte system, and the need for translocation across the capillary bed for tissue penetration. To assess MSNP and protocell behavior in a more relevant model, we employed the CAM model as an *in vivo (ex ovo)* model of the vascular system in which to observe nanoparticle circulation, flow characteristics, non-specific interactions, and particle stability in a living system using intravital imaging.[9-11] Fluorescently labeled nanoparticles can be injected intravenously into the CAM vasculature and imaged over time. As investigated previously *in vitro*, we examined mMSNP cores as well as EISA and mMSNP protocells to assess the influence of the SLB and polydispersity on biodistribution in this more complex *ex ovo* CAM environment. The influence of the SLB on

Figure 4.3 – *Fluorescence Microscopy of Non-Specific Binding*

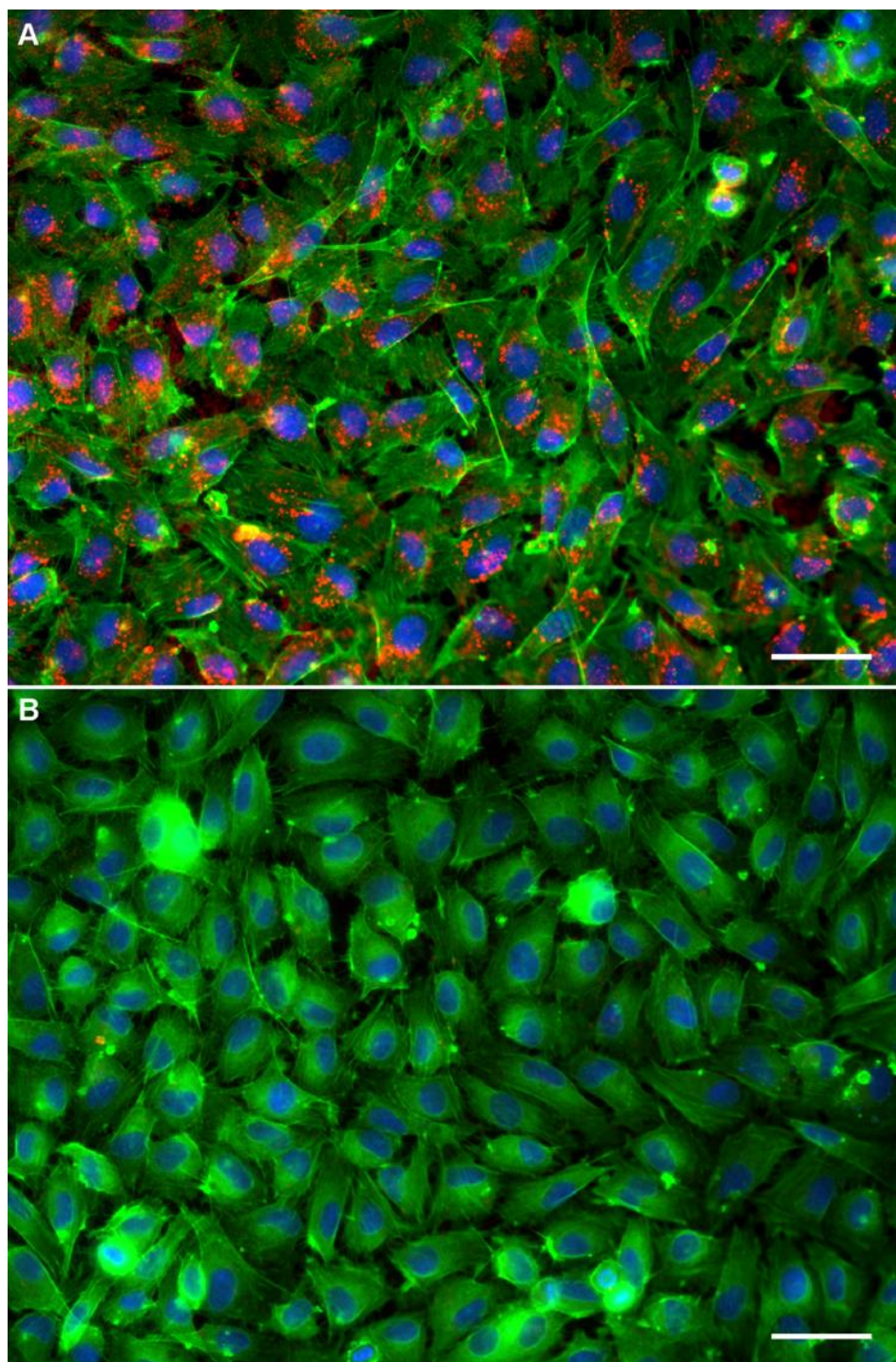**Figure 4.3** – Differential binding of Hexagonal mMSNPs and protocells observed after 4 hours incubation in complete medium. A) Bare Hexagonal mMSNPs (red) bind non-specifically to EA.hy926 (blue – DAPI stained nuclei, green – phalloidin stained actin), while B) protocells (red) do not interact with cells in culture. Scale bar = 50 µm. Adapted and reproduced with permission.[3] © 2016, The American Chemical Society.

nanoparticle flow dynamics and non-specific binding was immediately evident as bare mMSNP cores bound to endothelial cells and arrested in the vessels of the CAM within 5 minutes of injection (**Figure 4.4A**) and were largely taken up by phagocytic white blood cells after 30 minutes, reducing correspondingly the concentration of circulating mMSNPs (**Figure 4.4B**). By comparison, monosized protocells exhibited significantly lower non-specific binding and uptake by white blood cells leading to greatly improved circulation characteristics (**Figures 4.5A and 4.5B**). A representative video of stable monosized protocell circulation is reported in the Supporting Information, Video S1, by Durfee et.al.[3] Striking was the contrast between mMSNP and EISA protocells. Even though the *in vitro* outcomes were nearly identical, rapid sequestration of EISA protocells by immune cells, aggregation, and diminished circulation was noted within 5 minutes in the vascular CAM system (**Figure 4.6A**), with a more pronounced effect after 30 minutes (**Figure 4.6B**). The rapid uptake and reduced circulation are likely due to polydispersity leading to the majority of particles falling within a size range that either encourages immune cell uptake or advances unpredictable systemic circulation and distribution.[12] The CAM results highlight the need for reduced size polydispersity to maintain circulation within highly vascularized networks and elucidate a major limitation of *in vitro* models in predicting *in vivo* results. In this regard, we view the vascularized CAM model to improve greatly on *in vitro* models of specific and non-specific binding and more realistically assess the behavior of nanoparticles designed for *in vivo* use.[9]

Figure 4.4 – *Hexagonal mMSNP Flow in the CAM*

Figure 4.4 – Fluorescently-labelled nanoparticle flow patterns observed using *ex ovo* CAM model. Representative panels highlight differential flow characteristics between A) Hexagonal mMSNPs 5 minutes post injection and B) 30 minutes post injection. Red: mMSNP; Blue: autofluorescence from tissue. Scale bar = 50 µm. Adapted and reproduced with permission.[3] © 2016, The American Chemical Society.

Figure 4.5 – *Monosized Protocell Flow in the CAM*

Figure 4.5 – Fluorescent monosized Hexagonal mMSNP protocell flow patterns observed using *ex ovo* CAM model. Representative panels highlight differential flow characteristics between A) monosized protocells 5 minutes post injection and B) 30 minutes post injection. Scale bar = 50 μm. Adapted and reproduced with permission.[3] © 2016, The American Chemical Society.

Figure 4.6 – *EISA Protocell Flow in the CAM*

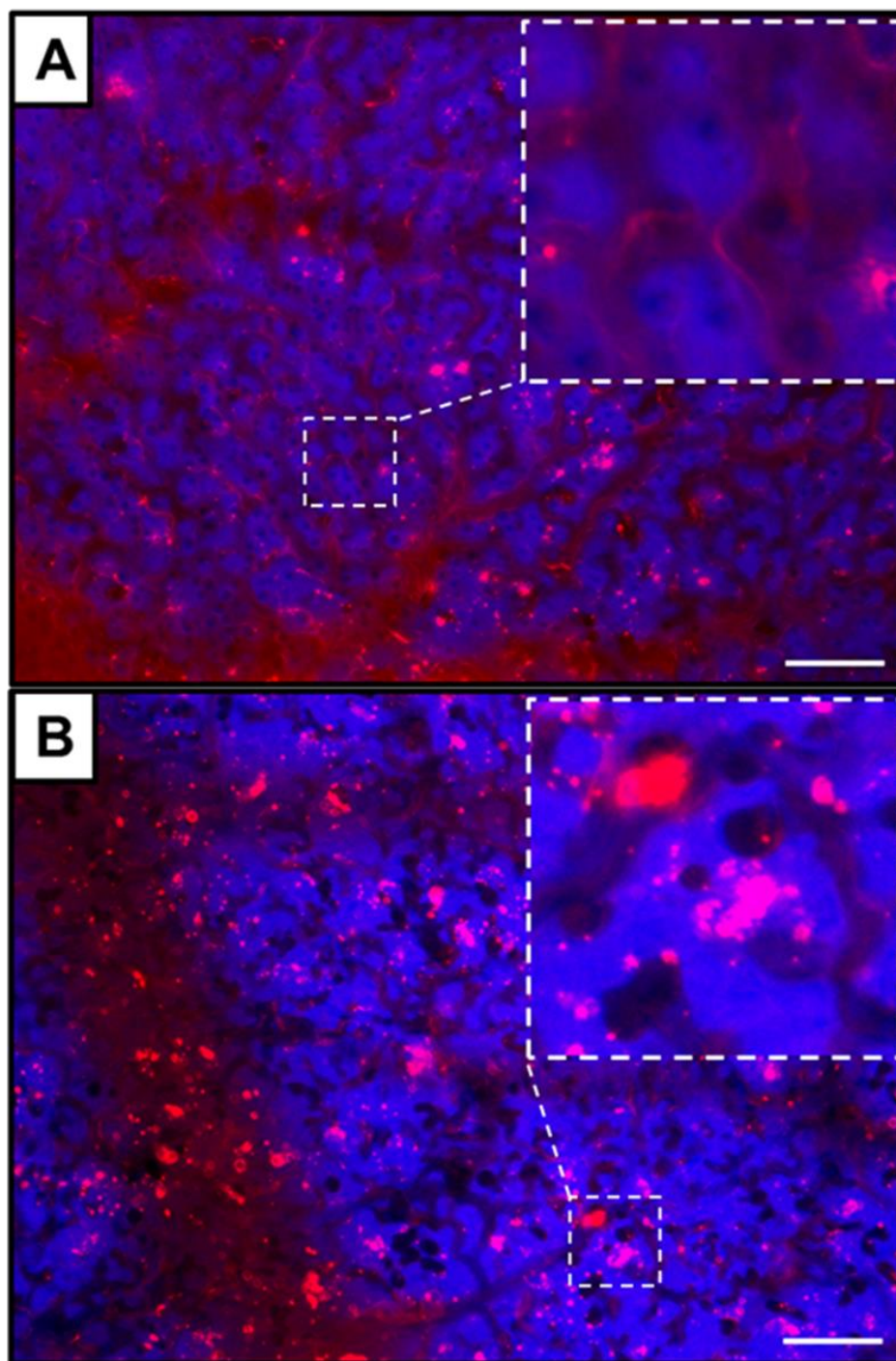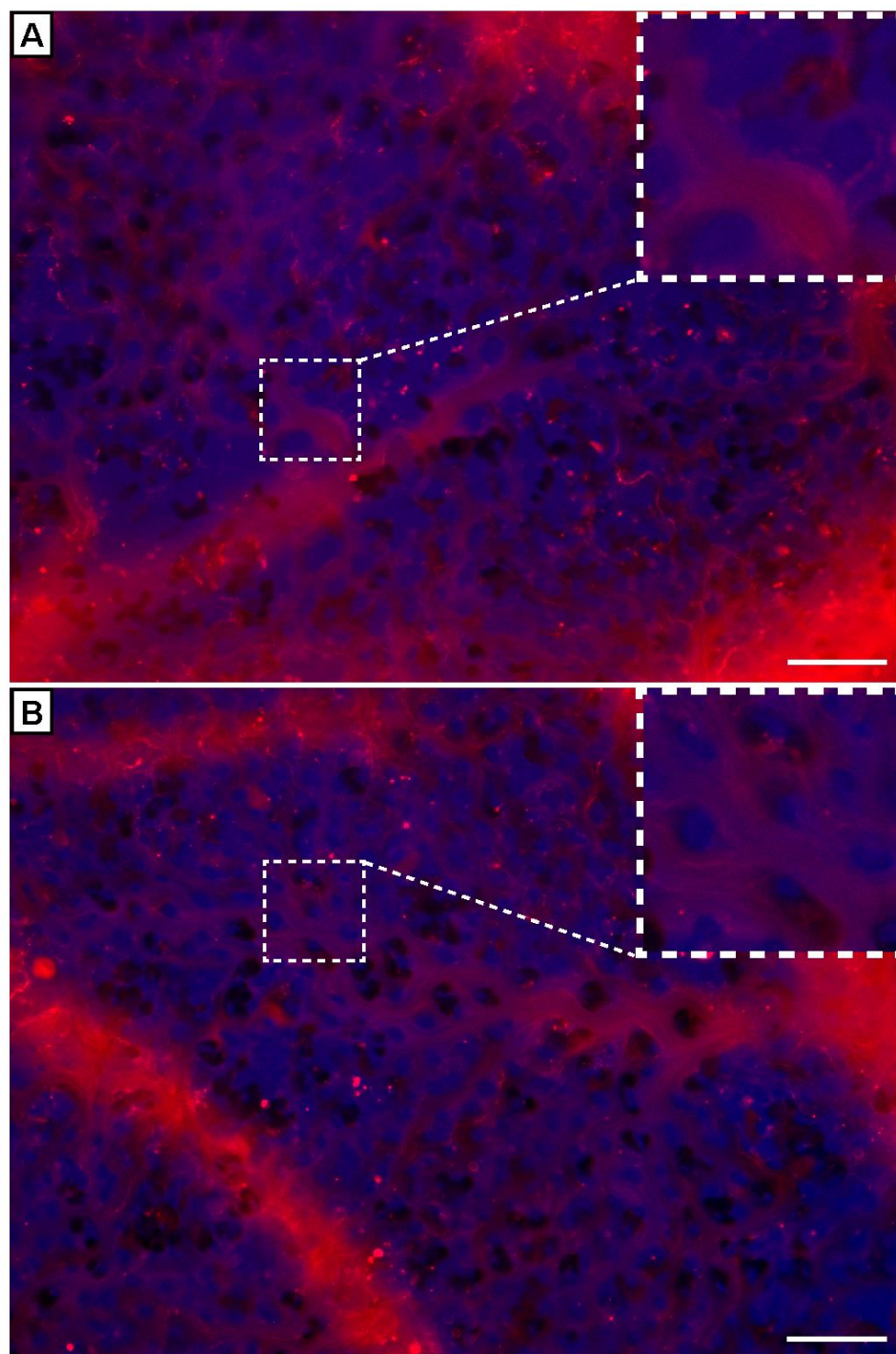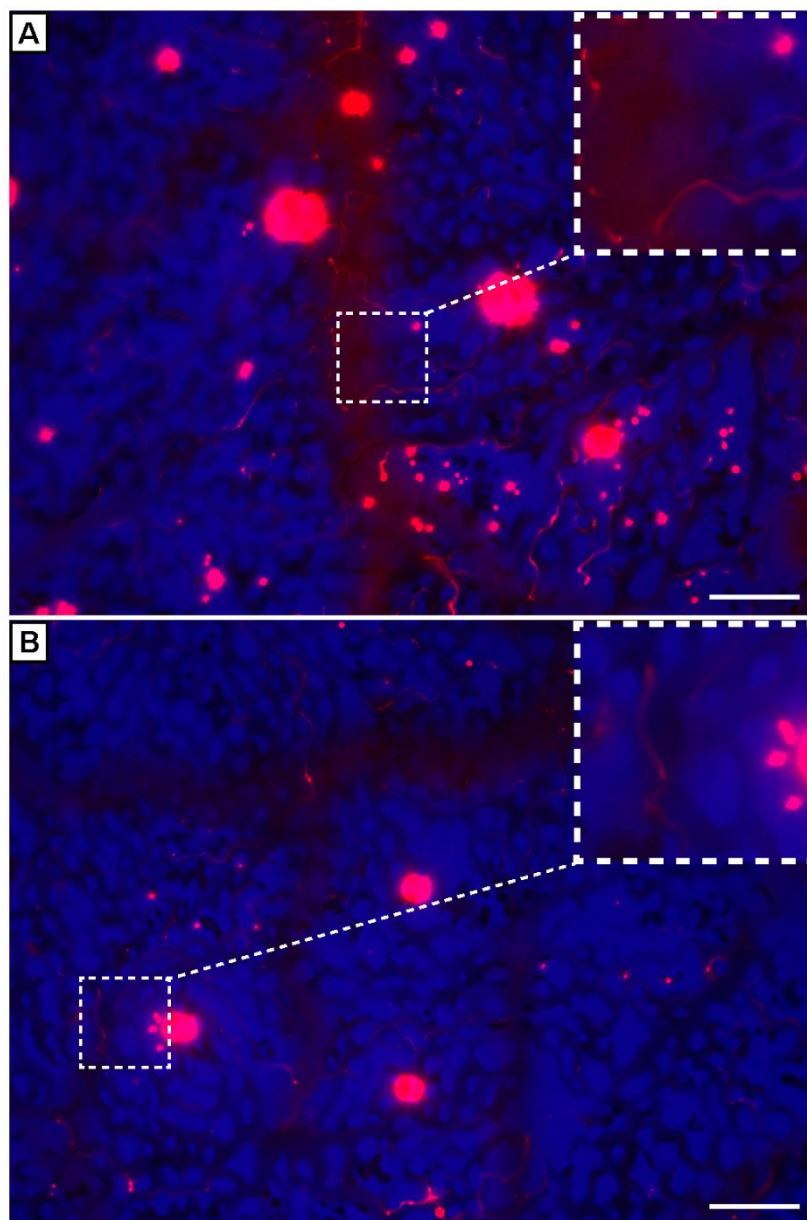**Figure 4.6** – Fluorescent EISA protocell flow patterns observed using *ex ovo* CAM model. Representative panels highlight differential flow characteristics between A) EISA protocells 5 minutes post injection and B) 30 minutes post injection. Scale bar = 50 μm. Adapted and reproduced with permission.[3] © 2016, The American Chemical Society.

4.3 Materials and Methods

4.3.1 Materials

All chemicals and reagents were used as received. See all protocell synthesis and assembly materials listed in **2.3.1 Materials**. Alexa Fluor®488 phalloidin, CellTracker™ Blue CMAC dye, and CellTracker™ green CMFDA dye were purchased from Life Technologies (Eugene, OR). Triton X-100 and Formaldehyde were purchased from Sigma-Aldrich (St. Louis, MO). Hoechst 33342 was obtained from Thermo Scientific (Rockford, IL). Heat inactivated fetal bovine serum (FBS), 10X phosphate buffered saline (PBS), 1X trypsin-EDTA solution, and penicillin streptomycin (PS) were purchased from Gibco (Logan, UT). Dulbecco's Modification of Eagle's Medium with 4.5 g/L glucose, L-glutamine and sodium pyruvate (DMEM) was obtained from CORNING cellgro (Manassas, VA).

4.3.2 Endothelial Cell Culture and Nanoparticle Non-Specific Binding and Uptake Procedure

Human endothelial cells, EA.hy926 (CRL-2922) were purchased from American Type Culture Center (ATCC, Manassas, VA). We seeded 5×10^5 EA.hy926 cells in 6-well plates with 2 mL of DMEM + 10 % FBS and 1 % PS at 37 °C in 5 % CO_2 humidified atmosphere. After 24 hours, the media was removed and replaced with 2 mL of fresh complete media supplemented with 20 µg/mL of bare mMSNPs or protocells for 4 hours at 37 °C under 5 % CO_2. After nanoparticle incubation, the media was removed and the cells were gently

washed twice with PBS. For imaging purposes, the nanoparticle treated cells were fixed in 3.7 % formaldehyde (in PBS) at room temperature for 10 minutes, washed with PBS, then treated with 0.1 % Triton X-100 for another 10 minutes. The fixed cells were washed with PBS and stored in 1 mL of PBS. The cell nuclei and F-actin were stained with 1 mL of Hoechst 33342 (3.2 µM in PBS) and 0.5 mL of Alexa Fluor®488 phalloidin (20 nM in PBS) for 20 minutes, respectively. After staining, the cells were washed with PBS twice and stored in PBS prior to fluorescence microscope imaging. For preparation of flow cytometry samples, the control and nanoparticle treated cells were removed from plate bottom using Trypsin-EDTA (0.25 %). The suspended cells were centrifuged, washed with PBS, and suspended in PBS for flow cytometry measurements.

4.3.3 Nanoparticle Characterization and Non-Specific Binding Analyses and Fluorescence Microscopy

TEM images were acquired on a JEOL 2010 (Tokyo, Japan) equipped with a Gatan Orius digital camera system (Warrendale, PA) under a 200 kV voltage. Hydrodynamic size data were acquired on a Malvern Zetasizer Nano-ZS equipped with a He-Ne laser (633 nm) and Non-Invasive Backscatter optics (NIBS). All samples for DLS measurements were suspended in D.I. water or PBS at 1 mg/mL. Measurements were acquired at 25 °C. DLS measurements for each sample were obtained in triplicate. The Z-average diameter was used for all reported hydrodynamic size measurements. All reported values correspond to the average of at least three independent samples. Flow cytometry data were performed on a Becton-Dickinson FACScalibur flow cytometer (Sunnyvale, CA).

The raw data obtained from the flow cytometer was processed with FlowJo software (Tree Star, Inc. Ashland, OR). The fluorescence images were captured with a Zeiss AxioExaminer fixed stage microscope (Gottingen, Germany).

4.4 References

1. Krishnan, V.; Rajasekaran, A. K. Clinical Nanomedicine: A Solution to the Chemotherapy Conundrum in Pediatric Leukemia Therapy. *Clin. Pharmacol. Ther.* 2014, 95, 168-178.

2. Lu, Y.; Fan, H.; Stump, A.; Ward, T. L.; Rieker, T.; Brinker, C. J. Aerosol-Assisted Self-Assembly of Mesostructured Spherical Nanoparticles. *Nature* 1999, 398, 223-226.

3. Durfee, P. N.; Lin, Y.-S.; Dunphy, D. R.; Muñiz, A. J.; Butler, K. S.; Humphrey, K. R.; Lokke, A. J.; Agola, J. O.; Chou, S. S.; Chen, I. M.; Wharton, W.; Townson, J. L.; Willman, C. L.; Brinker, C. J. Mesoporous Silica Nanoparticle-Supported Lipid Bilayers (Protocells) for Active Targeting and Delivery to Individual Leukemia Cells. *ACS Nano* 2016.

4. Liu, J.; Stace-Naughton, A.; Jiang, X.; Brinker, C. J. Porous Nanoparticle Supported Lipid Bilayers (Protocells) as Delivery Vehicles. *J. Am. Chem. Soc.* 2009, 131, 1354-1355.

5. Meng, H.; Yang, S.; Li, Z.; Xia, T.; Chen, J.; Ji, Z.; Zhang, H.; Wang, X.; Lin, S.; Huang, C.; Zhou, Z. H.; Zink, J. I.; Nel, A. E. Aspect Ratio Determines the Quantity of Mesoporous Silica Nanoparticle Uptake by a Small Gtpase-Dependent Macropinocytosis Mechanism. *ACS Nano* 2011, 5, 4434-4447.

6. Ashley, C. E.; Carnes, E. C.; Phillips, G. K.; Padilla, D.; Durfee, P. N.; Brown, P. A.; Hanna, T. N.; Liu, J.; Phillips, B.; Carter, M. B.; Carroll, N. J.; Jiang, X.; Dunphy, D. R.; Willman, C. L.; Petsev, D. N.; Evans, D. G.; Parikh, A. N.; Chackerian, B.; Wharton, W.; Peabody, D. S.; Brinker, C. J. The Targeted Delivery of Multicomponent Cargos to Cancer Cells by Nanoporous Particle-Supported Lipid Bilayers. *Nat. Mater.* 2011, 10, 389-397.

7. Ashley, C. E.; Carnes, E. C.; Epler, K. E.; Padilla, D. P.; Phillips, G. K.; Castillo, R. E.; Wilkinson, D. C.; Wilkinson, B. S.; Burgard, C. A.; Kalinich, R. M.; Townson, J. L.; Chackerian, B.; Willman, C. L.; Peabody, D. S.; Wharton, W.; Brinker, C. J. Delivery of Small Interfering Rna by Peptide-Targeted Mesoporous Silica Nanoparticle-Supported Lipid Bilayers. *ACS Nano* 2012, 6, 2174-2188.

8. Dobrovolskaia, M. A.; McNeil, S. E. Understanding the Correlation between *in Vitro* and *in Vivo* Immunotoxicity Tests for Nanomedicines. *J. Controlled Release* 2013, 172, 456-466.

9. Townson, J. L.; Lin, Y.-S.; Agola, J. O.; Carnes, E. C.; Leong, H. S.; Lewis, J. D.; Haynes, C. L.; Brinker, C. J. Re-Examining the Size/Charge

Paradigm: Differing *in Vivo* Characteristics of Size- and Charge-Matched Mesoporous Silica Nanoparticles. *J. Am. Chem. Soc.* 2013, 135, 16030-16033.

10. Vargas, A.; Zeisser-Labouèbe, M.; Lange, N.; Gurny, R.; Delie, F. The Chick Embryo and Its Chorioallantoic Membrane (Cam) for the *in Vivo* Evaluation of Drug Delivery Systems. *Adv. Drug Delivery Rev.* 2007, 59, 1162-1176.

11. Leong, H. S.; Steinmetz, N. F.; Ablack, A.; Destito, G.; Zijlstra, A.; Stuhlmann, H.; Manchester, M.; Lewis, J. D. Intravital Imaging of Embryonic and Tumor Neovasculature Using Viral Nanoparticles. *Nat. Protoc.* 2010, 5, 1406-1417.

12. He, Q.; Zhang, Z.; Gao, F.; Li, Y.; Shi, J. *In Vivo* Biodistribution and Urinary Excretion of Mesoporous Silica Nanoparticles: Effects of Particle Size and Pegylation. *Small* 2011, 7, 271-280.

CHAPTER 5

PROTOCELL TARGETING AND CARGO DELIVERY TO INDIVIDUAL CELLS
IN VITRO, *EX OVO*, AND *IN VIVO*

5.1 Overview

It is now widely recognized that nanoparticle based drug delivery provides a new ability to package poorly soluble and/or highly toxic drugs, protect drugs and molecular cargos from enzymatic degradation, and enhance their circulation and biodistribution compared to free drug. Furthermore 'passive' or 'active' targeted delivery promises precise administration of therapeutic cargos to specific cells or tissues, while sparing collateral damage to healthy cells and tissues and potentially overcoming multiple drug resistance mechanisms.[1-3] So-called passive targeting occurs through the EPR effect resulting from 200 – 2000 nm fenestrations in the tumor vasculature that are permeable to blood components including nanoparticles.[1] Nanoparticles are retained because the lymphatic function of the tumor may be defective and does not support convective flow back into the interstitial fluid,[4] and because diffusion of nanoparticles may be highly limited due to their dimensions.[5] Arguably all nanoparticle therapeutics smaller than several micrometers could accumulate in tumor microenvironments according to the EPR effect; but their efficiency is strongly dependent on physicochemical factors such as size, shape, surface charge, and hydrophobicity, which control colloidal stability, and accordingly circulation time, non-specific binding, opsonization, and uptake by the mononuclear phagocyte system.[1, 6] Active targeting relies on modifying the nanocarrier with ligands that bind to receptors that are over expressed or uniquely expressed on targeted cancer cells *versus* normal cells.[7] Typically, active targeting also relies upon the EPR effect, and its efficiency is governed by

the same physicochemical factors as those for passive targeting.[8, 9] The difference is that targeting ligands can enhance binding and, therefore, retention by the targeted cell and can often promote internalization *via* receptor-mediated endocytotic pathways.[1, 8] Targeting ligands, however, increase size, complexity, and cost and potentially alter the same physicochemical parameters that govern the EPR effect, requiring re-optimization of the surface chemistry.[1] For this reason, the benefits of active targeting are often not clear-cut, and consequently considerably fewer actively targeted nanoparticle therapeutics are used clinically.[10, 11] A major exception is targeted delivery to individual or small groups of cells or circulating cells, for which the EPR effect is likely inoperative. Here, nanoparticle delivery to leukemias is an important case in point. Because conventional anticancer drugs used for leukemia therapy are systemic and non-targeted, they may result in significant acute and long term toxic side effects to normal tissues. Thus, there is a critical need to increase the efficacy and reduce toxicity of therapeutic interventions by direct targeting of specific sites or cells.[12, 13] Individual cell targeting, however, remains a significant challenge in cancer nanomedicine and has yet to be thoroughly demonstrated.[14] In the case of leukemia therapeutics, active targeting is required to allow specific delivery to leukemic cells in circulation and those in organ reservoirs such as bone marrow and spleen. It should be emphasized that targeting cannot be achieved at the expense of colloidal stability because increased circulation half-life has been shown to increase delivery to bone marrow, spleen, and liver disease sites, where leukemia cells may frequently home.[15]

To date, protocell based nanocarriers have shown to be effective for the delivery of multiple classes of cargos and cargo combinations to various cell types.[16] The majority of studies conducted have reported efficacy *in vitro*,[17-19] but numerous recent reports also show excellent *in vivo* results, where passive and active targeting to solid tumors *via* the EPR effect have been demonstrated.[20-23] However, the targeting of individual cells *in vivo* or in living systems has yet to be reported, and there have been no direct observations/determinations of *in vivo* colloidal stability. Here, based on our hypothesis that *in vivo* colloidal stability is paramount to achieving effective targeting, we explore how synthetic factors (*e.g.*, the lipid/silica ratio and ionic strength during SLB formation) and variation of modular protocell components (*i.e.*, MSNP size, shape, and pore size, lipid bilayer fluidity, extent of PEGylation, and surface display of targeting ligands) influence colloidal stability as judged *in vitro* and *in vivo* by particle size stability and polydispersity and by direct observation *ex ovo* in a CAM model. We establish processing conditions whereby we achieve particle size monodispersity and size stability for protocells with differing size, shape, and pore morphology. Using optimized processing conditions, we further demonstrate long circulation times, avoidance of non-specific binding and minimal opsonization *ex ovo* and *in vivo*. Having achieved *in vivo* colloidal stability, we finally demonstrate targeted binding and cargo delivery to individual leukemia cells *in vitro* and *ex ovo* by direct observation in the CAM model.

5.2 Results and Discussion

5.2.1 Protocell Targeting Specificity *In Vitro* and *Ex Ovo*

Once we verified the biological compatibility and *in vivo* stability of the monosized protocell platform, we examined receptor specific targeting both *in vitro* and *ex ovo*. As a model system we chose a human B cell precursor ALL cell line (REH) that was engineered to express the epidermal growth factor receptor (EGFR) and we compared the performance of these REH-EGFR leukemia cells to the parental (EGFR-negative) cell line so as to have a matched negative control for our experiments. Targeting was accomplished using the NeutrAvidin/biotin conjugation strategy to modify an amine functionalized SLB (prepared with mol ratio DSPC:chol:DSPE-PEG$_{2000}$-NH$_2$ = 49:49:2 – **Table 2.1**) with anti-EGFR monoclonal antibodies as depicted in **Figure 2.1**.

To examine targeting specificity, we compared protocell interactions with both the human REH parental cell line controls and also with a murine B precursor ALL cell line (Ba/F3) also lacking EGFR. We compared the performance of these parental EGFR-negative control cell lines to corresponding REH and Ba/F3 clones engineered to express ectopic human EGFR, designated REH-EGFR and Ba/F3-EGFR, respectively.[24] To assess the kinetics of protocell binding, we incubated anti-EGFR antibody-labeled fluorescent protocells with REH parental and REH-EGFR cells for various time points *in vitro*. We observed significant binding within 5 minutes and maximal binding at 30 minutes of incubation in complete media under normal cell culture conditions by both flow

cytometry (**Figure 5.1A**) and fluorescence microscopy (**Figure 5.2**). As expected, from the absence of non-specific binding shown previously (**Figures 4.2 and 4.3**), protocell binding was not observed in the REH parental cell line (**Figure 5.1B**), nor did we observe non-targeted (anti-EGFR negative) protocell binding to either REH or REH-EGFR cell lines, as measured by flow cytometry (**Figure 5.3**). To confirm that target specific binding is not cell line specific, we incubated anti-EGFR protocells with Ba/F3 and Ba/F3-EGFR cells for 60 minutes using previously described conditions for REH and REH-EGFR cells. Using fluorescence microscopy, we observed minimal non-specific binding of EGFR-targeted protocells to parental Ba/F3 cells; conversely we observed significant selective binding to Ba/F3-EGFR cells (**Figures 5.4A and 5.4B**). Flow cytometry analyses revealed the targeted protocells had a much greater binding affinity to Ba/F3-EGFR cells compared to the control Ba/F3 parental cell line *in vitro* (**Figures 5.4C and 5.4D**).

To provide an *in vivo* relevant assessment of targeted binding, we evaluated the characteristics of the targeted protocell binding using real-time intravital imaging in the *ex ovo* CAM model of the vasculature. We injected green fluorescent labelled REH or REH-EGFR cells into the CAM and allowed the cells to arrest in the capillary bed (~ 30 minutes). Next, we injected either anti-EGFR targeted or non-targeted red fluorescent protocells into the CAM and imaged protocell flow and binding dynamics at 1-hour, 4-hour, and 9-hour time points. We observed protocells flowing in the blood stream at 1 hour (**Figure 5.5A**), as well as cell specific binding of the anti-EGFR protocells to the REH-

Figure 5.1 – *Flow Cytometry Analysis of EGFR-Targeted Protocell Binding*
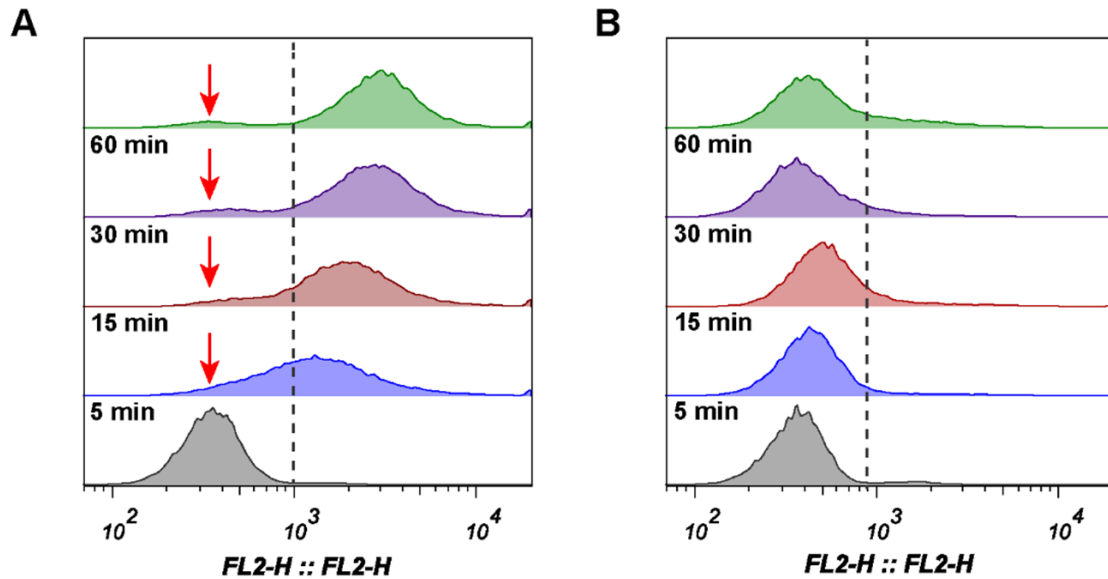
Figure 5.1 – Flow cytometry analysis of A) REH-EGFR and B) parental REH cells incubated with red fluorescent EGFR targeted protocells at multiple time points. A) This data illustrates rapid specific *in vitro* protocell binding to REH-EGFR in as little as 5 minutes in complete medium, and maximal protocell accumulation after 30 minutes. Red arrows highlight non-EGFR expressing population of the engineered REH-EGFR cell line. B) There is minimal non-specific binding to parental REH cells. Adapted and reproduced with permission.[25] © 2016, The American Chemical Society.

Figure 5.2 – *Fluorescence Microscopy Analysis of EGFR-Targeted Protocell Binding*

Figure 5.2 – Fluorescent microscopy analysis of REH-EGFR cells incubated with EGFR-targeted protocells at multiple time points, fixed and stained (blue– nuclei, green–cytoskeleton, red–protocells): A) untreated, B) 5 minutes, C) 15 minutes, D) 30 minutes, and E) 60 minutes. These data illustrate rapid *in vitro* protocell binding in as little as 5 minutes in complete medium, and maximal protocell accumulation after 30 minutes. Scale bar = 5 µm. Adapted and reproduced with permission.[25] © 2016, The American Chemical Society.

Figure 5.3 – *Flow Cytometry Analysis of EGFR-Targeted Protocell Specificity*

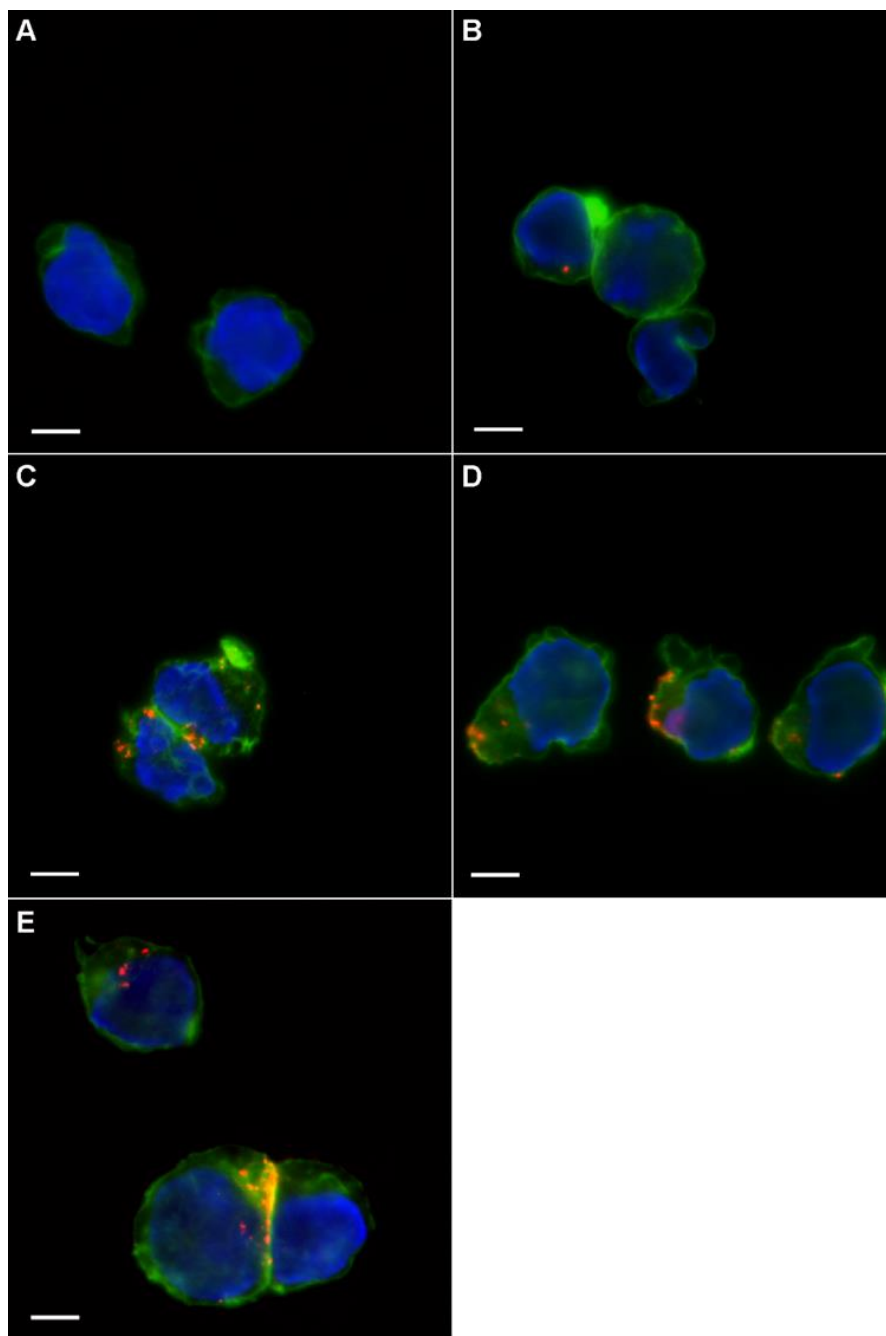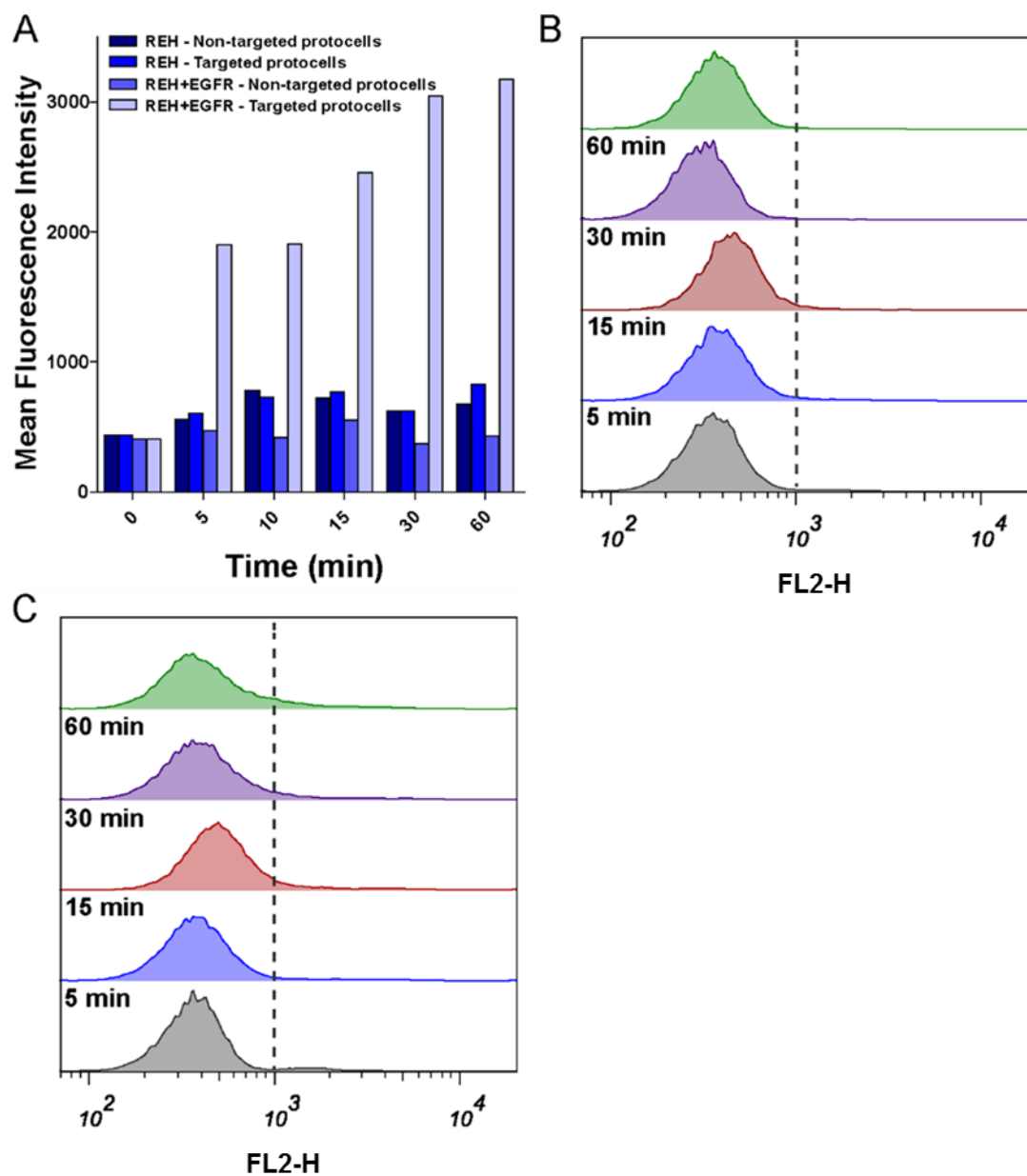**Figure 5.3** – A) Mean fluorescence intensity graph of REH and REH-EGFR cells incubated with either non-targeted or EGFR-targeted protocells shows targeting specificity of EGFR-targeted protocells. B) Flow cytometry analysis of REH-EGFR cells incubated with red fluorescent non-targeted protocells at multiple time points.   C) Flow cytometry analysis of parental REH cells incubated with red fluorescent non-targeted protocells at multiple time points. These data demonstrate the high specific binding of EGFR-targeted protocells to REH-EGFR and low non-specific binding of both targeted and non-targeted to protocells.   Adapted and reproduced with permission.[25]   © 2016, The American Chemical Society.

Figure 5.4 – *Targeted Protocell Specificity for Ba/F3-EGFR Cells*
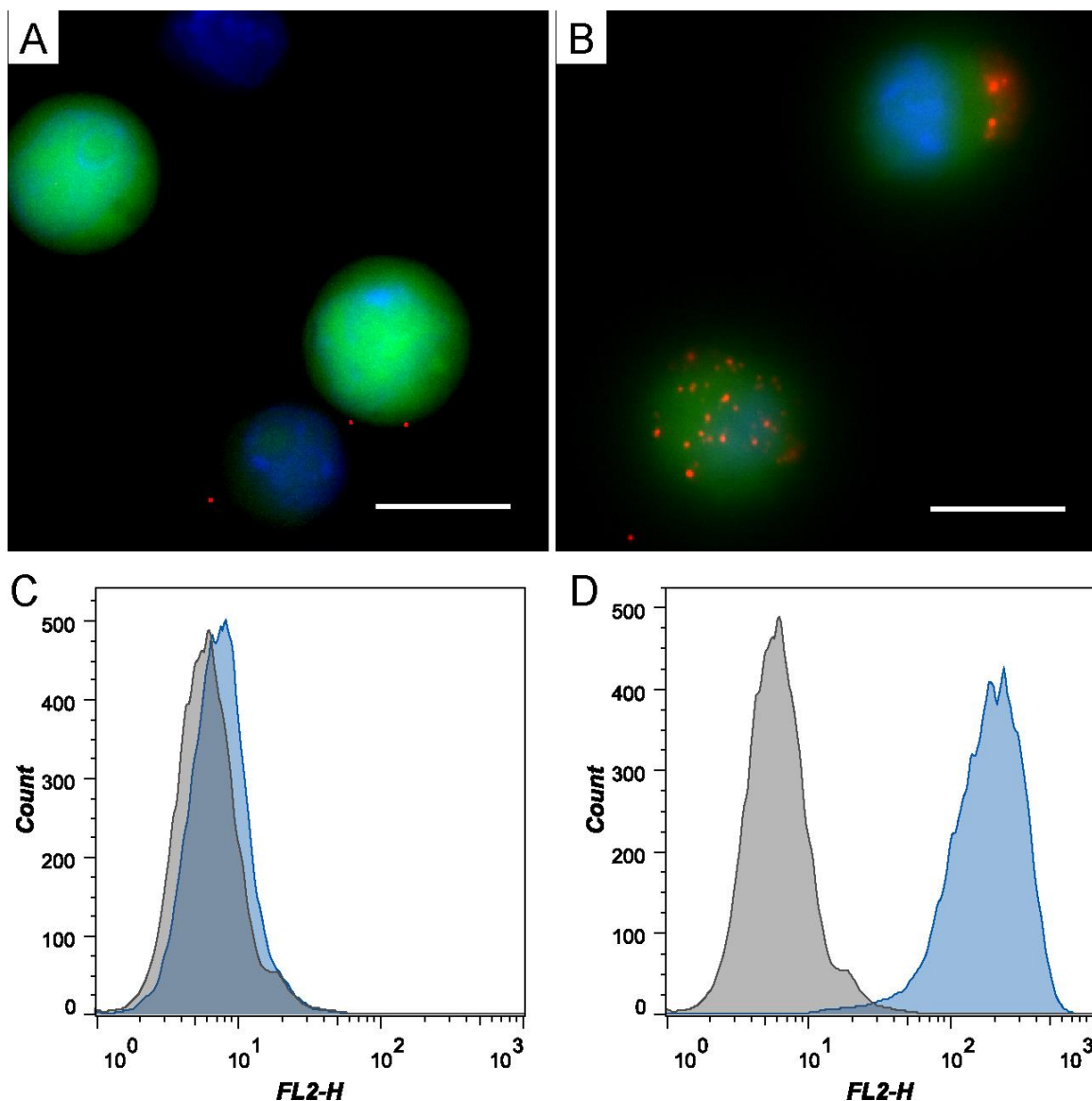
Figure 5.4 – A) Fluorescent microscopy shows minimal EGFR-targeted protocell (red) interactions with a non-EGFR expressing BAF cell line after 1-hour incubation (blue – DAPI stained nuclei, green – phalloidin stained actin), while B) targeted protocells (red) exhibit a high degree of binding to an EGFR expressing BAF cell line. Flow cytometry analysis of protocells incubated with C) BAF and D) BAF-EGFR confirm fluorescent microscopy analysis (grey = no protocell control, blue = EGFR-targeted protocells).   Scale bar = 10 µm. Adapted and reproduced with permission.[25] © 2016, The American Chemical Society. See **Appendix B.3** for 20X magnification of Ba/F3 and Ba/F3-EGFR cells.

Figure 5.5 – *Targeted Protocells bind REH-EGFR Cells in the CAM*
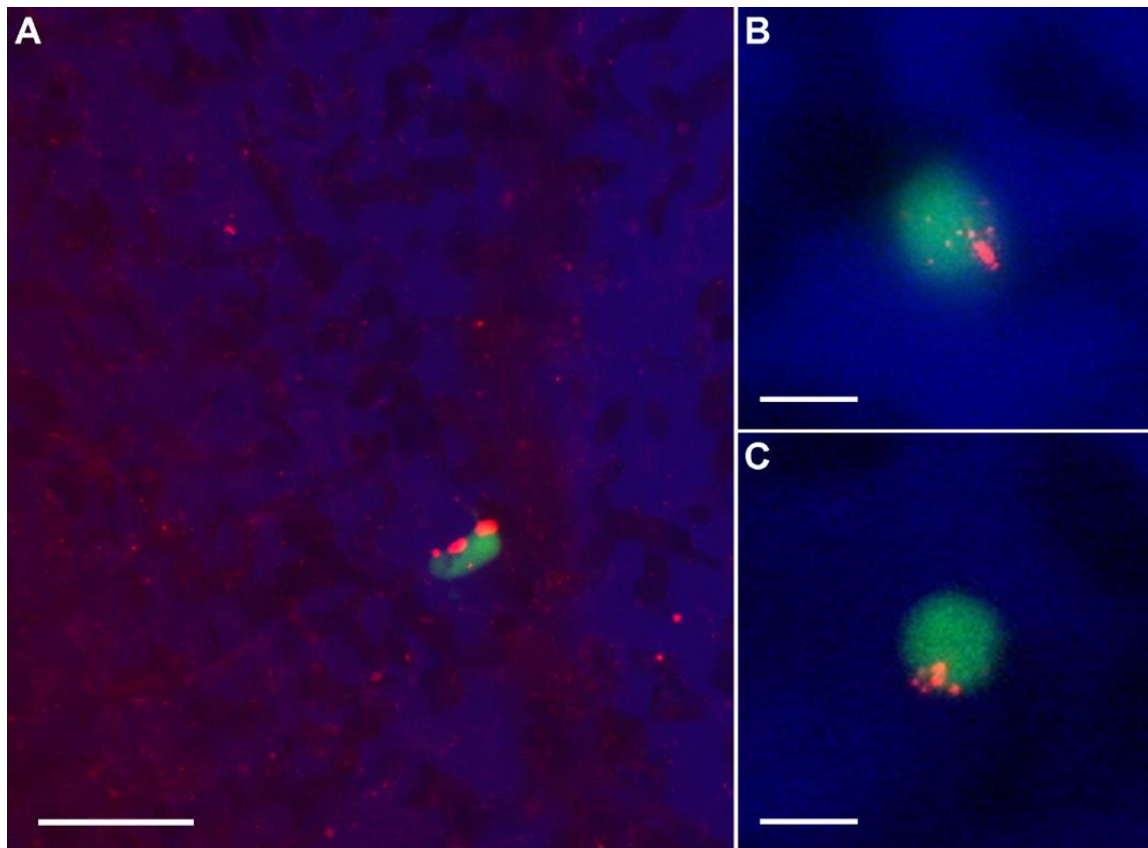
Figure 5.5 – Intravital fluorescent microscopy images acquired *ex ovo* in the CAM model reveal stable circulation of EGFR targeted protocells (red) and binding to REH-EGFR cells (green) in circulation at A) 1-hour, B) 4-hour, and C) 9-hour time points. Systemic protocell circulation is diminished after 4 hours, however, protocells remain associated with target cells for up to 9 hours. Scale bar A) = 50 µm, Scale bars B) and C) = 10 µm.   Adapted and reproduced with permission.[25] © 2016, The American Chemical Society. See additional targeted binding images in **Appendix B.4**.

EGFR cells. While flow had diminished at 4-hour and 9-hour time points, we still observed targeted protocell co-localization with the target cells (**Figures 5.5B and 5.5C**). Since we observed a significant targeted protocell binding to REH-EGFR cells at 1 hour and our *in vitro* experiments showed binding within 5 minutes, we sought to capture targeted protocell binding within a vascularized system in real time; thus, we performed intravital imaging in the CAM immediately after protocell injection and observed several binding events on multiple cells (**Figure 5.6 and** reported in the Supporting Information, Video S2, by Durfee et.al.[25]) within 5 to 10 minutes post protocell injection. To verify that protocell binding was indeed EGFR specific, we tested anti-EGFR targeted protocells with REH cells and non-targeted protocells with REH and REH-EGFR cells lines and found similar flow patterns for the protocells at 1-hour time points; however, the protocells did not interact with the leukemia cells (**Figures 5.7, 5.8, and 5.9**) providing further support for our targeting methodology. As a final step, we investigated whether EGFR-targeted protocell binding was influenced by the particular engineered cell line. We injected Ba/F3-EGFR cells *ex ovo*, followed by anti-EGFR protocell injection, and observed target cell specific binding at 10 minutes and 20 hours (**Figure 5.10**). Based on these findings, we are confident that we have engineered biologically stable protocells with a high degree of specificity evaluated both *in vitro* and by intravital imaging in the CAM model to bind to individual target cells.

Figure 5.6 – *Still Frames Capture Protocell Binding Events in CAM*
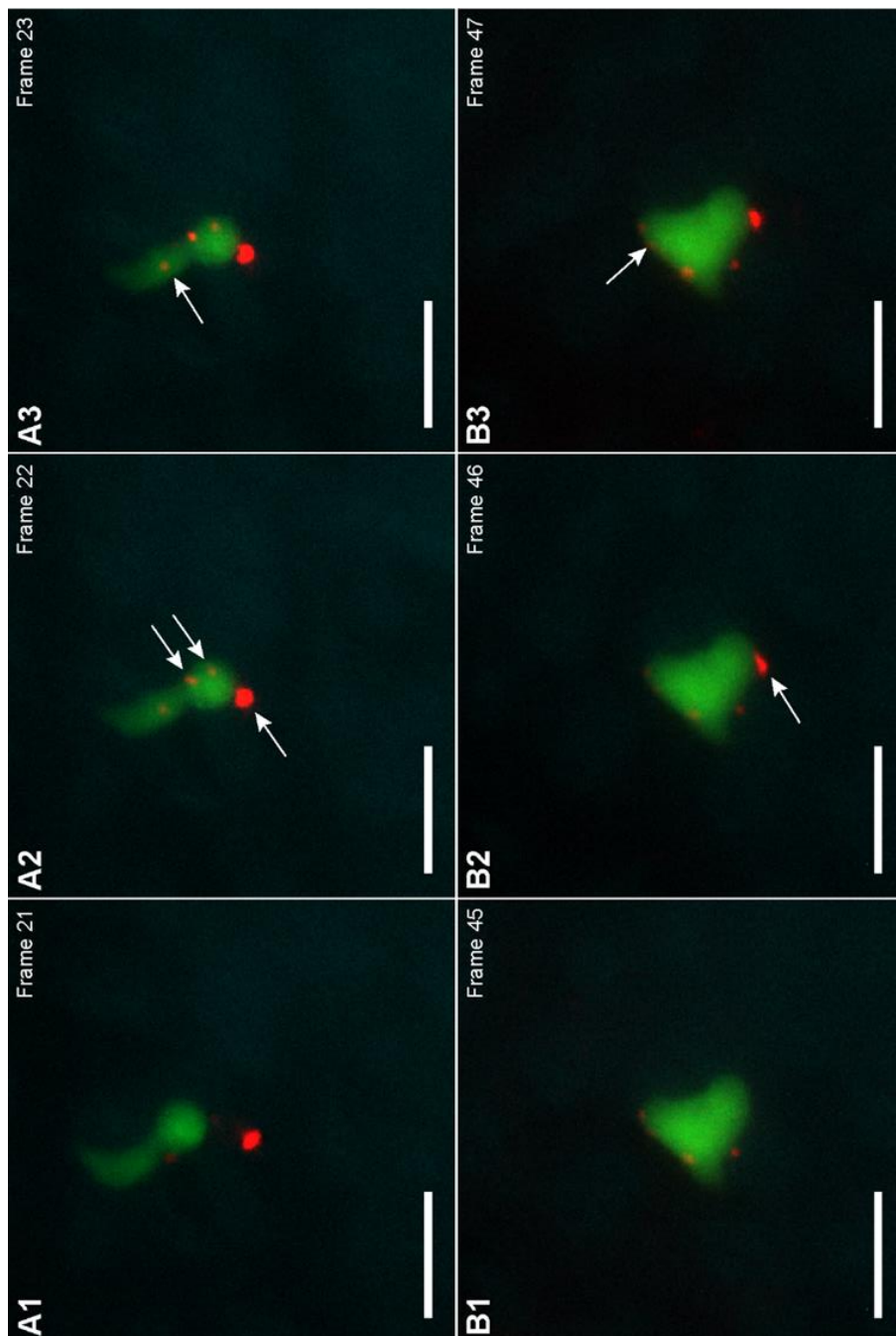
Figure 5.6 – Still frames which capture red fluorescent targeted protocell binding to green fluorescent labeled REH-EGFR cells captured in successive frames from Video S2 (reported in the Supporting Information, by Durfee et.al.[25]) with arrows indicating points where red fluorescent protocells appear to bind and remain associated with the cells. Frame rate = 4.35 seconds. Scale bar = 20 μm. Adapted and reproduced with permission.[25] © 2016, The American Chemical Society.

Figure 5.7 – *Targeted Protocells Avoid REH Cells in the CAM*

Figure 5.7 – Intravital fluorescent microscopy images acquired *ex ovo* in the CAM model reveal stable circulation of EGFR-targeted protocells (red) but no association with parental REH cells (green) in circulation at A) 1-hour, B) 4-hour, and C) 9-hour time points. Scale bar (left) = 50 µm, Scale bars (right top and bottom) = 10 µm. Adapted and reproduced with permission.[25] © 2016, The American Chemical Society.

Figure 5.8 – *Non-targeted Protocells Avoid REH Cells in the CAM*
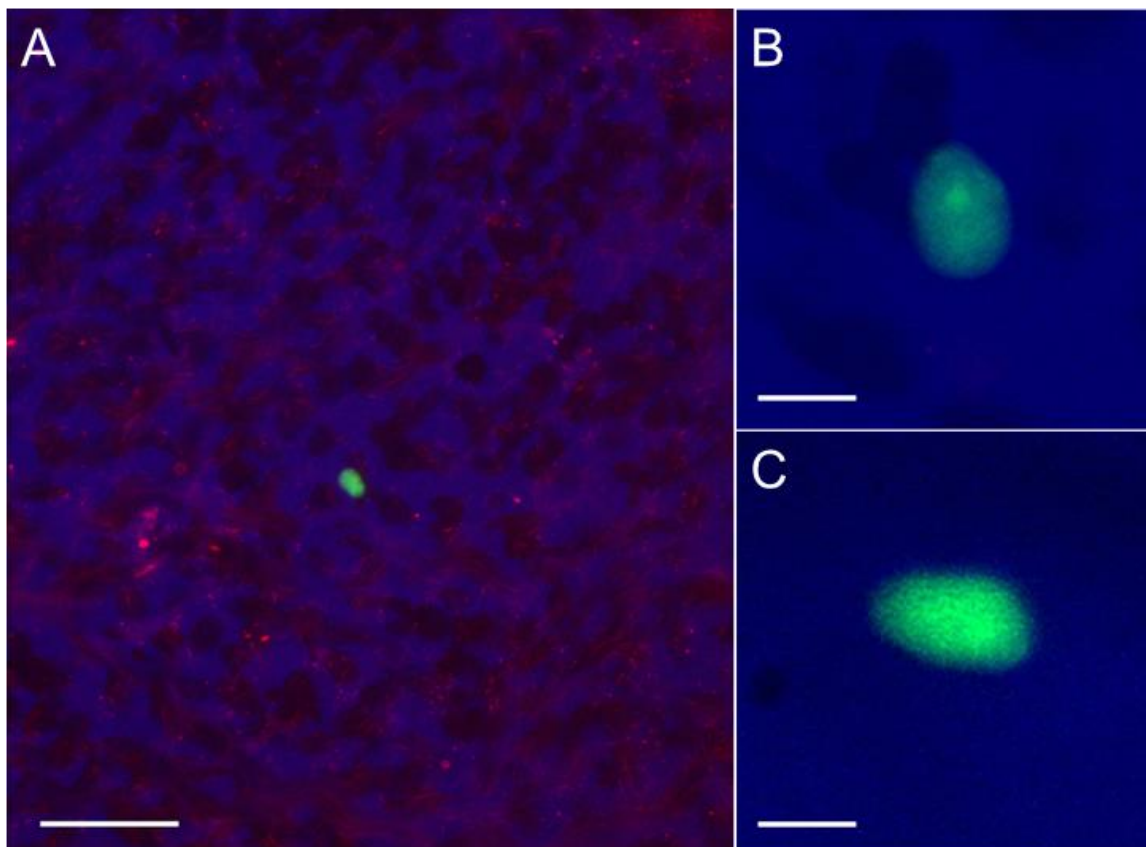
Figure 5.8 – Intravital fluorescent microscopy images acquired *ex ovo* in the CAM model reveal stable circulation of non-targeted protocells (red) but no association with parental REH cells (green) in circulation at A) 1-hour, B) 4-hour, and C) 9-hour time points. Scale bar (left) = 50 μm, Scale bars (right top and bottom) = 10 μm. Adapted and reproduced with permission.[25] © 2016, The American Chemical Society.

Figure 5.9 – *Non-targeted Protocells Avoid REH-EGFR Cells in the CAM*
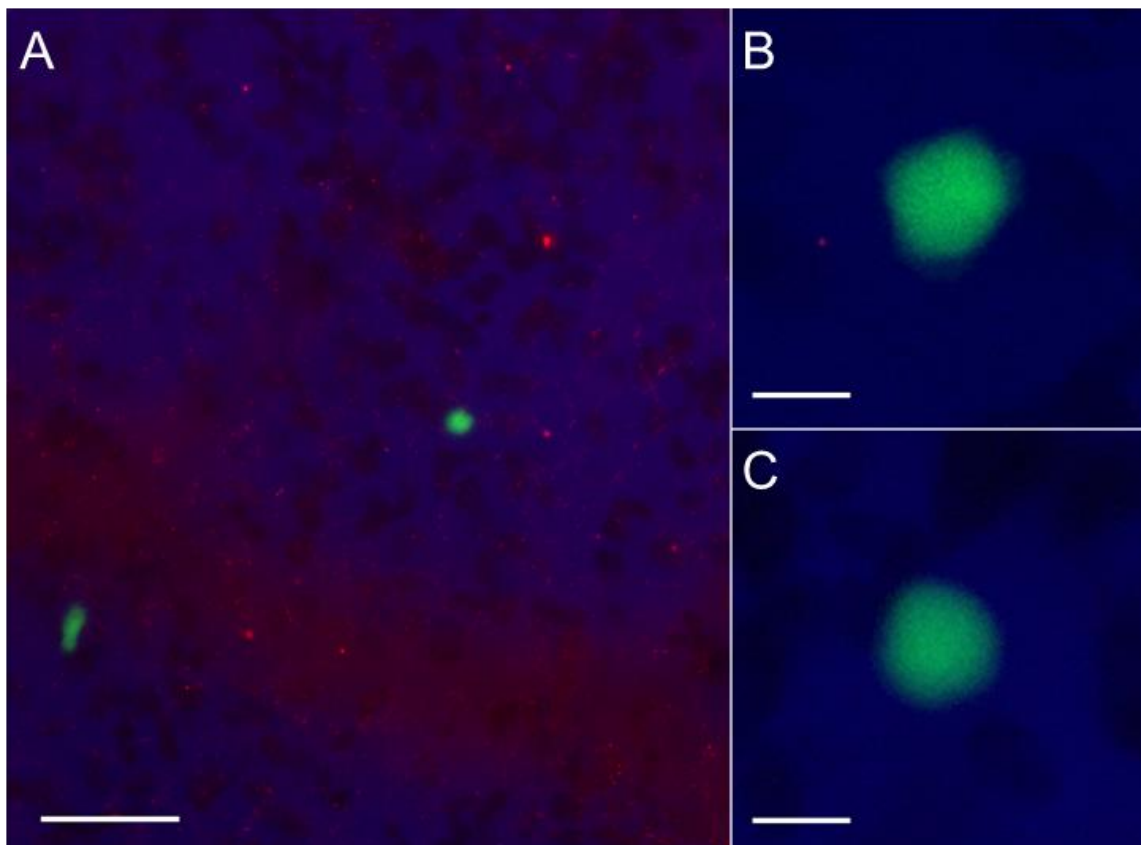
Figure 5.9 – Intravital fluorescent microscopy images acquired *ex ovo* in the CAM model reveal stable circulation of non-targeted protocells (red) but no association with REH-EGFR cells (green) in circulation at A) 1-hour, B) 4-hour, and C) 9-hour time points. Scale bar (left) = 50 μm, Scale bars (right top and bottom) = 10 μm. Adapted and reproduced with permission.[25] © 2016, The American Chemical Society.

Figure 5.10 – *Targeted Protocells bind Ba/F3-EGFR Cells in the CAM*

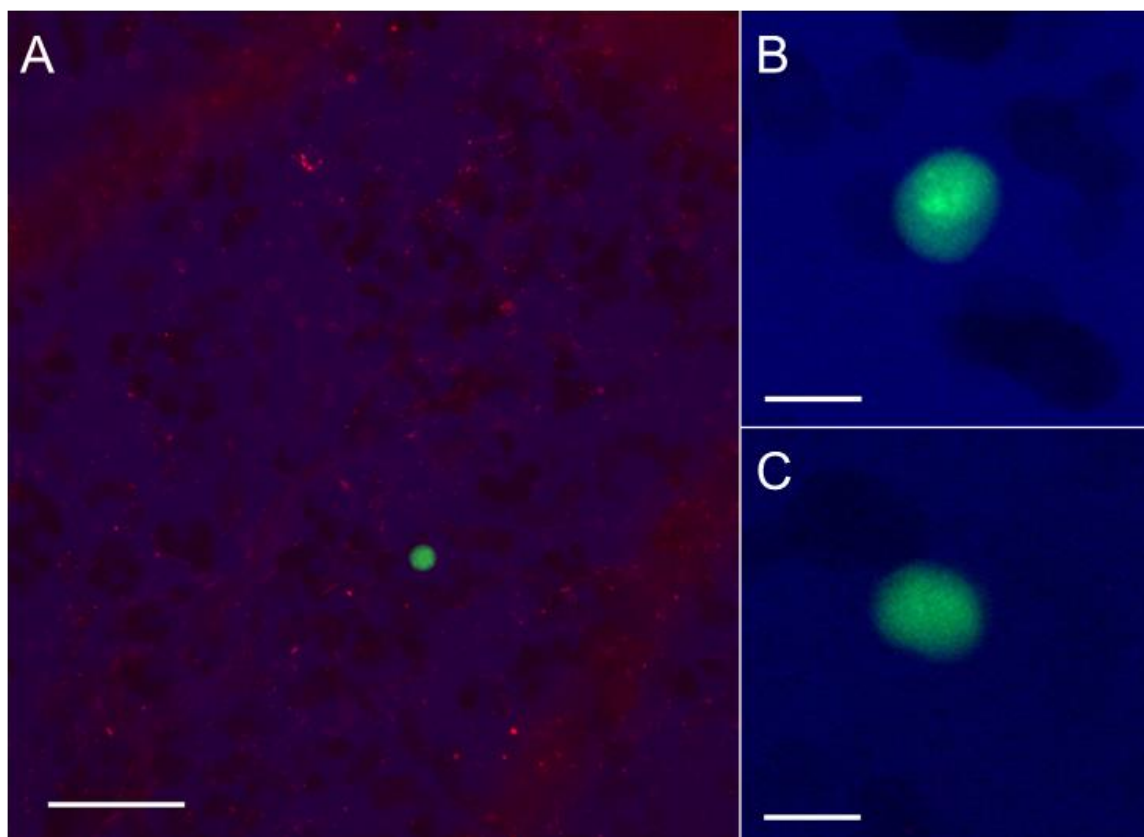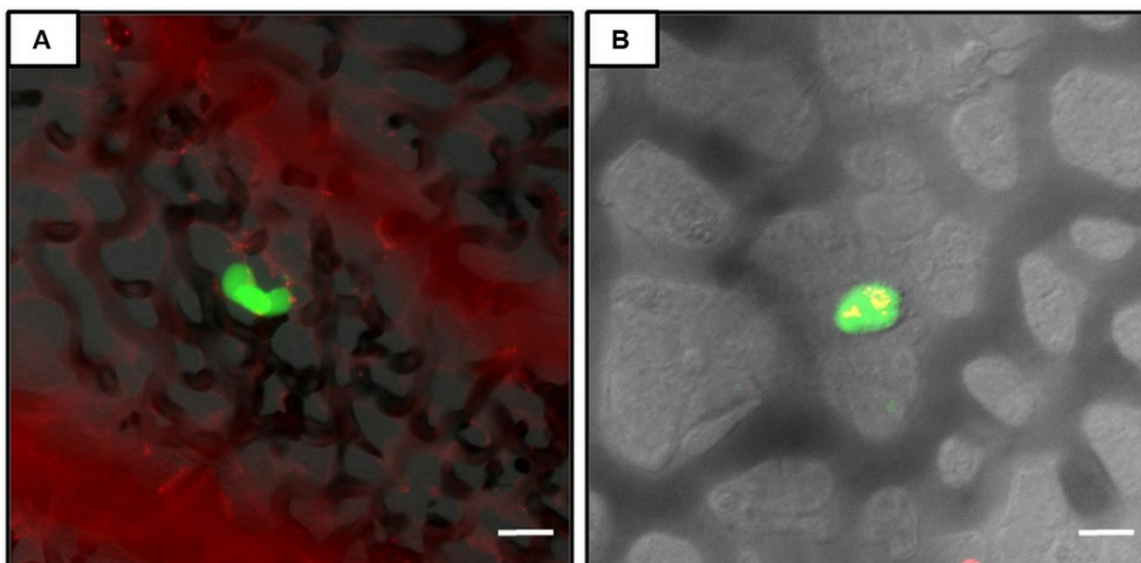**Figure 5.10** – Intravital fluorescent microscopy images acquired in the CAM model show: A) stable circulation of EGFR-targeted protocells (red) and the initial stages binding to Ba/F3-EGFR (green) 10 minutes post injection; B) maintained association of EGFR-targeted protocells (yellow, due to merged green and red) with Ba/F3-EGFR (green) 20 hours post-injection. Scale bar = 10 µm. Adapted and reproduced with permission.[25] © 2016, The American Chemical Society.

5.2.2 Protocell Cargo Loading and Delivery to Targeted Cells

Next, we evaluated the cargo loading and targeted delivery characteristics of monosized protocells both *in vitro* and *ex ovo*. As a surrogate for a true drug, we chose YO-PRO®-1, a green fluorescent membrane impermeable molecular cargo. We added YO-PRO®-1 to red-fluorescent mMSNPs, fused liposomes, and conjugated anti-EGFR targeting components to the surface following the steps illustrated in **Figure 2.1**. Anti-EGFR targeted protocells loaded with YO-PRO®-1 exhibited similar size and zeta potential characteristics to unloaded protocells assembled under identical conditions (**Table 5.1**). We calculated a 25 % loading efficiency by disrupting the SLB of loaded protocells with a detergent and measuring the fluorescence intensity of YO-PRO®-1 extracted in DMSO (**Details in – 5.3.8 Cargo loading and release kinetics and Appendix A.4**). Next, we assayed targeted protocell internalization as a measure of time using an acid wash technique to remove surface bound protocells at specific time points. Using flow cytometry and fluorescence microscopy, we found that anti-EGFR targeted protocell binding and internalization occurs within 1 hour (**Figures 5.11A and 5.12**); however, cargo release as measured by intracellular green fluorescent cargo diffusion, occurred more slowly (**Figures 5.11B, and 5.12**). To assess protocell targeted cell specific killing, *in vitro*, we chose gemcitabine (GEM) as a model anti-cancer cytotoxic agent due to its low molecular weight, which allows it to access and adsorb to the high surface area mMSNP mesostructure, as well as its relative membrane impermeability,[26, 27] which allows the SLB to essentially seal the cargo in the protocells and to

Table 5.1 – *Unloaded and Loaded Protocell Size and Zeta Potential Analysis*

Sample	Medium	Hydrodynamic Diameter (nm)	PdI	Zeta potential (mV)
EGFR-Targeted Protocells				
*Unloaded	PBS	156.6 ± 4.9	0.167 ± 0.022	-4.0 ± 1.3
*YO-PRO®-1 Loaded	PBS	151.8 ± 2.0	0.198 ± 0.015	-5.0 ± 0.6
**Unloaded	PBS	178.9 ± 1.8	0.206 ± 0.005	--
**GEM Loaded	PBS	167.8 ± 3.1	0.182 ± 0.010	--

Table 5.1 – Hydrodynamic size characteristics and zeta potential measurements of loaded and unloaded targeted protocells. Multiple batches were synthesized, superscript (* and **) denotes mMSNP cores prepared from the identical batches. Data represent mean ± SD, n = 3. Adapted and reproduced with permission.[25] © 2016, The American Chemical Society.

Figure 5.11 – *Flow Cytometry Analysis of EGFR-Targeted Protocell Internalization*
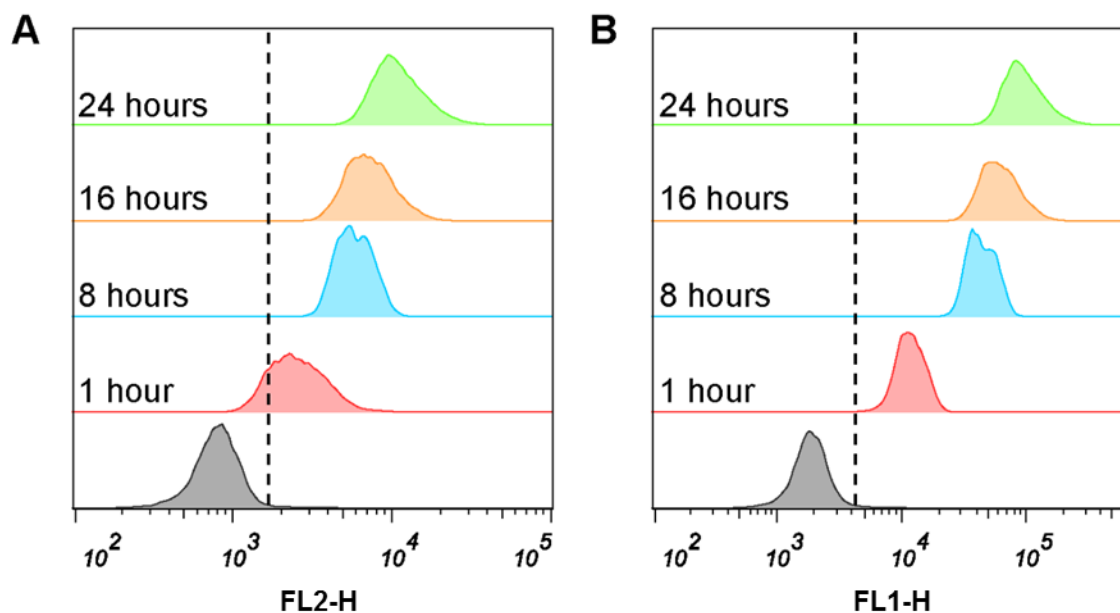
Figure 5.11 – Flow cytometry analysis to assess internalization of A) red fluorescent EGFR-targeted protocells by REH-EGFR cells *in vitro* at multiple time points and B) delivery of model drug, YO-PRO®-1, a green cell impermeant dye. After each time-point, cells were acid washed to strip surface bound protocells then fixed. These data show an increase in the internalization of protocells and release of cargo with increasing incubation time. Adapted and reproduced with permission.[25] © 2016, The American Chemical Society.

Figure 5.12 – Fluorescence Microscopy *of Internalization and Cargo Release*
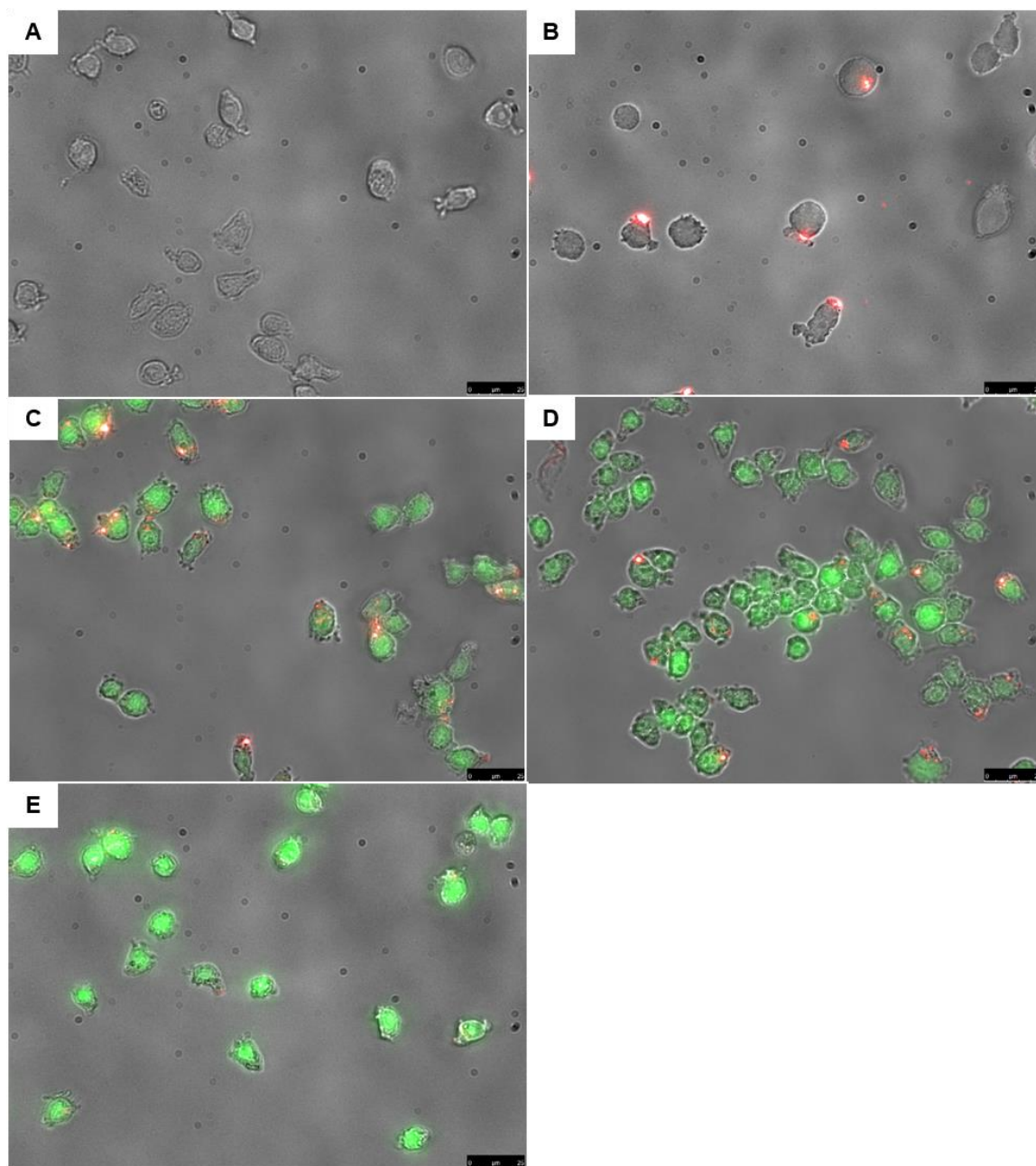
Figure 5.12 – Fluorescence microscopy analysis to assess delivery of model drug, YO-PRO®-1 a green cell impermeant dye, *via* targeted protocells to REH-EGFR cells at multiple time points. After each time-point, cells were acid washed to strip surface bound protocells then fixed. REH-EGFR cells (DIC– cell structure, red–protocells, green–YO-PRO®-1) at A) untreated, B) 1-hour, C) 8-hour, D) 16-hour, and E) 24-hour incubation times. These data illustrate internalization of protocells within 1 hour and the release of YO-PRO®-1 cargo which appears to localize in the nucleus of the target cells at later time points. Scale bar = 25μm.   Adapted and reproduced with permission.[25] © 2016, The American Chemical Society.

prevent off-target effects due to drug leakage. Moreover, GEM requires a nucleoside transporter to cross the cell membrane, and reduced expression of the nucleoside transporter is known to be associated with gemcitabine resistance.[26, 27] Furthermore, the plasma half-life of GEM is only 8-17 minutes due to rapid conversion to an inactive form that is excreted by the kidneys;[26] therefore, GEM requires frequent doses to overcome this clearance rate. Thus, encapsulation of GEM within a targeted protocell may overcome many of the challenges associated with conventional GEM-based therapy.

We assessed cargo delivery using REH and REH-EGFR cells incubated with GEM loaded anti-EGFR protocells *in vitro*. To prepare GEM loaded, anti-EGFR targeted protocells, we suspended mMSNPs in a solution of GEM prepared in H_2O then assembled protocells by fusing GEM-soaked mMSNPs with liposomes following the steps illustrated in **Figure 2.1**. The supernatant from each step was collected and combined; the GEM content was determined by measuring the absorbance (265 nm) using a microplate reader. Our described GEM loading strategy resulted in a calculated 15 wt. % GEM encapsulation (**Details in – 5.3.8 Cargo loading and release kinetics and Appendix A.4**). We found cargo loading did not influence the final targeted protocell size (**Table 5.1**), a result consistent with GEM loading of the internal mesoporosity. To examine the drug release profile under simulated lysosomal conditions, we prepared GEM loaded protocells in PBS, then dialyzed the samples in either PBS (pH 7.4) or 1 M citrate buffer (pH 5.0) for 72 hours at 37 °C. We measured the absorbance (265 nm) of supernatant collected at several

time points to determine the quantity of GEM released under these conditions. We observed a greater total drug release percentage at pH 5.0 (~ 30 %) compared to pH 7.4 (~ 14 %) after 72 hours (**Figure 5.13**). We also observed a significant hydrodynamic size increase at 48 hours in pH 5.0, correlating with the increase in drug release observed at the same time point, while protocells maintain size stability at pH 7.4 under the same experimental conditions (**Figure 5.13**). These data suggest that drug release is increased at a lower pH primarily due to SLB destabilization as evidenced by aggregation. However, we are only examining the influence of a single variable (pH), while other conditions exist in the lysosomal pathway including degradative enzymes, for example phospholipase A2,[28] which could affect drug release. Therefore, we next examined the functional release of GEM as a measure of cell viability *in vitro*. To evaluate the target specific drug delivery, we incubated REH and REH-EGFR cells with increasing concentrations of anti-EGFR GEM-loaded protocells in complete media under normal culturing conditions. We observed a distinct EGFR-target specific decrease in viability correlating to an increase in targeted protocell concentration (**Figure 5.14A**). Finally, we assessed the killing specificity of free-GEM, and observed decreased cell viability with increasing GEM concentration in a non-specific manner (**Figure 5.14B**). To verify that the cargo is responsible for the killing as opposed to the protocell itself, we incubated anti-EGFR targeted protocells with REH and REH-EGFR cells with increasing concentrations and observed no loss in viability for up to 200 µg/mL of protocells (**Figure 5.14C**). Worth mentioning, a subset of REH-EGFR engineered cells

Figure 5.13 – *Size Stability and GEM Release at pH 7.4 and pH 5.0*
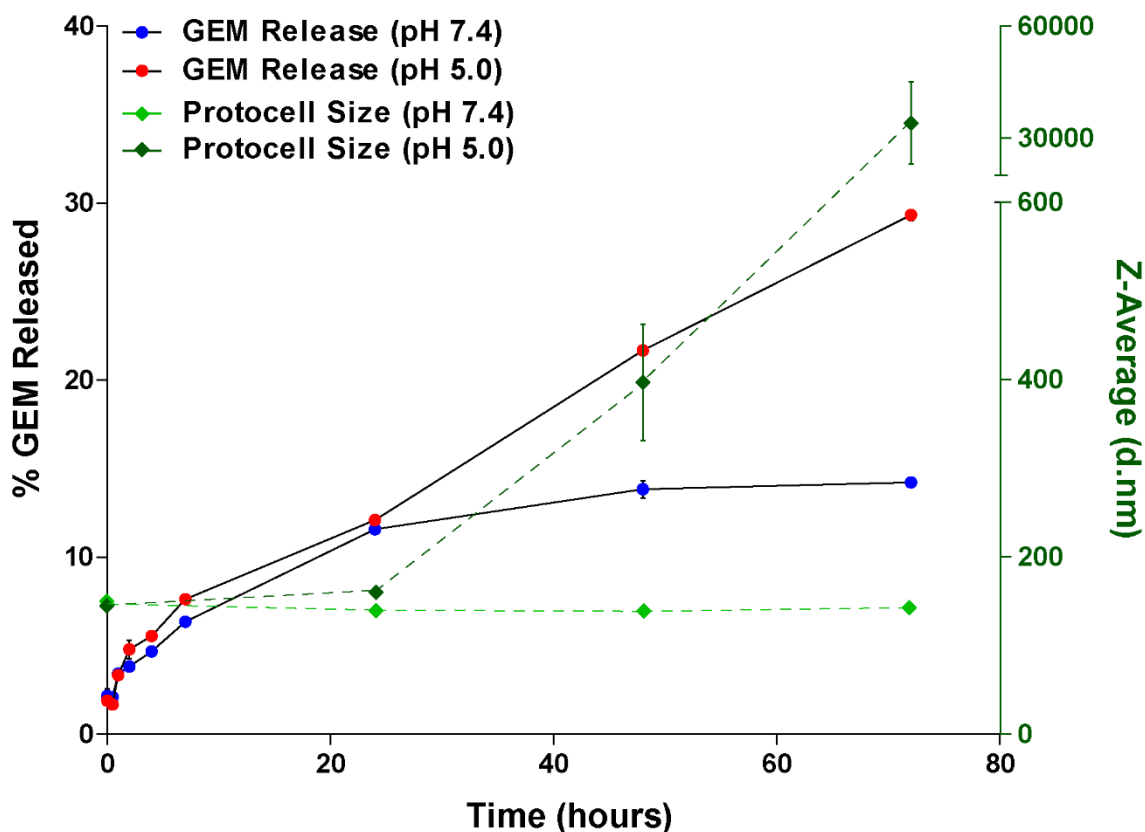
Figure 5.13 – Comparison of drug release percentage (left axis) and protocell size change (right axis) for GEM-loaded protocells maintained in extracellular physiological conditions (PBS, pH 7.4) and simulated lysosomal conditions (citrate buffer, pH 5.0) for 72 hours at 37 °C. We observe increased GEM release at pH 5.0 and significant size increase at 48 hours with a 228-fold size increase at 72 hours suggesting protocell destabilization and aggregation due to lower pH conditions. Drug release at pH 5.0 correlates with protocell size increase over time. Protocells maintain size stability at pH 7.4 for 72 hours at 37 °C, however they do appear to release ~ 14 % GEM after 72 hours. Adapted and reproduced with permission.[25] © 2016, The American Chemical Society.

Figure 5.14 – *EGFR-Targeted Drug Delivery and Cell Viability Assessment*
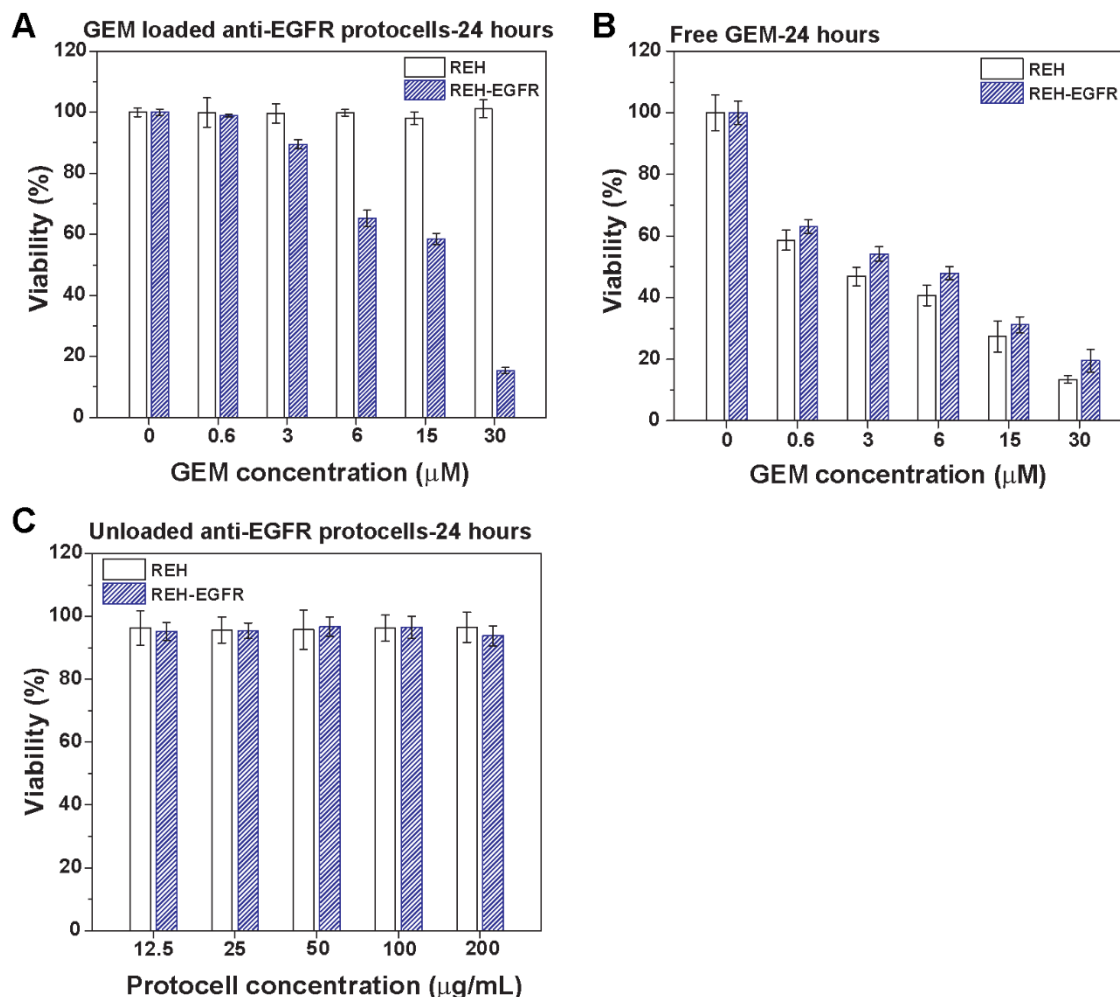
Figure 5.14 – A) Maintained viability of REH cells and decrease in viability of REH-EGFR cells with increasing concentration of GEM loaded EGFR-targeted protocells. REH and REH-EGFR cells incubated with protocells from 0 to 50 ug/ml for 1 hour, then washed to remove unbound protocells. Viability was assessed at 24 hours. B) Loss in cell viability of REH and REH-EGFR cells with exposure to increasing concentration of free GEM. Both cell lines were incubated with free GEM from 0 to 30 uM for 1 hour, then washed to remove unassociated free drug. Viability was assessed at 24 hours. Viability data highlights target specific delivery of cytotoxic cargo using monosized protocell platform and the non-specific cytotoxicity of free drug under the same conditions. C) Cell viability of parental REH and REH-EGFR cells incubated with increasing concentrations of cargo-free anti-EGFR protocells for 1 hour followed by washing to remove unbound protocells. Viability was assessed at 24 hours. Viability data supports the biocompatibility of the monosized protocell platform. Data represents mean ± SD, n = 3. Adapted and reproduced with permission.[25] © 2016, The American Chemical Society.

appear to lose EGFR expression over time (**Figure 5.15 and Figure 5.1A – red arrow**); therefore, the remaining viable cells in the maximum dose tested (50 µg protocells / 30 µM GEM) (**Figure 5.14A**) are likely to be EGFR negative.

To test targeted binding and cargo delivery in a complex living system, we injected the CAM with fluorescent labelled REH-EGFR cells followed after 30 minutes by injection of YO-PRO®-1 loaded anti-EGFR protocells. Prior to intravital imaging a lectin vascular stain was injected to provide contrast in the blood vessels. Intravital fluorescent imaging of the steps of binding, internalization, and cargo release was performed at 4 hours and 16 hours post *ex ovo* injection based on *in vitro* experiments that showed binding in as little as five minutes **(Figures 5.1A and 5.2B)** but YO-PRO®-1 delivery and release to the cytosol to occur between 1 hour and 8 hours **(Figure 5.12)**. **Figure 5.16A** shows target specific binding to an individual REH-EGFR cell trapped within the CAM vasculature 4 hours post injection with no evidence of cargo release. **Figure 5.16B** shows targeted binding to an individual REH-EGFR cell 16 hours post injection, where YO-PRO®-1 is dispersed throughout the cell similar to the *in vitro* results (**Figure 5.12**). Additional figures in **Appendix B.5** illustrate further evidence supporting targeted delivery *ex ovo.* To better illustrate the targeted protocell binding, internalization, and cargo release at 16 hours, we imaged 0.25 µm sections of a targeted cell and stacked the images into a video (Video S3) reported in the Supporting Information, by Durfee et.al.[25]

We recognize the need to assess the targeted killing of REH-EGFR cells by anti-EGFR GEM-loaded protocells in an animal model; however, determining

Figure 5.15 – *Evidence of EGFR Expression Loss in REH-EGFR Cells*
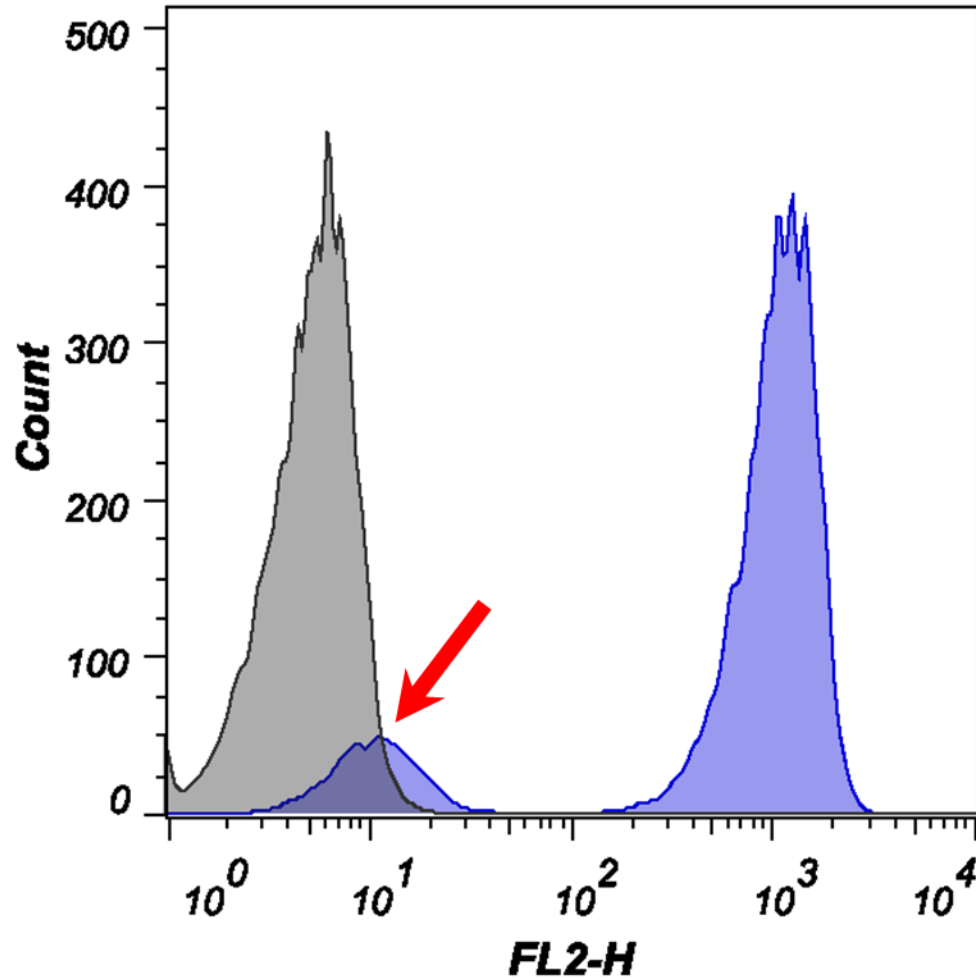
Figure 5.15 – Flow cytometry analysis of EGFR expression in REH-EGFR cells as detected by binding of a PE-conjugated anti-EGFR antibody. Right-shifted histogram (blue) shows a majority of the population to be expressing EGFR. However, a minority population (red arrow) does not shift correspondingly likely due to REH-EGFR cells that have lost EGFR expression. Adapted and reproduced with permission.[25] © 2016, The American Chemical Society.

Figure 5.16 – *Targeted Cargo Delivery Ex Ovo*
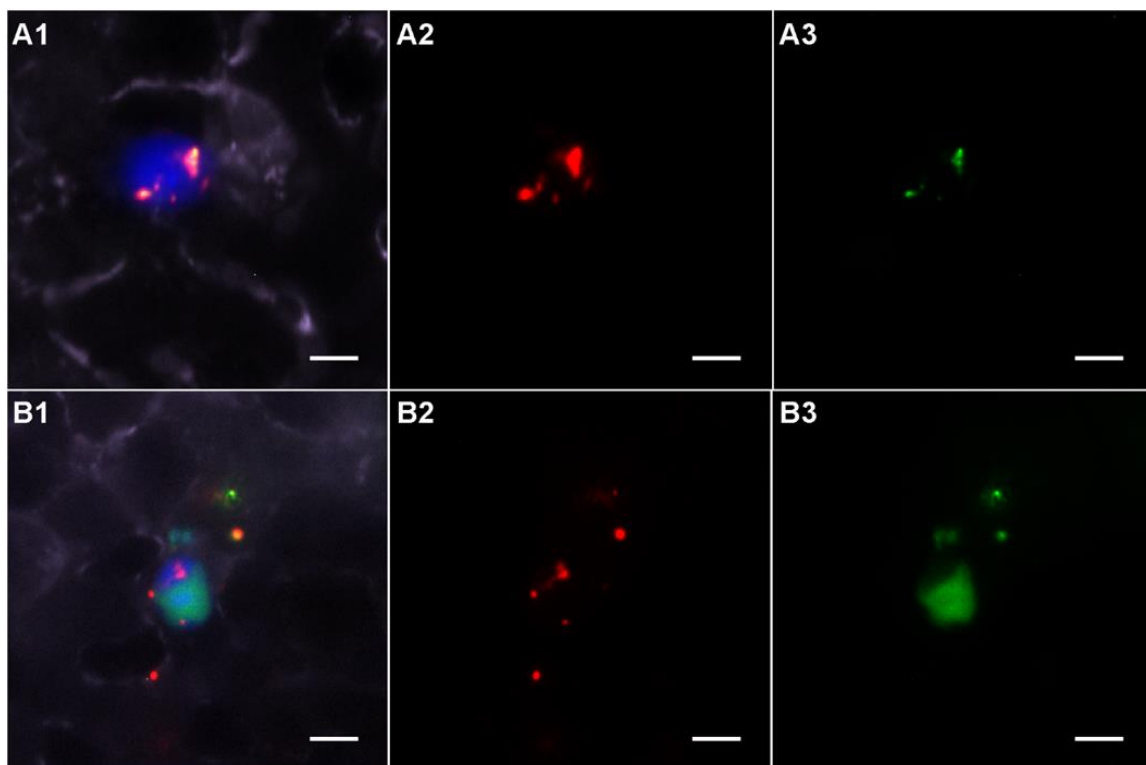
Figure 5.16 – Intravital fluorescent microscopy images acquired *ex ovo* in the CAM model showing green YO-PRO®-1 cell impermeant cargo loaded, red fluorescent EGFR-targeted protocells binding to and releasing cargo within REH-EGFR cells in a live animal model. A1) Fluorescent overlay of (blue) REH-EGFR cell, (red) protocell, (green) YO-PRO®-1 cargo, (lavender) lectin vascular stain at 4 hours post injection. A2) Red channel shows protocell fluorescence, and A3) green channel shows YO-PRO®-1 fluorescence associated with the protocells. However, after 16 hours, B1) fluorescent overlay shows release of YO-PRO®-1 cargo within the cell. B2) Red channel shows protocell fluorescence at 16 hours and B3) green channel shows YO-PRO®-1 release into the cell. Images acquired at 63x magnification, Scale bar = 5 μm. Adapted and reproduced with permission.[25] © 2016, The American Chemical Society. See **Appendix B.5** for more images of YO-PRO®-1 delivery to REH-EGFR cells in the CAM.

conclusively that protocells are directly responsible for killing target cells in the *ex ovo* system is difficult, since many of the cells are eliminated by the chick immune system and possess a limited life-span in this host. Further targeted delivery studies in a murine leukemia model to test protocell co-localization and disease elimination must be evaluated. Nonetheless, our demonstrated highly specific targeted drug delivery *in vitro* combined with surrogate drug delivery *ex ovo* provide compelling evidence for the single-cell targeting utility of the monosized protocell therapeutic delivery platform.

5.2.3 Testing the "Plug-and-Play" Capability of Our Cell-Targeting Strategy

After confirmation that our targeting strategy was not influenced by the type of cell line used, we were interested in determining the ease of switching cell-targets, in an effort to engineer a disease agnostic nanocarrier platform. To achieve this goal, as a model system, we chose a human T cell leukemia cell line (MOLT4) that was engineered to express the CD19 receptor (MOLT4-CD19) and we compared protocell interactions with MOLT4-CD19 cells to the parental (CD19-negative) cell line so as to have a matched negative control for our experiments.   In addition, we tested binding on a native CD19 expressing human B cell precursor leukemia (NALM6).

We used the same NeutrAvidin/biotin targeting chemistry illustrated in **Figure 2.1** and the same amine functionalized SLB described earlier (**Table 2.1**), however, we substituted Biotin Anti-Human CD19 Antibody (Biolegend, CA) or custom synthesized Biotin Anti-CD19 single chain variable fragment (scFv)

(GenScript, NJ) in place of the Biotin Anti-EGFR Antibody. To examine targeting specificity, we compared protocell interactions with MOLT4 parental cell line controls, MOLT4-CD19, and NALM6 cell lines.

To assess the kinetics of CD19-targeted protocell binding, we incubated either anti-CD19 antibody-labelled protocells or anti-CD19-scFv-labelled protocells with MOLT4 parental and MOLT4-CD19 cells for various time points *in vitro*. We observed detectable binding of the antibody-labelled protocells within 5 minutes and maximal binding at 240 minutes of incubation in complete media under normal cell culture conditions as assessed by flow cytometry (**Figure 5.17**). By fluorescence microscopy, we observed comparable cell-specific binding *in vitro* of both antibody- and scFv-labelled protocells (**Figure 5.18**). Similar to the non-specific binding profile shown previously (**Figures 4.2 and 4.3**), protocell binding was not observed in the MOLT4 parental cell line (**Figure 5.19**). We also observed cell-specific targeting using antibody-labelled protocells incubated with NALM6 cells for 1 hour in complete media, under normal cell culture conditions (**Figure 5.20**). Therefore, we have demonstrated *in vitro* targeted binding in multiple cell lines, with multiple targeting ligands.

Next, we loaded untargeted, antibody-labelled, and scFv-labelled protocells with YO-PRO®-1 and evaluated targeting and delivery *in vitro* by incubating with MOLT4-CD19 cells at multiple time-points. We loaded protocells with YO-PRO®-1 as described previously in **5.2.2 Protocell Cargo Loading and Delivery to Targeted Cells**. Next, we incubated protocells with MOLT4-CD19 cells in complete media under normal cell culture conditions for 1 hour, 2 hours, 4

Figure 5.17 – *Flow Cytometry Analysis of CD19-Targeted Protocell Specificity*
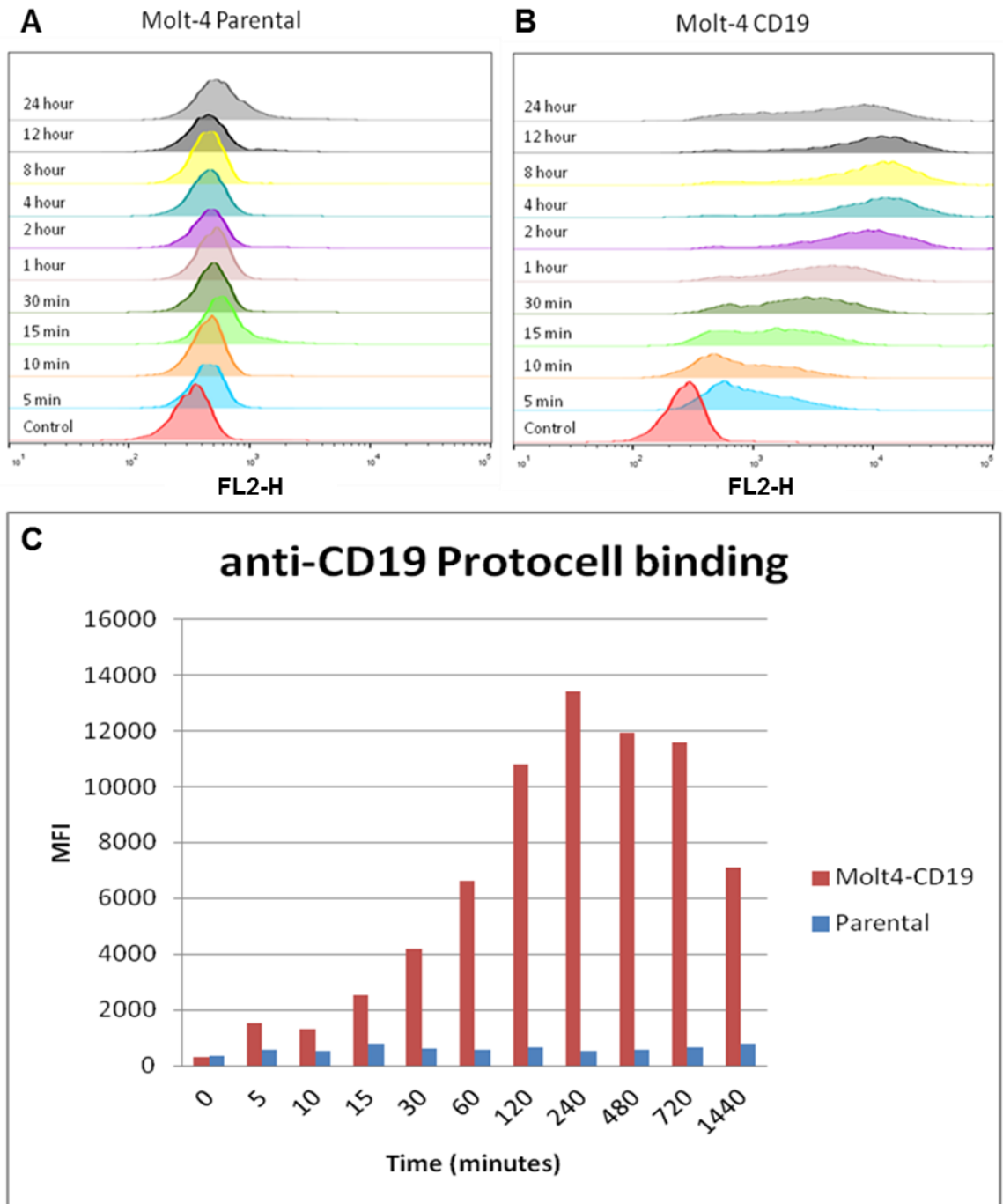
Figure 5.17 – Flow cytometry analysis of A) parental MOLT4 and B) MOLT4-CD19 cells incubated with red fluorescent CD19 targeted protocells at multiple time points. This data illustrates rapid specific *in vitro* protocell binding to MOLT4-CD19 in as little as 5 minutes in complete medium, and maximal protocell accumulation after 240 minutes. C) Mean fluorescence intensity graph of protocell bind further illustrates CD19-targeted protocell specificity.

Figure 5.18 – *Comparable Antibody- and scFv-modified Protocell Binding to MOLT4-CD19 Cells In Vitro*

Figure 5.18 – Fluorescent microscopy analysis of MOLT4-CD19 cells incubated with either CD19 untargeted, antibody-targeted, or scFv-targeted protocells at multiple time points, fixed and stained (blue–cells, red–protocells). These data illustrate rapid *in vitro* protocell binding in complete medium with a high degree of specificity.

Figure 5.19 – *CD19-Targeted Protocell Binding to MOLT4-CD19 Cells*
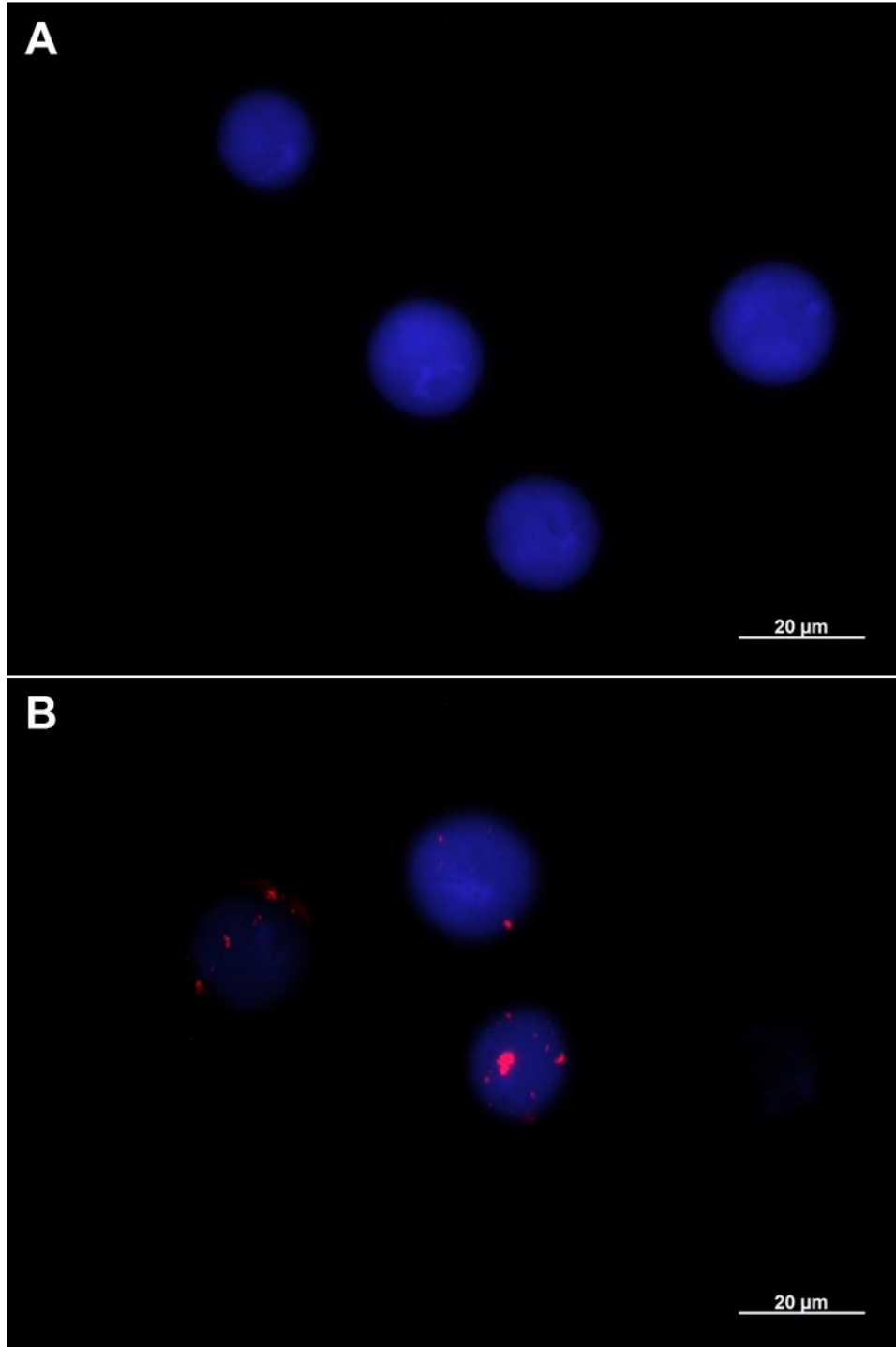
Figure 5.19 – A) Fluorescent microscopy shows absent CD19-targeted protocell (red) interactions with parental MOLT4 cell line after 1-hour incubation (blue – CMFDA live cell stain – false colored blue), while B) targeted protocells (red) exhibit a high degree of binding to MOLT4-CD19 cell line.

Figure 5.20 – *CD19-Targeted Protocell Binding to NALM6 Cells*

Figure 5.20 – A) Fluorescent microscopy shows absent untargeted protocell (red) interactions with NALM6 cell line (green) after 1-hour incubation 20x magnification, B) 63x magnification, while C) CD19-targeted protocells (red) exhibit a high degree of binding to NALM6 cell line at 20x magnification and D) 63x magnification.

hours, 8 hours, 12 hours, and 24 hours, then fixed and imaged the cells. We observed no binding, nor cargo delivery in the untargeted protocell control, and CD19 target-specific delivery of the membrane impermeable cargo, YO-PRO®-1, after 8 hours of incubation, with more significant cargo release at 12 hours (**Figure 5.21 –** See **Appendix B.6** for more detailed images of cargo release).

Following the steps described previously, we evaluated the targeted binding characteristics of the CD19-targeted protocell binding using real-time intravital imaging in the *ex ovo* CAM model. We injected blue fluorescent labelled MOLT4, MOLT4-CD19, or NALM6 cells into the CAM and allowed the cells to arrest in the capillary bed (~ 30 minutes). Next, we injected (either antibody- or scFv-labelled) CD19-targeted protocells into the CAM and imaged protocell flow and binding dynamics after 4 hours in circulation. We observed protocells flowing in the blood stream but not interacting with the parental MOLT4 cells (**Figures 5.22A and B)**, however, we detect significant binding to the MOLT4-CD19 cells (**Figures 5.22C and D)** and NALM6 cells (**Figures 5.22E and F)** in the CAM.

Next, we assessed protocell targeted cell specific killing, *in vitro.* We used GEM as our cytotoxic agent as described previously, and incubated MOLT4, MOLT4-CD19, and NALM6 cells with increasing concentrations of CD19-targeted GEM-loaded protocells in complete media under normal cell culture conditions. Similar to EGFR-targeted GEM delivery (**Figure 5.14A**), we detect a CD19-target specific decrease in cell viability correlating to an increase in CD19-targeted protocell concentration in both antibody- and scFv-labelled systems (**Figure**

Figure 5.21 – *Comparable Antibody- and scFv-modified Protocell Binding and Cargo Delivery to MOLT4-CD19 Cells In Vitro*
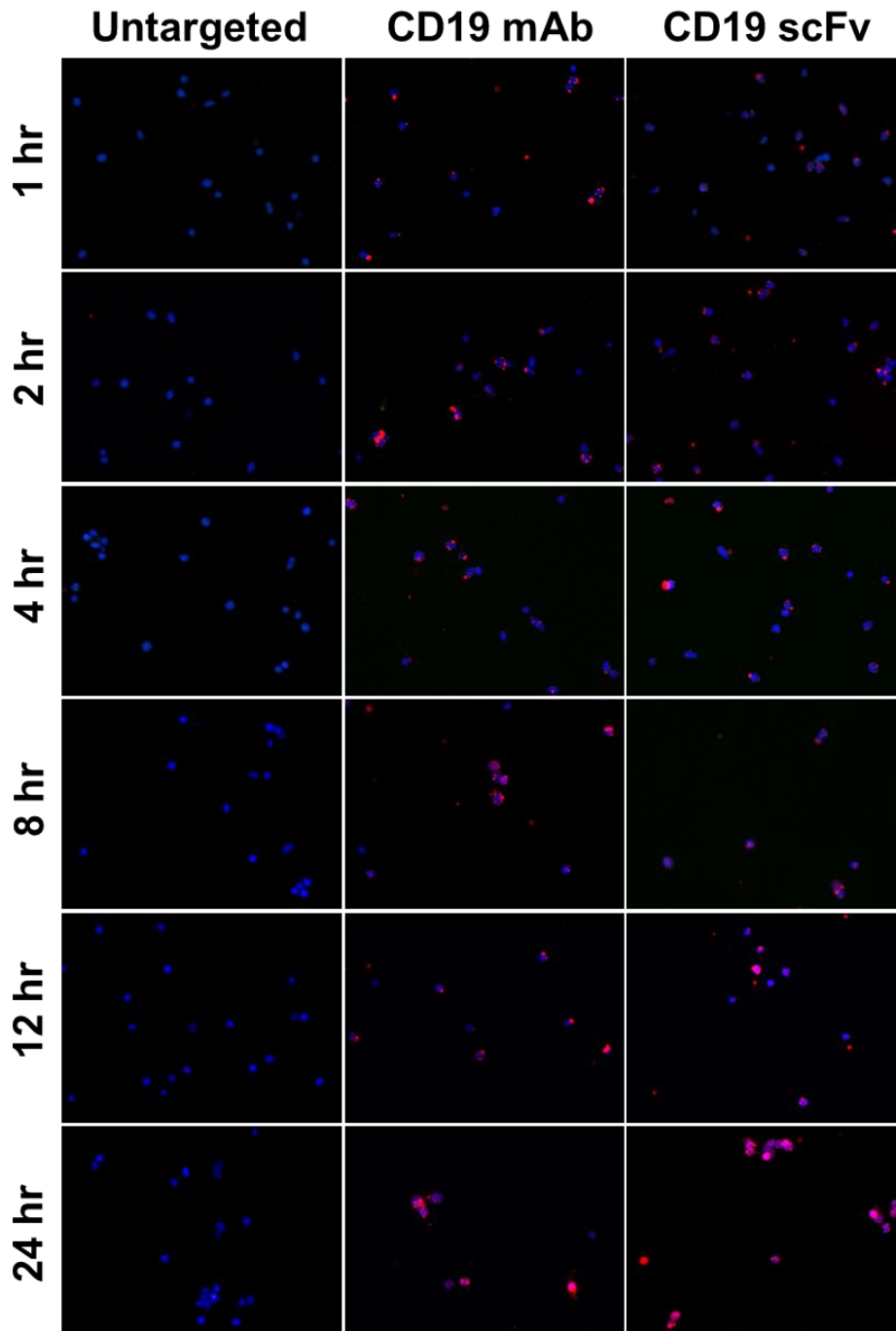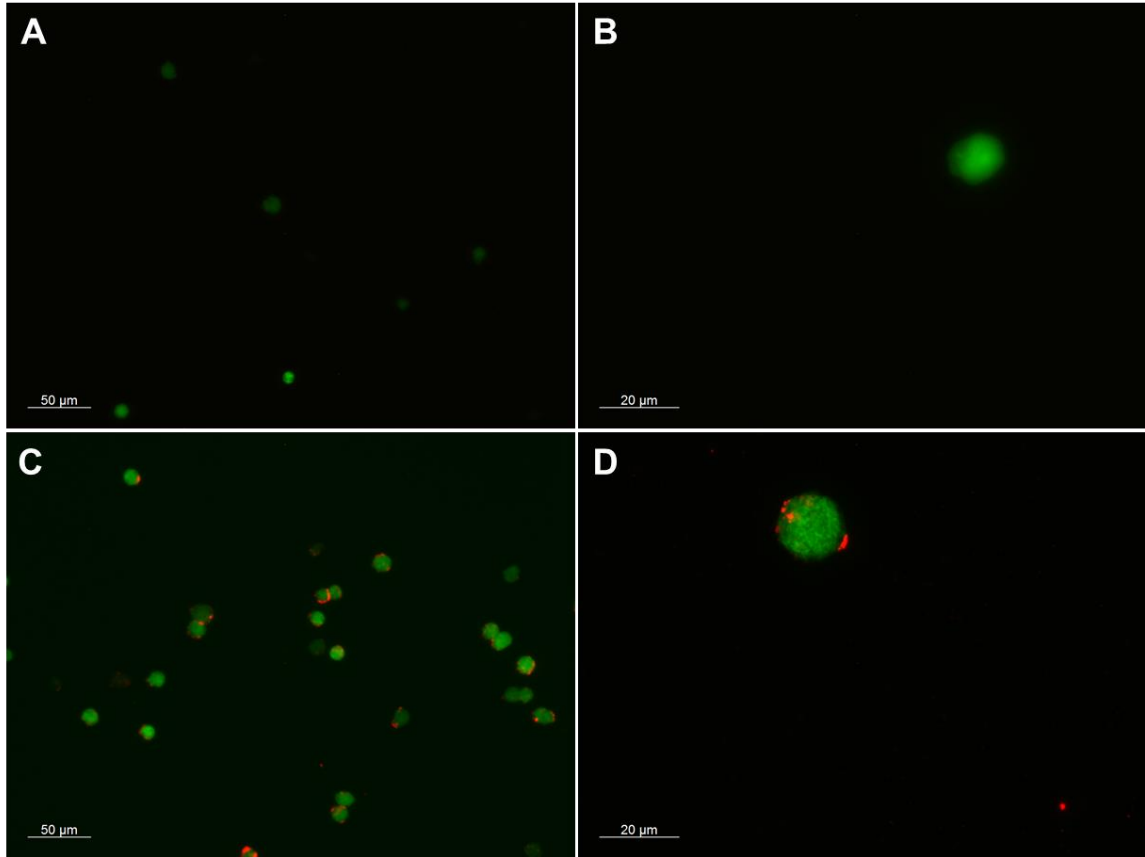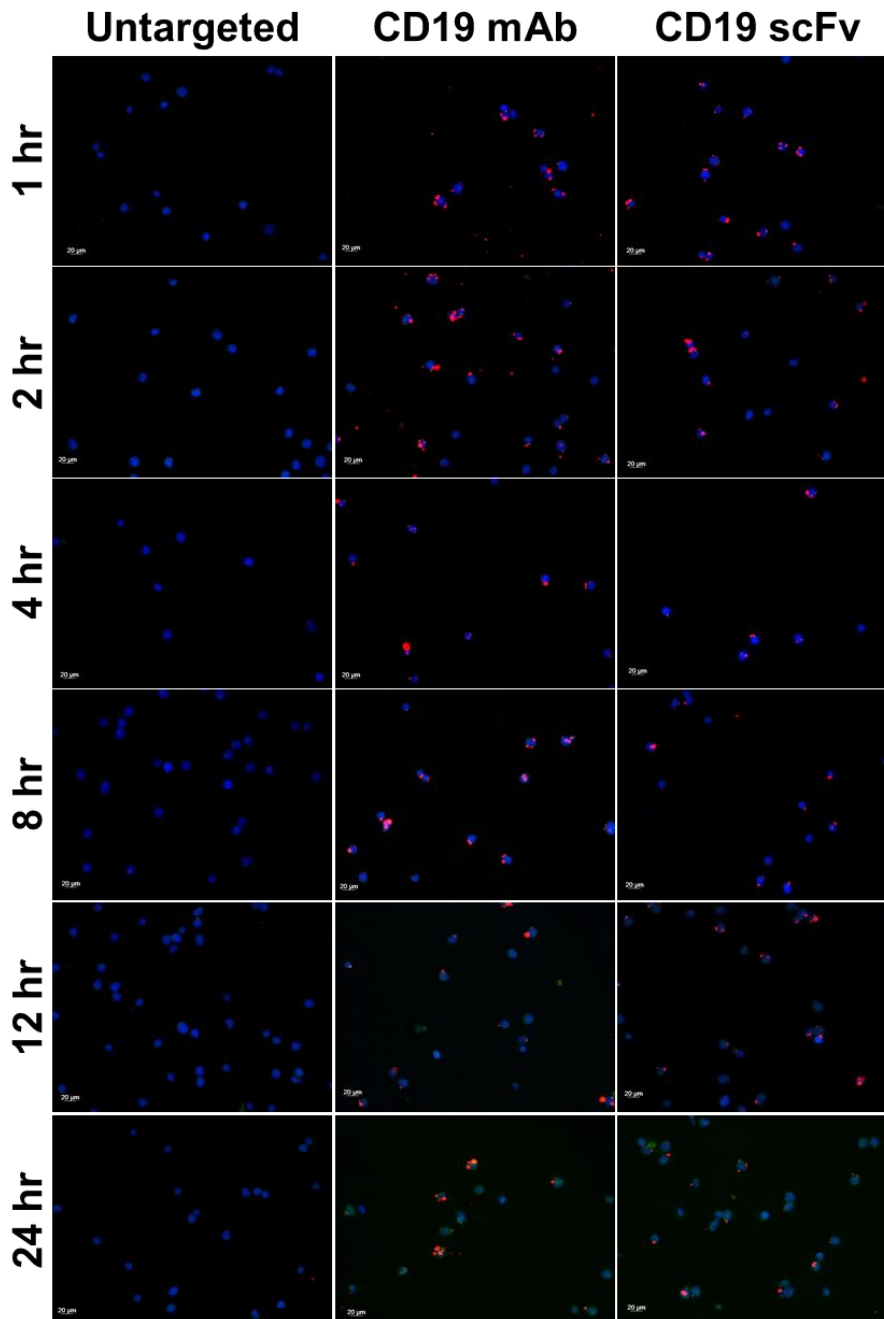

Figure 5.21 – Fluorescent microscopy analysis of MOLT4-CD19 cells incubated with either CD19 untargeted, antibody-targeted, or scFv-targeted protocells at multiple time points, fixed, and stained (blue–cells, red–protocells, green- YO-PRO®-1). We observe protocell binding at 1 hour in complete medium, with cargo release occurring between 8 and 24 hours. See **Appendix B.6** for more select detailed images.

Figure 5.22 – *Targeted Protocells bind MOLT40CD19 and NALM6 Cells in the CAM*
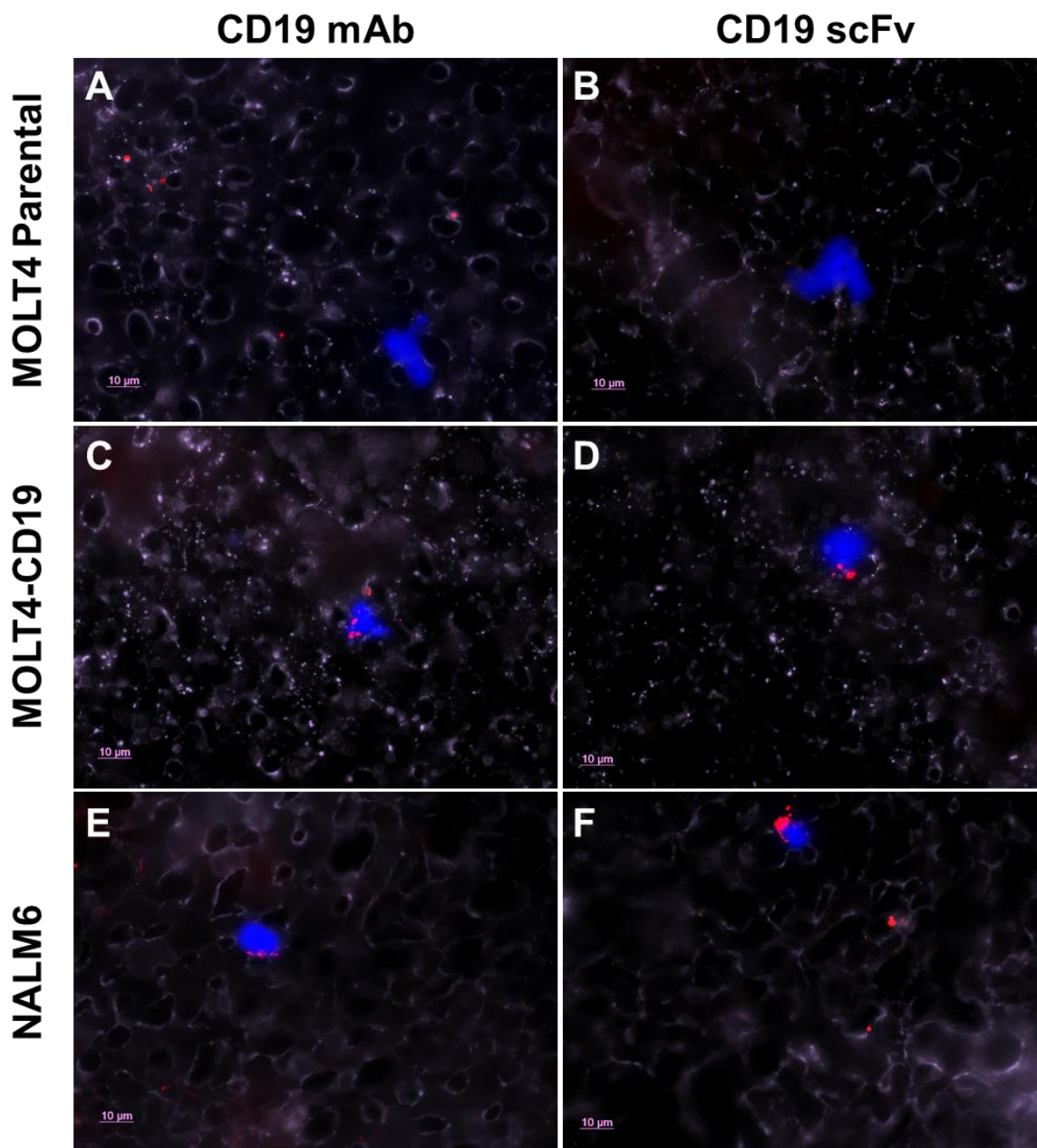
Figure 5.22 – Intravital fluorescent microscopy images acquired *ex ovo* in the CAM model reveal stable circulation of CD19 targeted antibody- and scFv-modified protocells (red) avoiding MOLT4 cells and binding to CD19 positive cells MOLT4-CD19 and NALM6 (blue) in circulation at 4 hours. Additional flow and binding images in **Appendix B.7**.

5.23). Since we had already verified GEM was responsible for the cell killing as opposed to the protocell itself, using EGFR-targeted protocells with REH and REH-EGFR cells (**Figure 5.14C**), we did not examine the effect of the unloaded-protocell on MOLT4, MOLT4-CD19, and NALM6 cell lines.

Next, we loaded the protocells with YO-PRO®-1 and evaluated targeting and delivery in an *ex ovo* system. We injected the CAM with fluorescent labelled MOLT4-CD19 cells, then 30 minutes later, injected YO-PRO®-1 loaded antibody- or scFv-labelled CD19-targeted protocells. We used intravital imaging a lectin vascular stain to provide contrast in the blood vessels. Intravital fluorescent imaging of binding, internalization, and cargo release were taken at 30 hours (MOLT4-CD19) and 20 hours (NALM6) post *ex ovo* injection. After 30 hours, we observe YO-PRO®-1 dispersed throughout MOLT4-CD19 cells (**Figure 5.24**) and 20 hours with NALM6 cells (**Figure 5.25**), similar to the EGFR-targeted cargo release in the CAM (**Figure 5.16**). The differences in cargo release between the two cell lines may be due to the artificial expression of CD19 on the MOLT4 cell line, since NALM6 has native CD19 expression, it is likely to possess a more complete CD19-mediated internalization system, therefore more rapid internalization and cargo release.

These results demonstrate the "plug-and-play" simplicity of target modification to the protocell platform, and further support the advantages of the SLB to prevent non-specific cell interactions that are paramount to a disease agnostic drug-delivery nanocarrier platform.

Figure 5.23 – *CD19-Targeted Drug Delivery and Cell Viability Assessment*
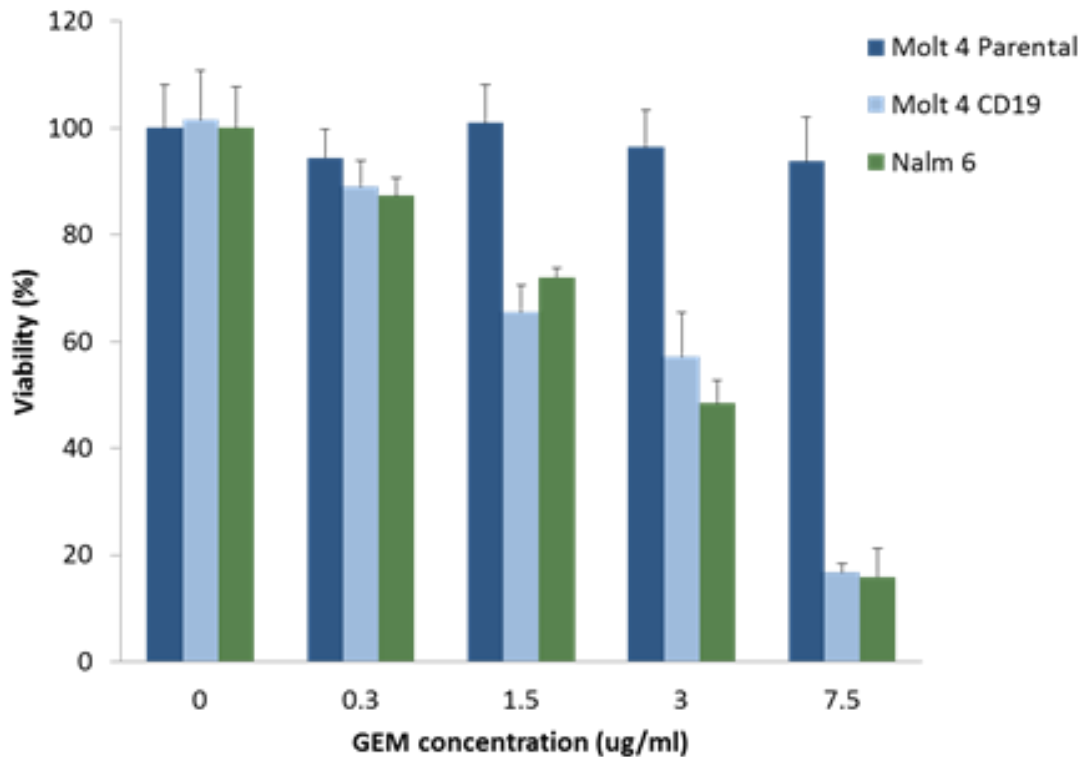
Figure 5.23 - Maintained viability of CD19 negative MOLT4 cells and decrease in viability of MOLT4-CD19 and NALM6 cells with increasing concentration of GEM loaded CD19-targeted protocells.   Viability was assessed at 48 hours. Viability data supports EGFR-targeted killing described in **Figure 5.14** and further highlights target specific delivery of cytotoxic cargo using the monosized protocell platform. Data represents mean ± SD, n = 3.

Figure 5.24 – *CD19-Targeted Cargo Delivery to MOLT4-CD19 Cells Ex Ovo*
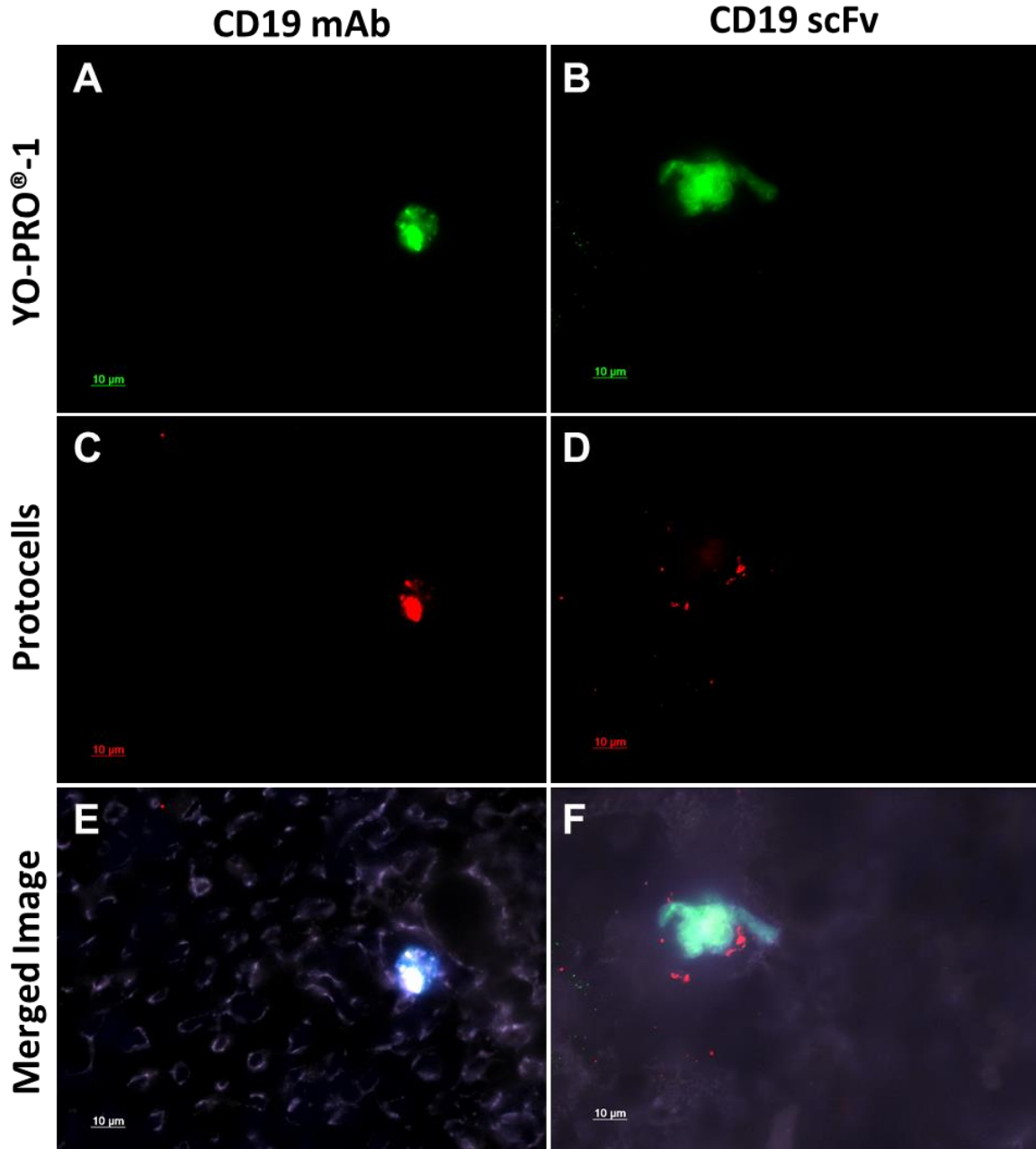
Figure 5.24 – Intravital fluorescent microscopy images acquired *ex ovo* in the CAM model showing green YO-PRO®-1 cell impermeant cargo loaded, red fluorescent CD19 antibody- and scFv-targeted protocells binding to and releasing cargo within MOLT4-CD19 cells in a live animal model. A) and B) Green channel shows YO-PRO®-1 fluorescence associated with the protocells, C) and D) Red channel shows protocell fluorescence, and E) and F) show fluorescent overlay of (blue) MOLT4-CD19 cell, (red) protocell, (green) YO-PRO®-1 cargo, (lavender) lectin vascular stain at 30 hours post injection. Images acquired at 63x magnification.

Figure 5.25 – *CD19-Targeted Cargo Delivery to NALM6 Cells Ex Ovo*
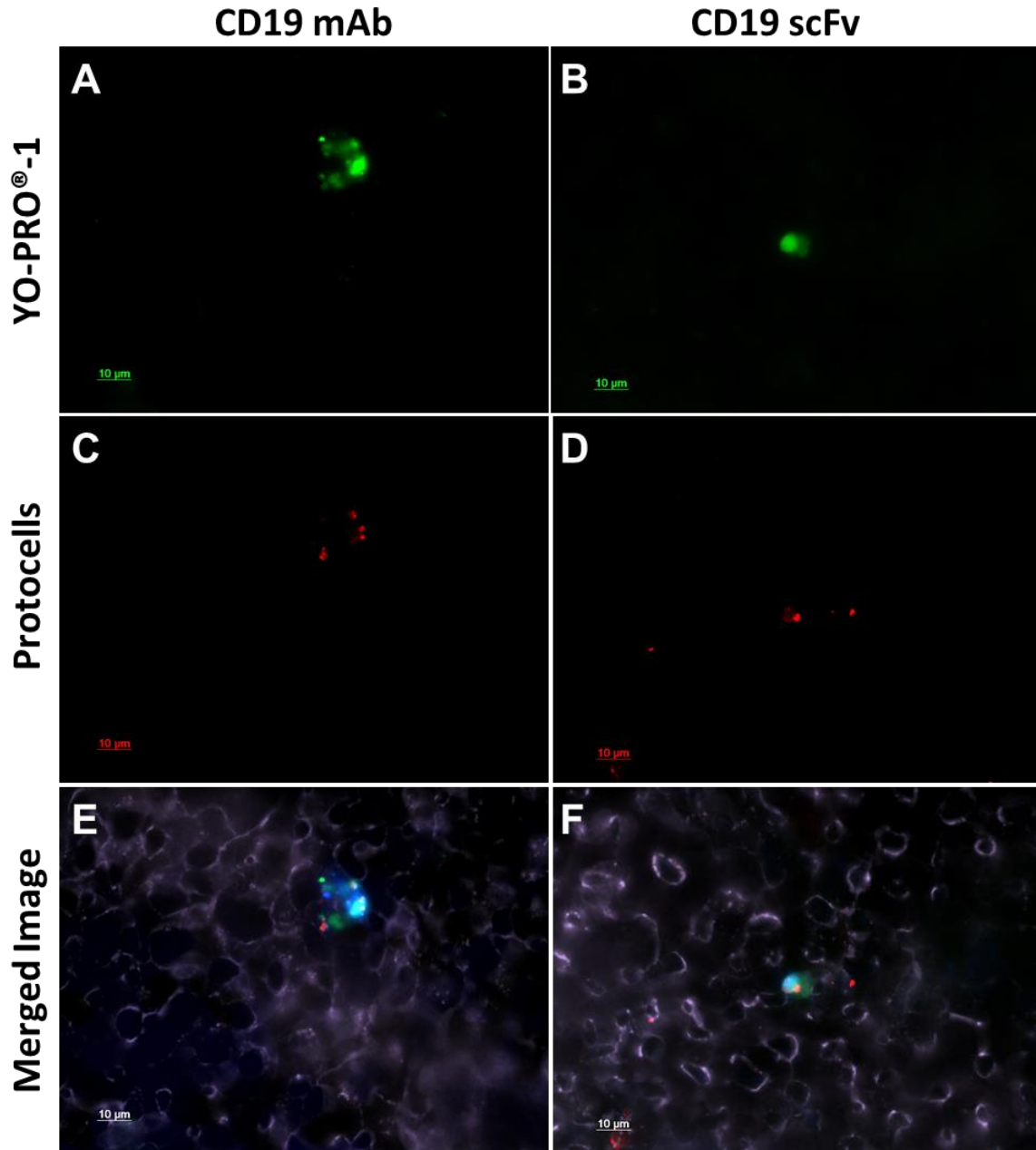
Figure 5.25 – Intravital fluorescent microscopy images acquired *ex ovo* in the CAM model showing green YO-PRO®-1 cell impermeant cargo loaded, red fluorescent CD19 antibody- and scFv-targeted protocells binding to and releasing cargo within NALM6 cells in a live animal model. A) and B) Green channel shows YO-PRO®-1 fluorescence associated with the protocells, C) and D) Red channel shows protocell fluorescence, and E) and F) show fluorescent overlay of (blue) NALM6 cell, (red) protocell, (green) YO-PRO®-1 cargo, (lavender) lectin vascular stain at 20 hours post injection. Images acquired at 63x magnification.

5.3 Materials and Methods

5.3.1 Materials

All chemicals and reagents were used as received. See all protocell synthesis and assembly materials listed in **2.3.1 Materials.** All chemicals and reagents were used as received. Ammonium hydroxide (NH_4OH, 28 – 30 %), 3-aminopropyltriethoxysilane (98 %, APTES), ammonium nitrate (NH_4NO_3), benyldimethylhexadecylammonium chloride (BDHAC), n-cetyltrimethylammonium bromide (CTAB), N,N-dimethyl formamide (DMF), dimethyl sulfoxide (DMSO), rhodamine B isothiocyanate (RITC), tetraethyl orthosilicate (TEOS), Triton X-100, and Buffer solution pH 5.0 (citrate buffer) were purchased from Sigma-Aldrich (St. Louis, MO). Hydrochloric acid (36.5 – 38 %, HCl) was purchased from EMD Chemicals (Gibbstown, NJ). Absolute (99.5 %) and 95 % ethanol were obtained from PHARMCO-AAPER (Brookfield, CT). 1,2-dioleoyl-sn-glycero-3-phosphocholine (DOPC), 1,2-distearoyl-snglycero-3-phosphocholine (DSPC), 1,2-dioleoyl-*sn*-glycero-3-phosphoethanolamine-N-[methoxy(polyethylene glycol)-2000] (ammonium salt) (DOPE-PEG$_{2000}$), 1,2-distearoyl-sn-glycero-3-phosphoethanolamine-N-[methoxy(polyethylene glycol)-2000] (ammonium salt) (DSPE-PEG$_{2000}$), 1,2-distearoyl-*sn*-glycero-3-phosphoethanolamine-N-[amino(polyethylene glycol)-2000] (DSPE-PEG$_{2000}$-NH$_2$) phospholipids and cholesterol (chol, ovine wool, > 98 %) were purchased from Avanti Polar Lipids (Birmingham, AL). Hoechst 33342, Traut's reagent, YO-PRO®-1, and maleimide-activated NeutrAvidin protein were obtained from Thermo Scientific (Rockford, IL). Alexa Fluor®488 phalloidin, CellTracker™ Blue

CMAC dye, and CellTracker™ green CMFDA dye were purchased from Life Technologies (Eugene, OR). Heat inactivated fetal bovine serum (FBS), 10X phosphate buffered saline (PBS), 1X trypsin-EDTA solution, and penicillin streptomycin (PS) were purchased from Gibco (Logan, UT). Dulbecco's Modification of Eagle's Medium with 4.5 g/L glucose, L-glutamine and sodium pyruvate (DMEM) and RPMI-1640 medium were obtained from CORNING cellgro (Manassas, VA). Gemcitabine (GEM) was purchased from LC Laboratories (Woburn, MA). Anti-EGFR antibody [EGFR1] (Biotin) (ab24293) was purchased from Abcam (Cambridge, MA). Biotin Anti-Human CD19 Antibody [HIB19] was purchased from Biolegend (San Diego, CA) and Biotin Anti-CD19 single chain variable fragment (scFv) (GenScript, NJ). CellTiter-Glo® 2.0 Assay was purchased from Promega (Madison, WI). DyLight 649 Lens Culinaris Agglutinin was purchased from Vector Laboratories (Burlingame, CA). Spectra-Por® Float-A-Lyzer® G2 Dialysis Device MWCO: 3.5 – 5 kD was purchased from Spectrum Laboratories Inc. (Rancho Dominguez, CA).

5.3.2 Anti-EGFR / Anti-CD19 Protocell Preparation

First, DSPC:chol:DSPE-PEG-NH$_2$ liposomes were prepared according to the method described previously. Next, a ratio (2:1, w:w) of DSPC:chol:DSPE-PEG$_{2000}$-NH$_2$ liposomes to bare fluorescent-labeled Hexagonal mMSNP were combined in a conical tube at room temperature for 30 minutes. The excess liposomes were removed by centrifugation (15,000 x g, 10 minutes). The pelleted protocells were redispersed in 1 mL of PBS with bath sonication. To convert the surface -NH$_2$ to -SH groups, 50 µL of freshly prepared Traut's reagent (250 mM

in PBS) was added to the protocells. After 1 hour, the particles were centrifuged, and the supernatant was removed. The particles were again redispersed in 1 mL of PBS. Then, 0.15 mg of maleimide-activated NeutrAvidin protein was added to 0.25 mL of thiolated protocells and incubated at room temperature for 12 hours. The NeutrAvidin conjugated protocells were washed with PBS *via* centrifugation and suspended in 0.25 mL of PBS. Then, 50 µL of biotinlyated EGFR antibody (0.1 mg/mL) or 10 µL biotinylated CD19 antibody (0.5 mg/mL) was mixed with 50 µL of NeutrAvidin conjugated protocells for at least 30 minutes. Finally, the antibody conjugated protocells were pelleted and redispersed in 100 µL PBS for *in vitro* targeting experiments.

5.3.3 Targeted Protocell Biocompatibility Assessment

To examine the biocompatibility of anti-EGFR targeted protocells *in vitro*, we incubated ~ 1.5×10^5 cells/mL of REH and REH-EGFR cell lines with either 12.5, 25, 50, 100, and 200 µg/mL of anti-EGFR targeted protocells in complete medium for 1 hour at 37 °C. Cells were washed twice in complete media and transferred to a 96-well plate for 24 hours at 37 °C. Cell viability was assessed by CellTiter-Glo® 2.0 Assay as measured by BioTek microplate reader. The cell viability was calculated as a percentage of non-protocell treated sample.

5.3.4 *In Vitro* Targeting Comparison of REH and REH-EGFR Cell Lines

The human leukemia cell lines, REH and REH-EGFR[24] were a kind gift from Professor David F. Stern, Yale University. The REH and REH-EGFR cells were suspended in RPMI 1640 supplemented with 10 % FBS media at a

concentration of ~ 5 x 10^5 cells/mL. Then one mL of cells was incubated with either NeutrAvidin terminated protocells or anti-EGFR protocells at 10 µg/mL for 5, 15, 30, and 60 minutes respectively at 37 °C under 5 % CO_2. The nanoparticle-treated cells were pelleted using a benchtop centrifuge, washed with PBS twice. Cells were fixed in 4 % paraformaldehyde for 5 minutes, then washed in PBS, then permeabilized with 0.1 % Triton X100 for 5 minutes. The cell cytoskeleton and nuclei were stained by 0.1 mM of Alexa Fluor®488 phalloidin in PBS for 15 minutes, then washed in PBS, followed by 1.6 µM Hoechst 33342 in PBS for 10 minutes, followed by a final wash in PBS. Stained cells were imaged on a glass slide using the Zeiss AxioExaminer upright microscope. Binding quantification of targeted protocells was determined by a fluorescence shift measured by a BD Accuri™ C6 flow cytometer.

5.3.5 Single Cell Targeting and Model Drug Delivery in the CAM

First, ~ 1 x 10^7 of either REH or REH-EGFR cells were suspended in 1 mL PBS and incubated with 2 µL of CellTracker™ green CMFDA dye (2.7 mM in DMSO) for 10 minutes at 37 °C. The stained cells were centrifuged, washed, and suspended in 500 µL of PBS. Next, 50 µL of cell solution was administered to *ex ovo* avian embryos *via* the previously described procedure. After 30 minutes cell circulation, the anti-EGFR protocells (100 µL, 0.2 mg/mL) were injected into embryos intravenously. Binding of targeted protocells was assessed by fluorescence microscopy at 1 hour, 4 hours, and 9 hours using the Zeiss AxioExaminer upright microscope. To assess internalization and cargo delivery, REH-EGFR cells were stained with CellTracker™ Blue CMAC dye and injected

as described above, followed by injection of YO-PRO®-1 loaded RITC labelled protocells (50 μL, 1 mg/mL). Prior to imaging of we injected with DyLight 645 Len Culinaris Agglutin lectin stain to visualize the vasculature, we then imaged the binding, internalization, and cargo release by fluorescence microscopy at 4 hours and 16 hours using the Zeiss AxioExaminer upright microscope. We used the same conditions to image CD19-targeted protocell binding using MOLT4, MOLT4-CD19, and NALM6 cell lines.

5.3.6 Characterization

TEM images were acquired on a JEOL 2010 (Tokyo, Japan) equipped with a Gatan Orius digital camera system (Warrendale, PA) under a 200 kV voltage. Flow cytometry data were performed on a Becton-Dickinson FACScalibur flow cytometer (Sunnyvale, CA). The raw data obtained from the flow cytometer was processed with FlowJo software (Tree Star, Inc. Ashland, OR). Hydrodynamic size and zeta potential data were acquired on a Malvern Zetasizer Nano-ZS equipped with a He-Ne laser (633 nm) and Non-Invasive Backscatter optics (NIBS). All samples for DLS measurements were suspended in various media (D.I. water, PBS, and DMEM + 10 % FBS) at 1 mg/mL. Measurements were acquired at 25 °C or 37 °C. DLS measurements for each sample were obtained in triplicate. The Z-average diameter was used for all reported hydrodynamic size measurements. The zeta potential of each sample was measured in 1xPBS using monomodal analysis. All reported values correspond to the average of at least three independent samples. The

fluorescence images were captured with a Zeiss AxioExaminer fixed stage microscope (Gottingen, Germany).

5.3.7 *In Vitro* Targeting Comparison of Ba/F3 and Ba/F3-EGFR Cell Lines

The murine precursor B cell ALL cell lines, Ba/F3 and Ba/F3-EGFR[24] were a kind gift from Professor David F. Stern, Yale University. The Ba/F3 and Ba/F3-EGFR cells were suspended in RPMI 1640 supplemented with 10 % FBS media at a concentration of ~ 1 x 10^6 cells/mL. Then one mL of cells was incubated with anti-EGFR protocells at 5 µg/mL for 1 hour at 37 ℃ under 5 % CO_2. The cell nuclei and membrane were stained by 1 µL of Hoechst 33342 (1.6 mM in DI) and 2 µL of CellTracker™ green CMFDA dye (2.7 mM in DMSO) for 10 minutes. The nanoparticle-treated cells were pelleted using a benchtop centrifuge, washed with PBS twice, and dispersed in PBS. The live cells were imaged on a glass slide using the Zeiss AxioExaminer upright microscope. To further examine the specificity of targeted protocells, the binding of particles was determined by a fluorescence shift measured by a Becton-Dickinson FACScalibur flow cytometer.

5.3.8 Cargo Loading and Release Kinetics

Model drug loading was achieved by adding 1 % volume YO-PRO®-1 (1 mM in DMSO) to mMSNPs (1 mg/mL in H_2O) and stored for 12 hours at 4 °C. After loading, targeted protocells were prepared using method described earlier in Anti-EGFR targeted protocell preparation. We observed a color change in the pelleted YO-PRO®-1 loaded protocells and did not observe any color in the supernatant during protocell assembly. We suspect that the interaction between

YO-PRO®-1 and mMSNPs to be largely driven by electrostatics, since YO-PRO®-1 carries a positive charge. Moreover, YO-PRO®-1 is membrane impermeable, therefore, it should remain encapsulated by the SLB of the protocell until it is broken down in the intracellular environment. To quantify YO-PRO®-1 loading, protocells were pelleted by centrifugation and resuspended in DMSO with bath sonication, this step was repeated twice. Supernatants were pooled and concentration was determined using a microplate reader fluorescence measurement at 480/510 nm. We used a 3.5 – 5 kDa MWCO Float-A-Lyzer to evaluate GEM release kinetics in either PBS (pH 7.4) or citrate buffer (pH 5.0). GEM was encapsulated into protocells as described above, then protocells were loaded into Float-A-lyzers and sealed in 50 mL conical tubes containing either PBS or citrate buffer, and stored at 37 °C while stirring. We removed 0.5 mL of dialysate for 265 nm absorbance analysis on a BioTek microplate reader at multiple time points, then added 0.5 mL of fresh dialysate solution to the conical tube. To assess protocell size at 24 hours and 72 hours we removed sample from the Float-a-Lyzer, and measured the hydrodynamic size on Malvern Zetasizer Nano ZS, then placed back inside the Float-a-Lyzer and stored at 37 °C while stirring. Consistent with findings reported by Meng *et.al*,[20] we did not see evidence of drug precipitation and we determined the effective release of GEM by cell viability analysis, in addition, our loaded and targeted protocell maintained monodispersity.

5.3.9 Targeted Protocell GEM Delivery and Cytotoxicity Assessment

We incubated ~ 1.5 x 10^5 cells/mL of REH and REH-EGFR cell lines with

either 0, 1, 5, 10, 25, or 50 µg/mL of GEM loaded (~ 15 % w/w) anti-EGFR

targeted protocells in complete medium for 1 hour at 37 °C. We used the same

conditions for CD19-targeted delivery to MOLT4, MOLT4-CD19, and NALM6

cells. Cells were centrifuged (500 x g, 3 minutes) and washed twice in complete

media and transferred to a white 96-well plate for 24 hours at 37 °C. In

comparison, we incubated ~ 1.5 x 10^5 cells/mL of REH and REH-EGFR cell lines

with either 0, 0.6, 3, 6, 15, or 30 µM of free GEM, the equivalent doses based on

15 % (w/w) GEM loading into protocells, under identical experimental conditions.

Cell viability was assessed by CellTiter-Glo® 2.0 Assay as measured by BioTek

microplate reader. The cell viability was calculated as a percentage of non-

protocell treated sample.

5.3.10 *In Vitro* Internalization and Cargo Release Assay

REH-EGFR cells were suspended in RPMI 1640 supplemented with 10 %

FBS media at a concentration of 5 x 10^5 cells/mL. Then one mL of cells was

incubated with YO-PRO®-1 loaded, RITC-labelled anti-EGFR protocells at 10

µg/mL for 60 minutes at 37 °C, washed twice in media to remove unbound

protocells, and incubated for 1, 8, 16, and 24 hours respectively at 37 °C under 5

% CO_2. The protocell-treated cells were pelleted using a benchtop centrifuge, at

each time point, and resuspended in an acid wash solution (0.2 M acetic acid,

0.5 M NaCl, pH 2.8) and incubated on ice for 5 minutes. Cells were then washed

twice with PBS by centrifugation and protocell internalization was assessed by a

red fluorescence shift and cargo release was assessed by a green fluorescence

shift as measured by a BD Accuri™ C6 flow cytometer. Additionally, live cells

were imaged on a glass slide using the Leica DMI3000 B inverted microscope. We used the same conditions for CD19-targeted delivery to MOLT4, MOLT4-CD19, and NALM6 cells.

5.3.11 *In Vitro* Targeting Comparison of MOLT4, MOLT4-CD19, and NALM6 Cell Lines

The MOLT4, MOLT4-CD19, and NALM6 cells were suspended in RPMI 1640 supplemented with 10 % FBS media at a concentration of ~ 5×10^5 cells/mL. Then ~ 5×10^5 cells were incubated with either NeutrAvidin terminated (untargeted) protocells, CD19-targeted antibody-, or scFv-modified protocells at 10 µg/mL for 5, 10, 15, 30, 60 minutes, 2, 4, 8, 12, or 24 hours respectively at 37 ºC under 5 % CO_2. The nanoparticle-treated cells were pelleted using a benchtop centrifuge, washed with PBS twice. Cells were stained with CMAC (live cell stain) then fixed in 4 % paraformaldehyde for 5 minutes, then washed in PBS. Stained cells were imaged on a glass slide using the Zeiss AxioExaminer upright microscope. Binding quantification of targeted protocells was determined by a fluorescence shift measured by a BD Accuri™ C6 flow cytometer and analyzed using FlowJo software.

5.4 References

1.   Bertrand, N.; Wu, J.; Xu, X.; Kamaly, N.; Farokhzad, O. C. Cancer Nanotechnology: The Impact of Passive and Active Targeting in the Era of Modern Cancer Biology. *Adv. Drug Delivery Rev.* 2014, 66, 2-25.

2.   Sun, T.; Zhang, Y. S.; Pang, B.; Hyun, D. C.; Yang, M.; Xia, Y. Engineered Nanoparticles for Drug Delivery in Cancer Therapy. *Angew. Chem., Int. Ed.* 2014, 53, 12320-12364.

3.   Tarn, D.; Ashley, C. E.; Xue, M.; Carnes, E. C.; Zink, J. I.; Brinker, C. J. Mesoporous Silica Nanoparticle Nanocarriers: Biofunctionality and Biocompatibility. *Acc. Chem. Res.* 2013, 46, 792-801.

4.   Padera, T. P.; Stoll, B. R.; Tooredman, J. B.; Capen, D.; Tomaso, E. d.; Jain, R. K. Pathology: Cancer Cells Compress Intratumour Vessels. *Nature* 2004, 427, 695-695.

5.   Chauhan, V. P.; Stylianopoulos, T.; Martin, J. D.; Popovic, Z.; Chen, O.; Kamoun, W. S.; Bawendi, M. G.; Fukumura, D.; Jain, R. K. Normalization of Tumour Blood Vessels Improves the Delivery of Nanomedicines in a Size-Dependent Manner. *Nat. Nanotechnol.* 2012, 7, 383-388.

6.   Blanco, E.; Shen, H.; Ferrari, M. Principles of Nanoparticle Design for Overcoming Biological Barriers to Drug Delivery. *Nat. Biotechnol.* 2015, 33, 941-951.

7.   Peer, D.; Karp, J. M.; Hong, S.; Farokhzad, O. C.; Margalit, R.; Langer, R. Nanocarriers as an Emerging Platform for Cancer Therapy. *Nat. Nanotechnol.* 2007, 2, 751-760.

8.   Bartlett, D. W.; Su, H.; Hildebrandt, I. J.; Weber, W. A.; Davis, M. E. Impact of Tumor-Specific Targeting on the Biodistribution and Efficacy of Sirna Nanoparticles Measured by Multimodality *in Vivo* Imaging. *Proc. Natl. Acad. Sci. U. S. A.* 2007, 104, 15549-15554.

9.   Bae, Y. H. Drug Targeting and Tumor Heterogeneity. *J. Controlled Release* 2009, 133, 2-3.

10.   Lammers, T.; Kiessling, F.; Hennink, W. E.; Storm, G. Drug Targeting to Tumors: Principles, Pitfalls and (Pre-) Clinical Progress. *J. Controlled Release* 2012, 161, 175-187.

11.   Shi, J.; Xiao, Z.; Kamaly, N.; Farokhzad, O. C. Self-Assembled Targeted Nanoparticles: Evolution of Technologies and Bench to Bedside Translation. *Acc. Chem. Res.* 2011, 44, 1123-1134.

12. Iyer, A. K.; Singh, A.; Ganta, S.; Amiji, M. M. Role of Integrated Cancer Nanomedicine in Overcoming Drug Resistance. *Adv. Drug Delivery Rev.* 2013, 65, 1784-1802.

13. Markman, J. L.; Rekechenetskiy, A.; Holler, E.; Ljubimova, J. Y. Nanomedicine Therapeutic Approaches to Overcome Cancer Drug Resistance. *Adv. Drug Delivery Rev.* 2013, 65, 1866-1879.

14. Adamson, P. C. Improving the Outcome for Children with Cancer: Development of Targeted New Agents. *Ca-Cancer J. Clin.* 2015, 65, 212-220.

15. Krishnan, V.; Rajasekaran, A. K. Clinical Nanomedicine: A Solution to the Chemotherapy Conundrum in Pediatric Leukemia Therapy. *Clin. Pharmacol. Ther.* 2014, 95, 168-178.

16. Butler, K. S.; Durfee, P. N.; Theron, C.; Ashley, C. E.; Carnes, E. C.; Brinker, C. J. Protocells: Modular Mesoporous Silica Nanoparticle-Supported Lipid Bilayers for Drug Delivery. *Small* 2016.

17. Ashley, C. E.; Carnes, E. C.; Epler, K. E.; Padilla, D. P.; Phillips, G. K.; Castillo, R. E.; Wilkinson, D. C.; Wilkinson, B. S.; Burgard, C. A.; Kalinich, R. M.; Townson, J. L.; Chackerian, B.; Willman, C. L.; Peabody, D. S.; Wharton, W.; Brinker, C. J. Delivery of Small Interfering Rna by Peptide-Targeted Mesoporous Silica Nanoparticle-Supported Lipid Bilayers. *ACS Nano* 2012, 6, 2174-2188.

18. Epler, K.; Padilla, D.; Phillips, G.; Crowder, P.; Castillo, R.; Wilkinson, D.; Wilkinson, B.; Burgard, C.; Kalinich, R.; Townson, J.; Chackerian, B.; Willman, C.; Peabody, D.; Wharton, W.; Brinker, C. J.; Ashley, C.; Carnes, E. Delivery of Ricin Toxin a-Chain by Peptide-Targeted Mesoporous Silica Nanoparticle-Supported Lipid Bilayers. *Adv. Healthcare Mater.* 2012, 1, 348-353.

19. Ashley, C. E.; Carnes, E. C.; Phillips, G. K.; Padilla, D.; Durfee, P. N.; Brown, P. A.; Hanna, T. N.; Liu, J.; Phillips, B.; Carter, M. B.; Carroll, N. J.; Jiang, X.; Dunphy, D. R.; Willman, C. L.; Petsev, D. N.; Evans, D. G.; Parikh, A. N.; Chackerian, B.; Wharton, W.; Peabody, D. S.; Brinker, C. J. The Targeted Delivery of Multicomponent Cargos to Cancer Cells by Nanoporous Particle-Supported Lipid Bilayers. *Nat. Mater.* 2011, 10, 389-397.

20. Meng, H.; Wang, M.; Liu, H.; Liu, X.; Situ, A.; Wu, B.; Ji, Z.; Chang, C. H.; Nel, A. E. Use of a Lipid-Coated Mesoporous Silica Nanoparticle Platform for Synergistic Gemcitabine and Paclitaxel Delivery to Human Pancreatic Cancer in Mice. *ACS Nano* 2015, 9, 3540-3557.

21. Liu, X.; Situ, A.; Kang, Y.; Villabroza, K. R.; Liao, Y.; Chang, C. H.; Donahue, T.; Nel, A. E.; Meng, H. Irinotecan Delivery by Lipid-Coated Mesoporous Silica Nanoparticles Shows Improved Efficacy and Safety over Liposomes for Pancreatic Cancer. *ACS Nano* 2016, 10, 2702-2715.

22. Wang, D.; Huang, J.; Wang, X.; Yu, Y.; Zhang, H.; Chen, Y.; Liu, J.; Sun, Z.; Zou, H.; Sun, D.; Zhou, G.; Zhang, G.; Lu, Y.; Zhong, Y. The Eradication of Breast Cancer Cells and Stem Cells by 8-Hydroxyquinoline-Loaded Hyaluronan Modified Mesoporous Silica Nanoparticle-Supported Lipid Bilayers Containing Docetaxel. *Biomaterials* 2013, 34, 7662-7673.

23. Zhang, X.; Li, F.; Guo, S.; Chen, X.; Wang, X.; Li, J.; Gan, Y. Biofunctionalized Polymer-Lipid Supported Mesoporous Silica Nanoparticles for Release of Chemotherapeutics in Multidrug Resistant Cancer Cells. *Biomaterials* 2014, 35, 3650-3665.

24. Riese, D. J.; van Raaij, T. M.; Plowman, G. D.; Andrews, G. C.; Stern, D. F. The Cellular Response to Neuregulins Is Governed by Complex Interactions of the Erbb Receptor Family. *Mol. Cell. Biol.* 1995, 15, 5770-5776.

25. Durfee, P. N.; Lin, Y.-S.; Dunphy, D. R.; Muñiz, A. J.; Butler, K. S.; Humphrey, K. R.; Lokke, A. J.; Agola, J. O.; Chou, S. S.; Chen, I. M.; Wharton, W.; Townson, J. L.; Willman, C. L.; Brinker, C. J. Mesoporous Silica Nanoparticle-Supported Lipid Bilayers (Protocells) for Active Targeting and Delivery to Individual Leukemia Cells. *ACS Nano* 2016.

26. Federico, C.; Morittu, V. M.; Britti, D.; Trapasso, E.; Cosco, D. Gemcitabine-Loaded Liposomes: Rationale, Potentialities and Future Perspectives. *Int. J. Nanomed.* 2012, 7, 5423-5436.

27. de Sousa Cavalcante, L.; Monteiro, G. Gemcitabine: Metabolism and Molecular Mechanisms of Action, Sensitivity and Chemoresistance in Pancreatic Cancer. *Eur. J. Pharmacol.* 2014, 741, 8-16.

28. Schulze, H.; Kolter, T.; Sandhoff, K. Principles of Lysosomal Membrane Degradation: Cellular Topology and Biochemistry of Lysosomal Lipid Degradation. *Biochimica et Biophysica Acta (BBA) - Molecular Cell Research* 2009, 1793, 674-683.

CHAPTER 6

CONCLUSIONS AND FUTURE DIRECTIONS

This chapter was adapted in part from
Durfee, P. N.; Lin, Y-S.; Dunphy, D. R.; Muñiz, A. J.; Butler, K. S.; Humphrey, K. R.; Lokke, A. J.; Agola, J. O.; Chou, S. S.; Chen, I-M.; Wharton, W.; Townson, J. L.; Willman, C. L.; Brinker, C. J. Mesoporous Silica Nanoparticle-Supported Lipid Bilayers (Protocells) for Active Targeting and Delivery to Individual Leukemia Cells. ACS Nano 2016, DOI: 10.1021/acsnano.6b02819. © 2016 American Chemical Society.

And in part from from
Butler, K. S.*; **Durfee, P. N.***; Theron, C.; Ashley, C. E.; Carnes, E. C.; Brinker, C. J. Protocells: Modular Mesoporous Silica Nanoparticle-Supported Lipid Bilayers for Drug Delivery. Small 2016, 12, 2173−2185. (*Authors contributed equally to this work) © 2016 Wiley-VCH Verlag GmbH & Co. KGaA, Weinheim

6.1 Conclusions

The modular design of protocell constructs promises a new drug and disease agnostic platform for customized delivery and controlled release of multiple types of cargos and cargo combinations. Packaging drugs within MSNP core protected by the SLB may enable the re-purposing of drugs that have to date failed clinical trials due to poor solubility, high toxicity, and/or susceptibility to degradation. The supported bilayer can retain and protect fragile and/or highly soluble cargos and enable triggered release of the cargo upon acidification within the tumor or tumor microenvironment. The ability to add imaging agents to the core of the protocells gives rise to the potential for more specific imaging agents and even the development of theranostics which can provide both imaging and therapy simultaneously. The modularity of the protocell size, shape, pore architecture and surface chemistry further suggest applications in personalized medicine requiring individualized cargo combinations, targeting, and release profiles. However, the modularity and versatility of protocell technology means that there are many factors which must be accounted for in assessing biocompatibility, toxicity, drug release, and utility *in vivo* before protocell technology can be applied in patient populations.

Here, by systematically evaluating the influence of $SA_{lipid}:SA_{silica}$ and ionic strength on vesicle fusion to MSNPs, we established a robust processing protocol to prepare colloidally stable mMSNP supported lipid bilayers aka protocells characterized by size uniformity (PdI < 0.1) and long-term stability in biologically relevant media. The protocol we developed ($SA_{lipid}:SA_{silica} \approx 2:1$ and

ionic strength = 40 mM) using prismatic Hexagonal mMSNPs was shown to be transferable to MSNPs of differing size, shape, and pore morphology. Only for mMSNPs prepared with the largest pores (~ 18 nm) did we find fusion not to occur – presumably due to reduced van der Waals and electrostatic interactions and/or surface roughness arrested bilayer spreading.

Having established a robust process to prepare monosized protocells, we evaluated their long-term stability in biologically relevant media *in vitro* as well as in *ex ovo* and *in vivo* models and systems. We found that zwitterionic SLBs prepared with or without PEG conferred excellent stability to the protocells compared to the parent mMSNP. DSPC-based SLBs were shown to have longer-term stability than DOPC-based protocells in PBS at 37°C. However, DOPC-based protocell stability was restored by the removal of soluble oxygen. Furthermore, protocells prepared with both unsaturated DOPC and saturated DSPC SLBs were stable for over 72 hours in FBS enriched media suggesting that preparation and storage in de-oxygenated buffer or exposure to proteins prior to use would allow either formulation to be implemented *in vivo* depending on the desired characteristics of the specific application. While saturated SLBs, with demonstrated stability in standard PBS are easier to prepare and store, we believe protocells prepared with unsaturated SLBs could be used for *in vivo* targeting, where the fluid bilayer could support lateral diffusion of targeting ligands, enabling high avidity binding with low targeting ligand density, as previously reported *in vitro*.[1]

The behavior of DSPC-PEG-based protocells was assessed *ex ovo* in the CAM model whose diverging and converging vasculature recapitulates features of the liver and spleen and whose immune system is replete with professional phagocytic cells including Kupffer cells and sinusoidal macrophages. High-speed intravital imaging of protocells and target cells injected into the vasculature of the CAM model allowed direct observation of circulation, non-specific binding to the endothelium, uptake by white blood cells, and binding to target cells in a complex setting, containing blood proteins and a developing immune system. While *in vitro* assessment is standard practice and provides important information, we contend it lacks the complexity to accurately forecast *in vivo* outcomes. For example, by comparing monosized protocells with highly size polydisperse protocells, we demonstrated size monodispersity to be important for avoiding arrest in the capillary bed and uptake by immune cells. Monosized DSPC-PEG-based protocells, shown to be stable within complex CAM and *in vivo* mouse models, were conjugated with anti-EGFR antibodies while maintaining size monodispersity.

Flow cytometry combined with fluorescence microscopy showed a high degree of binding specificity of EGFR-targeted protocells to REH-EGFR and Ba/F3-EGFR ALL cells compared to EGFR-negative parental control cells. Using intravital imaging in the CAM, we directly observed selective binding of EGFR-targeted protocells to individual leukemic cells followed by delivery of a membrane impermeant cargo, while avoiding non-specific binding to endothelial cells and uptake by immune cells. Overall, we demonstrate that zwitterionic

monosized protocells prepared by vesicle fusion on mMSNP cores have long-term stability in complex biological media as judged by intravital imaging in the experimentally accessible CAM model. Colloidal stability is crucial to achieving targeting to individual (leukemic) distributed cells, where the EPR effect is inoperative.

Finally, we demonstrated the highly specific therapeutic efficacy of targeted protocells by delivery of the cytotoxic anti-cancer drug cargo gemcitabine to an engineered EGFR-expressing leukemic cell line, while sparing EGFR-negative parental cells from off-target effects. Further, we confirmed the biocompatibility of the protocell platform. We believe our optimized monosized protocell design has great potential for the *active* targeting, detection and treatment of highly disseminated metastatic cells including difficult to target circulating leukemia cells as well as combined *passive and active* tumor targeting employing the EPR effect. The logical next steps will include identifying the size limitations of the protocell platform, testing of alternative targeting conjugation chemistries, identifying unique targeting ligands for important diseases, and examining a large array of therapeutic cargo types to be evaluated *in vitro, ex ovo,* and ultimately in *in vivo* models of leukemia, including xenograft and primagraft model systems.

6.2 Preliminary *In Vivo* Targeting Experiments

With the success of monosized protocell development and evaluation in a complex embryonic CAM system, we have started to evaluate the targeted

binding of protocells *in vivo*, using MOLT4-CD19 and antibody-labelled protocells in a leukemia mouse model through a collaboration with the Children's Hospital of Philadelphia (CHOP), and funded through a grant from the Leukemia and Lymphoma Society (LLS). Our preliminary *in vitro* and *ex ovo* CD19 targeting studies are outlined in Chapter 5. The next aim is to undertake *in vivo* studies of ALL-targeted protocell and evaluate stability, biodistribution, uptake in normal and leukemic cells and tissues, and preliminary determinations of pharmacologic dose range, toxicology, and therapeutic efficacy in ALL xenograft models.

To examine biodistribution and ALL-targeted binding, we injected MOLT4-CD19 (cell line expresses green fluorescent marker) xenograft mice with either 1 mg of non-targeted or CD19-targeted protocells and imaged the mice using IVIS Lumina live animal imaging system at 4 hours post-injection. We detected the fluorescence of the cells and the protocells in circulation (**Figure 6.1**). While the number of mice used in this experiment is not sufficient, the biodistribution profile of targeted protocells appears more systemic than the untargeted protocells. The wider biodistribution of targeted protocells could be due to binding with MOLT4-CD19 cells in circulation; however, a larger study with more mice is needed to accurately assess the biodistribution of protocells *in vivo*.

At 48 hours post-injection, mice were sacrificed, blood and tissues were harvested to assess co-localization of protocells with MOLT4-CD19 cells. Interestingly, in the *ex vivo* fluorescence analysis of the long bones, we see a higher intensity of protocell fluorescence co-localized with the MOLT4-CD19 cells

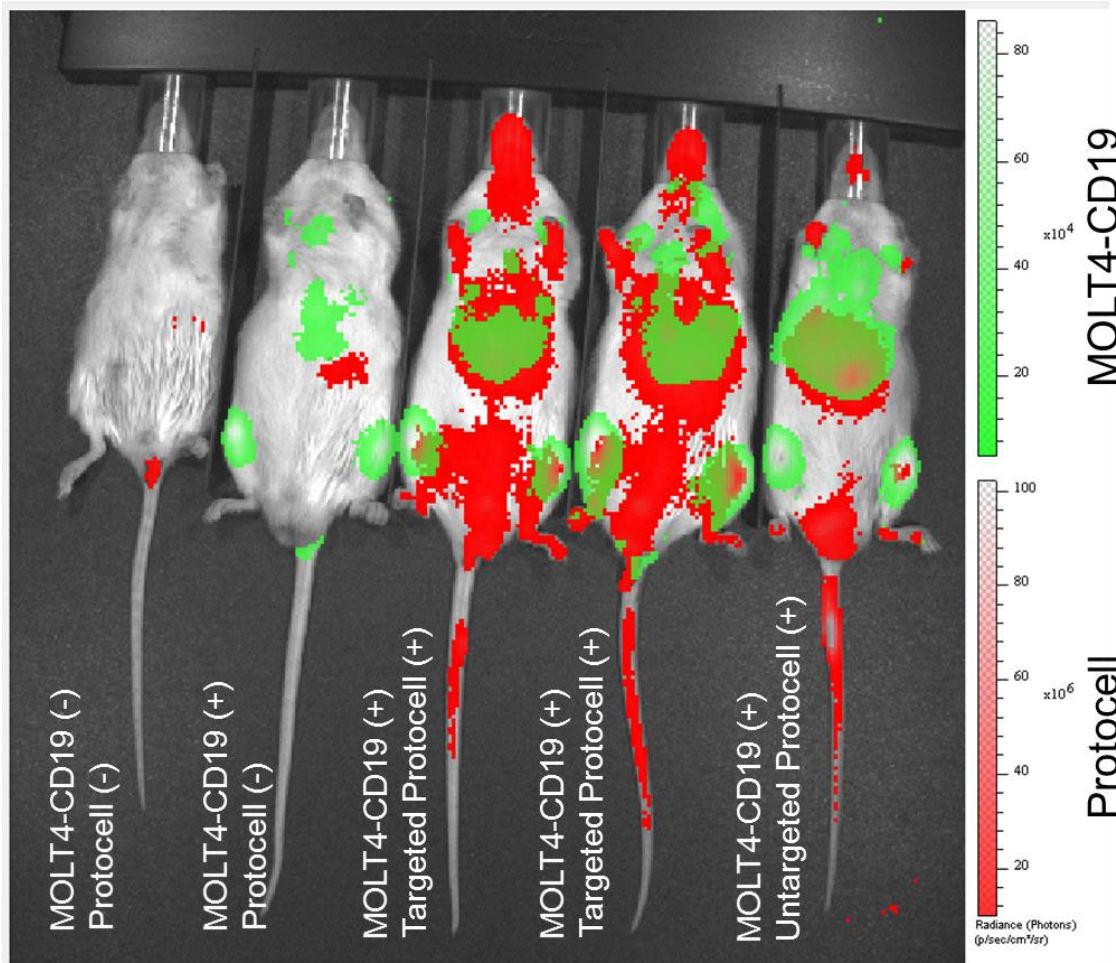**Figure 6.1 –** *Live Animal Imaging of Protocell Biodistribution*

Figure 6.1 – IVIS live animal imaging system used to image differential biodistribution of CD19-targeted and untargeted protocells (red) in the CHOP MOLT4-CD19 (green) xenograft model. Protocell/MOLT4+CD19 overlay image shows targeted protocells more systemic than untargeted protocells, with higher targeted protocell signal in the extremities.

(**Figure 6.2**). These preliminary results offer promising insight into the targeting potential for protocells *in vivo*. Larger scale experiments are planned in the near future and will require careful preparation of large batches of protocells to be loaded with therapeutic cargo to be shipped to CHOP for *in vivo* validation.

6.3 Future Directions

The modular design of the protocell platform has led to rapid advancement in this field; however, there are still many areas in which improvements can be made. For example, modifications can be made to the MSNP core, the external lipid layer, the targeting chemistry, and the cargo to create unique protocells for specific applications. Although the protocell has demonstrated utility in therapeutic delivery for cancer using both in *ex ovo*[2] and *in vivo* systems,[3-5] technological improvements could still be utilized to increase the therapeutic efficiency. In the case of Leukemia, we created monosized protocells with a prolonged circulation profile, with the addition of targeting chemistry to target cells in circulation,[2] however, we could use the same size control to optimize delivery of cancer therapeutics using the EPR effect. Size control could effect or direct site specific dissemination of protocells to differing body tissues in addition to the peripheral vasculature and other tissues (liver, spleen, bone marrow) which may harbor leukemic cells, or, protected tissues which serve as sanctuaries for leukemic cells (testes, brain) and are frequent sites of recurrent or relapsed disease following systemic chemotherapy treatment. For example, to target the bone marrow, a nanoparticle size range of 70 – 200 nm and spherical or rod shape is desirable; to target the brain and testicular region requires
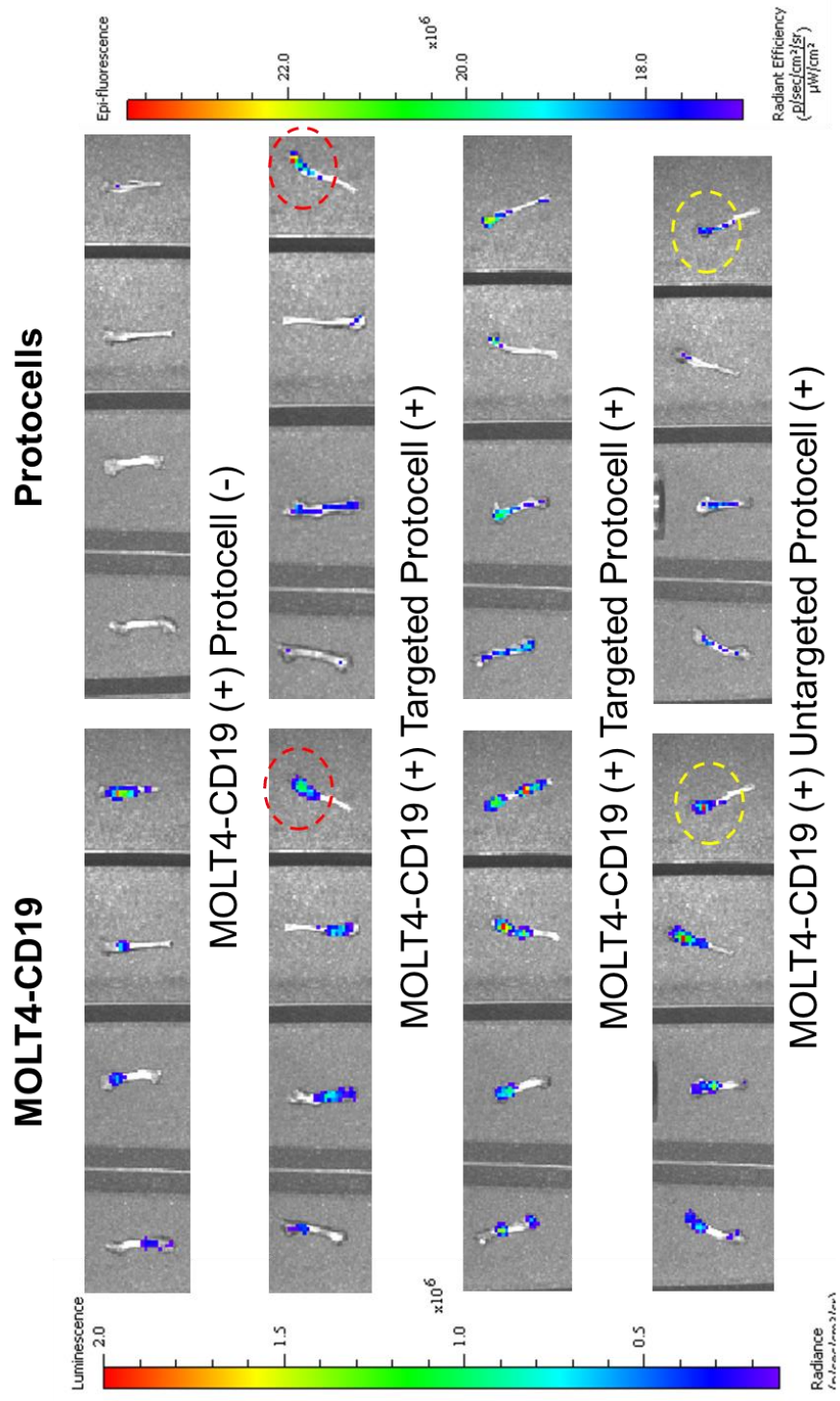
Figure 6.2 – *Ex Vivo Co-localization Imaging*

Figure 6.2 - *Ex vivo* IVIS analysis 48 hours post-injection of long bones shows protocells/MOLT4-CD19 cells co-localization with higher fluorescent intensity in the targeted protocells in regions containing target cells, highlighted by red dashed circles. Untargeted protocells also co-localize with MOLT4-CD19 cells, however the protocell intensity is much lower than that of targeted protocells (yellow dashed circles).

smaller 40 – 50 nm nanoparticles; to target the spleen and liver spherical nanoparticles greater than 100 nm in diameter are most effective.[6]

In addition to core MSNP size / shape modifications, the multitude of lipid formulations available for protocell assembly (**Table 3.5**) allows for a large variety of surface chemistries which can be used add functional targeting ligands. With the emergence of new chemical reactions more commonly known as click-chemistry combined with the ability to custom manufacture peptide, single chain variable fragment antibodies (scFv), antibodies, and other targeting ligands, many conjugation chemistry options are available to protocell modification.[7] In particular, copper-catalyzed or copper-free click chemistries are of particular interest for the conjugation of targeted ligands, as they possess the potential to reach quantitative yields and avoid immunogenicity due to strictly click-reactive lipids, while still allowing the addition of a wide variety of targeting ligands (**Figure 6.3**). While click-chemistry targeting modifications have yet to be reported in protocell research, they have the potential to greatly increase the utility of the protocell for *in vivo* applications.

Although the targeting modification reported in this dissertation has been shown to be highly specific, and can be used across multiple cell and target types, some limitations exist with this method. For example, using multiple steps to modify the lipid head groups with the targeting ligands including centrifugation, and bath sonication could potentially disrupt the SLB and cause cargo to leak during the process. In addition, NeutrAvidin is a large globular protein, as are full length antibodies and both can be recognized by the immune system and could

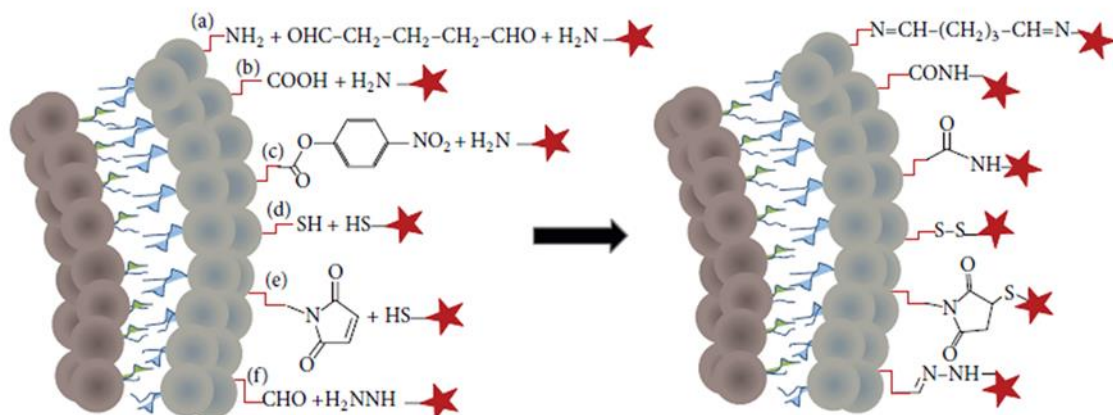**Figure 6.3 –** *Targeting Chemistry Strategies Schematic*

Figure 6.3 – New chemistry approaches for coupling ligands to the lipid bilayer of the protocell. Schematic shows a cross section of a lipid bilayer containing functional groups that form the basis for: copper (I)-catalyzed Huisgen 1,3-dipolar cycloaddition ligation (a and b), copper-free click chemistry ligation (c), Staudinger ligation (d), and tetrazine/trans-cyclooctene inverse electron demand Diels-Alder cycloaddition (e). Coupling ligands for each reaction are represented by a red star. Adapted and reproduced with permission.[7] © 2014, The Authors.

potentially limit the repeated use of the protocell platform due to an adaptive immune response. Regardless of the success demonstrated using the NeutrAvidin/Biotin "plug-and-play" targeting strategy, decreasing the size and number of targeting ligands on the surface would be highly beneficial to a reusable nanocarrier platform.

In addition to improved targeting chemistry, a comprehensive study in the delivery of a wide range of therapeutic cargo is needed. The protocell platform, may provide a second-life for drugs that have failed trials due to insolubility, non-specific cytotoxicity, and other undesirable side-effects, by sequestering drugs within the highly porous MSNP surface and sealing cargo within a SLB envelope until they can be delivered to the target destination. While the delivery of many cargos by protocells have been demonstrated *in vitro*, many have yet to be translated to *in vivo* systems. Therefore, further studies are needed to examine the loading, stability, and delivery of a wide variety of therapeutic cargos including: small molecules (hydrophilic, hydrophobic, neutral, and charged), proteins (enzymes and toxins), nucleic acids (DNA, mRNA, siRNA, and shRNA), and aptamers. These cargo-types can be evaluated *in vitro*, and using *ex ovo* methods described in this dissertation, we can rapidly evaluate the potential behavior of cargo delivery in a complex animal system prior to expensive and time-intensive *in vivo* animal experiments.

In addition to the evaluation of different cargo classes, a comprehensive examination of cargo release or leakage which can lead to toxicity and limit therapeutic effectiveness must be implemented. A simple method to prevent

premature leakage from the protocell would be to use a hydrophobic modification of the MSNP surface, then soaking these hydrophobic cores in an organic solvent with hydrophobic cargo, followed by the addition of a lipid monolayer and transferred to an aqueous phase, thereby sealing hydrophilic drugs within a hybrid-bilayer protocell.[8, 9] Another method for controlled drug release which could allow the protocells to react to the tumor microenvironment is the use of lipids covalently attached to the MSNP surface through disulfide bonds. This method provides a controlled release mechanism for cargo only in the presence of disulfide reducing conditions likely to be present in tumors and endocytic vesicles.[10] Other potential agents such as complex nanomachines or molecular valves can be incorporated to increase the specificity of drug release from the MSNP core.[11] These technologies have only been tested in *in vitro* systems, but have the potential to greatly reduce the toxicity of therapeutic chemotherapy delivered by the protocell. Although, as we increase the complexity of the protocell platform, we create more potential failure points, therefore a less complicated method such as, electrostatic attraction and/or hydrophobic interactions will likely lead to greater success.

Perhaps the most attractive feature of the protocell is the MSNP core in which we have fine control over the synthesis and incorporation of diagnostic components, making protocells ideal imaging and theranostic agents. Fluorescent-labelled protocells have been used *in vivo* to examine biodistribution in a tumor model.[3] Further studies varying the size, shape, and SLB composition have yet to be examined and are crucial in the development of disease specific

protocells. Moreover, theranostic protocells allow for real-time assessment of the biodistribution in both normal and diseased tissue, providing invaluable information for the development and monitoring of protocells in a clinical setting. The ability to synthesize MSNP cores that incorporate a metallic or magnetic core,[11-14] fluorophores,[3-5] positron emission tomography (PET) imaging agents,[15] or even other nanoparticles such as quantum dots[1] would allow the development of protocells as imaging agents for a variety of imaging technologies.

While this dissertation focuses on the optimization, characterization, and application of targeted protocells for use in cancer therapeutics, many of the protocell features discussed have potential for several other applications, including antiviral and antibacterial therapy, vaccine development, synthetic red blood cells (i.e. oxygen carriers), diagnostic devices, as well as other non-medical material applications including energy and surface coating.

6.3 References

1. Ashley, C. E.; Carnes, E. C.; Phillips, G. K.; Padilla, D.; Durfee, P. N.; Brown, P. A.; Hanna, T. N.; Liu, J.; Phillips, B.; Carter, M. B.; Carroll, N. J.; Jiang, X.; Dunphy, D. R.; Willman, C. L.; Petsev, D. N.; Evans, D. G.; Parikh, A. N.; Chackerian, B.; Wharton, W.; Peabody, D. S.; Brinker, C. J. The Targeted Delivery of Multicomponent Cargos to Cancer Cells by Nanoporous Particle-Supported Lipid Bilayers. *Nat. Mater.* 2011, 10, 389-397.

2. Durfee, P. N.; Lin, Y.-S.; Dunphy, D. R.; Muñiz, A. J.; Butler, K. S.; Humphrey, K. R.; Lokke, A. J.; Agola, J. O.; Chou, S. S.; Chen, I. M.; Wharton, W.; Townson, J. L.; Willman, C. L.; Brinker, C. J. Mesoporous Silica Nanoparticle-Supported Lipid Bilayers (Protocells) for Active Targeting and Delivery to Individual Leukemia Cells. *ACS Nano* 2016.

3. Meng, H.; Wang, M.; Liu, H.; Liu, X.; Situ, A.; Wu, B.; Ji, Z.; Chang, C. H.; Nel, A. E. Use of a Lipid-Coated Mesoporous Silica Nanoparticle Platform for Synergistic Gemcitabine and Paclitaxel Delivery to Human Pancreatic Cancer in Mice. *ACS Nano* 2015, 9, 3540-3557.

4. Wang, D.; Huang, J.; Wang, X.; Yu, Y.; Zhang, H.; Chen, Y.; Liu, J.; Sun, Z.; Zou, H.; Sun, D.; Zhou, G.; Zhang, G.; Lu, Y.; Zhong, Y. The Eradication of Breast Cancer Cells and Stem Cells by 8-Hydroxyquinoline-Loaded Hyaluronan Modified Mesoporous Silica Nanoparticle-Supported Lipid Bilayers Containing Docetaxel. *Biomaterials* 2013, 34, 7662-7673.

5. Zhang, X.; Li, F.; Guo, S.; Chen, X.; Wang, X.; Li, J.; Gan, Y. Biofunctionalized Polymer-Lipid Supported Mesoporous Silica Nanoparticles for Release of Chemotherapeutics in Multidrug Resistant Cancer Cells. *Biomaterials* 2014, 35, 3650-3665.

6. Krishnan, V.; Rajasekaran, A. K. Clinical Nanomedicine: A Solution to the Chemotherapy Conundrum in Pediatric Leukemia Therapy. *Clin. Pharmacol. Ther.* 2014, 95, 168-178.

7. Marqués-Gallego, P.; de Kroon, A. I. Ligation Strategies for Targeting Liposomal Nanocarriers. *BioMed research international* 2014, 2014.

8. Wang, L.-S.; Wu, L.-C.; Lu, S.-Y.; Chang, L.-L.; Teng, I. T.; Yang, C.-M.; Ho, J.-a. A. Biofunctionalized Phospholipid-Capped Mesoporous Silica Nanoshuttles for Targeted Drug Delivery: Improved Water Suspensibility and Decreased Nonspecific Protein Binding. *ACS Nano* 2010, 4, 4371-4379.

9. Han, N.; Zhao, Q.; Wan, L.; Wang, Y.; Gao, Y.; Wang, P.; Wang, Z.; Zhang, J.; Jiang, T.; Wang, S. Hybrid Lipid-Capped Mesoporous Silica for

Stimuli-Responsive Drug Release and Overcoming Multidrug Resistance. *ACS Appl. Mater. Interfaces* 2015, 7, 3342-3351.

10.   Roggers, R. A.; Lin, V. S. Y.; Trewyn, B. G. Chemically Reducible Lipid Bilayer Coated Mesoporous Silica Nanoparticles Demonstrating Controlled Release and Hela and Normal Mouse Liver Cell Biocompatibility and Cellular Internalization. *Molecular Pharmaceutics* 2012, 9, 2770-2777.

11.   Tarn, D.; Ashley, C. E.; Xue, M.; Carnes, E. C.; Zink, J. I.; Brinker, C. J. Mesoporous Silica Nanoparticle Nanocarriers: Biofunctionality and Biocompatibility. *Acc. Chem. Res.* 2013, 46, 792-801.

12.   Chen, Y.; Wang, X.; Liu, T.; Zhang, D. S.-z.; Wang, Y.; Gu, H.; Di, W. Highly Effective Antiangiogenesis Via Magnetic Mesoporous Silica-Based Sirna Vehicle Targeting the Vegf Gene for Orthotopic Ovarian Cancer Therapy. *International journal of nanomedicine* 2014, 10, 2579-2594.

13.   Kim, J.; Kim, H. S.; Lee, N.; Kim, T.; Kim, H.; Yu, T.; Song, I. C.; Moon, W. K.; Hyeon, T. Multifunctional Uniform Nanoparticles Composed of a Magnetite Nanocrystal Core and a Mesoporous Silica Shell for Magnetic Resonance and Fluorescence Imaging and for Drug Delivery. *Angewandte Chemie International Edition* 2008, 47, 8438-8441.

14.   Wu, S. H.; Lin, Y. S.; Hung, Y.; Chou, Y. H.; Hsu, Y. H.; Chang, C.; Mou, C. Y. Multifunctional Mesoporous Silica Nanoparticles for Intracellular Labeling and Animal Magnetic Resonance Imaging Studies. *ChemBioChem* 2008, 9, 53-57.

15.   Kumar, R.; Roy, I.; Ohulchanskky, T. Y.; Vathy, L. A.; Bergey, E. J.; Sajjad, M.; Prasad, P. N. In Vivo Biodistribution and Clearance Studies Using Multimodal Organically Modified Silica Nanoparticles. *ACS nano* 2010, 4, 699-708.

APPENDIX A

Appendix A.1 was adapted from
Durfee, P. N.; Lin, Y-S.; Dunphy, D. R.; Muñiz, A. J.; Butler, K. S.; Humphrey, K. R.; Lokke, A. J.; Agola, J. O.; Chou, S. S.; Chen, I-M.; Wharton, W.; Townson, J. L.; Willman, C. L.; Brinker, C. J. Mesoporous Silica Nanoparticle-Supported Lipid Bilayers (Protocells) for Active Targeting and Delivery to Individual Leukemia Cells. ACS Nano 2016, DOI: 10.1021/acsnano.6b02819. © 2016 American Chemical Society.

A.1 – Calculations to Identify Optimal Liposome to mMSNP Surface Area Ratio

To estimate the number of particles in solution *(n)*, we employed a shape applicable model to calculate mMSNP exterior surface area *(SA)* and volume *(V$_{mMSNP}$)* from dimensional measurements obtained from TEM image analysis *(n = 50)*, pore volume *(V$_{pore}$)* measurements from nitrogen adsorption–desorption isotherms, a mesoporous silica density (ρ) of 2 g/cm^3, and a sample mass (*m*). The equations below were used to estimate the number of particles in solution per unit concentration (mg/mL) and the external particle surface areas (nm^2) used in determination of the lipid:silica surface area ratio.

A.1.1 Hexagonal mMSNP Calculations
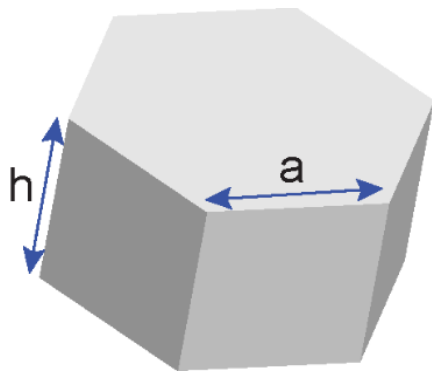
$$SA_{mMSNP} = 6ah + 3\sqrt{3} * a^2$$
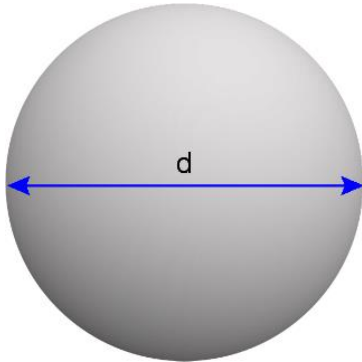
$$V_{mMSNP} = \frac{3\sqrt{3}}{2}a^2h$$

$$n_{mMSNP} = \frac{(m/\rho) + (m * V_{pore})}{V_{mMSNP}}$$

For example – **a = 44.80 nm**, **h = 50.68 nm**, *m* = 0.1 g, ρ = 2 g/cm^3, *V$_{pore}$* = 0.83 cm^3/g

SA$_{mMSNP}$ = 2.41 x 10^4 nm^2, **V$_{mMSNP}$** = 2.64 x 10^5 nm^3, **n$_{mMSNP}$** = 4.99 x 10^{14} mMSNPs

A.1.2 Spherical mMSNP Calculations

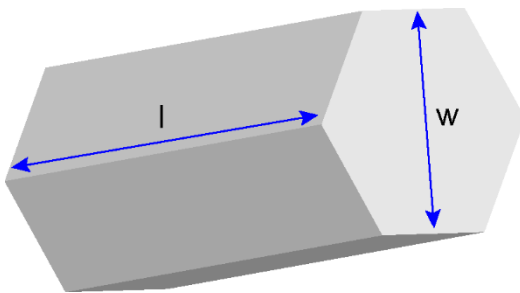$$SA_{mMSNP} = 4\pi(d/2)^2$$

$$V_{mMSNP} = \frac{4}{3}\pi(d/2)^3$$

$$n_{mMSNP} = \frac{(m/\rho) + (m * V_{pore})}{V_{mMSNP}}$$

For example, (5 nm pore mMSNP) – **d = 99.32 nm**, m = 0.1 g, ρ = 2 g/cm³, V_{pore} = 0.86 cm³/g

SA_{mMSNP} = 3.11 x 10⁴ nm², **V_{mMSNP}** = 5.17 x 10⁵ nm³, **n_{mMSNP}** = 2.69 x 10¹⁴ mMSNs

A.1.3 Rod-like mMSNP Calculations

$$SA_{mMSNP} = 2\pi(w/2)(l) + 2\pi(w/2)^2$$

$$V_{mMSNP} = \pi(w)^2 l$$

$$n_{mMSNP} = \frac{(m/\rho) + (m * V_{pore})}{V_{mMSNP}}$$

For example – **w = 81.97 nm**, **l = 176.68 nm**, m = 0.1 g, ρ = 2 g/cm³, V_{pore} = 0.87 cm³/g

SA_{mMSNP} = 5.69 x 10⁴ nm², **V_{mMSNP}** = 9.77 x 10⁵ nm³, **n_{mMSNP}** = 1.42 x 10¹⁴ mMSNPs

Next we estimated the surface area (*SA*) of liposomes by calculating the number of lipid molecules per unit mass (*m*) and assumed 0.59 nm^2 to represent the area of a single lipid head group. We also assume cholesterol area does not contribute to the external surface area of liposomes. Finally, we assume the internal surface area (*SA$_{innner}$*) is equal to half the total SA of the liposomes per unit mass.

$$Moles_{component} = \frac{m_{component}}{MW_{component}} N_A$$

$$SA_{inner} = (0.59 * \sum_{i=1}^{n} Moles_{i_{component}})/2$$

For example – DSPC:chol:DSPE-PEG$_{2000}$ liposomes – mol ratio (49:49:2)

DSPC *MW* = 790.145 g/mol, DSPE-PEG$_{2000}$ *MW* = 2805.497 g/mol, *m* = 0.2 g

SA$_{innner}$ = 2.54 x 10^{19} nm^2

To estimate the interior liposome surface area to total exterior mMSNP surface area, we multiplied the SA$_{mMSN}$ by the number of mMSNPs (*n*) per unit mass, then we divided liposomes interior SA by mMSNPs surface area per unit mass at the 2:1 mass ratio experimentally determined as optimal (See **Figure 3.3**).

$$SA_{total\ mMSNPs} = n_{mMSNP} * SA_{mMSNP}$$

$$SA\ ratio = SA_{liposome\ inner} / SA_{total\ mMSNPs}$$

For example – Hexagonal mMSNPs (calculated above) m = 0.1 g, SA_{mMSN} = 2.41 x 10^4 nm^2, n_{mMSN} = 4.99 x 10^{14} mMSNPs, Liposomes (calculated above) SA_{innner} = 2.54 x 10^{19} nm^2

SA ratio = 2.11 : 1

The calculated mass of fluorescent liposome (DSPC:chol:DSPE-PEG$_{2000}$:22-(N-(7-Nitrobenz-2-Oxa-1,3-Diazol-4-yl)Amino)-23,24-Bisnor-5-Cholen-3β-Ol (NBD-Chol) – 54:43:2:1 mol %) to mMSNP (118.7 nm) is 0.263 to 1. The experimental quantification of mass of fluorescent labeled liposome to mMSN is 0.276 to 1, as measured from fluorescence intensity of unbound liposomes in the supernatant following centrifugation of the protocells compared to a standard curve generated from known fluorescent liposome concentration. The calculated and experimental values are within 4.7 % of each other, which is supportive of our method of surface area ratio calculations.

A.2 – Calculations to Quantify Surface Area and Pore Volume

The surface area and pore size of MSNPs described in this dissertation were calculated following the Brunauer-Emmet-Teller (BET) equation and standard Barrett-Joyer-Halenda (BJH) method.
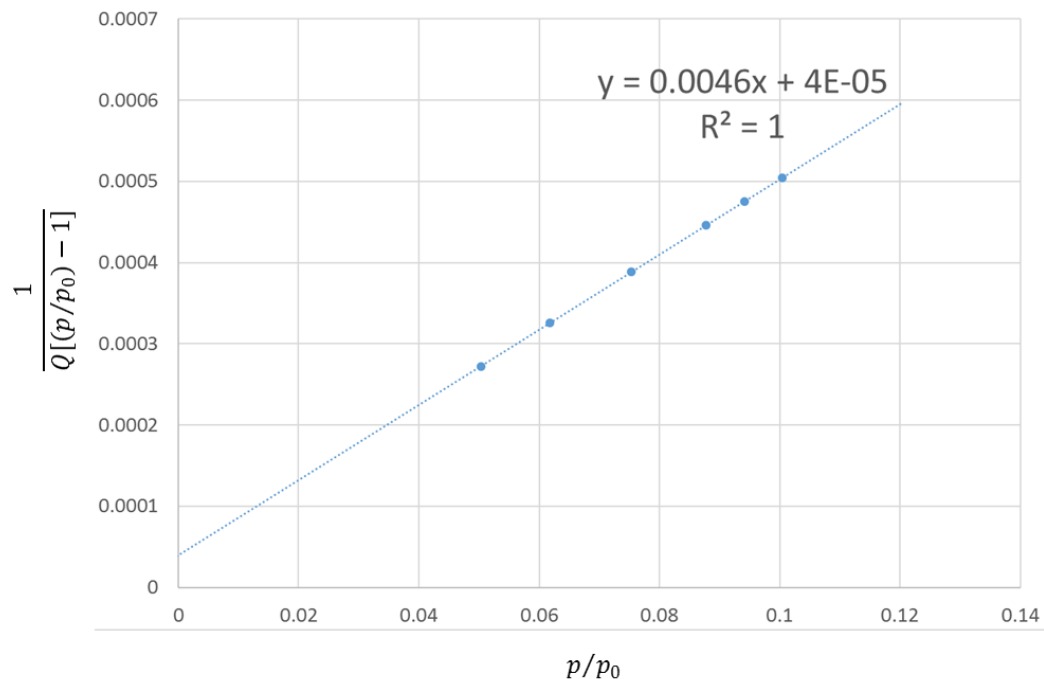
Example calculations for SA and pore size for Hexagonal mMSNPs below:
First, we generate the data obtained from the adsorption isotherm as a straight line using quantity adsorbed (Q) in cm³/g at STP, and relative pressure (p/p_0) from 0.05 to 0.1

$$y = \frac{1}{Q[(p/p_0) - 1]}$$

$$x = p/p_0$$

BET Plot

$y = 0.0046x + 4E\text{-}05$
$R^2 = 1$

x-axis: p/p_0
y-axis: $\frac{1}{Q[(p/p_0) - 1]}$

Next we use the trendline equation to calculate the monolayer adsorbed gas quantity (v_m) and the BET constant (c). We use the value of the slope (A) and the y-intercept (I) in the equations below.

$$v_m = \frac{1}{(A + I)} = \frac{1}{(4.63 \times 10^{-3} + 3.7 \times 10^{-5})} = \mathbf{214.27 \; cm^3/g \; STP}$$

$$c = 1 + \frac{A}{I} = 1 + \frac{4.63 \times 10^{-3}}{3.7 \times 10^{-5}} = \mathbf{126.14}$$

To calculate the surface area (SA), we use the values v_m, Avogadro's Number (N_A), the adsorption cross section of N_2 (s) = **0.162 nm²**, the molar volume of the adsorbate gas (V) = **34.65 cm³mol⁻¹** at 77K, and a total of mass of mMSNPs (a) = **0.183 g**.

$$SA = \frac{(v_m \cdot N_A \cdot s \cdot a)}{V} = \frac{(214.27 \cdot N_A \cdot 1.62 \times 10^{-19} \; m^2 \cdot 0.0183 \; g)}{34.65} = \mathbf{1103 \; m^2}$$

BET values are typically calculated by the software used to run the program. Pore size determination uses a modified Kelvin equation to relate the amount of adsorbate removed as the *p/p₀* is decreased. Solving pore size using BJH equations contains many variables and is complicated to solve manually but can simply be tabulated by the same software used to run the program.

A.3 – Calculations to Quantify Percent Hemolysis

Whole human blood (5 mL) stabilized in K$_2$EDTA tubes (BD Biosciences) and purified by centrifugation at 500 x g for 10 minutes to isolate RBCs from serum. This step was repeated five times, then RBCs were diluted in 50 mL PBS. Next, either bare mMSNPs or protocells were added the diluted RBCs and stored at 37 °C for 3 hours. Samples were centrifuged at 300 x g for 3 minutes, then 100 µL of supernatant from each sample was transferred to a 96-well plate. Hemoglobin absorbance was measured using a BioTek microplate reader (Winooski, VT) at 541 nm. Percent hemolysis was calculated using equation below. Where *negative control* = RBCs diluted in PBS, and *positive control* = RBCs diluted in D.I. water.

$$Percent\ hemolysis = \left(\frac{Sample\ Abs_{541\ nm} - Neg.Control\ Abs_{541\ nm}}{Pos.Control\ Abs_{541\ nm} - Neg.Control\ Abs_{541\ nm}}\right) \times 100\%$$

For example – 100 µg of MSNPs (n = 2) were incubated with RBCs and the average measurement **Abs$_{541\ nm}$ = 0.446**, the Positive control average **Abs$_{541\ nm}$ = 0.5745** and the Negative control average **Abs$_{541\ nm}$ = 0.034**.

$$Percent\ hemolysis_{MSNP} = \left(\frac{0.446 - 0.034}{0.5745 - 0.034}\right) \times 100\% = \mathbf{76.22\ \%}$$

For example – 100 µg of protocells (n = 2) were incubated with RBCs and the average measurement **Abs$_{541\ nm}$ = 0.04**, the Positive control average **Abs$_{541\ nm}$ = 0.5745** and the Negative control average **Abs$_{541\ nm}$ = 0.034**.

$$Percent\ hemolysis_{Protocell} = \left(\frac{0.04 - 0.034}{0.5745 - 0.034}\right) \times 100\% = \mathbf{1.11}\ \%$$

Percent hemolysis experiments were performed using three independent experiments with (n = 2) for each MSNP / protocell formulation. Values obtained using equations above were averaged and the mean ± SD were plotted on the graph in **Figure 3.10**.

A.4 – Calculations to Quantify Loading Efficiency of YO-PRO®-1 and GEM

To quantify YO-PRO®-1 loading, protocells were pelleted by centrifugation and resuspended in DMSO with bath sonication, this step was repeated twice. Since YO-PRO®-1 is more soluble in DMSO and the SLB is unstable, the wash steps destabilize the protocell membrane and extract the YO-PRO®-1 from the pores. Supernatants were pooled and concentration was determined using a microplate reader fluorescence measurement at 480/510 nm. The fluorescence numbers obtained were compared to a standard curve generated using a serial dilution YO-PRO®-1. We calculated a mean 25 % loading efficiency of YO-PRO®-1 for protocells used in the model drug delivery experiments *in vitro* and *ex ovo*.

To load and quantify GEM, 0.5 mg of Hexagonal mMSNPs (m_{mMSNP}) were suspended in 50 µL of GEM dissolved in D.I. water at 10 mg/mL ($m_0 = 0.5$ mg) and stored for 12 hours at 4 °C. After drug loading, targeted protocells were prepared using method described earlier in Anti-EGFR targeted protocell preparation (**Details in – 5.3.2 Anti-EGFR protocell preparation**). At each step, supernatant was collected, pooled ($v_1 = 2.55$ mL), and GEM loading was determined using a microplate reader absorbance measurement at 265 nm. A standard curve generated from a serial dilution of GEM in PBS (n = 3) was used to calculate the concentration of GEM in the supernatant. To account for absorbance signal from non-GEM components in the supernatant, unloaded protocells were prepared simultaneously under identical conditions and measured at 265 nm. This absorbance value ($Abs_{control}$) was subtracted from the

value obtained from supernatant containing GEM (*Abs*GEM) prior to calculation of

GEM concentration based on standard curve (equation below).

$$c_1 = \frac{(Abs - 0.0507)}{7.7115}$$

For example, we used ($m_{mMSNP} = 0.5$ mg), and ($m_0 = 0.5$ mg) and we obtained

(*Abs*GEM = 2.51) and (*Abs*control = 1.18).

$$c_1 = \frac{(2.51 - 1.18) - 0.0507}{7.7115} = \boldsymbol{0.17\ mg/mL}$$

The total volume of the pooled supernatant is used to calculate the

amount of GEM in the supernatant where $c_1 = 0.17$ mg/mL and $v_1 = 2.55$ mL (see

equation below).

$$m_1 = c_1 \times v_1$$

$$m_1 = 0.17 \times 2.55 = \boldsymbol{0.43\ mg}$$

The supernatant amount (m_1) was then subtracted from the starting GEM

amount (m_0) to estimate the total amount loaded into protocells (see equation

below)

$$m_{loaded} = m_0 - m_1$$

$$m_{loaded} = 0.5 - 0.43 = \boldsymbol{0.07\ mg}$$

To estimate the loading capacity as a percentage of weight we use the

formula below.

$$Loading\ capacity = \left(\frac{m_{loaded}}{m_{mMSNP}}\right) \times 100\ \%$$

$$Loading\ capacity = \left(\frac{0.07}{0.5}\right) \times 100\ \% = \boldsymbol{14}\ \% \ (\boldsymbol{w/w})$$

This experiment was repeated 4 times with different Hexagonal mMSNP preparations and we determined the average GEM loading capacity of protocell = 15.25 % ± 1.6 % (mean ± SD). While the loading percentage of our protocells is lower than what was reported by Dr. Nel's group, our loading conditions contain half the amount of GEM that was described by the Meng *et.al.*[20] Since GEM is neutral at physiological pH, and mMSNPs are negatively charged, we do not suspect an electrostatic interaction to play a significant role in loading, instead suspect the GEM and mMSNPs will reach an equilibrium state where the small molecule drug will occupy the high internal space of the pores and will then be encapsulated with the addition of the lipid bilayer in protocell assembly.

APPENDIX B

B.1 – Example TEM Measurements of MSNP Dimensional Features

Use scale bar to determine number of pixels / nm then draw lines to calculate length
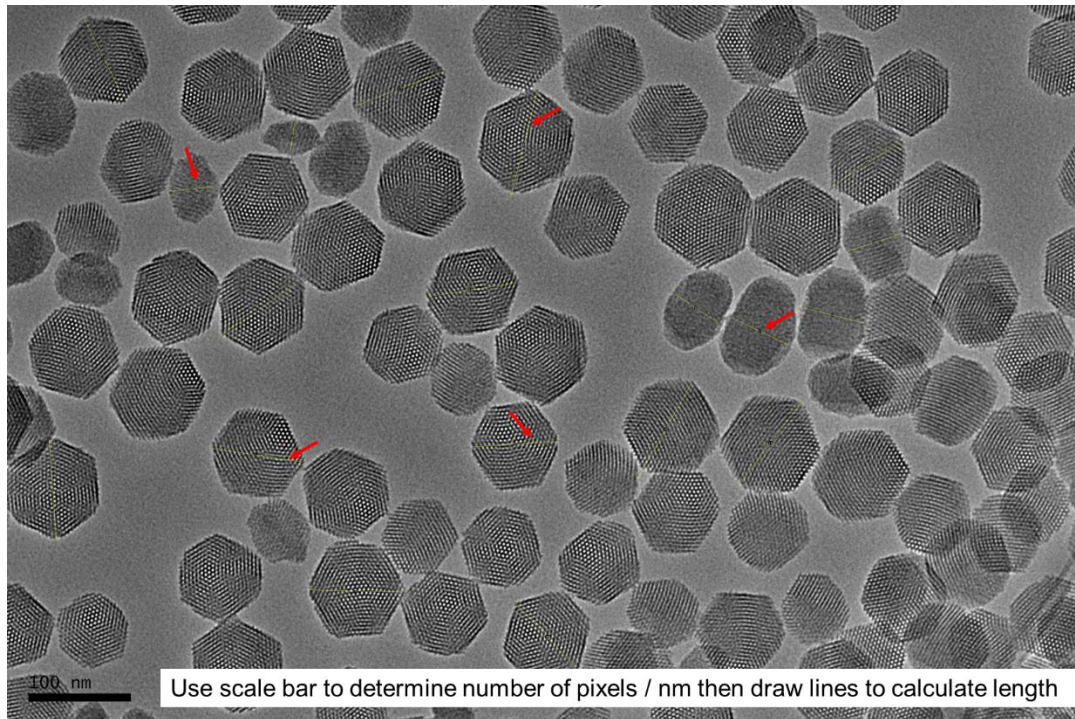
B.1 – Example image analyzed in ImageJ software, I draw a line along the scale bar provided by the TEM software, then draw several lines across the long-axis and short axis of the Hexagonal MSNPs. I used 50 measurements of each MSNP and calculated the mean ± SD for each particle, and used these measurements in the size and SA ratio analyses in **Table 3.1** and **Figure 3.3**.

B.2 – Example TEM Measurements of Bilayer Thickness
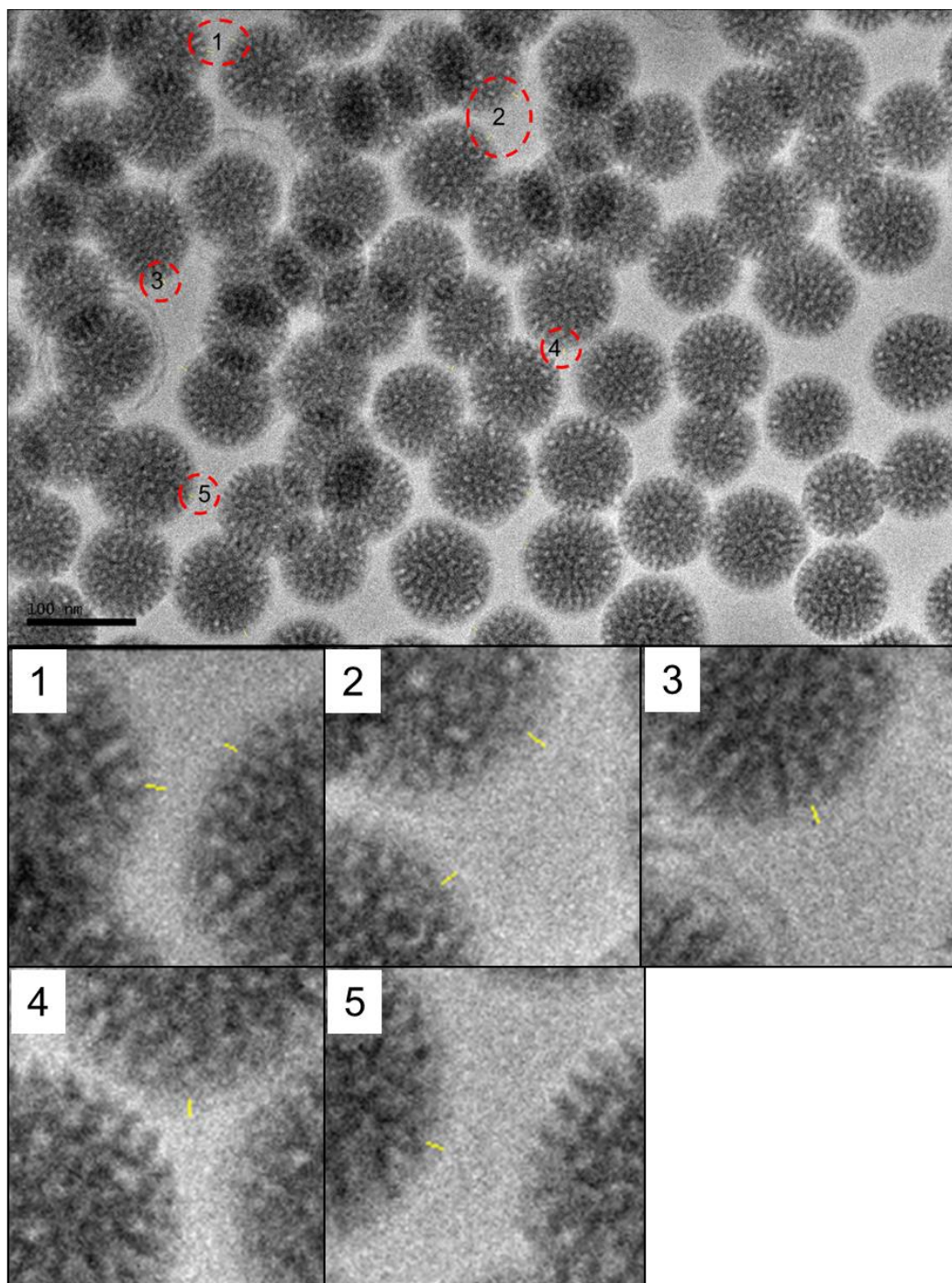
B.2 – Example image analyzed in ImageJ software, I draw a line along the scale bar provided by the TEM software, then draw several lines across the edge of the high contrast MSNPs across the slightly lower contrast SLB perimeter around the MSNP. I highlighted 5 regions to show the yellow measurement lines. I used 33 measurements of each protocell shape and calculated the mean ± SD for each particle, and used these measurements in the bilayer thickness analyses in **Figure 3.4**.

## B.3 – Fluorescent Microscopy Imaging of Ba/F3 and Ba/F3-EGFR Cells
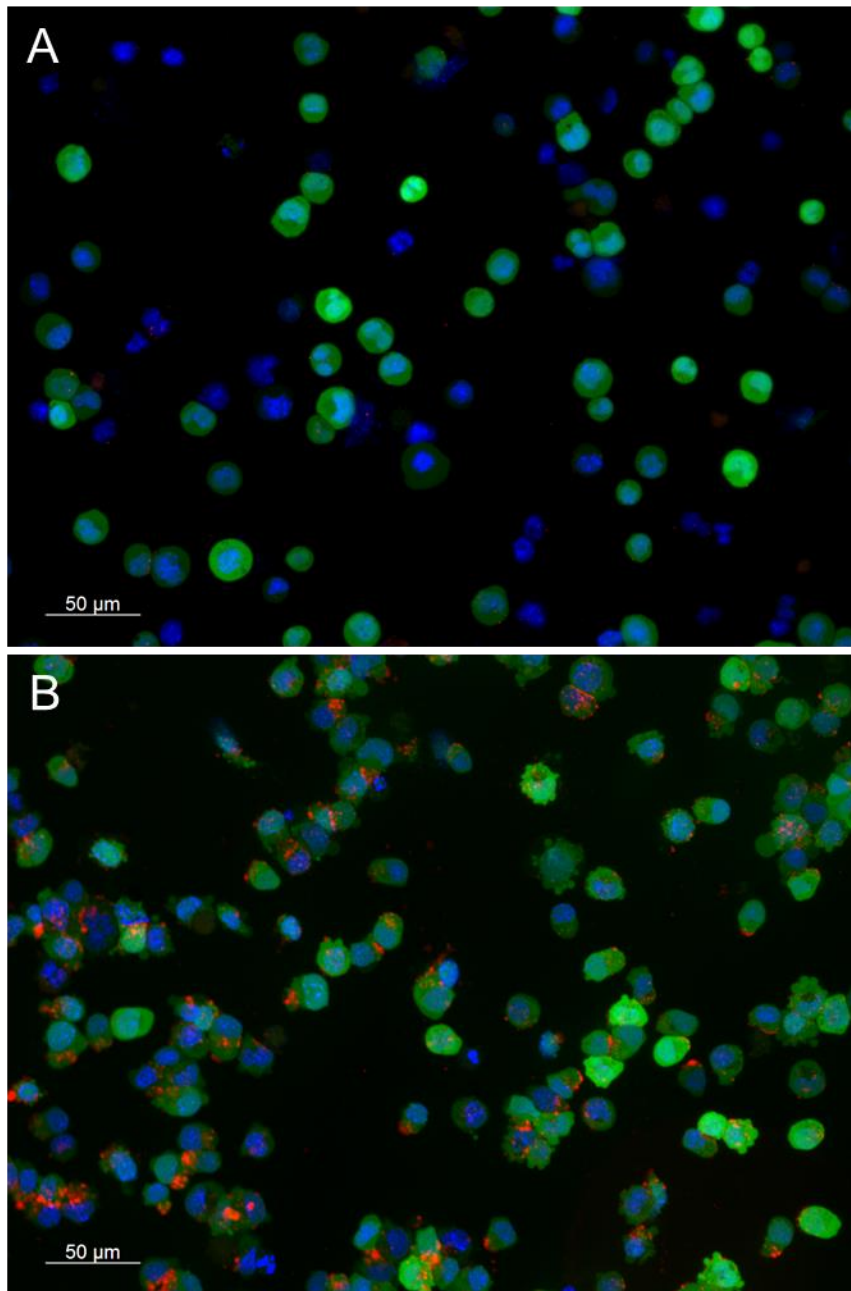
B.3 - A) Fluorescent microscopy shows minimal EGFR-targeted protocell (red) interactions with a non-EGFR expressing BAF cell line after 1-hour incubation (blue – DAPI stained nuclei, green – phalloidin stained actin), while B) targeted protocells (red) exhibit a high degree of binding to an EGFR expressing BAF cell line. Flow cytometry analysis of protocells incubated with C) BAF and D) BAF-EGFR confirm fluorescent microscopy analysis (grey = no protocell control, blue = EGFR-targeted protocells). These images correspond to **Figure 5.4**.

## B.4 – Additional REH-EGFR Targeted Binding in the CAM Images
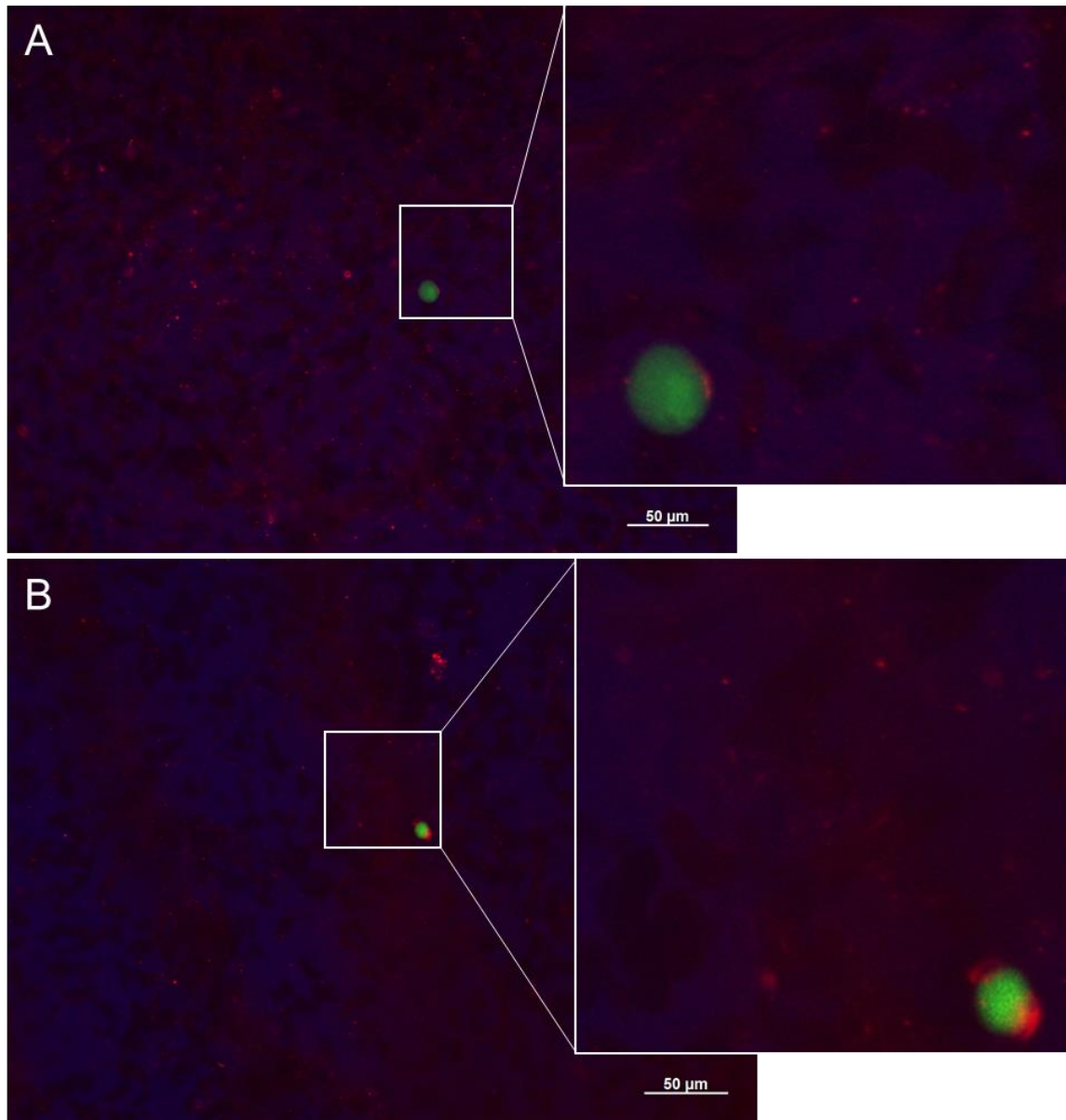
B.4 – Intravital fluorescent microscopy images acquired *ex ovo* in the CAM model reveal stable circulation of EGFR targeted protocells (red) and binding to REH-EGFR cells (green) in circulation. Both A) and B) were taken 1-hour post injection. Highlighted region shows individual protocells in flow and magnifies the protocell/cell interactions. These images correspond to **Figure 5.5**.

**B.5 – Additional REH-EGFR Targeted YO-PRO®-1 Delivery CAM Images**
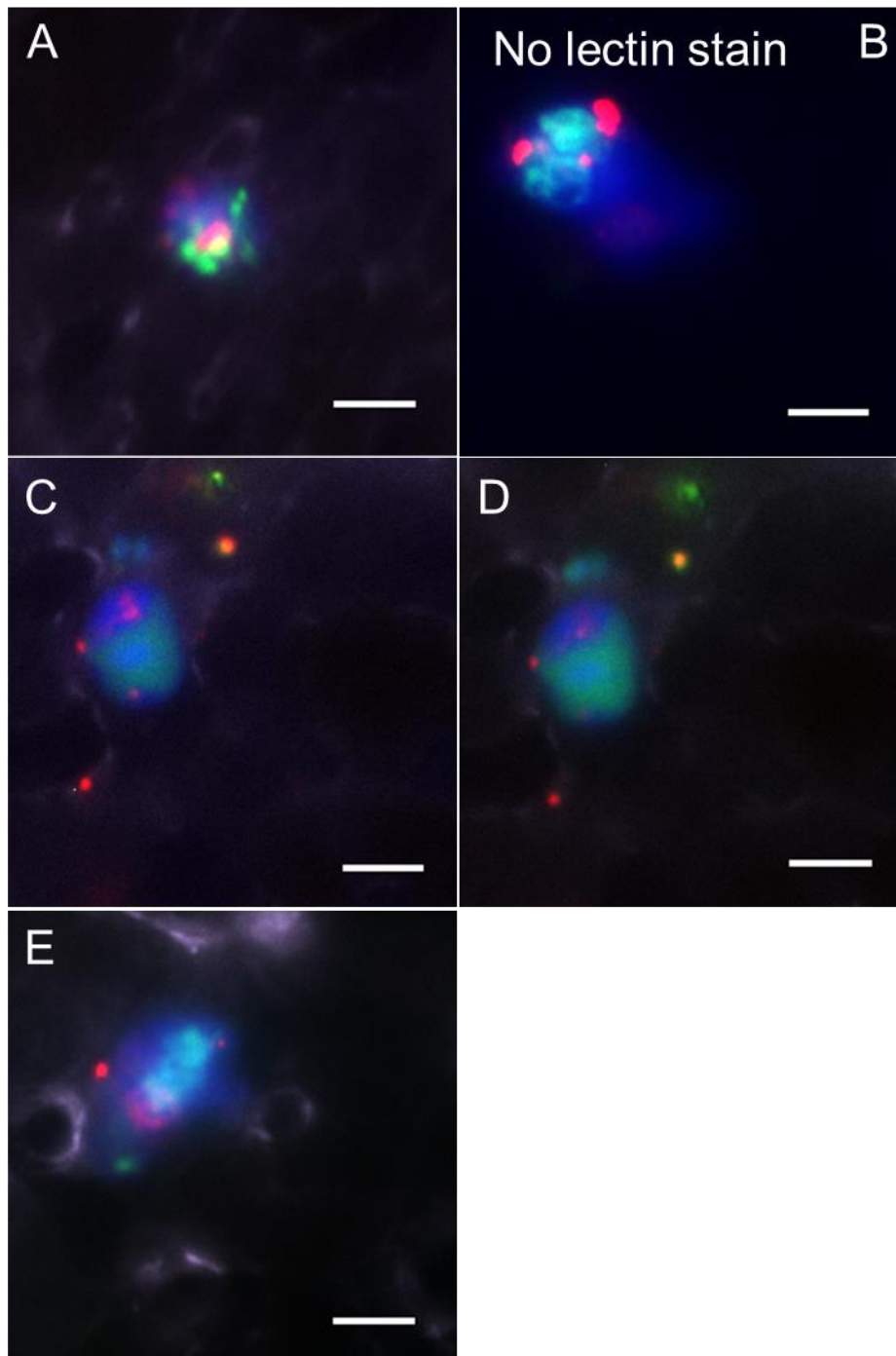
B.5 - Intravital fluorescent microscopy images acquired *ex ovo* in the CAM model showing YO-PRO®-1 cell impermeant cargo (green) loaded, fluorescent EGFR-targeted protocells (red) binding to and releasing cargo within REH-EGFR cells (blue) in a live animal model. Lectin vascular stain (lavender) added and targeting was imaged at 16 hours post injection. Images acquired at 63x magnification, Scale bar = 5 µm. Figures C) and D) are the same cell imaged in different focal planes. These images correspond to **Figure 5.16**.

B.6 – High Resolution Images of YO-PRO®-1 Delivery to MOLT4-CD19 cells *In Vitro.*
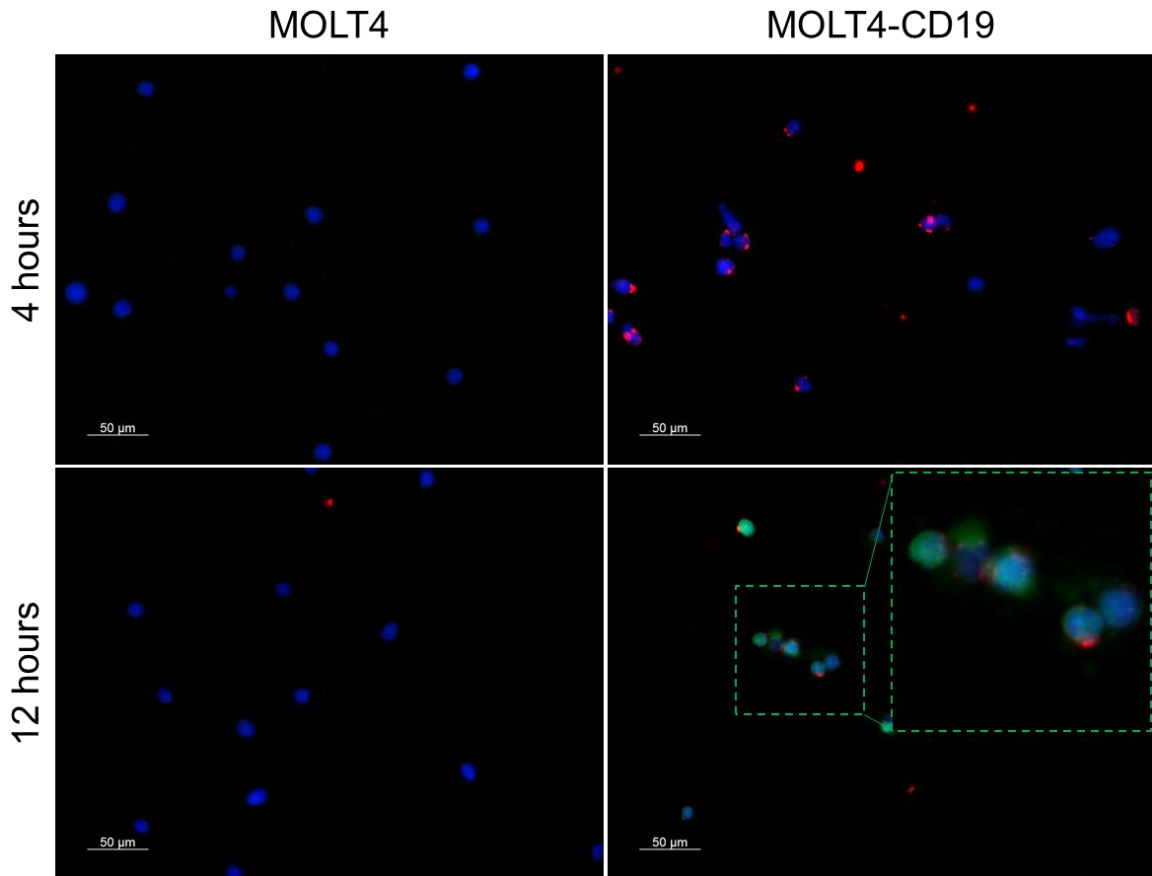
B.6 – High resolution imaging of MOLT4 and MOLT4-CD19 (blue) cells incubated with YO-PRO®-1 loaded CD19 antibody-targeted protocells at 4 and 12-hour time points. There is no significant binding by CD19 targeted protocells in the parental MOLT4 cell line, however we see significant binding at 4 hours and 12 hours with YO-PRO®-1 release in the targeted cells only. Inset (bottom right) highlights a cluster of cells with a high degree of YO-PRO®-1 release. These images correspond to **Figure 5.21**.

B.7 – Additional CD19-targeted Protocells and MOLT4, MOLT4-CD19, and NALM6 Cell in the CAM
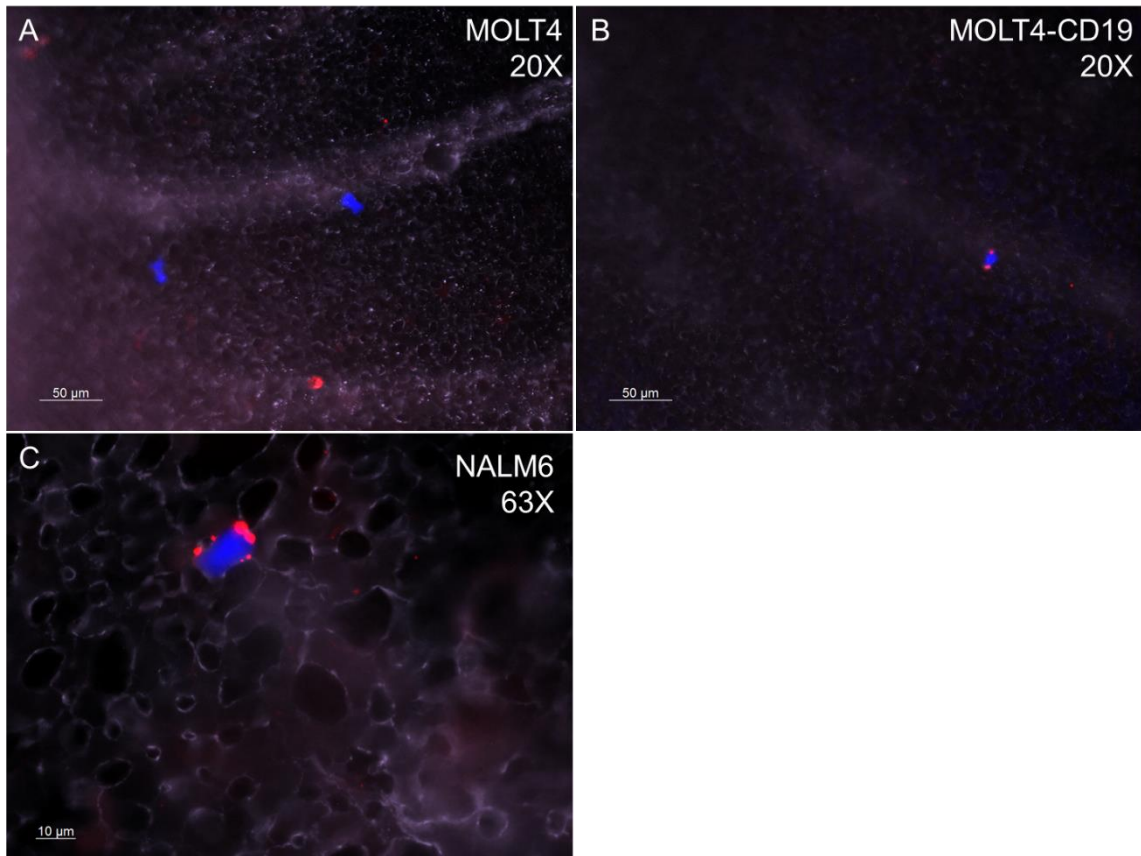
B.7 - Intravital fluorescent microscopy images acquired *ex ovo* in the CAM model showing red fluorescent CD19-targeted protocells circulating 4 hours post-injection not binding to A) parental MOLT4 cells but binding specifically to B) MOLT4-CD19, and C) NALM6 cells. Lectin vascular stain (lavender) highlight the CAM vasculature. Images A) and B) acquired at 20x and C) at 63x magnification. Images correspond to **Figure 5.22**.